



University  
of Glasgow

Brotosudarmo, Tatas Hardo Panintingjati (2010) *Studies on the different types of LH2 complexes from the purple non-sulphur photosynthetic bacterium Rhodospseudomonas palustris strain 2.1.6*. PhD thesis.

<http://theses.gla.ac.uk/1619/>

Copyright and moral rights for this thesis are retained by the author

A copy can be downloaded for personal non-commercial research or study, without prior permission or charge

This thesis cannot be reproduced or quoted extensively from without first obtaining permission in writing from the Author

The content must not be changed in any way or sold commercially in any format or medium without the formal permission of the Author

When referring to this work, full bibliographic details including the author, title, awarding institution and date of the thesis must be given

Studies on the different types of LH2 complexes from  
the purple non-sulphur photosynthetic bacterium  
*Rhodospseudomonas palustris* strain 2.1.6

Tatas Hardo Panintingjati Brotosudarmo

Submitted in part fulfilment for the degree of Doctor of Philosophy



Department of Biochemistry & Cell Biology

Faculty of Biomedical & Life Sciences

University of Glasgow

2009

## Abstract

Some purple bacteria species, such as *Rhodopseudomonas palustris* 2.1.6, produce light harvesting antenna (LH2) with unusual absorption spectra when they are grown under low-light intensities. This ability is often related to the presence of multiple genes encoding the LH2 apoproteins. This thesis describes isolation of pure stable LH2s from *Rhodopseudomonas palustris* 2.1.6 grown at different light intensities, determination of the polypeptide composition of high- (HL) and low-light (LL) LH2 complexes and characterisation their spectroscopic properties using various optical spectroscopies. The question of whether rings with a heterogeneous apoprotein composition exist has been addressed by single-molecule spectroscopy. For the first time, direct evidence that individual LL LH2 complexes have a heterogeneous  $\alpha\beta$ -apoprotein composition has been found. Such mixed rings feature Bchl *a* molecules with both B820-like and B850-like site-energies. This finding was supported by a femtosecond study on the energy transfer reactions and exciton relaxations within both HL and LL LH2 complexes. This thesis also describes attempts to crystallise the HL and LL LH2s. Even though three-dimensional crystals of both HL and LL LH2 complexes only diffracted to low resolution, it was possible to use molecular replacement to obtain structures that suggest both these types of LH2s are nonamers.

## Table of contents

ABSTRACT.....	II
TABLE OF CONTENTS.....	III
LIST OF TABLES.....	VI
LIST OF FIGURES.....	VII
LIST OF ACCOMPANYING MATERIAL .....	XIV
ACKNOWLEDGEMENT .....	XV
AUTHOR’S DECLARATION.....	XVII
ABBREVIATION .....	XVIII
<b>1 INTRODUCTION .....</b>	<b>1</b>
1.1 Systematics of purple bacteria .....	2
1.2 Photosynthesis in purple bacteria .....	4
1.3 Interaction between molecules and light .....	6
1.3.1 Absorption .....	7
1.3.2 Fluorescence .....	8
1.3.3 Dipole-dipole interaction and energy transfer .....	9
1.3.4 Antenna complexes and reaction centres .....	11
1.4 The pigments .....	12
1.4.1 Bacteriochlorophyll .....	12
1.4.2 Carotenoid.....	15
1.5 Structures of Light-harvesting complexes .....	18
1.5.1 Structure of LH2.....	18
1.5.2 Structure of LH1-RC (Core) complexes .....	21
1.5.3 Variants of LH2 complexes .....	23
1.6 Excitons .....	25
1.7 Electronic energy transfer in LH2 .....	27
1.8 Regulation of photosynthetic unit .....	28
1.9 Principle of single molecule spectroscopy .....	32
1.10 Principles of protein crystallisation.....	37
1.11 Project background.....	41
1.12 Thesis aims .....	42

<b>2 MATERIALS AND METHODS .....</b>	<b>43</b>
2.1 Culture storage .....	43
2.2 Culture growth and harvest .....	43
2.3 Isolation of light-harvesting complexes.....	44
2.4 Characterisation of LH2 complexes .....	45
2.4.1 Apoprotein identification by NuPAGE Gels .....	45
2.4.2 Protein identification by mass spectroscopy .....	45
2.4.3 Bacteriochlorophyll assay.....	45
2.4.4 Carotenoid assay .....	46
2.4.5 Steady state absorption spectroscopy.....	47
2.4.6 Circular dichroism spectroscopy.....	47
2.4.7 Raman spectroscopy .....	48
2.5 Single molecule spectroscopy.....	48
2.5.1 Sample preparation .....	48
2.5.2 Experimental setup .....	49
2.6 Transient absorption measurements.....	50
2.7 Crystallisation .....	51
<b>3 ISOLATION, PURIFICATION AND CHARACTERISATION OF LH2 COMPLEXES .</b>	<b>53</b>
3.1 Isolation and purification protocols .....	53
3.1.1 Growing cells at different light intensities .....	53
3.1.2 Isolation, purification and identification of LH2 proteins .....	55
3.2 Spectroscopic characterisation.....	63
3.2.1 Photosynthetic membrane.....	63
3.2.2 LT absorption spectra of LH2 complexes .....	65
3.2.3 LT circular dichroism (CD) spectra of LH2 complexes .....	67
3.2.4 Resonance raman spectra of LH2 complexes.....	70
3.3 Carotenoid composition .....	73
3.4 Conclusions.....	75
<b>4 SINGLE MOLECULE SPECTROSCOPY OF LOW-LIGHT LH2 FROM <i>RPS. PALUSTRIS</i> .....</b>	<b>77</b>
4.1 Introduction.....	77
4.2 Results .....	78
4.3 Discussion .....	84
4.4 Conclusions.....	100
<b>5 LOW LIGHT ADAPTATION: ENERGY TRANSFER PROCESSES IN DIFFERENT TYPES OF LIGHT HARVESTING COMPLEXES FROM <i>RPS. PALUSTRIS</i> .....</b>	<b>101</b>
5.1 Introduction.....	101
5.2 Global analysis.....	101
5.3 Results and discussion .....	102

5.3.1	Analysis of ground state absorption spectra.....	102
5.3.2	Transition absorption spectra measurements.....	105
5.3.3	ET rate constants for HL from global fitting .....	111
5.3.4	Relaxation and dispersive decay of B850 excited states in LL samples .....	112
5.3.5	LH2 apoproteins vs. spectral properties of B850 Bchl a in LL.....	115
5.4	Conclusions.....	116
<b>6</b>	<b>B800-850 HL AND B800-LOW-850 LL LH2 COMPLEXES FROM <i>RPS. PALUSTRIS</i>: CRYSTALLISATION TRIALS AND LOW-RESOLUTION MODEL STRUCTURES .....</b>	<b>117</b>
6.1	Crystallisation trials.....	117
6.2	Low resolution model structure.....	123
6.2.1	HL LH2 complex .....	123
6.2.2	LL LH2 complex.....	127
6.3	Conclusions.....	130
<b>7</b>	<b>SUMMARY AND OUTLOOK .....</b>	<b>131</b>
<b>8</b>	<b>APPENDICES .....</b>	<b>133</b>
8.1	Composition growth media .....	133
8.1.1	C-succinate media (Bose, 1969) per litre .....	133
8.1.2	Concentrated base per 5 litre .....	133
8.1.3	Metos 44 per litre .....	133
8.1.4	Growth factor per 100 ml.....	134
8.2	Identification of major carotenoid isolated from HL and LL LH2 <i>Rps. palustris</i> by <sup>1</sup> H-NMR	135
8.3	MemStart screen (Molecular Dimension, UK).....	137
8.4	MemSys screen (Molecular Dimension, UK).....	138
8.5	MemGold screen (Molecular Dimension, UK) .....	139
8.6	Additive Screen (Hampton Research) .....	141
8.7	PEG /ION Screen (Hampton Research) .....	143
8.8	JCSG-Plus Screen (Molecular Dimension) .....	147
8.9	Figure of merit from the molecular replacement solutions and the refinement REFMAC	151
8.9.1	HL LH2 crystal P2 <sub>1</sub> .....	151
8.9.2	LL LH2 crystal C2.....	151
8.9.3	LL LH2 crystal P2 <sub>1</sub> .....	152
<b>9</b>	<b>LIST OF REFERENCES.....</b>	<b>153</b>
<b>10</b>	<b>BIOGRAPHY.....</b>	<b>168</b>

## List of tables

Table 1-1 Current genera of anoxygenic purple bacteria (taken from (Madigan, 2009)).....	3
Table 1-2 Comparison of single molecule fluorescence methods.....	37
Table 3-1 Peptide identification of the gel bands H1-H4 and L1-L4 (see Figure 3-4) by nLC-ESI-MS/MS.....	58
Table 3-2 Peptide identification of the gel bands H1, H2, L1 and L2 from the RESOURCE-Q purified LH2 complexes (Figure 3-6B) by nLC-ESI-MS/MS .....	62
Table 3-3 Retention times and $\lambda_{\max}$ wavelengths obtained from all five carotenoids identified in HL and LL LH2 complexes from <i>Rps. palustris</i> and the carotenoid standards used as references. The solvent was 2.5% (v/v) acetone in benzene.....	74
Table 3-4 Comparison of the amount (%) of all five carotenoids collected from HL and LL LH2 complexes <i>Rps. palustris</i> . .....	75
Table 4-1 The coordinates of the arrangement of Bchl <i>a</i> molecules in an LH2 complex according to the x-ray structural data. ....	93
Table 5-1 Fitting parameters for the reproduction of ground state absorption spectra (Figure 5-1) at 293 K (values for 77 K are in brackets). All data are in meV except the ratio $r(\Gamma_{1H}/\Gamma_{1L})$ , which has no unit.....	104
Table 5-2 Rate constants from global fitting of transient absorption spectra; $k_1$ for energy transfer B800→B850 is not dispersive, $k_2$ for the process of exciton relaxation has the dispersive parameter $\gamma_2$ ; $k_3$ for exciton decay to the ground state with dispersive parameter $\gamma_3$ . .....	112
Table 6-1 Initial crystallisation conditions tested with the LH2 complexes from <i>Rps. palustris</i> . .....	117
Table 6-2 Optimisation of the initial crystallisation conditions of LH2 complexes from <i>Rps. palustris</i> . .....	119
Table 6-3 Summary of data-processing statistics for a HL LH2 crystal .....	124
Table 6-4 Summary of data-processing statistics for the LL LH2 crystals .....	127

## List of figures

Figure 1-1 Schematic representation of intracytoplasmic membrane of purple bacteria <i>Rba. sphaeroides</i> (adapted from Naylor et al. 1999 (Naylor <i>et al.</i> , 1999)).	6
Figure 1-2 The Jablonski diagram displaying processes occurring after a molecule absorbs a photon. Abbreviations: A-absorption (black solid arrow); F-fluorescence (black heavy solid arrow); P-phosphorescence (black double dashed arrow); IC-internal conversion (red dashed arrow); VR-vibrational relaxation (blue arrow); ISC-intersystem crossing (green dashed arrow).	7
Figure 1-3 Effect of the strength of interaction ( $V$ ) and the site energy difference ( $\Delta E_{nm}$ ) on the energy level of two molecules $ n\rangle$ and $ m\rangle$ . A. In the case of weak coupling interaction the excitation energy is localised on the individual pigments. B. In the case of strong coupling interaction this results two new delocalised exciton states.	10
Figure 1-4 Chemical structure of Bchl <i>a</i> according to IUPAC. The grey arrows denote the $Q_x$ and $Q_y$ dipole moments, respectively.	12
Figure 1-5 The pattern of the $\pi$ -frontier orbitals of the porphyrins according to the Gouterman four-orbital model are shown in colour (Gouterman, 1978). Orbitals $e_{gx}$ and $e_{gy}$ : LUMO; $a_{2u}$ and $a_{1u}$ : HOMO; classification according to $D_{4h}$ point group. Here the different phases of the p orbital are shown in red (+) and in blue (-). The big arrows indicate the x and y axes.	14
Figure 1-6 Scheme of energy of molecular orbital for porphyrin, chlorin and bacteriochlorin (Hanson, 1991).	14
Figure 1-7 Influence of the conjugation system shown on the room temperature (RT) steady state absorption spectra of cyclic conjugated tetrapyrroles in organic solvent. Shown are the spectra of the porphyrin type (PChlide <i>a</i> = protochlorophyllide <i>a</i> ), the chlorin type (Chl <i>a</i> = chlorophyll <i>a</i> ) and the bacteriochlorin type (Bchl <i>a</i> = bacteriochlorophyll <i>a</i> ) and the assignments of the major absorption bands according to the four-orbital model. This figure is taken from (Scheer, 2003).	15
Figure 1-8 Lycopene: the chemical structure and its steady state RT absorption spectrum in MeOH. Taken from (Shinichi, 2004).	16
Figure 1-9 The high resolution (2.0 Å) structure of LH2 complex from <i>Rps. acidophila</i> 10050 (Papiz <i>et al.</i> , 2003). A. Front and side views of the LH2 complex showing nine-membered circular module of $\alpha$ - (cyan) and $\beta$ - (green) polypeptides with B800 Bchl (blue), B850 Bchl (red) and the carotenoid (orange) (B). The spatial organisation and distances between the Bchl <i>a</i> pigments in LH2. The numbers indicate the size of LH2 and centre-to-centre distances between the macrocycles of the Bchl <i>a</i> molecules in Å. The arrows indicate the direction of the $Q_y$ transition moments. The phytol chain is cropped off for clarity. (SEE AVAILABLE MOVIE). C. The room temperature absorption spectrum of LH2 complex. The red and blue lines correspond to B850 and B800, respectively.	18
Figure 1-10 Diagrams showing the binding pocket of the B850 Bchl <i>a</i> (A) and the B800 Bchl <i>a</i> (B). The coordinates for this figure were taken from the high resolution (2.0 Å) structure of the LH2 complex from <i>Rps. acidophila</i> 10050 (PDB: 1NKZ) (Papiz <i>et al.</i> , 2003).	19
Figure 1-11 Diagram showing the interaction of the phytol chain of the B800 Bchl <i>a</i> (blue) and $\beta$ -bound Bchl <i>a</i> (red) (A) and the position of all- <i>trans</i> carotenoid rhodopin-glucoside in the heterodimeric pair of $\alpha\beta$ -polypeptides. The coordinate is taken from high resolution (2.0 Å) structure of LH2 complex from <i>Rps. acidophila</i> 10050 (Papiz <i>et al.</i> , 2003).	20
Figure 1-12 A. The room temperature absorption spectrum of LH1-RC "Core" from <i>Rps. palustris</i> . B. The crystal structure at 4.8 Å resolution of LH1-RC from <i>Rps. palustris</i> (Roszak <i>et al.</i> , 2003). C. The recent model of the dimeric LH1-RC from <i>Rba. sphaeroides</i> (Sener <i>et al.</i> , 2009).	21
Figure 1-13 Room temperature (RT) steady state absorption spectra of the B800-850 (black line) and the B800-820 (red line) LH2 complexes from <i>Rps. acidophila</i> 7050 (A)	

(Figure courtesy of Dr. Alastair T. Gardiner). (B) The RT absorption spectra of B800-850 (black line) and B800-low-850 (red line) LH2 complexes from <i>Rps. palustris</i> 2.1.6. ....	23
Figure 1-14 Comparisons of the $\alpha$ - and $\beta$ -bound Bchl <i>a</i> in B850 (green) and B820 (cyan) LH2. A. Diagram showing the interaction of the C <sub>3</sub> -acetyl group of Bchl <i>a</i> with the key potential H-bonding residues. B. Highlighting the twisting of the C <sub>3</sub> -acetyl group of Bchl <i>a</i> with respect to the bacteriochlorin plane. The coordinates used to produce this figure were taken from the high resolution (2.0 Å) structure of B800-850 LH2 complex from <i>Rps. acidophila</i> 10050 (Papiz <i>et al.</i> , 2003) and the 3.0 Å resolution structure of the B800-820 LH2 from <i>Rps. acidophila</i> 7050 (PDB: 1IJJ) (McLuskey <i>et al.</i> , 2001). (SEE AVAILABLE MOVIE).....	24
Figure 1-15 The energy level scheme of the excited state manifold of the B850 ring of LH2 ( <i>Rps. acidophila</i> ) (Matsushita <i>et al.</i> , 2001). The symmetric and antisymmetric manifolds consist of one nondegenerate, A, ( $k = 0$ ) and four doubly degenerate, E, ( $k = \pm 1, \pm 2, \dots, \pm 4$ ). ....	26
Figure 1-16 Model for photosynthetic unit (PSU) of purple bacteria showing the light-harvesting complexes (LHs) and the reaction centre (RC) (adapted from (Law <i>et al.</i> , 2008)). The flow energy transfer is also illustrated. (SEE AVAILABLE MOVIE).....	27
Figure 1-17 Schematic diagram of the major known regulatory components of photosynthetic unit gene expression in <i>Rba. sphaeroides</i> . Green corresponds to the components that act as effectors of gene expression. Red stands for the sensory components. The component in blue (PpsR) can function as both sensor and effector. The genes are shown in boxes. (+) means enhances expression of target gene; (-) means represses expression of target gene; ? indicates putative pathway of regulation; P <sub>i</sub> is inorganic phosphate. Taken from (Law <i>et al.</i> , 2008). ....	29
Figure 1-18 The polycistronic <i>puf</i> and <i>puc</i> operons encode the pigment binding proteins of <i>Rba. capsulatus</i> and <i>Rba. sphaeroides</i> . Taken from (Klug, 1993). ....	30
Figure 1-19 A sequence comparison of selected LH2 $\alpha$ - and $\beta$ -polypeptides. The <i>Rps. palustris</i> (Pal-) sequences have been deduced from gene sequences. Both the <i>Rps. acidophila</i> (Ac-) and <i>Phs. molischianum</i> (Molisch-) sequences are from the proteins. The amino acid highlighted in the red boxes are the ones that control the spectral shifts of the tightly coupled Bchl <i>a</i> molecules. ....	31
Figure 1-20 Point-spread-function (PSF) at the focal plane (A) and numerical aperture (NA) with focal point into PSF (B). Adapted from (Murphy, 2001) ....	33
Figure 1-21 Rayleigh criterion for spatial resolution. (a) Profile of a single diffraction pattern: The bright Airy disk and 1 <sup>st</sup> - and 2 <sup>nd</sup> -order diffraction rings are visible. (b) Profile of two disks separated at the Rayleigh limit such that the maximum of a disk overlaps the first minimum of the other disk: The points are now just barely resolved. (c) Profile of two disks at a separation distance such that the maximum of each disk overlaps the second minimum of the other disk: The points are clearly resolved. Taken from (Murphy, 2001). ....	35
Figure 1-22 Single molecule fluorescence microscopy methods. The laser beam is in green and the fluorescence from the sample is in red. In wide-field the molecules spread over an area are simultaneously excited by a widened laser beam. In confocal, the laser beam is focused into the diffraction limited focal volume. The pinhole assures that only light from the focal volume is detected. ....	36
Figure 1-23 Schematic illustration of a protein crystallisation phase diagram, a systematic approach in crystallography (Chayen, 2004). Methods used in crystallisation are (i) batch, (ii) vapour diffusion, (iii) Dialysis, and (iv) free interface diffusion. The black spot indicates the initial condition of the protein. The progress of the protein crystallisation is indicated in dashed lines. The arrows indicate the final state. ....	38
Figure 1-24 Typical apparatus used for vapour diffusion crystallisation. For hanging drops (A), the protein droplet hangs from the lid (D), whereas for the case of sitting drops (B), the protein droplet sits in the bridge well (E). The vapour diffusion plate from EasyXtal (QIAGEN) (C) offers 24-well plates easier setup for hanging or sitting drop. Bridges (E) are needed for sitting drop.....	39
Figure 2-1 A. Stab culture of purple bacteria in agar media on the laboratory shelf. B. Liquid cell culture in 500 ml flat-sided bottles placed in the high-light area. C. Growing	

cultures at different light intensities by varying the distance of the culture from the light bulb.....	44
Figure 2-2 Optical setup for 1.4K single molecule spectroscopy. The objective is a single aspheric lens (NA 0.55).....	49
Figure 3-1 (A) Room temperature absorption spectra of whole cells from <i>Rps. palustris</i> grown at decreasing light intensities: high-light (HL, 220 lx, black line), intermediate 1 low-light (LL1, 90 lx, red line), intermediate 2 low-light (LL2, 20 lx, green line), low-light (LL, 10 lx, blue line), far 1 low-light (FLL1, 6.5 lx, cyan line) and far 2 low-light (FLL2, 5.5 lx, magenta line). A magnification of the NIR region is shown (B).....	53
Figure 3-2 (A) Typical results of sucrose gradient centrifugation runs of <i>Rps. palustris</i> 2.1.6 solubilised membranes. From the left to the right the <i>Rps. palustris</i> 2.1.6 were grown at HL, LL1, LL2 and LL, respectively. The solubilised membranes of HL, LL1, LL2 and LL were adjusted to have an equal concentration of the Bchl <i>a</i> and then gently layered onto the top of the gradients. After high-speed centrifugation (149,000 g at 4°C) for 14 h the two major LH complexes were separated. The two complexes have different colour, the LH2 is red and the LH1-RC (core) is pink. The low-density cellular materials and denatured complex are yellow. (B) Absorption spectra of LH2 and LH1/RC (core) complexes collected from the HL sucrose gradient tubes. ....	55
Figure 3-3 The intensity ratio of bands B850:800 of the whole cell RT absorption spectra (red line) and molar ratio of LH2:Core (black) depending on the light intensity at which the cells were grown. The bars indicate standard deviations with n = 4. ....	56
Figure 3-4 Progress in purification of LH2 complexes examined by a NuPAGE 12% Bis-Tris-Gel. (A) Lane Core and LH2 succ correspond to the two complexes isolated from sucrose-density gradient. Lane LH2 DE52 indicates the LH2 after DE 52 purification. (B) The LH2 complexes were further purified by gel filtration.....	57
Figure 3-5 Elution profile of HL (A) and LL (B) LH2 complexes from <i>Rps. palustris</i> when purified using RESOURCE 15Q 1 ml. The LH2s were desalted using PD10 column prior to application. RESOURCE 15Q was connected to AKTA system and equilibrated with Tris-HCl (20mM, pH 8.0) containing 0.1% LDAO. Elution of the bound complex was achieved with a salt gradient 0-100% (1 M NaCl in Tris-HCl [20mM, pH 8.0] containing 0.1% LDAO). Flow rate was 4 ml min <sup>-1</sup> . The eluting protein was monitored at 280 nm and collected in 0.5 ml fractions. The purification experiments were carried out in the temperature-controlled room (4°C). ....	60
Figure 3-6 (A) The purity of the LH2 complexes was monitored using room temperature (RT) absorption spectrum. The absorption spectra of HL (top) and LL (bottom) LH2 complexes before (black line) and after (red line) purification using RESOURCE-Q are presented. The higher the ratio of A850/A280 (for HL) or A800/A280 (for LL), the greater is the purity of the LH complex is. (B) A NuPAGE 12% Bis-Tris gel profile of the apoproteins of the HL and LL LH2 complexes after their purification using the RESOURCE-Q column. The apoproteins are indicated in boxes. The large bands at the bottom correspond to pigments and lipids. ....	61
Figure 3-7 <i>In situ</i> identification of the LH2 and LH1-RC complexes in the intracytoplasmic membrane (ICM) can be directly demonstrated by absorption spectroscopy at cryogenic temperatures. Absorption spectra measured at 10 K of the photosynthetic membranes from <i>Rps. palustris</i> grown at high- (black line) and low-light (red line) intensities are shown. Membranes were prepared in 60% (v/v) glycerol in Tris-HCl (20 mM, pH 8.0). The spectra are normalized at Q <sub>x</sub> .....	63
Figure 3-8 Absorption spectra at 10 K of high-light (HL, black line), low-light intermediate 1 (LL1, red line), low-light intermediate 2 (LL2, green line) and low-light (LL, blue line) LH2 complexes. A. The absorption spectra at 350-950 nm regions. B. Magnification at NIR region. C. Difference spectra of LL1-HL (red line), LL2-HL (green line) and LL-HL (blue line) recorded at NIR region. The spectra are normalised at Q <sub>x</sub> band. The LH2 complexes were diluted in 60 % glycerol in Tris-HCl (20 mM, pH 8.0) containing 0.1% LDAO. ....	65
Figure 3-9 77K NIR Circular Dichroism (CD) spectra of HL (black line), LL1 (red line), LL2 (green line) and LL (blue line) LH2 complexes. The spectra are normalized at Q <sub>x</sub> band.....	67
Figure 3-10 A. Low-temperature UV resonance Raman spectra of the HL (black line), LL1 (red line), LL2 (green line) and LL (blue line) LH2 complexes. B. The magnification at	

- carbonyl region (1640-1710  $\text{cm}^{-1}$ ). The spectra were normalised at the 1609  $\text{cm}^{-1}$  peak. Excitation wavelength of 363.8 nm,  $T = 77$  K. ....70
- Figure 3-11 HPLC elution profile for the extracts from high- and low-light LH2 from *Rps. palustris* strain 2.1.6 The HPLC analysis was performed by the use of normal-phase chromatography using a silica gel column (Lichrosorb Si-60, 4.6×300 nm), the eluent was with 2.5% (v/v) acetone in benzene, the flow rate was 0.6 ml/min and the detection was at a wavelength of 480 nm. ....73
- Figure 4-1 LT (1.5K) widefield fluorescence images of low-light LH2 complexes from *Rps. palustris* showing the ensemble (A) and single LH2 complexes (B) are obvious after the LH2 complexes were diluted less than  $10^{-9}$  M in Tris-HCl buffer (20 mM, pH 8.0) containing 0.1% LDAO. Red circles indicate candidates for single LH2 complex. Green circle shows an aggregate. ....78
- Figure 4-2 LT (1.4 K) fluorescence-excitation spectra of LH2 complexes from LL *Rps. palustris* 2.1.6. The top traces show the spectrum from an ensemble (grey line) and the spectrum that corresponds to the sum of 31 spectra from individual LH2 complexes (black line). The lower three traces display typical fluorescence-excitation spectra from individual LH2 complexes. The spectra have been averaged over all polarisations of the incident laser field. The bars indicate the spectral positions of the 800, 820 and 850 nm bands, respectively. The excitation intensity was 50  $\text{W cm}^{-2}$ . The vertical scale is given in counted photons per second (cps). ....79
- Figure 4-3 Fluorescence-excitation spectra from an individual B800-820/850 LH2 complex from *Rps. palustris* as a function of the polarisation of the excitation light. (A) Top: Stack of 410 individual spectra recorded consecutively. Between two successive spectra the polarisation of the incident radiation has been rotated by  $6.4^\circ$ . The horizontal axis corresponds to the photon energy; the vertical axis to the scan number or equivalently to the polarisation angle and the intensity is given gray coded. The excitation intensity was 50  $\text{W cm}^{-2}$ . Bottom: Spectrum that corresponds to the average of the 410 consecutively recorded spectra. B) Top: Expanded view of the fluorescence intensity of the four bands B1 - B4 marked by the arrows in the lower part as a function of the polarisation of the incident radiation (dots) together with  $\cos^2$ -type functions (black) fitted to the data. Bottom: Two fluorescence-excitation spectra from the stack that correspond to mutually orthogonal polarisation of the excitation light. (SEE AVAILABLE MOVIE).....81
- Figure 4-4 Top: Distributions of the energetic separations  $\Delta E$  observed between A) B1 and B2, B) B1 and B3, and C) B1 and B4. Bottom: Distributions of the mutual angles  $\Delta\alpha$  between the transition-dipole moments that are associated with D) B1 and B2, E) B1 and B3, and F) B1 and B4. ....83
- Figure 4-5 Examples for simulated absorption spectra for an individual LH2 complex (solid line). The spectra correspond to a single realisation of the disorder. The calculated energies of the exciton states have been dressed by a Lorentzian with a width of 5  $\text{cm}^{-1}$  for the  $k=0$  state and a width of 130  $\text{cm}^{-1}$  for all other exciton states (dashed lines). The simulations A-C (left) are based on a nonameric structure; the simulations D-F (right) are based on an octameric structure. The simulations vary with respect to the type of diagonal disorder: A, D: random diagonal disorder taken from a Gaussian distribution of width 160  $\text{cm}^{-1}$  (FWHM). B, E: random diagonal disorder like for A, D and additionally correlated diagonal disorder. C, F: like B, E and additionally using B820-pair ( $E_0(\alpha\text{B820}) = 12,860 \text{ cm}^{-1}$ ,  $dE = 260 \text{ cm}^{-1}$ ) and B850-pair ( $E_0(\alpha\text{B850}) = 12,300 \text{ cm}^{-1}$ ,  $dE = 240 \text{ cm}^{-1}$ ) like randomly distributed site energies across the ring assembly. For more details see text. ....86
- Figure 4-6 Comparison of the energetic separation of the bands B1-B4 with those of the respective exciton states (left) and the mutual orientation of the associated transition-dipole moments (right) as predicted from Monte Carlo simulations for 2000 realisations of the disorder (circles, -○-) for the model shown in Figure 4-5E, (triangles, -△-) the model shown in Figure 4-5F and (squares, -■-) the model shown in Figure 4-5C. ....89
- Figure 4-7 Simulations of ensemble spectra of B850 band (black, red and blue lines) were overlaid on 10K absorption spectrum (grey line) of low-light LH2 from *Rps. palustris*. The simulations using the site energies of LH2 (B850, black line) [ $E_0(\alpha\text{B850}) = 12,300 \text{ cm}^{-1}$ ,  $E_0(\beta\text{B850}) = 12,060 \text{ cm}^{-1}$  (B850-pair) (Hofmann *et al.*, 2004)] and LH3 (B820, red line) [ $E_0(\alpha\text{B820}) = 12,860 \text{ cm}^{-1}$ ,  $E_0(\beta\text{B820}) = 12,600 \text{ cm}^{-1}$  (B820-pair) (de Ruijter *et al.*, 2007)]. The blue line shows a simulation using the site-energies of  $E_0(\alpha\text{B820-like}) = 12,640 \text{ cm}^{-1}$

with  $dE = 240 \text{ cm}^{-1}$  and the B850-pair site energy of  $E_0(\alpha\text{B850}) = 12,300 \text{ cm}^{-1}$  with  $dE = 240 \text{ cm}^{-1}$ ; the position of the pairs are randomly distributed. 3000 realisations were carried out in order to build the simulated ensemble spectra. ....91

Figure 4-8 A schematic representation of the transition-dipole moments and the coordinate arrangement of the  $\alpha$ - and  $\beta$ -bound Bchl *a* molecules in the xy-plane (left) and zy-plane (right). The  $|n_\alpha\rangle$  etc. correspond to the wavefunctions of the electronically excited state localised on the  $\alpha$ -bound Bchl *a* molecule in dimer *n*, respectively. The strongest contributions to the interaction result from the matrix elements for the intradimer nearest-neighbour interaction  $V_{n,i}$ , the interdimer nearest neighbour interaction  $V_{n,e}$ , the  $\alpha$ -next-nearest-neighbour interaction  $W_\alpha$ , and the  $\beta$ -next-nearest-neighbour interaction  $W_\beta$ , respectively. The geometrical arrangement of the  $\alpha$ - and  $\beta$ -bound Bchl *a* molecules are defined by the radius of  $\alpha$ - and  $\beta$ -unit circle in xy-plane  $R_u$  ( $u = \alpha, \beta$ ), the geometrical angle of the pigment of  $\alpha$ - and  $\beta$ -unit in xy-plane  $A_u$ , the in-plane tilt of the transition-dipole moment of the  $\alpha$ - and  $\beta$ -Bchl *a* from the circular tangent in xy-plane  $\Pi_u$ , the height differences between the centres of the  $\alpha$ - and  $\beta$ -Bchl *a* in the z-plane  $dH_u$ , and the out-of-plane tilt of the transition-dipole moment of the  $\alpha$ - and  $\beta$ -Bchl *a* in the z-plane  $\Phi$ . The actual values of these parameters are summarised in Table 4-1 together with the respective data for LH2 and LH3 from *Rhodospseudomonas acidophila*. The circles with the dashed line help to orient our eyes. ....92

Figure 4-9 Extended simulations based on the model shown in Fig. 4C, i.e. a nonameric structure with random- and correlated diagonal disorder and multipolypeptide composition. The B820-like-pair site-energies of  $E_0(\alpha\text{B820}) = 12,640 \text{ cm}^{-1}$  with  $dE = 240 \text{ cm}^{-1}$  and the B850-pair site energy of  $E_0(\alpha\text{B850}) = 12,300 \text{ cm}^{-1}$  with  $dE = 240 \text{ cm}^{-1}$ . The position of the B820-like-pairs are randomly distributed. ....94

Figure 4-10 Extended simulations based on the nonameric structure model with random- and correlated diagonal disorder and multipolypeptide composition. Top: The model structures show variations in positioning the B820-like-pairs (red lines, the dashed red lines indicate the  $\alpha$ -bound-Bchl*a*). Bottom: Comparison of the experimental data with the Monte Carlo simulation (2000 realisations) of model A (squared black lines), model B (squared red lines) and model C (squared green lines). B820-like-pair site-energies of  $E_0(\alpha\text{B820}) = 12,640 \text{ cm}^{-1}$  with  $dE = 240 \text{ cm}^{-1}$  and the B850-pair site energy of  $E_0(\alpha\text{B850}) = 12,300 \text{ cm}^{-1}$  with  $dE = 240 \text{ cm}^{-1}$ . ....95

Figure 4-11 Extended simulations from Figure 4-10 showing the model structures with more variations in positioning the B820-like-pairs pairs (red lines, the dashed red lines indicate the  $\alpha$ -bound-Bchl*a*). Bottom: Comparison of the experimental data with the Monte Carlo simulation (2000 realisations) of model A (squared black lines), model B (squared red lines) and model C (squared green lines). B820-like-pair site-energies of  $E_0(\alpha\text{B820}) = 12,640 \text{ cm}^{-1}$  with  $dE = 240 \text{ cm}^{-1}$  and the B850-pair site energy of  $E_0(\alpha\text{B850}) = 12,300 \text{ cm}^{-1}$  with  $dE = 240 \text{ cm}^{-1}$ . ....96

Figure 4-12 Top: Model structure that features 6 820-like-pair Bchl *a* molecules pairs (red lines, the dashed red lines indicate the  $\alpha$ -bound-Bchl*a*) distributed in  $C_3$  symmetry around the ring. Bottom: Comparison of the experimental data with the results from Monte Carlo simulations (2000 realisations) for the nonameric structure as shown in the top part taking random- and correlated diagonal disorder into account (black squares). The site energies of the pigments have been chosen as detailed in Fig. 6. The intracomplex heterogeneity ( $\Gamma_{\text{intra}}$ ) is  $320 \text{ cm}^{-1}$ . The full and the dashed lines in the top part of the figure indicate the B820 like (dashed) and B850 like (full) site energies. ....97

Figure 4-13 Comparison between the experimental data and the summation of Monte Carlo simulations (each 2000 realisations) for best 8-mer, 9-mer and 10-mer models (black line), the summation for best 8-mer and 9-mer model (red line) and the simulation for best 10-mer model only (green line). ....98

Figure 4-14 Comparison of the experimental data with simulations based on octameric model structures with symmetrical (A) and unsymmetrical (B) distributions for the  $\alpha$ -B820-like Bchl molecules. The squared black lines and the squared red lines (bottom) correspond to the results based on the model A (top left) and on the model B (top right). ....99

Figure 5-1 Ground state absorption spectra (thick red lines, normalized to Bchl *a*  $Q_x$  band) as a function of growth conditions (rows) measured at two different temperatures (left

column, 77 K; right column, 293 K). Thick green lines: calculated spectra according to the model explained in the text; thin red lines: calculated $\Gamma_{1L}$ , thin blue lines: calculated $\Gamma_{1H}$ , thin black lines: molecular transition of $Q_y$ band in B800 molecule including vibronic progression. Panel D shows the labelling of the transitions that is used in the text.....	103
Figure 5-2 Contour plots of measured transient absorption spectra of LH2 complexes from <i>Rps. palustris</i> grown at four different illumination; changes in differential absorption (colour scale is identical in all four panels) is dependent on pump probe delay and probe energy are shown in high light (HL), two intermediate (LL1, LL2), and low light (LL) sample (A, B, C, and D, resp.); red colour, photoinduced absorption; green and blue, transient bleach. ....	106
Figure 5-3 Difference absorption spectra of LH2 complexes at individual pump-probe delays; HL complex (A) shows $\Gamma_{1L}$ transition, there is no change after 3.2 ps (pink curve), LL complex (D) presents an additional transition $\Gamma_{1H}$ changing till ~10 ps (yellow and olive curves); panels of intermediate samples LL1 and LL2 (B, and C, respectively) represent increasing contribution of $\Gamma_{1H}$ band to the spectra. In all panels: solid lines, measured values; dashed lines, global fit. The difference spectra ( $\Delta A$ ) is the absorption spectrum of the excited molecule minus the absorption spectrum of the molecule in the ground state. ....	107
Figure 5-4 Time traces of differential absorption spectra of LH2 complexes from HL (A), LL1 (B), LL2 (C) and LL (D) samples at three representative probe energies: 1.54 eV (805 nm), 1.48 eV (838 nm), and 1.35 eV (918 nm) (green, red, and black lines, resp.). Panels show processes from $t = 0$ until 20 ps, inserts processes until 200 ps. In all panels: solid lines, measured values; dashed lines, global fit.....	108
Figure 5-5 Photophysical model of energy transfer paths and associated rate constants between Bchl <i>a</i> molecules in the B800 and the B850 ring. Processes for HL and LL samples are given as solid and dashed arrows, and the population probes that can be detected in transient absorption are given as dot-dashed and dotted lines.....	110
Figure 5-6 Photoexcitation spectra of LH2 complexes calculated by global fitting of pump probe spectra. Absolute absorption cross-section spectra are given for the initial, intermediate and final photoexcitation (dotted, solid, and dashed lines, resp.) of HL, LL1, LL2, and LL complexes (A, B, C, and D, respectively).....	110
Figure 5-7 Differential spectra for LL, LL2, and LL1 samples (solid, dashed, and dotted line, respectively), calculated from second and third photoexcitation spectra. A clear signature of $\Gamma_{1H}$ band in each LL sample and no change in B800 bleach contribution (no sign of delayed B800→B850 ET) suggesting B850 exciton relaxation. ....	113
Figure 6-1 Typical results of initial crystallisation screens from HL and LL LH2 <i>Rps. palustris</i> grown at 20°C : .....	118
Figure 6-2 Monitoring the crystallisation process using a visualisation robot. In this example, the HL LH2 complex from <i>Rps. palustris</i> was crystallised using a condition from the MemGold screen containing 0.1 M Tris-HCl pH9.5, 0.1 M NaCl, 0.1 M MgCl <sub>2</sub> and 30% PEG 400. The reservoir volume was 50 $\mu$ l, while the sample drop size was 1 $\mu$ l (0.5 $\mu$ l LH2 protein:0.5 $\mu$ l precipitant). Temperature for the crystal growth was 20°C. (SEE AVAILABLE MOVIE).....	120
Figure 6-3 HL and LL LH2 crystals of <i>Rps. palustris</i> grown in 0.1 M Tris-HCl pH9.5, 0.1 M NaCl, 0.1 M MgCl <sub>2</sub> containing different PEG 400 concentration. 0.1 % LDAO was as the detergent. Temperature in the incubator was kept constant at 10°C.....	121
Figure 6-4 LL LH2 crystals of <i>Rps. palustris</i> grown in 0.1 M Tris-HCl pH9.5, 0.1 M NaCl, 0.1 M MgCl <sub>2</sub> containing different PEG 400 concentration. 0.1 % LDAO was used as detergent. Temperature in the incubator was kept constant at 19°C. ....	122
Figure 6-5 RT absorption spectra of a dissolved single crystal of HL (35% PEG 400, black line) and LL (37% PEG 400, red line) LH2. ....	123
Figure 6-6 Axial view (A) and side view (B) of the low resolution (6.5 Å) electron density map (at 1.5 sigma) of HL LH2 complex <i>Rps. palustris</i> generated by molecular replacement solution using B800-850 LH2 complex from <i>Rps. acidophila</i> 10050 as a model for the HL LH2 P2 <sub>1</sub> crystal. Viewed by Coot Program (Emsley <i>et al.</i> , 2004).....	126
Figure 6-7 Low resolution (6.7 Å) electron density map (at 1.5 sigma) of LL LH2 complex <i>Rps. palustris</i> generated by molecular replacement solution using model from B800-850	

LH2 complex from <i>Rps. acidophila</i> 10050 (A and B) and from <i>Phs. molischianum</i> (C and D). Image generated using the Coot Program (Emsley <i>et al.</i> , 2004). .....	128
Figure 6-8 Detailed view of the low resolution (6.7 Å) electron density map (at 1.5 sigma) of LL LH2 complex <i>Rps. palustris</i> , generated by molecular replacement solution using model from B800-850 LH2 complex from <i>Rps. acidophila</i> 10050, shows the occupancy of the electron density in $\alpha\beta$ -polypeptides as well as the B800 and B850 Bchl <i>a</i> molecules. ....	129

## List of accompanying material

This thesis is accompanied with a DVD containing movies of the following animations:

1. The structure of B800-850 LH2 complex from *Rps. acidophila* 10050.
2. An overlaid of the structure of B800-850 LH2 complex from *Rps. acidophila* 10050 and B800-820 LH2 complex from *Rps. acidophila* 7050.
3. A model for photosynthetic unit (PSU) of purple bacteria showing the light-harvesting complexes (LHs) and the reaction centre (RC) with the flow of the energy transfer.
4. 1.4 K fluorescence excitation spectra of a single LL LH2 complex.
5. A time course of crystallisation of HL LH2 complexes from *Rps. palustris* followed by the imaging robot.

## Acknowledgement

I would like to begin my sincere gratitude to my supervisor, Prof. Richard J. Cogdell FRS, for the opportunity to work in his laboratory, the use of the facilities, his excellent supervision and for opening the way for collaborative work with internationally reputable scientists across the globe. I always enjoyed having discussions with him. His infectious enthusiasm for science made my project intellectually stimulating and demanding, yet always become more interesting and exciting. It was a privilege to work under his supervision.

I acknowledge the European Commission through the Human Potential Program (Marie Curie Research Training Network BIMORE grant MRTN-CT-2006-035859) for funding my research, living expenses and travel allowance. I would like to thank Dr. Larry Luer, Instituto Madrileño de Estudios Avanzados (IMDEA) Nanociencia, Spain, as the coordinator of the project for providing superb communications and for fostering intensive collaborations between the Fellows across all disciplines through workshops, summer schools and project group meetings. I also would like to express my appreciation to all my BIMORE Fellows (Dr. Vladimira Moulisova, Sajjad Hoseinkhani, Stefan Bilan, Anna Kochalska, Jess Lycoops, Dr. Linda Zotti, Dr. Catherine Kitts, Dr. Petro Lutsyk, Dr. Marius Trouw and Dr. Ekaterina Obraztsova) for intellectual scientific discussions often enjoyed over a glass of beer.

I would like to thank to all my collaborators. Thanks are due to Prof. Jürgen Köhler, University of Bayreuth, Germany, for showing me the beauty of the single molecule technique, allowing me to work with the optics, stimulating and insightful discussions, training in analysing the data and entertaining me with mathematical equations. My thanks also go to Ralf Kunz and Paul Böhm for helping me in the optical alignment and for good chats accompanied with good Bavarian Weißwurst, sauerkraut and beer. I am very grateful again to Dr. Larry Luer during my stay in ULTRAS INFM Politecnico di Milano, Italy for the training in femtosecond optics and the data analysis. I thank Dr. Vladimira Moulisova for measuring my samples during her stay at ULTRAS INFM. I also thank Prof. Yasushi Koyama, Kwansai Gakuin University, Japan for the opportunity to experience

research in his laboratory and explore Japanese culture. I would like to thank Aaron Collins from Prof. Robert Blankenship's Laboratory, Washington University of St. Louis, for measuring my samples. I would also like to thank Dr. Andrew Gall, who gave me for the opportunity to visit Paris and for training me in low temperature absorption and resonance Raman measurements. I really enjoyed my stay at Saclay.

I would like to thank to Dr. Alastair T. Gardiner for his kind assistance, frontier help in training me to isolate and purify LH2, friendship and encouragement. Many thanks to Dr. Aleksander Roszak for taking me to the synchrotron and training me in how to test the crystals as well as helping me to process the data. I would like to extend my thanks to all members of Cogdell lab: June Southall, Dr. Nicola Picken, Dr. Vladimira Moulisova and Dr. Sarah Henry. Many thanks are also due to Gillian Young, Alette Brinth, Dr. Mads Gabrielsen and Dr. Dai Wang for their friendship and encouragement during my study.

I would like to extend my gratitude also to Prof. Hugo Scheer, Dr. Sebastian Mackowski and Dr. Stephan Wörmke for their many discussions, encouragement and with the writing of the paper about the peridinin-chlorophyll-protein from Dinoflagellates.

Special thanks to my wife, Leenawaty Limantara, for her steadfast love, motivation, encouragement and prayers. I would also like to thank to my parents for their constant support and prayers.

Finally, I would like to thank all of you, who read this thesis, find it useful and become encouraged to study further the early events in photosynthesis, especially the structure of, and the energy transfer in, light harvesting complexes. I hope this thesis will be helpful for your future studies!

## Author's declaration

This thesis has been written in accordance with the regulations of the University of Glasgow and is less than 50,000 words in length. This thesis is an original contribution, which describes work performed entirely by myself unless otherwise cited or acknowledged. Its contents have not previously been submitted for any other degree. The research for this thesis was performed between April 2007 and September 2009.

Parts of this thesis have been published in:

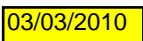
V. Moulisová, L. Luer, S. Hoseinkhani, T.H.P. Brotosudarmo, A.M. Collins, G. Lanzani, R.E. Blankenship, R.J. Cogdell (2009) Low light adaptation: Energy transfer processes in different types of light harvesting complexes from *Rhodopseudomonas palustris*, *Biophys. J.* 97: 3019-3028

T.H.P. Brotosudarmo, R. Kunz, P. Böhm, A.T. Gardiner, V. Moulisová, R.J. Cogdell and J. Köhler (2009) Single-molecule spectroscopy reveals that individual low-light LH2 complexes from *Rhodopseudomonas palustris* 2.1.6. have a heterogeneous polypeptide composition, *Biophys. J.* 97: 1491-1500

R.J. Cogdell, A.T. Gardiner, T.H.P. Brotosudarmo and H. Hashimoto (2008) A Comparative Look at the First Few Milliseconds of the Light Reactions of Photosynthesis, *Photochem. Photobiol. Sci.*, 7: 1150-1158

Signed.....  


Tatas Hardo Panintingjati Brotosudarmo

Date:  03/03/2010

## Abbreviation

Å	Ångström or Angstrom ( $10^{-10}$ m)
ATP	Adenosine-tri-phosphate
Bchl	Bacteriochlorophyll
Car	Carotenoid
CD	Circular dichroism
EET	Electronic energy transfer
ET	Energy transfer
FLL	Far low-light
FWHM	Full width at half maximum
HL	High-light
K	Kelvin (0 K = -273.15 °C)
LDAO	Lauryldimethylamine-oxide
LHC	Light harvesting complex
LL	Low-light
LLG	Log likelihood gain
LT	Low temperature
Lux	The SI unit of illuminance ( lumen per square meter)
<u>N</u>	Number of conjugated double bonds
NIR	Near infra-red
PEG	Poly(ethylene) glycol
PSF	Point spread function
PSU	Photosynthetic unit
$Q_x$ $Q_y$	Bacteriochlorophyll porphyrin ring dipole moment in the x- and y-planes respectively
RC	Reaction centre
RET	Resonance energy transfer
<i>Rps.</i>	<i>Rhodopseudomonas</i>
RR	Resonance raman
RT	Room temperature (293 K)
SE	Simulated emission
SMS	Single molecule spectroscopy
SNR	Signal to noise ratio

---

# 1 Introduction

---

*“All that is gold does not glitter, not all those who wander are lost;  
The old that is strong does not wither, deep roots are not reached by  
the frost. From the ashes a fire shall be woken, A LIGHT from the  
shadows shall spring; Renewed shall be blade that was broken, the  
crownless again shall be king.”*

A letter from Gandalf, which the innkeeper gives to Frodo (The Lord of the Rings, The Fellowship of the Ring Book 1, Chapter ‘Strider’)

Life on earth depends on photosynthesis. The process through which the energy of light is converted into the biochemical energy needed to sustain all life on earth. Long before the oxygenic phototrophs, e.g. green plants, algae and cyanobacteria, existed on the surface of the earth, the anoxygenic phototrophs evolved photosynthesis (Blankenship, 2002). They used light energy to produce ATP and utilized reductants, such as H<sub>2</sub>, H<sub>2</sub>S, or organic molecules, as electron donors to generate NADH and NADPH. Subsequently bacteria evolved the ability to split water and to produce oxygen. A new era then ensued, our atmosphere began to fill up with oxygen, and heterotrophic existence based on aerobic respiration became possible.

Early research on photosynthesis tried to understand the exact nature of the processes and the basic building blocks of the machinery that catalysed these processes. R. Emerson and W. Arnold conducted a clever experiment in 1932 to try to understand the basic building blocks (Rabinowitch *et al.*, 1969). They used a suspension of *Chlorella* cells, exposed them to flashing light (10<sup>-5</sup> sec) and measured the production of oxygen per flash. This experiment suggested that the cooperation of 2500 chlorophyll molecules is needed to produce one molecule of O<sub>2</sub>. This consideration led to the concept of the photosynthetic unit, the number of chlorophyll molecules required to work together to produce one O<sub>2</sub> molecule. The concept of photosynthetic unit has now been revised as the average number of (bacterio)chlorophyll molecules per reaction centre (RC) in the photosynthetic membrane (Messinger, 2008, Renger, 2008).

In the anoxygenic purple bacteria, the light absorbing photosynthetic apparatus is located in intracytoplasmic membranes. It consists of two types of pigment-protein complexes, the light-harvesting (LH) complexes and the reaction centres (RC). The LH complexes capture light energy and then transfer the energy efficiently to the RC, where the charge separation process is initiated leading to the synthesis of ATP. These processes have inspired the development of photovoltaic devices that mimic the photosynthetic apparatus (Makarow, 2008).

## 1.1 Systematics of purple bacteria

Anoxygenic phototrophic purple bacteria are photosynthetic gram-negative prokaryotes that can grow autotrophically with CO<sub>2</sub> as sole carbon source (Blankenship, 2002). Purple bacteria are currently classified into two main groups, purple sulphur bacteria (Gammaproteobacteria) and purple non-sulphur bacteria (Alpha- or Betaproteobacteria), according to their tolerance and utilisation of sulphide as an electron donor (Madigan, 2009).

**Table 1-1** lists the current recognized genera of purple bacteria. Over 25 genera of the sulphur purple and 20 genera of non-sulphur bacteria have been found and classified. In nature large masses of purple bacteria can be found in lakes, lagoons or even sewage. For example in lakes that contain high concentration of sulphide, such as Wintergreen and Burke in southwest Michigan, USA, layers of purple sulphur bacteria species such as *Thiopedia*, *Thiospirillum*, *Thiocystis* and *Chromatium* can be found (Caldwell *et al.*, 1975a, Caldwell *et al.*, 1975b). *Rba. sphaeroides*, *Rps. palustris* and *Blc. viridis* can all be found in the sewage plant in Göttingen, Germany, in large numbers ( $10^5$ - $10^6$  cells ml<sup>-1</sup>) (Siefert *et al.*, 1978).

Table 1-1 Current genera of anoxygenic purple bacteria (taken from (Madigan, 2009)).

Taxonomy/Phylogeny	Genus ( <i>abb.</i> )	Morphology	Species (Examples)
<b>Purple non-sulphur bacteria</b>	<i>Rhodobaca (Rca.)</i>	Cocci to short rods	<i>bogoriensis</i>
Alphaproteobacteria	<i>Rhodobacter (Rba.)</i>	Rods	<i>capsulatus, sphaeroides</i>
	<i>Rhodovulum (Rdv.)</i>	Rods-Cocci	<i>sulfidophilum</i>
	<i>Rhodospseudomonas (Rps.)</i>	Budding rods	<i>acidophila, palustris</i>
	<i>Rhodoblastus (Rbl.)</i>	Budding rods	<i>globiformis</i>
	<i>Blastochloris (Blc.)</i>	Budding rods	<i>sulfovirens, viridis</i>
	<i>Rhodomicrobium (Rmi.)</i>	Budding rods	<i>vanniellii</i>
	<i>Rhodobium (Rbi.)</i>	Rods	<i>marinum</i>
	<i>Rhodoplanes (Rpl.)</i>	Rods	<i>serenus</i>
	<i>Rhodocista (Rcs.)</i>	Spirilla	<i>centenaria</i>
	<i>Rhodospirillum (Rsp.)</i>	Spirilla	<i>rubrum, photometricum</i>
	<i>Phaeospirillum (Phs.)</i>	Spirilla	<i>molischianum</i>
	<i>Rhodopila (Rpi.)</i>	Cocci	<i>globiformis</i>
	<i>Rhodospira (Rsa.)</i>	Spirilla	<i>trueperi</i>
	<i>Rhodovibrio (Rhv.)</i>	Vibrio	<i>salinarum</i>
	<i>Rhodothallasium (Rts.)</i>	Spirilla	<i>salexigens</i>
	<i>Roseospira (Ros.)</i>	Spirilla	<i>mediosalina</i>
<i>Roseospirillum (Rss.)</i>	Spirilla	<i>parvum</i>	
Betaproteobacteria	<i>Rhodocyclus (Rcy.)</i>	Curled vibrios	<i>tenuis</i>
	<i>Rhodoferax (Rfx.)</i>	Rods, vibrios	<i>antarticus</i>
	<i>Rubrivivax (Rvi.)</i>	Rods, curved rods	<i>gelatinosus</i>
<b>Purple sulphur bacteria</b>			
<b>Gammaproteobacteria</b>			
Family <i>Chromatiaceae</i>	<i>Allochromatium (Alc.)</i>	Rods	<i>vinosum</i>
	<i>Amoebobacter (Amb.)</i>	Cocci in plates or clumps	<i>purpureus</i>
	<i>Chromatium (Chr.)</i>	Rods	<i>okenii, weissei</i>
	<i>Halochromatium (Hch.)</i>	Rods	<i>salexigens</i>
	<i>Isochromatium (Isc.)</i>	Rods	<i>buderi</i>
	<i>Laprobacter (Lpb.)</i>	Rods	<i>modestohapilophilus</i>
	<i>Laprocystis (Lpc.)</i>	Cocci in clusters	<i>roseopersicina</i>
	<i>Marichromatium (Mch.)</i>	Rods	<i>purpuratum</i>

	<i>Rhabdochromatium (Rbc.)</i>	Rods	<i>marinum</i>
	<i>Thermochromatium (Tch.)</i>	Rods	<i>tepidum</i>
	<i>Thioalkalicoccus (Tac.)</i>	Cocci	
	<i>Thiobaca (Tba.)</i>	Rods	
	<i>Thiocapsa (Tca.)</i>	Cocci	<i>roseopersicina</i>
	<i>Thiococcus (Tco.)</i>	Cocci	<i>pfennigii</i>
	<i>Thiocystis (Tcs.)</i>	Cocci to short rods	<i>violacea</i>
	<i>Thiodictyon (Tdc.)</i>	Rods in aggregates	<i>elegans</i>
	<i>Thioglavicoccus (Tfc.)</i>	Cocci	
	<i>Thiohalocapsa (Thc.)</i>	Cocci	<i>halophila</i>
	<i>Thiolamproyum (Tlp.)</i>	Cocci	<i>pedioforme</i>
	<i>Thiopedia (Tpd.)</i>	Cocci, often in plates	<i>rosea</i>
	<i>Thiorhodococcus (Trc.)</i>	Cocci	<i>minor</i>
	<i>Thiohodovibrio (Trv.)</i>	Vibrios to spirilla	<i>winogradskyi</i>
	<i>Thiospirillum (Tsp.)</i>	Spirilla	<i>jennese</i>
Family <i>Ectothiorhodospiraceae</i>	<i>Ectothiodhorospira (Ect.)</i>	Vibrios to spirilla	<i>shaposhnikovii</i>
	<i>Halorhodospira (Hlr.)</i>	Vibrios to spirilla	<i>neutrophilla</i>
	<i>Thiorhodospira (Trs.)</i>	Vibrios to spirilla	<i>sibirica</i>
	<i>Ectothiorhodosinus (Ets.)</i>	Rods	<i>mongolicus</i>

## 1.2 Photosynthesis in purple bacteria

Oxygenic phototrophs use H<sub>2</sub>O as a source of electrons to reduce CO<sub>2</sub> into organic compounds, for example carbohydrate, and produce oxygen. In 1930 Cornelis Bernardus van Niel studied the anoxygenic phototrophs, such as purple bacteria. He found that purple bacteria, in photoautotrophic growth, utilize H<sub>2</sub>S, other sulphur-containing compounds, or a variety of organic reductants, even H<sub>2</sub>, to assimilate CO<sub>2</sub> (Blankenship, 2002). As a result of his study he produced a general equation of photosynthesis



Where  $H_2A$  is e.g.  $H_2S$  in purple sulphur bacteria or succinic acid in purple non-sulphur bacteria. This formula is known as van Niel's equation as a tribute to his seminal contribution. This equation can be expanded:



The process of the  $CO_2$  fixation is actually driven by adenosine-tri-phosphate (ATP) and reduced nicotinamide-adenine-dinucleotide-(phosphate) (NAD(P)H), both which are formed during the light-dependent reactions. The light-dependent reactions in purple bacteria take place in and across intracytoplasmic membranes, in which the photosynthetic units embedded (**Figure 1-1**). First of all the electromagnetic radiation from the sun is captured by the pigments bound in the LH2 peripheral antenna (**Figure 1-1**). The resulting excitation energy is transferred from LH2 to LH1 and then on to the RC. The subsequent electron transfer within the RC produces a chemical potential gradient across the membrane and the resultant trans-membrane proton motive force is used by the ATP-synthase to generate ATP.

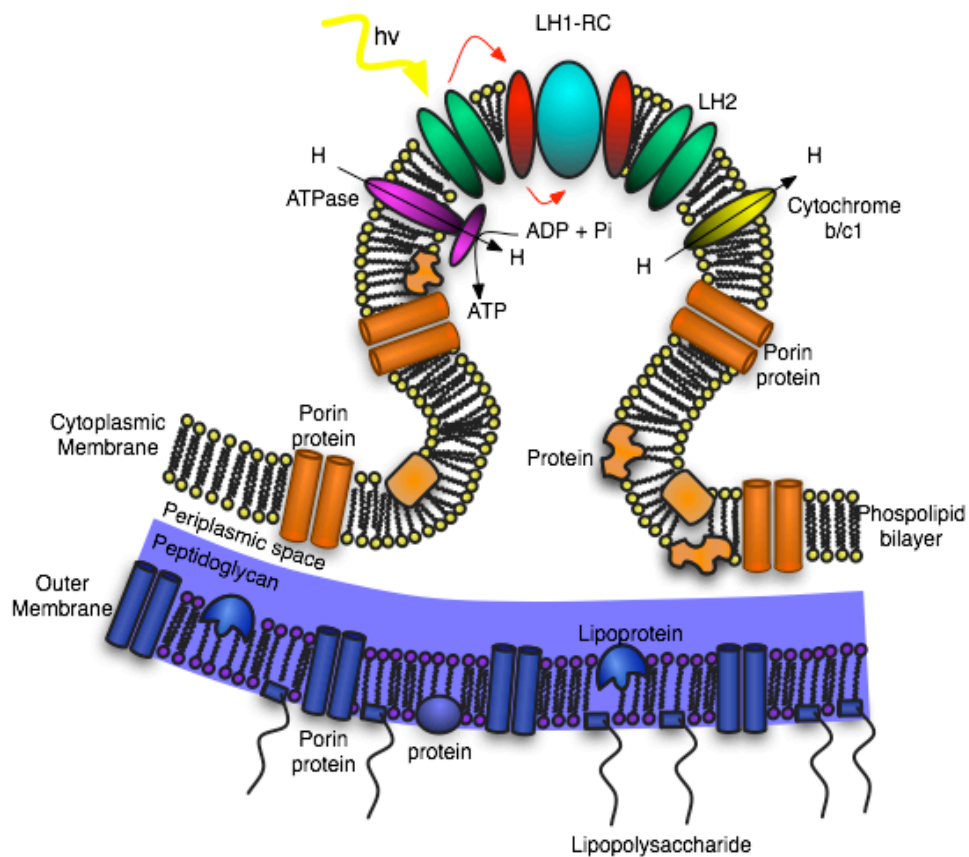
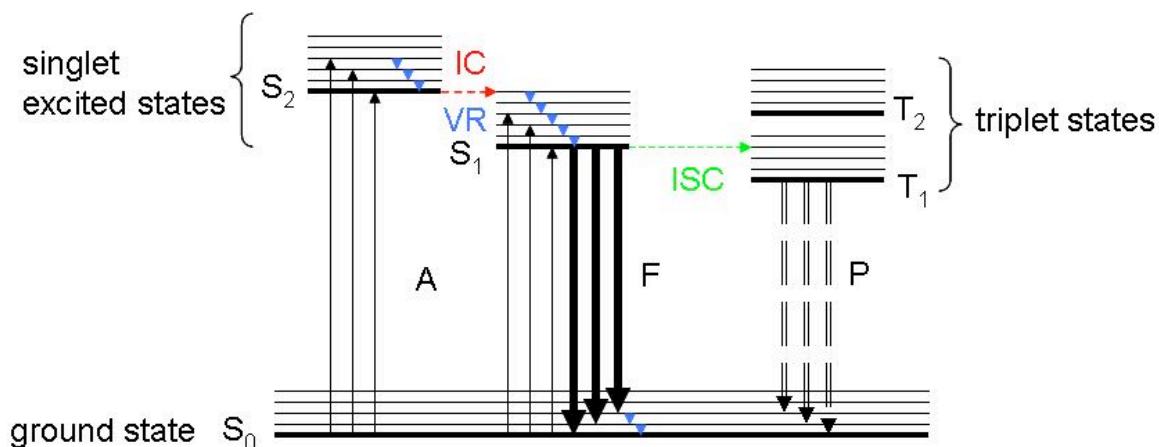


Figure 1-1 Schematic representation of intracytoplasmic membrane of purple bacteria *Rba. sphaeroides* (adapted from Naylor et al. 1999 (Naylor et al., 1999)).

### 1.3 Interaction between molecules and light

The interaction between molecules and light is best understood by the help of the Jablonski diagram as shown in **Figure 1-2**. The Jablonski diagram illustrates the electronic and vibrational levels of a molecule and the possible transitions between them. When a pigment absorbs light, it is promoted from the ground state ( $S_0$ ) to the excited state (e.g. the first singlet excited state,  $S_1$ , or the second singlet excited state,  $S_2$ ). A singlet state is a state of a molecule with zero net electron spin ( $S = 0$ ). For two electrons, a singlet state is one with antiparallel (paired) spins, and is denoted by  $\uparrow\downarrow$ .



**Figure 1-2** The Jablonski diagram displaying processes occurring after a molecule absorbs a photon. Abbreviations: A-absorption (black solid arrow); F-fluorescence (black heavy solid arrow); P-phosphorescence (black double dashed arrow); IC-internal conversion (red dashed arrow); VR-vibrational relaxation (blue arrow); ISC-intersystem crossing (green dashed arrow)

There are several processes possible after absorption of a photon by a molecule (**Figure 1-2**). If, after excitation, a higher vibrational level of  $S_1$  is reached, the excess vibrational energy will be quickly dissipated ( $10^{-13}$ - $10^{-12}$  s) by vibrational relaxation, resulting in the population of the lowest vibrational level of  $S_1$ . The internal conversion (IC) is a non-radiative transition between two electronic states of the same spin multiplicity ( $S_2$ - $S_1$  or  $T_2$ - $T_1$ ). Internal conversion is also possible from  $S_1$  to  $S_0$ . The efficiency of this transition depends on the energy gap between the vibrational ground state of  $S_1$  and higher vibrational levels of  $S_0$ . A radiative transition from  $S_1$  to  $S_0$  results in fluorescence. Intersystem crossing (ISC) is a non-radiative transition between a vibrational level of a singlet state to the isoenergetic vibrational level of a triplet state. ISC involves the flip of the spin, the electron spins then become unpaired (parallel,  $\uparrow\uparrow$ ) and the total spin quantum number,  $S = 1$ . ISC can be quite fast ( $10^{-7}$ - $10^{-9}$  s). A radiative transition from  $T_1$  to  $S_0$  is known as phosphorescence. This process is rather slow since it is formally forbidden.

### 1.3.1 Absorption

In the excitation process, the probability of photon absorption is given by the absorption cross-section ( $\sigma$ ), which corresponds to the fraction of the power absorbed by the acceptor averaged over all possible absorption dipole

orientations and the incident intensity (Valeur, 2001). The relationship between the molar extinction coefficient,  $\varepsilon$ , and the concentration of chromophore ( $c$ , in mol L<sup>-1</sup>) is expressed by the Beer-Lambert law:

$$A = -\log_{10}\left(\frac{I}{I_0}\right) = -\log_{10}(e^{-\varepsilon l c}) = \varepsilon l c \quad (1.1)$$

where  $A$  is absorbance,  $I_0$  is the intensity of incident light and  $I$  is the intensity of transmitted light.  $l$  denotes the path length of absorbing solution in cm.  $N$  is number or density of molecules.

### 1.3.2 Fluorescence

Fluorescence emission is a radiative relaxation from the  $S_1$  to the electronic ground state (Figure 1-2). The fluorescence band is located at higher wavelength (lower energy) than the absorption band because of energy loss in the excited state due to vibrational relaxation. The gap between the maximum of the lowest energy absorption band and the maximum of the fluorescence is called the Stokes shift.

The efficiency of the fluorescence process, the fluorescence quantum yield ( $\Phi_f$ ), is defined as the ratio of the number of photons emitted to the number of photons absorbed. It can be described using the rates of excited state decay by the formula (Valeur, 2001):

$$\Phi_f = \frac{k_r}{k_r + k_{nr}} \quad (1.2)$$

where  $k_r$  is the rate of radiative emission (fluorescence) and the  $k_{nr}$  is the rate of all possible non-radiative processes. The quantum efficiency of 0.9 indicates a very efficient fluorescence process, whereas  $\Phi_f = 0$  indicates that the molecule does not fluoresce.

### 1.3.3 Dipole-dipole interaction and energy transfer

After photoexcitation, the energy absorbed by a molecule, in principle, can be transferred efficiently to neighbouring molecules over a distance of several tens of angstroms through electronic energy transfer (EET). EET is also known as resonance energy transfer (RET), that is a transfer by inductive resonance. This process involves an electronic interaction promoting RET via a coupling of the transition dipole moments of donor and acceptor molecules due to a Coulombic interaction (Scholes, 2003, Turro, 1991). Two limits are distinguished: weak interaction, which leads to Förster type energy transfer, and strong interaction, leading to the formation of excitons.

The energy transfer process can be simply understood in a system of two interacting molecules  $n$  and  $m$ . The electronic interaction between the two pigments is mainly determined by the Coulombic interaction of the electrons and nucleus of one pigment with those of the neighbour and by an exchange interaction caused by overlap of molecular orbital of the adjacent pigments. The Coulombic interaction is often described by a dipole-dipole interaction between molecule  $n$  and  $m$ ,  $V_{nm}$ , that can be given by:

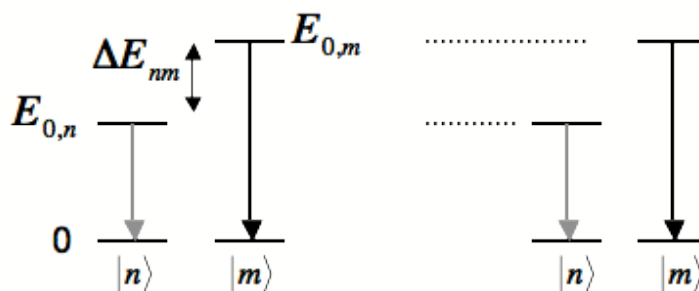
$$V_{nm} = \frac{1}{4\pi\epsilon} \frac{\mu^2}{r_{nm}^3} \kappa_{nm}, \quad \kappa_{nm} = \frac{1}{\mu^2} \left[ \left( \vec{\mu}_n \cdot \vec{\mu}_m \right) - 3 \frac{\left( \vec{\mu}_n \cdot \vec{r}_{nm} \right) \left( \vec{\mu}_m \cdot \vec{r}_{nm} \right)}{r_{nm}^2} \right] \quad (1.3 \ \& \ 1.4)$$

Where  $\vec{\mu}$  is the transition-dipole moment of the pigment. The magnitudes of dipole moments are in debye, D (1 D =  $3.33564 \times 10^{-30}$  C m). The distance between the transition-dipoles  $\vec{\mu}_n$  and  $\vec{\mu}_m$  is  $r_{nm}$ .  $\epsilon$  is the dimensionless permittivity of the medium. The mutual orientation and distance between the transition-dipole moments determines the orientation factor  $\kappa_{nm}$ , which is defined in terms of a unit vector. The electronically excited states of the pigments can be described by a Hamiltonian (Davydov, 1964)

$$H = \sum_{n=1}^N E_{0,n} |n\rangle\langle n| + \frac{1}{2} \sum_{n=1}^N \sum_{m \neq n} V_{nm} |n\rangle\langle m| \quad (1.5)$$

where  $N$  denotes the number of molecules ( $N = 2$  for dimer).  $|n\rangle$  and  $|m\rangle$  represent the excitation of the molecules,  $n$  and  $m$ , respectively.  $E_{0,n}$  is the site energy of an individual pigment  $n$ . Two limiting cases for the dipolar interaction can be distinguished. The weak coupling,  $|V/\Delta E_{nm}| \ll 1$ , is when the interaction between the transition-dipole moments is much smaller than the difference in site energies of two molecules ( $\Delta E_{nm} = |E_{0,n} - E_{0,m}|$ ). The result of weak coupling is that the excited state wavefunctions are localised on the individual pigments. Strong coupling,  $|V/\Delta E_{nm}| \gg 1$ , on other hand, occurs when the interaction is much stronger than the site energies between two molecules. As a result new delocalised excited states, namely excitons, are formed (Figure 1-3). The eigenfunctions of the excitons are no longer the eigenfunctions of the Hamiltonian (eq. 1.5), but new eigenfunctions are formed from linear combinations of the excited state wavefunctions of the pigments.

**A. Weak coupling:  $V \ll \Delta E_{nm}$**



**B. Strong coupling:  $V \gg \Delta E_{nm}$**

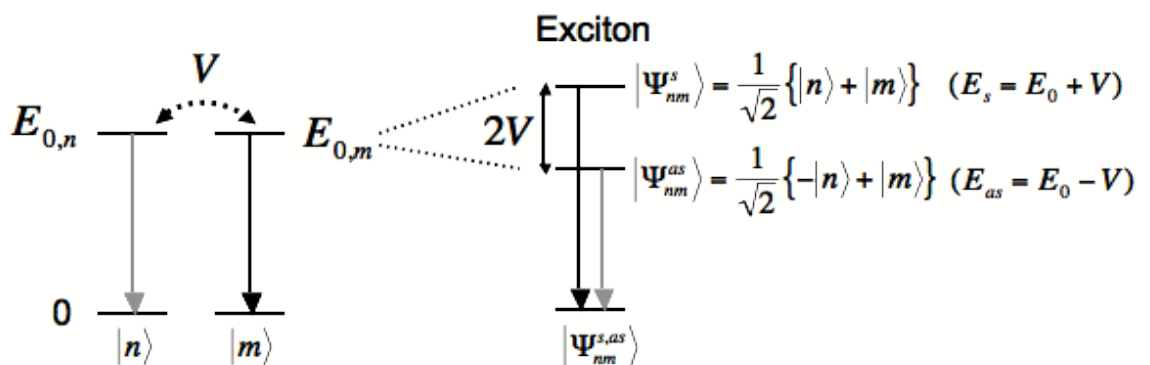


**Figure 1-3** Effect of the strength of interaction ( $V$ ) and the site energy difference ( $\Delta E_{nm}$ ) on the energy level of two molecules  $|n\rangle$  and  $|m\rangle$ . **A.** In the case of weak coupling interaction the excitation energy is localised on the individual pigments. **B.** In the case of strong coupling interaction this results two new delocalised exciton states.

These Frenkel excitons correspond to the two energy levels indicated in **Figure 1-3**. If the site-energies of the two molecule,  $|n\rangle$  and  $|m\rangle$ , are equal, the wavefunctions ( $|\Psi_{nm}^s\rangle$  and  $|\Psi_{nm}^{as}\rangle$ ) have equal amplitudes on both pigments. (**Figure 1-3**). Frenkel excitons can generally be described as follows

$$|k\rangle = \frac{1}{\sqrt{N}} \sum_{n=1}^N e^{i2\pi k \frac{n}{N}} |n\rangle \quad (1.6)$$

In case of weak coupling, i.e. the two molecules can still be thought as essentially independent of each other, it is appropriate to discuss the RET in term of the Förster theory. This theory is based on the equilibrium Fermi Golden Rule approach, in which the energy-transfer rate can be formulated as below (Cogdell *et al.*, 2006),

$$k_{DA} = \frac{2\pi}{\hbar} \int dE \left\langle \left\langle D\tilde{A} \left| V \right| \tilde{D}A \right\rangle \right\rangle^2 \rho(E) \delta(E_f - E_i) \quad (3)$$

where  $|\tilde{D}A\rangle$  denotes the initial condition with the donor in the excited state and the acceptor in the ground state. An interaction between donor and acceptor,  $V$ , is required for the energy transfer. In final state  $|D\tilde{A}\rangle$ , the donor is in the ground state, while the acceptor is in the electronic excited state.  $\rho(E)$  represents the density of states.  $\delta(E_f - E_i)$  ensures energy conservation for each particular energy-transfer process.

### 1.3.4 Antenna complexes and reaction centres

Photosynthesis could have evolved, in principle, only with RCs. However, this means, except under very high-light conditions, that there will be a relatively long time-gap between two photons reaching the same RC. A major problem will then occur because several of the redox reactions that take place within the reaction centres require multiple one-electron turnovers. If the RCs have to wait too long then back reactions will become favourable, and the whole charge-separation process becomes inefficient. The increased cross-sectional area for photon capture is achieved by LH complexes that enable the RCs to be supplied

with sufficient numbers of photons, thus the forward electron-transfer reactions take place frequently enough and the back reaction are reduced to a minimum (Cogdell *et al.*, 2008).

## 1.4 The pigments

As part of the building blocks of the LH complexes, the pigments function to absorb electromagnetic radiation. The major light-absorbing pigments in purple bacteria are bacteriochlorophyll *a* (Bchl *a*) or Bchl *b* and carotenoids. These pigments are non-covalently bound to two types of integral membrane proteins forming antenna complexes.

### 1.4.1 Bacteriochlorophyll

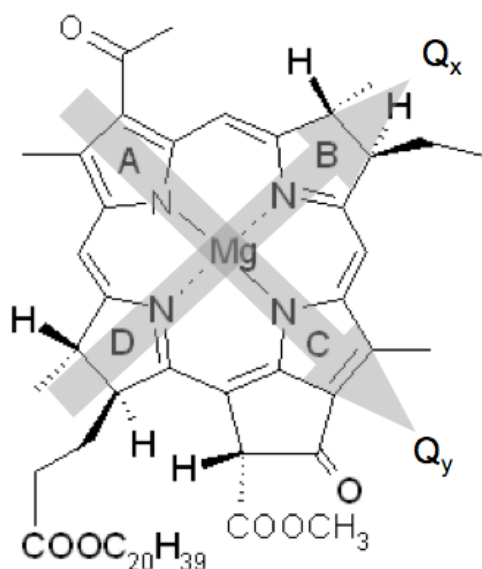


Figure 1-4 Chemical structure of Bchl *a* according to IUPAC. The grey arrows denote the  $Q_x$  and  $Q_y$  dipole moments, respectively.

Bchls are the major pigments found in anoxygenic photosynthetic bacteria. They are related to the chlorophyll, which is the primary pigment in plants, alga and cyanobacteria. The chemical structure of Bchl is a modified cyclic tetrapyrrole, with a structure comparable to that of the prosthetic heme group of haemoglobin and cytochromes, and is biosynthetically derived from

protoporphyrin IX (Scheer, 2003). The differences in the macrocycle between the Bchl and heme can be summarized as follows:

1. The central metal ion in the Bchl is  $Mg^{2+}$ , not  $Fe^{2+}$  or  $Fe^{3+}$ , although through coordination chemistry it can be replaced by several metal ions such as  $Ni^{2+}$ ,  $Pd^{2+}$ ,  $Zn^{2+}$ , etc.
2. In the Bchl *a*, *b* and *g* rings B are reduced.
3. The Bchl has a cyclopentanone ring, usually with an attached carboxylic ester group.
4. The propionyl group on ring D of Bchl *a* is generally esterified by the long-chain isoprenoid alcohol phytol.

There are three types of tetrapyrroles based on the degree of unsaturation of the macrocycle. The fully unsaturated porphyrins with an acrylic side chain at C-17 (porphyrin like system), 17,18-dihydrophorphyrins (chlorin system), and 7,8,17,18-tetrahydroporphyrins (bacterioporphyrin system) (Scheer, 1991, Scheer, 2003).

As Bchl *a* is a porphyrin derivative, the main characteristics of its optical spectrum can be understood in terms of the 4-orbital theory of Goutermann, by a perturbation of those of the porphyrin (Gouterman, 1978, Weiss, 1978). This model (**Figure 1-5**) was developed for the high-symmetry metallo-porphyrins ( $D_{4h}$ -symmetry) and, then applied, with minor modifications, to chlorin and bacteriochlorin structures (Gouterman, 1978, Weiss, 1978). The highest occupied molecular orbital (HOMO) consists of  $a_{2u}(\pi)$  and  $a_{1u}(\pi)$  orbitals and the lowest unoccupied molecular orbital (LUMO) consists of  $e_{gx}(\pi^*)$  and  $e_{gy}(\pi^*)$  orbitals. There are 4 transition possibilities (**Figure 1-5**). Those are the x-polarized transitions [ $a_{1u}(\pi) \rightarrow e_{gy}(\pi^*)$  and  $a_{2u}(\pi) \rightarrow e_{gx}(\pi^*)$ ], and the y-polarized transitions [ $a_{1u}(\pi) \rightarrow e_{gx}(\pi^*)$  and  $a_{2u}(\pi) \rightarrow e_{gy}(\pi^*)$ ]. The x and y refers to the B-D and A-C axes, respectively (**Figure 1-5**). The nomenclature of the principal electronic transitions are B (Soret) for the high energy transition  $a_{2u}(\pi) \rightarrow e_{gy}(\pi^*)$  denoted as  $B_y$  and  $a_{1u}(\pi) \rightarrow e_{gy}(\pi^*)$  denoted as  $B_x$ , hence Q for low energy transitions  $a_{2u}(\pi) \rightarrow e_{gx}(\pi^*)$  are denoted as  $Q_x$ , and  $a_{1u}(\pi) \rightarrow e_{gx}(\pi^*)$  denoted as  $Q_y$ .

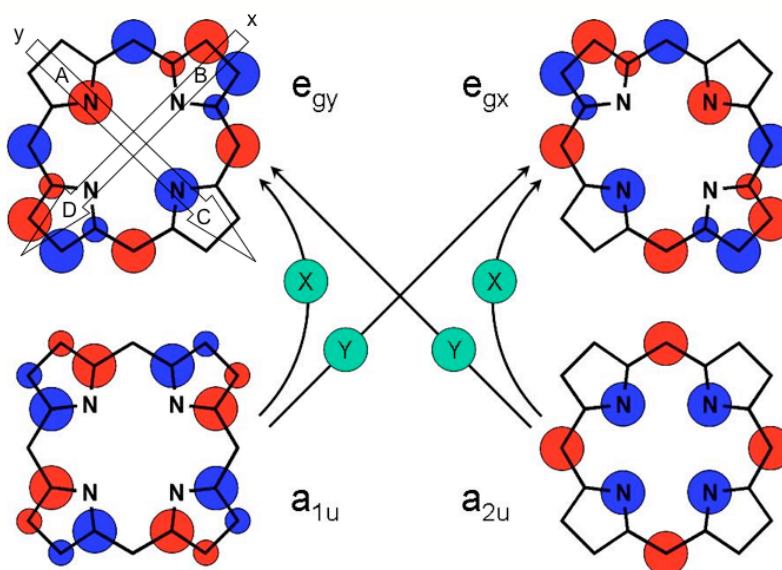


Figure 1-5 The pattern of the  $\pi$ -frontier orbitals of the porphyrins according to the Gouterman four-orbital model are shown in colour (Gouterman, 1978). Orbitals  $e_{gx}$  and  $e_{gy}$ : LUMO;  $a_{2u}$  and  $a_{1u}$ : HOMO; classification according to  $D_{4h}$  point group. Here the different phases of the p orbital are shown in red (+) and in blue (-). The big arrows indicate the x and y axes.

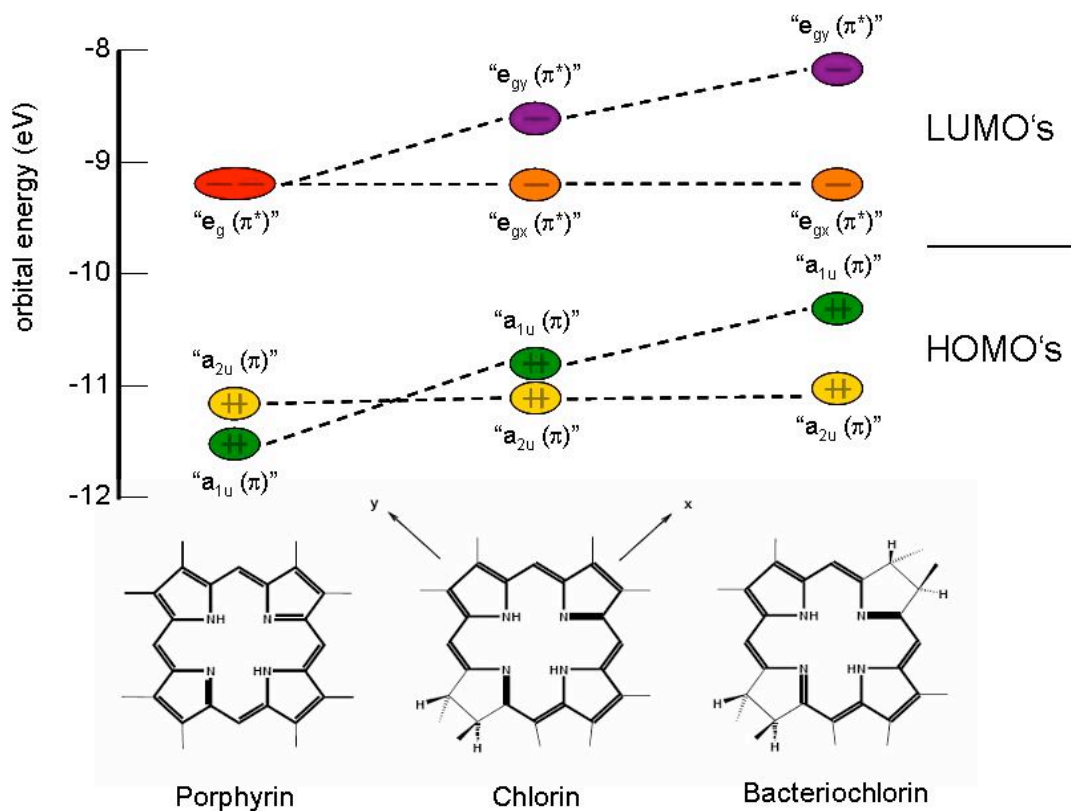
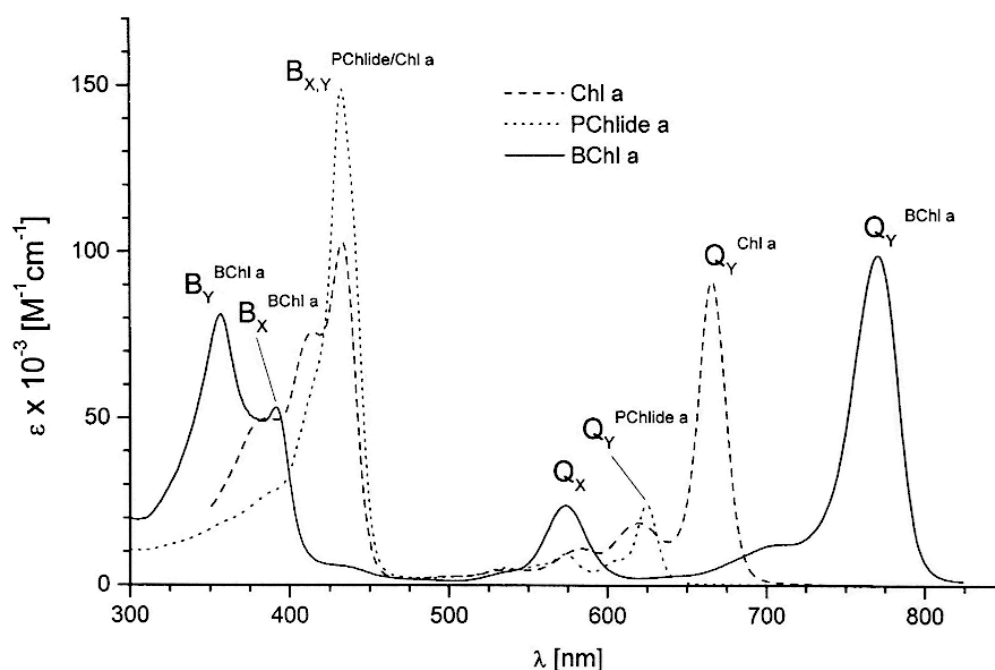


Figure 1-6 Scheme of energy of molecular orbital for porphyrin, chlorin and bacteriochlorin (Hanson, 1991)

When pyrrole rings B and/or D of the porphyrin are saturated (**Figure 1-6**), the  $a_{1u}(\pi)$  and  $e_{gy}(\pi)$  are raised in energy, whereas the  $a_{2u}(\pi)$  and  $e_{gx}(\pi^*)$  remain unaffected. Consequently, the energy gap between the  $a_{1u}$  HOMO and  $e_{gx}$  LUMO becomes smaller, the  $Q_y$  band shifts to the red and gains oscillator strength (Hanson, 1991). Of course, the  $D_{4h}$  symmetry is broken by saturation one or two of the pyrrole rings and, therefore the x-polarised transition will have considerably higher energy than the y-polarised one. Changes due to the reduction of the porphyrin-macrocycle at C-17, 18 in the chlorins (650-680 nm), and additionally at C-7, 8 the bacteriochlorins (750-800nm) can be seen clearly as a bathochromic shift of the lowest-energy absorption band (**Figure 1-7**).



**Figure 1-7** Influence of the conjugation system shown on the room temperature (RT) steady state absorption spectra of cyclic conjugated tetrapyrroles in organic solvent. Shown are the spectra of the porphyrin type (PChlide a = protochlorophyllide a), the chlorin type (Chl a = chlorophyll a) and the bacteriochlorin type (Bchl a = bacteriochlorophyll a) and the assignments of the major absorption bands according to the four-orbital model. This figure is taken from (Scheer, 2003).

### 1.4.2 Carotenoid

Carotenoids (Car) are classically diterpenes that consist of two  $C_{20}$ -units (originally geranyl-geraniol) joined tail-to-tail to form a chain of 32 carbon atoms bearing eight methyl side-chains (Frank, 1993). The photochemistry of Car can be traced to the electronic properties of their conjugated  $\pi$ -electron

system. The number of the conjugated C=C bonds in naturally occurring Cars ranges from 3 (e.g. phytoene) to 13 (e.g. spirilloxanthin). The excited state ordering of Cars is classified according to the  $C_{2h}$  point symmetry group. Within the  $C_{2h}$  symmetry group, the  $S_0 \rightarrow S_1$  transition from the  $1A_g^-$  ground state to the  $2A_g^-$  lowest electronic state is optically forbidden (Schulten *et al.*, 1972, Tavan *et al.*, 1986). The major optical absorption therefore arises from the allowed  $S_0 \rightarrow S_2$  transition, from the  $1A_g^-$  ground state to the  $1B_u^+$  state. It is generally split into several vibronic transitions, resulting in a series of three closely spaced absorption bands (Figure 1-8). Cars show different optical characteristics in various solvents, depending on the polarisability of the solvent (Frank, 1993, Kuki *et al.*, 1994, Nagae *et al.*, 1994).

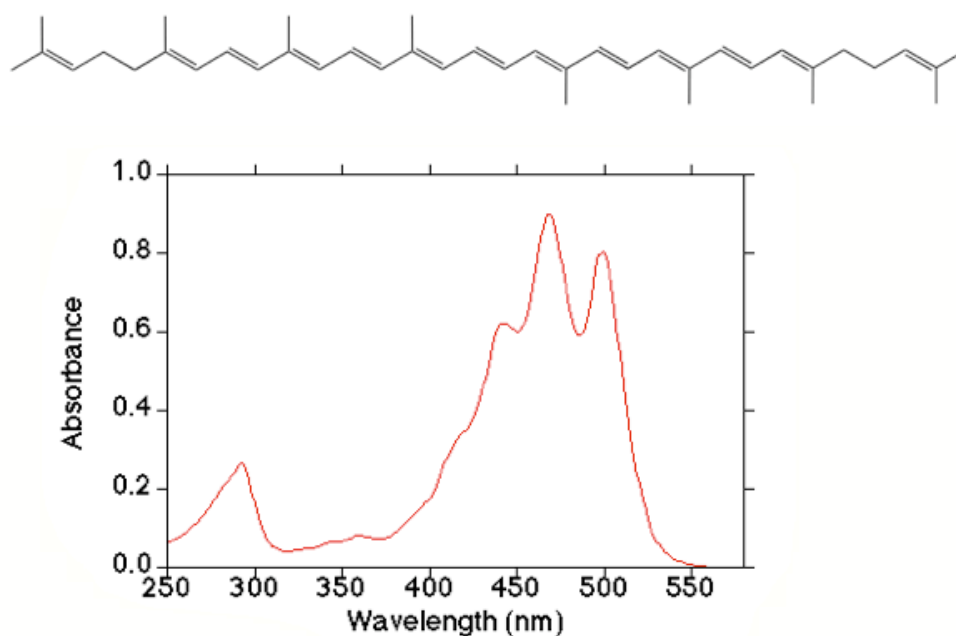


**Figure 1-8 Lycopene: the chemical structure and its steady state RT absorption spectrum in MeOH. Taken from (Shinichi, 2004)**

Cars have two major functions in photosynthesis: light harvesting and photoprotection (Cogdell *et al.*, 1987, Limantara *et al.*, 1998, Polli *et al.*, 2006). The Car absorption fills the “green gap” ( $\lambda_{\max} = 450\text{-}500$  nm), where the Bchls do not absorb efficiently and can transfer that absorbed energy to the Bchls molecules (Cogdell *et al.*, 1987, Frank, 1993, Griffiths *et al.*, 1955, Krueger *et al.*, 1999). The photoprotection function of the Car comes from their ability to quench the production of singlet oxygen, which is harmful to the cell

(Cogdell *et al.*, 1987, Foote *et al.*, 1970, Griffiths *et al.*, 1955). If cells of photosynthetic organism lacking Cars, such as the mutant *Rhodobacter (Rba.) sphaeroides* R26, are illuminated in the presence of oxygen, they sensitise their own death (Griffiths *et al.*, 1955, Hunter *et al.*, 1994, Lang *et al.*, 1994).

The photoprotective function of Cars is related to their ability to neutralise the singlet oxygen radical. From the excited singlet state, Bchls can undergo intersystem crossing to produce an excited triplet state (Eq. iv and Eq. v). The excited triplet state is characterised with a relatively long lifetime, sufficient to allow it to react with oxygen ( $^3O_2$ ) (in its triplet ground state ( $^3\Sigma_g$ )) resulting in the generation of the singlet-excited state ( $^1\Delta_g$ ) of oxygen (Eq. vi). Singlet oxygen ( $^1O_2^*$ ) is a very reactive compound, powerful enough to react with lipids, proteins and nucleic acids. The photoprotective function of Car is shown below. Due to the low-lying triplet state of Cars, the triplet states of Bchls can be efficiently quenched by Car by a triplet-triplet energy transfer (Eq. vii). Thus this prevents the formation of singlet oxygen (Frank, 1993). Car can also directly interact with the singlet oxygen and scavenge it (Eq. viii). The complete photoprotective reaction can be described as follows:



## 1.5 Structures of Light-harvesting complexes

### 1.5.1 Structure of LH2

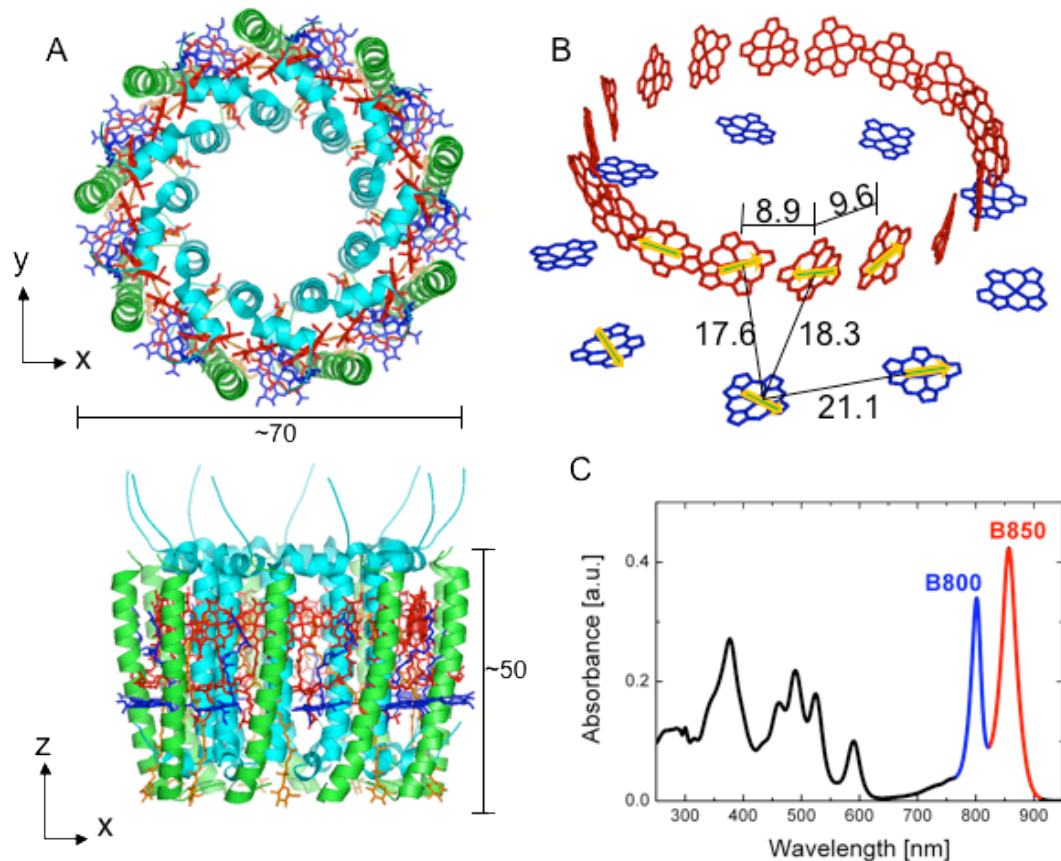


**Figure 1-9** The high resolution (2.0 Å) structure of LH2 complex from *Rps. acidophila* 10050 (Papiz *et al.*, 2003). **A.** Front and side views of the LH2 complex showing nine-membered circular module of  $\alpha$ - (cyan) and  $\beta$ - (green) polypeptides with B800 Bchl (blue), B850 Bchl (red) and the carotenoid (orange) (**B**). The spatial organisation and distances between the Bchl *a* pigments in LH2. The numbers indicate the size of LH2 and centre-to-centre distances between the macrocycles of the Bchl *a* molecules in **A**. The arrows indicate the direction of the Q<sub>y</sub> transition moments. The phytol chain is cropped off for clarity. ([SEE AVAILABLE MOVIE](#)). **C.** The room temperature absorption spectrum of LH2 complex. The red and blue lines correspond to B850 and B800, respectively.

The high-resolution X-ray structure of the LH2 complexes (McDermott *et al.*, 1995, McLuskey *et al.*, 2001, Papiz *et al.*, 2003) from *Rhodospseudomonas (Rps.) acidophila* strain 10050 and low-light adapted strain 7050 show a remarkable symmetry in the arrangement of the pigments embedded in the protein matrix (**Figure 1-9**). These complexes are modular. Each module consists of a protein

heterodimer ( $\alpha\beta$ ), which binds three Bchl *a* pigments and one carotenoid molecule. Nine such modules,  $\alpha\beta$ -polypeptides, are arranged circularly to form the single LH2 complex. In case of *Phaeospirillum* (*Phs.* previously *Rhodospirillum*) *molischianum* the LH2 complexes are octamers (Koepke *et al.*, 1996). The  $\alpha$ -polypeptide is located inside the ring and the  $\beta$ -polypeptide is on the outside (Figure 1-9). Inside the protein matrix the bacteriochlorin rings of the Bchl *a* molecule are organised in two ways (Figure 1-9A). Nine monomeric Bchl *a* molecules have their bacteriochlorin rings oriented parallel to the plane of the membrane (blue in Figure 1-9B and C), and absorb the light with absorption maximum ( $\lambda_{\text{max}}$ ) at ~800 nm. They are called B800 Bchl *as*. These monomeric B800 Bchl *as* are separated by 2.1 nm from each other. A further eighteen Bchl *a* molecules have their bacteriochlorin rings oriented perpendicular to the membrane plane. They are responsible for the absorption band at about 850 nm. The B850 Bchl *as* (red in Figure 1-9A and C) sit very close to each other (~0.9 nm) and, when viewed from above, superficially resembles the blades of a turbine.

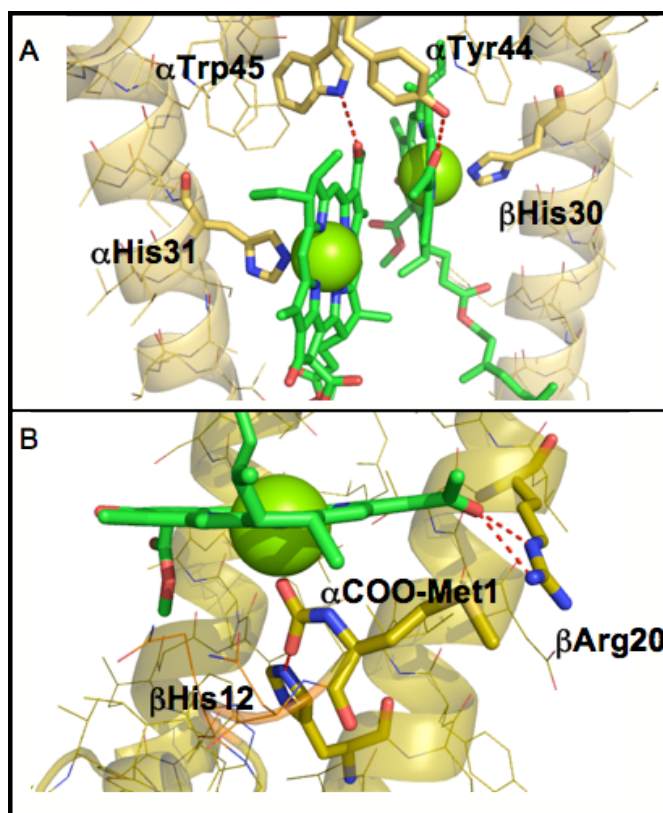


Figure 1-10 Diagrams showing the binding pocket of the B850 Bchl *a* (A) and the B800 Bchl *a* (B). The coordinates for this figure were taken from the high resolution (2.0 Å) structure of the LH2 complex from *Rps. acidophila* 10050 (PDB: 1NKZ) (Papiz *et al.*, 2003).

In their binding pocket, the B800 Bchl *a*s are stabilised by coordination between the  $Mg^{2+}$  of the Bchl *a* and COO- $\alpha$ -Methionine1, and a H-bond between the acetyl group of Bchl *a* and the guanidinium group of  $\beta$ -Arginine20 (Figure 1-10) (Papiz *et al.*, 2003). The B850 Bchl *a*s have their central  $Mg^{2+}$  liganded to the imidazole ring sidechain of histidine residues,  $\alpha$ -His31 and  $\beta$ -His30 (Figure 1-10) (McDermott *et al.*, 1995, Papiz *et al.*, 2003). A hydrogen bond is formed between the acetyl group in ring A and the phenol sidechain of  $\alpha$ -tyrosine44 for  $\alpha$ -B850 Bchl *a*s and the indole sidechain of  $\alpha$ -tryptophan45 for  $\beta$ -B850 Bchl *a* molecules (Figure 1-10) (Papiz *et al.*, 2003).

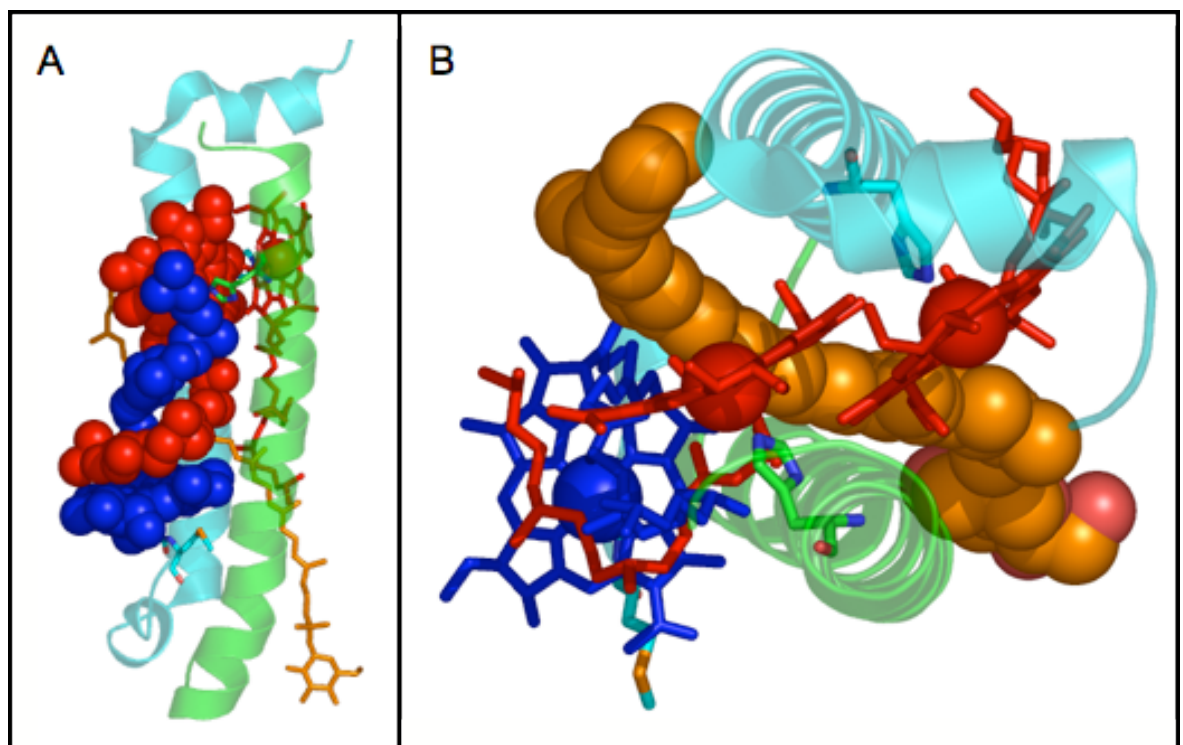
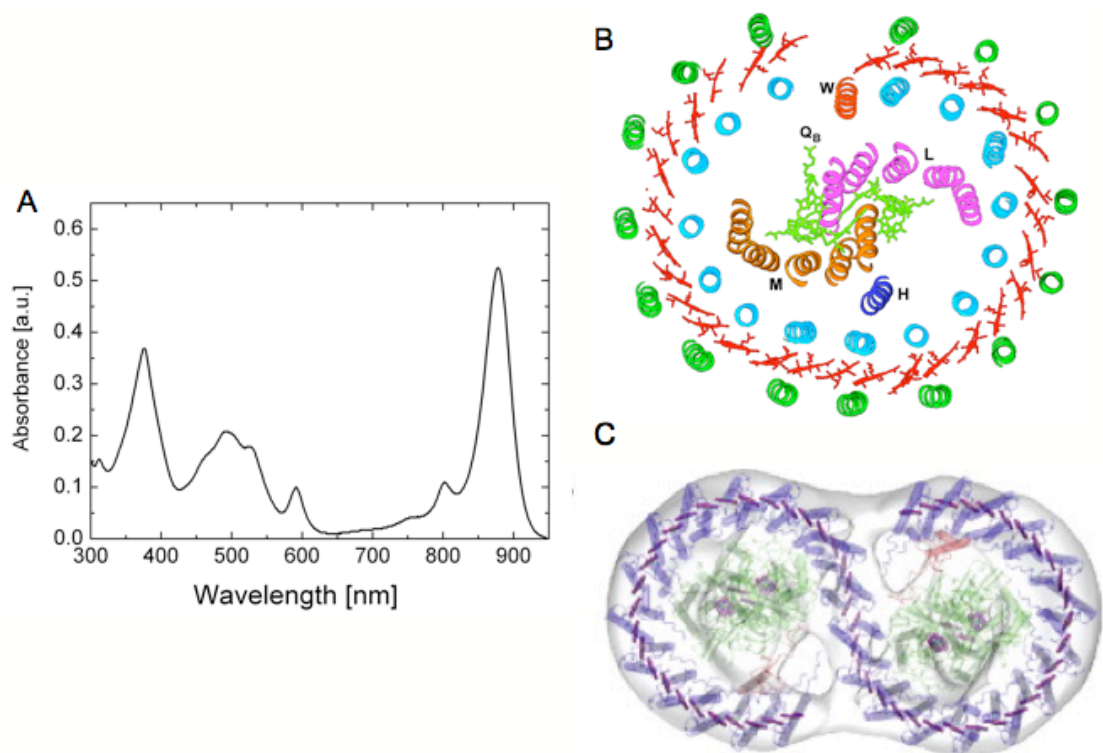


Figure 1-11 Diagram showing the interaction of the phytol chain of the B800 Bchl *a* (blue) and  $\beta$ -bound Bchl *a* (red) (A) and the position of all-*trans* carotenoid rhodopin-glucoside in the heterodimeric pair of  $\alpha\beta$ -polypeptides. The coordinate is taken from high resolution (2.0 Å) structure of LH2 complex from *Rps. acidophila* 10050 (Papiz *et al.*, 2003).

On a closer inspection, there is an interesting interaction between Bchl *a* molecules of B850 and B800, within an  $\alpha\beta$ -apoprotein pair, conducted by their hydrophobic phytol chains. The B800 phytol chain from B800 folds around the phytol chain of  $\beta$ -B850 Bchl, crossing it and passes across the macrocycle ring of the  $\beta$ -B850 (Figure 1-11A). The B800 phytol chain interacts *via* van der Waals contact with rings A and D of the  $\beta$ -B850 macrocycle.

The Car found in the *Rps. acidophila* strain 10050 is rhodopin-glucoside. The X-ray structure of LH2 from *Rps. acidophila* also reveals interactions between the Car and the polypeptide as well as between Car with the Bchl *a* molecules (**Figure 1-11B**). In the LH2 complex from *Rps. acidophila* 10050, the rhodopin-glucoside passes in close contact (3.4 Å) to the edge of the bacteriochlorin ring of the B800 Bchls. The polyene chain then runs perpendicular to the macrocycle of the  $\alpha$ -B850 Bchl *a* (**Figure1-11B**). The glucosyl group of the rhodopin-glucoside molecule is located in a hydrophilic binding pocket on the cytosolic side of the transmembrane-spanning protein. This Car has an extremely important structural role in LH2. It holds the  $\alpha\beta$ -polypeptide pairs together (**Figure1-11B**). In a mutant that lacks Car the LH2 complexes fail to assemble (Hunter *et al.*, 1994).

### 1.5.2 Structure of LH1-RC (Core) complexes



**Figure 1-12** A. The room temperature absorption spectrum of LH1-RC "Core" from *Rps. palustris*. B. The crystal structure at 4.8 Å resolution of LH1-RC from *Rps. palustris* (Roszak *et al.*, 2003). C. The recent model of the dimeric LH1-RC from *Rba. sphaeroides* (Sener *et al.*, 2009).

The LH1 complexes are constructed on a similar modular principle to that seen in the case of the LH2 complexes. LH1 consists of  $\alpha$ - and  $\beta$ -polypeptides, which are oligomerised and surround the RC (Qian *et al.*, 2005, Siebert *et al.*, 2004, Stark *et al.*, 1984). One pair of  $\alpha\beta$ -polypeptide binds two Bchl *a* molecules and one Car (Law *et al.*, 2008). The Bchl *a* molecules are strongly coupled, giving rise to the strong  $Q_y$  absorption band in 870 to 890 nm region (**Figure 1-12**) (Robert, 2003).

The first structure of LH1-RC resolved from a 3D crystal was reported in 2003 (Roszak *et al.*, 2003). The crystal structure at 4.8 Å resolution of the LH1-RC complex from *Rps. palustris*, **Figure 1-12 left** (Roszak *et al.*, 2003), shows an RC surrounded by open elliptical ring of LH1. The LH1 complex consists of 15  $\alpha\beta$ -polypeptides. The elliptical LH1 complex has the dimensions of approximately 110 × 95 Å, measured from the outer edges, formed by  $\beta$ -polypeptides, of the complex. The longest inside dimension, of the ellipse is about 78 Å, providing enough space for the RC to be accommodated (Roszak *et al.*, 2003). The gap, shown in the LH1 complex of *Rps. palustris*, is introduced by a protein called W (**Figure 1-12**). It has been suggested that the protein W is probably analogous to a protein found in *Rba. sphaeroides* and *Rba. capsulatus* called PufX (Cogdell *et al.*, 2006).

PufX is a protein composed of ~80 aminoacids polypeptide found in the core complex of *Rba. sphaeroides* and *Rb. capsulatus* and also probably in all *Rhodobacter* species (Bullough *et al.*, 2009). The structure of PufX from *Rba. sphaeroides* has been solved by NMR in organic solvent and modelled as both a bent (Tunncliffe *et al.*, 2006) and a straight (Wang *et al.*, 2007) helix. PufX plays an essential role in photosynthetic growth. It appears to be required for efficient ubiquinone/ubiquinol exchange between RC and the Cytochrome  $bc_1$  complex (Barz *et al.*, 1995a, Barz *et al.*, 1995b). Previously, the LH1 structure was modelled based on the 8.5 Å cryo-EM projection map of 2D crystals from reconstituted LH1 from *Rsp. rubrum* (Karrasch *et al.*, 1995). This reconstituted LH1 was modelled as a circle of 16  $\alpha\beta$ -polypeptides. Quite recently, a structural model of LH1-RC from wild-type *Rba. sphaeroides* containing PufX protein, based on the 8.5 Å cryo-EM projection map, has been described (**Figure 1-12C**) (Qian *et al.*, 2005, Sener *et al.*, 2009). The structural model of this complex features

S-shape dimeric Bchl array with the double gap due to two molecule of PufX. In a mutant of *Rba. sphaeroides* without PufX protein, the core complex becomes monomeric and forms a closed ring (Francia *et al.*, 1999, Richter *et al.*, 2007a, Siebert *et al.*, 2004).

### 1.5.3 Variants of LH2 complexes

Interestingly, in some species of purple bacteria, such as *Rps. acidophila* or *Rps. palustris*, the  $Q_y$  absorption band of the Bchl in the LH2 complexes can vary depending on the growth conditions. When *Rps. acidophila* strain 7050 and 7750 are grown under low-light conditions, a different LH2 complex is formed with the  $Q_y$  absorption bands at 800 and 820 nm (**Figure 1-13**) (Cogdell *et al.*, 1985, Gardiner *et al.*, 1993, McLuskey *et al.*, 2001). The ability to change the type of LH2 in response to growth at different light intensities is related to the presence of multiple  $\alpha\beta$ -polypeptides, which are (in the case of *Rps. acidophila*) encoded by at least four different  $\alpha\beta$ -apoprotein gene pairs (Bissig *et al.*, 1988, Gardiner *et al.*, 1993). In order to distinguish these two types of peripheral LH2 complexes they are often referred to as B800-850 and B800-820 complexes, or LH2 and LH3, respectively.

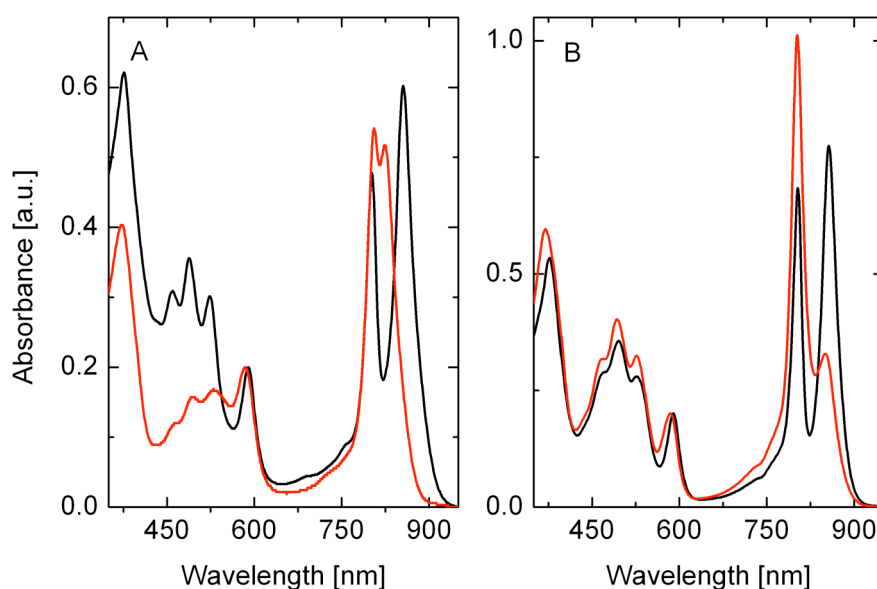


**Figure 1-13** Room temperature (RT) steady state absorption spectra of the B800-850 (black line) and the B800-820 (red line) LH2 complexes from *Rps. acidophila* 7050 (A) (Figure courtesy of Dr. Alastair T. Gardiner). (B) The RT absorption spectra of B800-850 (black line) and B800-low-850 (red line) LH2 complexes from *Rps. palustris* 2.1.6.

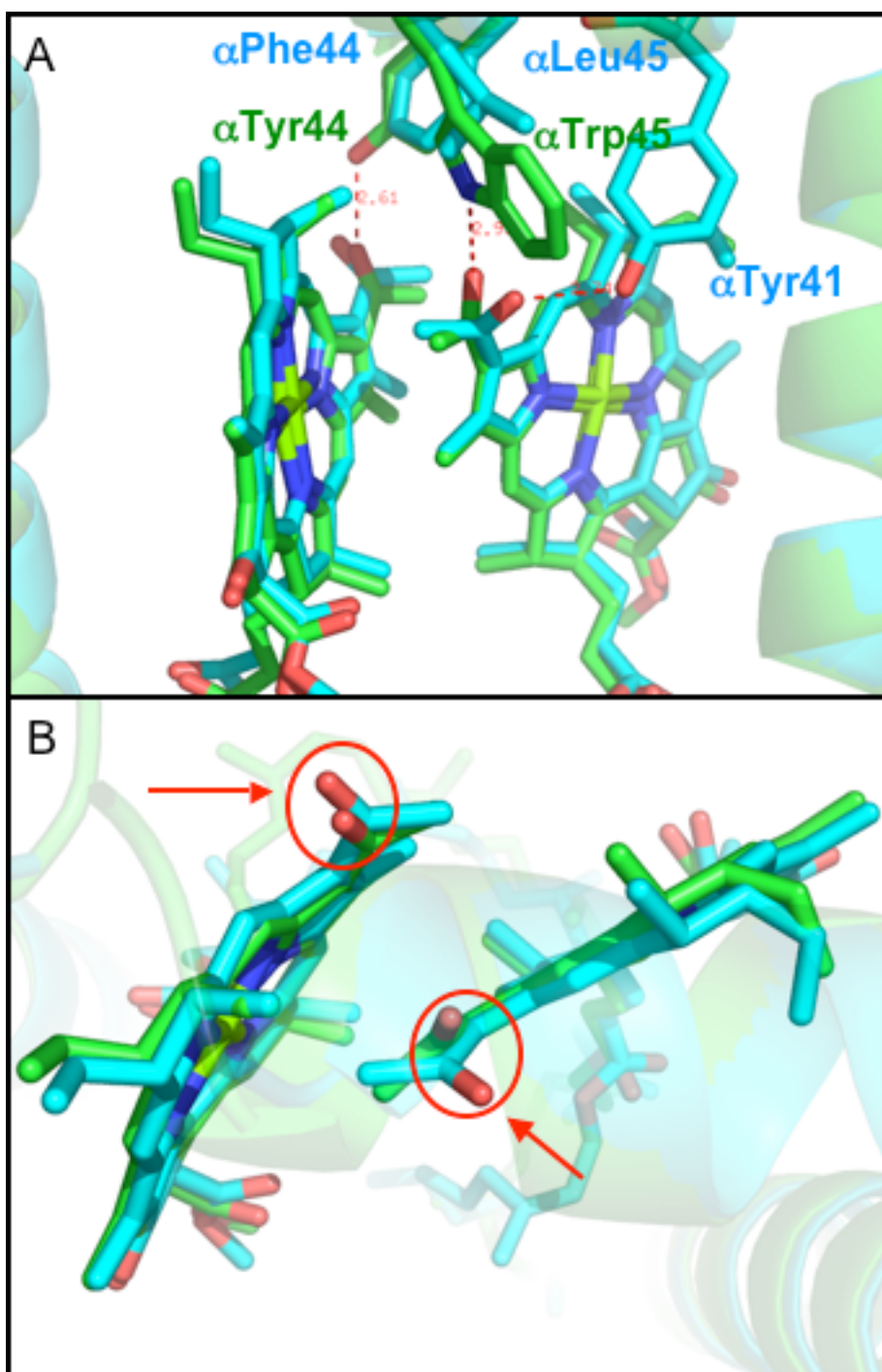


Figure 1-14 Comparisons of the  $\alpha$ - and  $\beta$ -bound Bchl *a* in B850 (green) and B820 (cyan) LH2. A. Diagram showing the interaction of the C<sub>3</sub>-acetyl group of Bchl *a* with the key potential H-bonding residues. B. Highlighting the twisting of the C<sub>3</sub>-acetyl group of Bchl *a* with respect to the bacteriochlorin plane. The coordinates used to produce this figure were taken from the high resolution (2.0 Å) structure of B800-850 LH2 complex from *Rps. acidophila* 10050 (Papiz *et al.*, 2003) and the 3.0 Å resolution structure of the B800-820 LH2 from *Rps. acidophila* 7050 (PDB: 1IJD) (McLuskey *et al.*, 2001). ([SEE AVAILABLE MOVIE](#))

The origin of this spectral variation comes from the fine-tuning of the electronic energy levels of the “B850” molecules, by altering the binding site of the Bchl *a* in the protein matrix. In the B800-850 complex, the C<sub>3</sub>-acetyl group of the  $\alpha$ -bound B850 Bchl *a* molecule is H-bonded to the  $\alpha$ Trp45 residue and the C<sub>3</sub>-acetyl group of the  $\beta$ -bound B850 Bchl *a* molecule is H-bonded to the  $\alpha$ Tyr44 residue (**Figure 1-14A**) (McLuskey *et al.*, 2001). In contrast, in the B800-820 complex, the respective residues in these positions, i.e.  $\alpha$ Phe44 and  $\alpha$ Leu45, are unable to form hydrogen bonds (**Figure 1-14A**). Instead the C<sub>3</sub>-acetyl group of the  $\alpha$ B820 Bchl *a* molecules is H-bonded to the  $\alpha$ Tyr41 residue and this locks the acetyl group into an out-of-plane position with respect to the bacteriochlorin plane (**Figure 1-14B**). Similarly, the  $\beta$ -bound B820 Bchl *a* molecule, lacking any hydrogen bonds, has its acetyl in an out-of-plane position with respect to the bacteriochlorin plane. Rotation of the acetyl group of the Bchl *a* molecule into an out-of-plane position reduces the extent of  $\pi$ -conjugation and results in a blue shift of the Bchl *a* site energies (McLuskey *et al.*, 2001, Sturgis *et al.*, 1995). This then is reflected in the shift of the absorption band from 850 nm to 820 nm. Conclusions from the structural studies comparing B800-850 with B800-820 are strongly supportive of the previous conclusion derived from site-directed mutagenesis experiments carried out on LH2 from *Rba. sphaeroides* (Fowler *et al.*, 1994, Olsen *et al.*, 1997). The importance of the H-bonding residues has also been shown in controlling the site-energy of Bchl *a* molecules (Cogdell *et al.*, 2006, Cogdell *et al.*, 2002).

## 1.6 Excitons

An exciton is a collective excited state, which is produced due to a strong interaction between molecules. The excitons in LH2 complexes are formed by the strongly coupled B850 Bchl *a* molecules. The LH2 complexes from *Rps. acidophila* and *Phs. molischianum* belong to the pure-rotational point groups C<sub>9</sub> and C<sub>8</sub>, respectively. The energy scheme of the excited state of the B850 manifold can then be constructed by the linear combinations of the symmetric or antisymmetric wavefunctions of the  $\alpha\beta$ -dimers,  $|\Psi_{\alpha\beta}^s\rangle$  and  $|\Psi_{\alpha\beta}^{as}\rangle$ , in such a way that they form bases for the irreducible representation of the C<sub>9</sub> and C<sub>8</sub> symmetries. In the case of the C<sub>9</sub>-point group each symmetric and antisymmetric state consists of one non-degenerate and four degenerate states. The excited

state wavefunction of the B850 LH2 from *Rps. acidophila* can be generally formulated as,

$$|\Psi_k^j\rangle = \frac{1}{\sqrt{9}} \sum_{n=1}^9 e^{kin\left(\frac{2\pi}{9}\right)} |\Psi_{\alpha\beta}^j\rangle \quad (1.7)$$

where  $k$  represents the quantum number ( $k= 0, \pm 1, \dots, (N-1)/2$ ) with  $N = 9$  for the number of dimers in the B850 ring. The subscript  $j$  represents the symmetric ( $s$ ) or antisymmetric ( $as$ ) wavefunctions. The energy levels are denoted by their quantum number and the symmetry species, A (non-degenerate) or E (degenerate) of their irreducible representation (Figure 1-15).

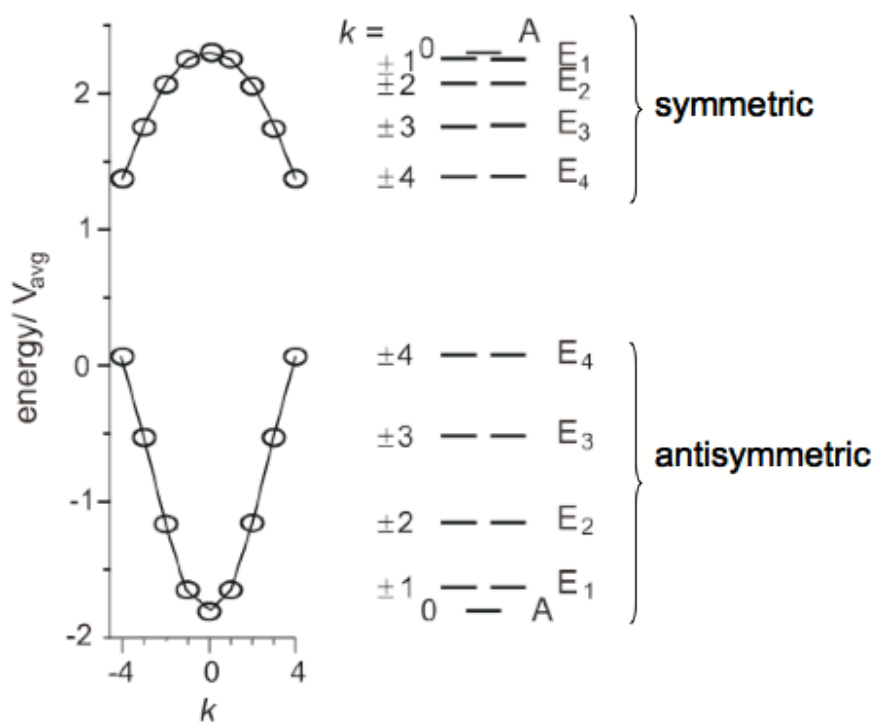


Figure 1-15 The energy level scheme of the excited state manifold of the B850 ring of LH2 (*Rps. acidophila*) (Matsushita *et al.*, 2001). The symmetric and antisymmetric manifolds consist of one nondegenerate, A, ( $k = 0$ ) and four doubly degenerate, E, ( $k = \pm 1, \pm 2, \dots, \pm 4$ ).

## 1.7 Electronic energy transfer in LH2

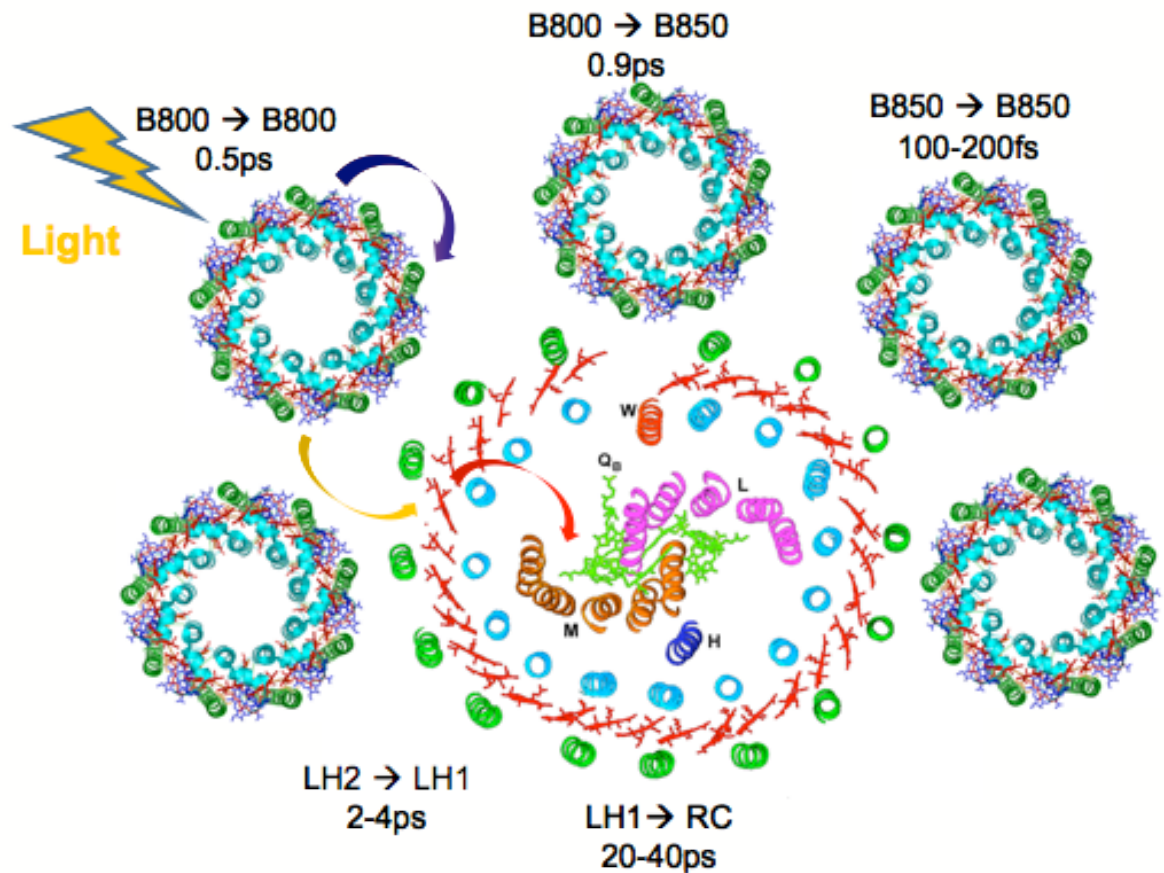


Figure 1-16 Model for photosynthetic unit (PSU) of purple bacteria showing the light-harvesting complexes (LHs) and the reaction centre (RC) (adapted from (Law *et al.*, 2008)). The flow energy transfer is also illustrated. ([SEE AVAILABLE MOVIE](#))

The energy transfer processes (B800→B800, B800→B850 and B850→B850) in the LH2 complexes have been well reviewed (Sundström, 1995, Sundström *et al.*, 1999). The hopping of excitation between B800 monomers occurs in 1.5 ps in the case of *Rps. acidophila* 10050 (Kennis *et al.*, 1997b) and 1-3 ps for *Phs. molischianum* (Novoderezhkin *et al.*, 2003). The B800→B850 energy transfer in *Rps. acidophila* takes place with a time constant of 0.7-0.9 ps at room temperature (Kennis *et al.*, 1997b) and only slows down to 1.8-2.4 ps at 1.4K (Kennis *et al.*, 1997a). Exciton relaxation in the B850 ring of the LH2 from *Rba. sphaeroides* has been measured to take place on the 100-200 fs timescale (Agarwal *et al.*, 2002). In *Rps. acidophila* 10050 the exciton relaxation in B850

ring has been recorded to be 160 fs (Mercer *et al.*, 2009). The LH2→LH1 energy transfer has been measured to be 3 ps at 296 K in *Rba. sphaeroides* (Hess *et al.*, 1995b) and LH1→RC transfer has been recorded to be about 20-50 ps in *Rba. sphaeroides* (Visscher *et al.*, 1989).

## 1.8 Regulation of photosynthetic unit

The transcriptional regulation of the photosynthetic unit in purple bacteria is mainly controlled by oxygen tension (Blankenship, 2002). All photosynthetic genes responsible for coding LH2 and LH1-RC are repressed in the presence of oxygen (Clark *et al.*, 1984, Hunter *et al.*, 1987, Zhu *et al.*, 1986). Under anaerobic conditions these genes are activated. The level of expression of these genes is then adjusted by the light intensity in order to tune the ratio of the amount of the RC to that of the LH complexes (Bauer *et al.*, 1996, Gregor *et al.*, 1999).

**Figure 1-17** illustrates in more detail the two-component bacterial regulatory systems, which are involved in the transcriptional regulation of photosystem genes in *Rba. sphaeroides*. These systems consist of a sensor kinase component and phosphorylatable, DNA-binding protein component (Law *et al.*, 2008). It has been shown (**Figure 1-17**) that the PrrB (photosynthetic response regulator) system mediates the transcriptional activation of most of the photosynthetic unit genes under the condition of low oxygen tension. This system works in response to a signal coming from *cbb*<sub>3</sub>/*Rdx*B oxygen-sensing pathway. PrrB is a sensor histidine kinase/phosphatase that responds to a low oxygen atmosphere. PrrA is a cytosolic response regulator protein. When the PrrA is activated, gene expression is initiated. FnrL can also indirectly effect *puc* operon transcription by regulating genes that encode the *cbb*<sub>3</sub>/*Rdx*B signal pathway, thus affecting the signal that reaches PrrB. Under high oxygen tension, the sensory component PpsR represses both the *puc* operon and Bchl and Car biosynthesis pathway genes.

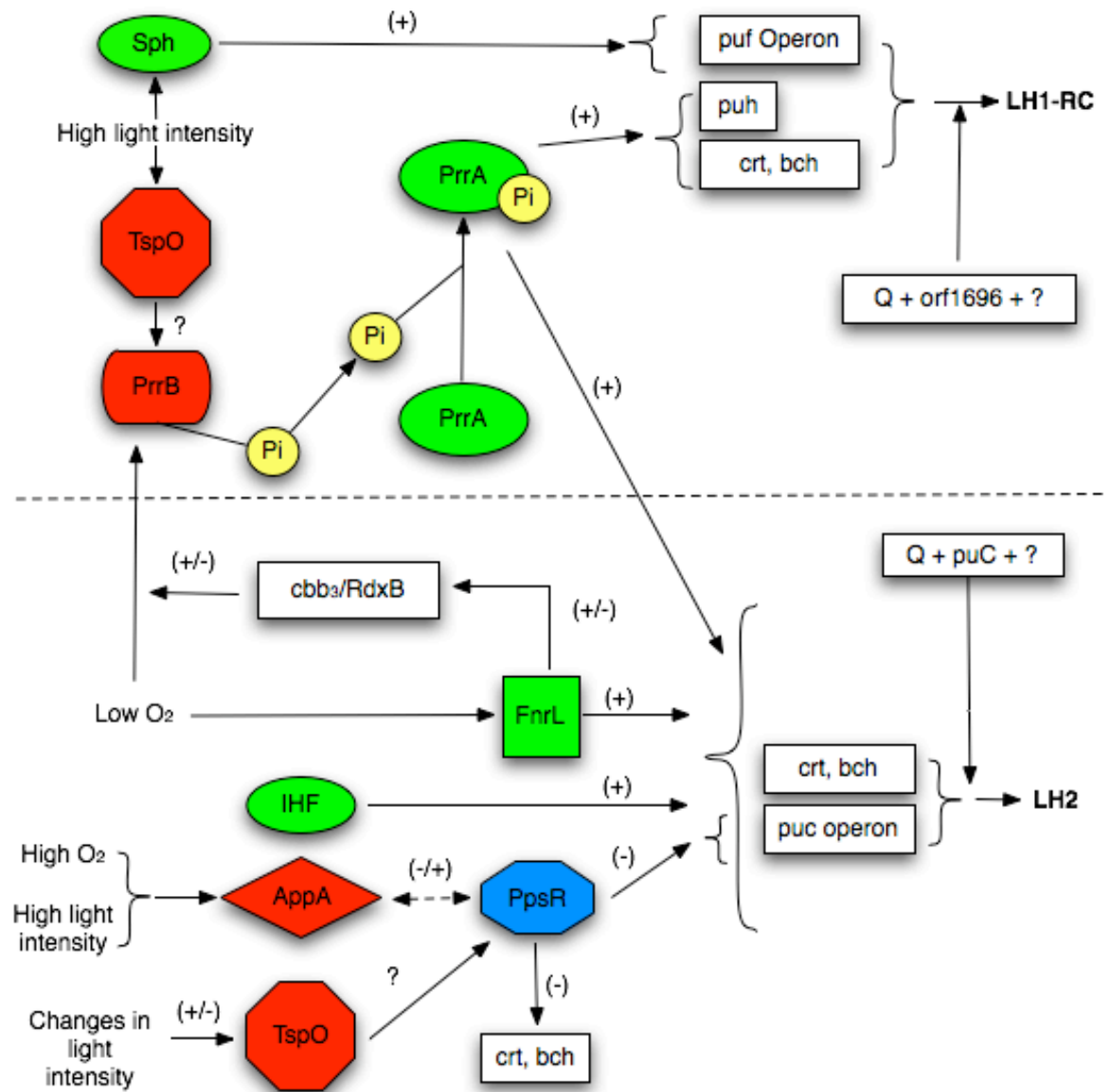


**Figure 1-17** Schematic diagram of the major known regulatory components of photosynthetic unit gene expression in *Rba. sphaeroides*. Green corresponds to the components that act as effectors of gene expression. Red stands for the sensory components. The component in blue (PpsR) can function as both sensor and effector. The genes are shown in boxes. (+) means enhances expression of target gene; (-) means represses expression of target gene; ? indicates putative pathway of regulation; P<sub>i</sub> is inorganic phosphate. Taken from (Law *et al.*, 2008).

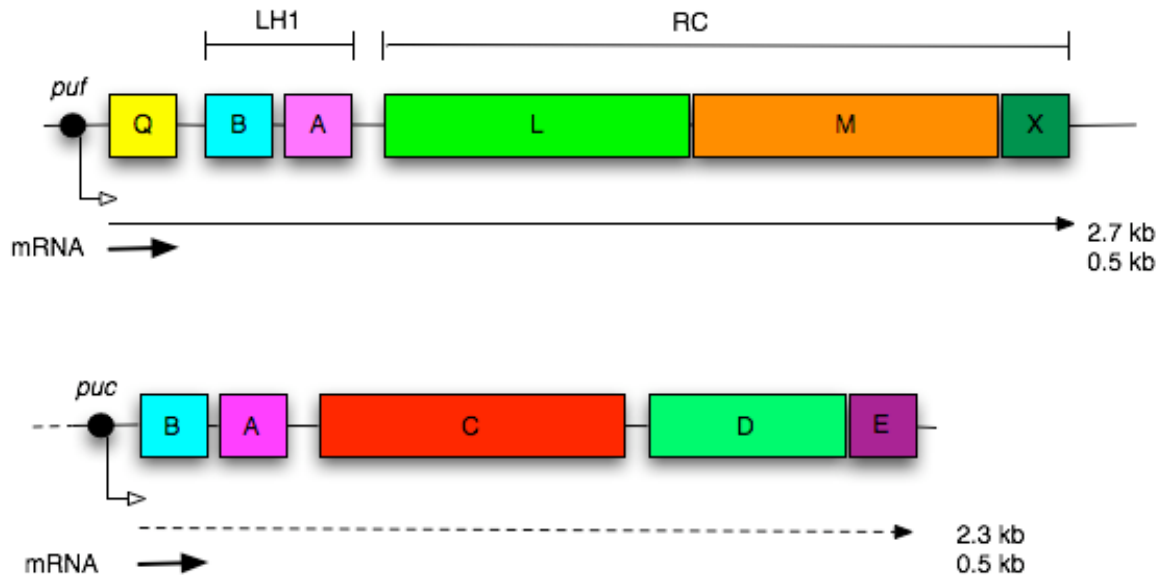


**Figure 1-18** The polycistronic *puf* and *puc* operons encode the pigment binding proteins of *Rba. capsulatus* and *Rba. sphaeroides*. Taken from (Klug, 1993).

**Figure 1-18** shows a schematic diagram of the photosynthetic *puf* and *puc* operons that encode for the biosynthesis of the pigment binding proteins. The *puf* operon comprises the genes for the pigment binding proteins of the LH1 complex (*pufB* and *pufA*), the RC (*pufL* and *pufM*) and open reading frames *pufQ* and *pufX*. The *puc* operon consists of genes *pucBA* responsible for encoding the pigment binding  $\beta$ - and  $\alpha$ -apoproteins of the LH2 complexes, respectively (**Figure 1-18**) (Burgess *et al.*, 1989, Klug, 1993, Youvan *et al.*, 1985), a regulatory gene (*pucC*) and genes *pucDE*, which encode proteins for stabilization of the LH2 complex (Lee *et al.*, 1989, Tichy *et al.*, 1991, Tichy *et al.*, 1989). The genes *pucCDE* are located downstream from *pucA*. It has been shown in the mutant NK3 from *Rba. capsulatus* that a lack of the *pucC* gene has a negative effect on the *pucB* and *pucA* genes located upstream resulting the absence of LH2 complex (Tichy *et al.*, 1991). The *pucD* and *pucE* genes encode the production of PucD and PucE proteins, which are important for the stability of the LH2 complex. Deficient amounts of PucD and PucE proteins result in the degradation of the complex (Tichy *et al.*, 1991, Tichy *et al.*, 1989).

	-20	1	20	
Ac10050-B800/850 alpha chain	-----	MNQGK	IWTVVNPA	IGIPALLGSVTVIAI 28
Ac7050-B800/850 alpha chain	-----	MNQGK	IWTVVNPSVGLP	LLLLGSVTVIAI 28
Ac7050-B800/820 alpha chain	-----	MNQGK	IWTVPPAFGLP	LMLGAVAITAL 28
Molisch-B800/850 alpha chain	-----	MSNPKDDYK	IWLVINPSTWLP	VIWIVATVVAI 32
Molisch-B800/820 alpha chain	-----	SNPKDDYK	IWLVINPSTWLP	VIWIVALLTAI 31
Pal-PucAa	-----	MNQAR	IWTVVKPTVGLP	LLLLGSVTVIAI 28
Pal-PucAb	-----	MNQGR	IWTVVNPGVGLP	LLLLGSVTVIAI 28
Pal-PucAc	-----	MNQGR	IWTVVSPTVGLP	LLLLGSVAAIAF 28
Pal-PucAd	-----	MNQGR	IWTVVKPTVGLP	LLLLGSVAIMVF 28
Pal-PucAe	-----	MNQGR	IWTVVKPTVGLP	LLLLGSVTVIAI 28
Ac10050-B800/850 beta chain	-----	ATLTA	EQSEELHKYV	IDGTRVFLGL-----AL 27
Ac7050-B800/850 beta chain	ADDVKGL	TGLTAAE	SEELHKHV	IDGTRVFFVI-----AI 34
Ac7050-B800/820 beta chain	-----	AEVLT	SEQAEELHKHV	IDGTRVFLVI-----AA 28
Molisch-B800/850 beta chain	-----	MAERS	LSGLTEEEA	IAVHDQFKTTFSAFIIL-----AA 33
Molisch-B800/820 beta chain	-----	AERS	LSGLTEEEA	VAVHDQFKTTFSAFILL-----AA 32
Pal-PucBa	MADKTL	TGLTVEE	SEELHKHV	IDGTRIFGAI-----AI 33
Pal-PucBb	MADDPNKVWP	TGLTIAE	SEELHKHV	IDGTRIFGAI-----AI 37
Pal-PucBc	MVDDSKKVWP	TGLTIAE	SEELHKHV	IDGARIFVAI-----AI 37
Pal-PucBd	MVDDPNKVWP	TGLTIAE	SEELHKHV	IDGSRIFVAI-----AI 37
Pal-PucBe	MADDPNKVWP	TGLTIAE	SEELHKHV	IDGTRIFGAI-----AI 37
		40	60	
Ac10050-B800/850 alpha chain	LVHLA	ILS	HTTWFPAYWQGGV	KKAA----- 53
Ac7050-B800/850 alpha chain	LVHAAVLS	HTTWFPAYWQGGV	LKKAA----- 53	
Ac7050-B800/820 alpha chain	LVHAAVLT	HTTWYAAFLQGGV	LKKAA----- 53	
Molisch-B800/850 alpha chain	AVHAAVLAAPG	FNWIAL	GAAKSAK----- 57	
Molisch-B800/820 alpha chain	AVHSFVLS	VPGYNFLAS	AAAKTAAK----- 56	
Pal-PucAa	LVHFAVLS	HTTWFSKYWNG	KAAAI ESSVNVG----- 59	
Pal-PucAb	LVHYAVLS	NTTWFPKYWNG	ATVAAPAAAPAPAAPAACK 66	
Pal-PucAc	AVHFAVLE	NTSWVAAFMNGK	SVAAAAPAPAAPAAPAKK 65	
Pal-PucAd	LVHFAVLT	HTTWVAKFMNG	KAAAI ESSIKAV----- 59	
Pal-PucAe	LVHFAVLS	NTTWFSKYWNG	KAAAI ESSVSI G----- 59	
Ac10050-B800/850 beta chain	VAHF	LAFS	ATPWLH----- 41	
Ac7050-B800/850 beta chain	FAHV	LAFAF	SPWLH----- 48	
Ac7050-B800/820 beta chain	IAHF	LAFTL	TPWLH----- 42	
Molisch-B800/850 beta chain	VAHV	LVWV	KPWF----- 46	
Molisch-B800/820 beta chain	VAHV	LVW	IWKPWF----- 45	
Pal-PucBa	VAHF	LAYVY	SPWLH----- 47	
Pal-PucBb	VAHF	LAYVY	SPWLH----- 51	
Pal-PucBc	VAHF	LAYVY	SPWLH----- 51	
Pal-PucBd	VAHF	LAYVY	SPWLH----- 51	
Pal-PucBe	VAHF	LAYVY	SPWLH----- 51	

**Figure 1-19** A sequence comparison of selected LH2  $\alpha$ - and  $\beta$ -polypeptides. The *Rps. palustris* (Pal-) sequences have been deduced from gene sequences. Both the *Rps. acidophila* (Ac-) and *Phs. molischianum* (Molisch-) sequences are from the proteins. The amino acid highlighted in the red boxes are the ones that control the spectral shifts of the tightly coupled Bchl *a* molecules.

Some purple bacteria such as *Rps. acidophila* are known to have multiple  $\beta$ - and  $\alpha$ -polypeptides that are encoded by multiple *puc* operons. In the case of *Rps. acidophila* from the four *pucBA* genes (*puc*<sup>1</sup>*BA* through to *puc*<sup>4</sup>*BA*) that have been identified so far, only *puc*<sup>4</sup>*BA* is expressed under high-light intensity (Gardiner *et al.*, 1993). When *Rps. acidophila* 7050 is grown under low light, the genes responsible for the production of the Ac7050-B800/820 apoproteins are expressed rather than of the Ac7050-B800/850 apoproteins (Figure 1-19) (McLuskey *et al.*, 2001).

This phenomenon of chromatic adaptation is also observed in *Rps. palustris*. In *Rps. palustris*, the complete genome has been sequenced (Larimer *et al.*,

2004). There are five different *pucBA* genes present in the *Rps. palustris* genome (*pucBA-a, b, c, d, and e*) and their expression is regulated by light intensity (Tadros *et al.*, 1993, Tadros *et al.*, 1989). The regulation of the LH2 complex from *Rps. palustris* is more complicated as 6 bacteriophytochrome (Bph)-like genes have also now been identified in the genome (Larimer *et al.*, 2004). Four of these genes are located near to genes coding for photosynthetic LH-apoproteins or pigment biosynthetic genes. This suggests that these Bphs are also involved in the regulation of the PSU. The regulation of the LH2 complex in *Rps. palustris* is, therefore, influenced by the light intensity as well as the light quality. The unusual B800-LH2 (LH4) complex, which has Q<sub>y</sub> absorption band at 800 nm only, is encoded by *pucB<sub>d</sub>* and *pucA<sub>d</sub>*, producing LH4 PucB<sub>d</sub>A<sub>d</sub> peptides, and is regulated by two Bph genes, Rpa3015 (Bph4) and Rpa3016 (Bph5) (Evans *et al.*, 2005). These Bph4 and Bph5 genes are activated under low light intensity or upon red light illumination. A trial expressing two LH2 gene pairs, which encode the high-light (*pucBA<sub>a</sub>*) and the low-light (*pucBA<sub>d</sub>*) proteins, from *Rps. palustris* in *Rba. sphaeroides* has been carried out (Fowler *et al.*, 1996). It was shown that the high-light B800-850 LH2 complex (*pucBA<sub>a</sub>*) and the low-light B800-830 LH2 complex (*pucBA<sub>d</sub>*) could be successfully produced in *Rba. sphaeroides*. There is also a B800-low-850 LH2 complex that has been reported when *Rps. palustris* is grown at low-light intensity (Gall *et al.*, 1999, van Mourik *et al.*, 1992). It is likely that bacteriophytochromes will be found in all species of purple bacteria and a fuller understanding of their operation will undoubtedly cause revision of the present model of PSU gene regulation.

## 1.9 Principle of single molecule spectroscopy

Single molecule spectroscopy (SMS) allows individual molecules in a population to be probed, yielding direct information regarding the distribution of their molecular properties. Detailed information, e.g. heterogeneity within a single complex, which is obscured due to ensemble averaging in ensemble spectroscopy, can be revealed by SMS (Xie, 1996). In the last ten years SMS has been utilised as a powerful tool to reveal the structural properties of LH complexes, such as disorder and the arrangement of the Bchl *a* molecules (Matsushita *et al.*, 2001, Richter *et al.*, 2007a, Richter *et al.*, 2007b, van Oijen *et al.*, 1999b).

In order to perform SMS, there are two general requirements that must be taken into account (Moerner *et al.*, 2003, Weiss, 1999): (1) guaranteeing that only one molecule is in a resonance in the volume probe by the laser, (2) having a signal to noise ratio (SNR) of a single molecule signal that is greater than the background for reasonable averaging time. The first requirement can be fulfilled generally by a combination of the high optical resolution of modern microscopes, that allows the spatial selection of a single molecule in a probe of very diluted sample ( $10^{-10}$  M in about  $10 \mu\text{m}^3$ ), and narrow band lasers that can provide coherent illumination in many different spectral regions. In order to achieve good SNR single molecule microscopy uses the fluorescence from dye molecules and, therefore, the molecules can be detected at a wavelength red-shifted compared to wavelength of illumination.

Single molecule detection employs modern high-resolution microscopes that are equipped with infinity-corrected objectives of high numerical aperture. The objectives set the magnification, the field of view and resolution, and their quality determines the light transmission, the contrast and the aberrations of the image (Murphy, 2001). Thus it is possible to detect an individual molecule of interest. The numerical aperture is a geometrical parameter related to the light-gathering power of the objective lens. It is the primary determinant of the spatial resolution of an objective.

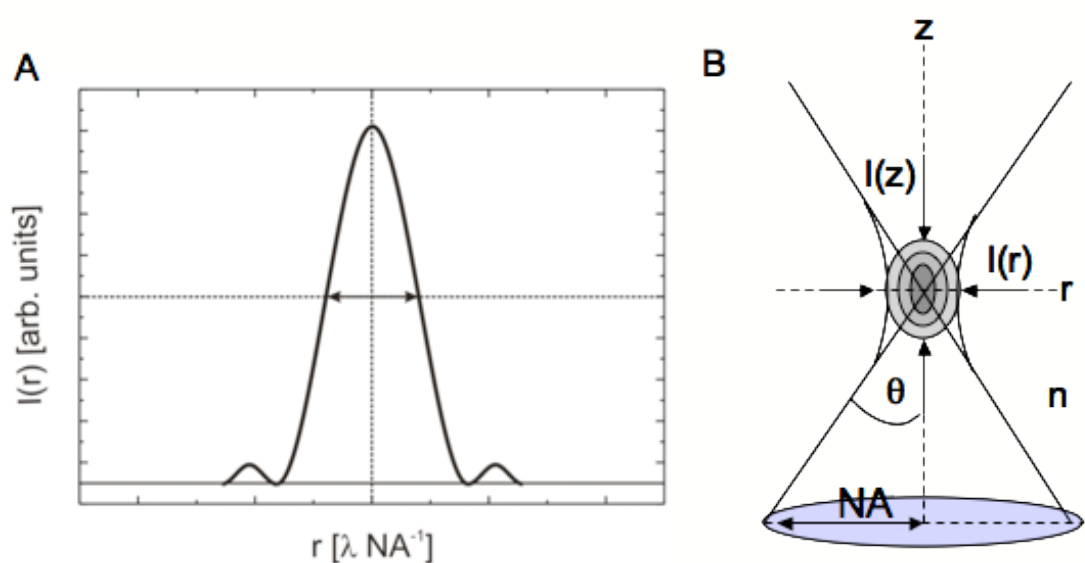


**Figure 1-20** Point-spread-function (PSF) at the focal plane (A) and numerical aperture (NA) with focal point into PSF (B). Adapted from (Murphy, 2001)

The numerical aperture (**Figure 1-20**), NA, is described as follows (Murphy, 2001):

$$NA = n \sin \theta \quad (1.8)$$

where  $\theta$  is the half angle of the cone of specimen light accepted by the objective lens and  $n$  is the refractive index of the medium between the lens and the specimen.

After being focused by the optical system the point-like object is spread into a diffraction pattern of finite width. The intensity map of that pattern is characterised by a point-spread-function (PSF), which defines the spread of a point source (**Figure 1-20A**). The PSF determines the spatial resolution. The narrower the PSF the better is the resolution of the optical system (Murphy, 2001). The PSF depends on wavelength,  $\lambda$ , NA, magnification as well as illumination and detection geometries. The resulting PSF of an optical system  $I_{PSF}(x,y,z)$  is given by the convolution of the illumination and detection intensity,  $I_{ill}(x,y,z)$  and  $I_{det}(x,y,z)$  respectively,

$$I_{PSF}(x,y,z) = I_{ill}(x,y,z) \cdot I_{det}(x,y,z) \quad (1.9)$$

As most microscope arrangements feature cylindrical symmetry PSF is commonly denoted as  $I(r,z)$  where  $r$  defines an arbitrary direction to the focal plane  $x,y$ , and  $z$  corresponds to optical axis (Webb, 1996).

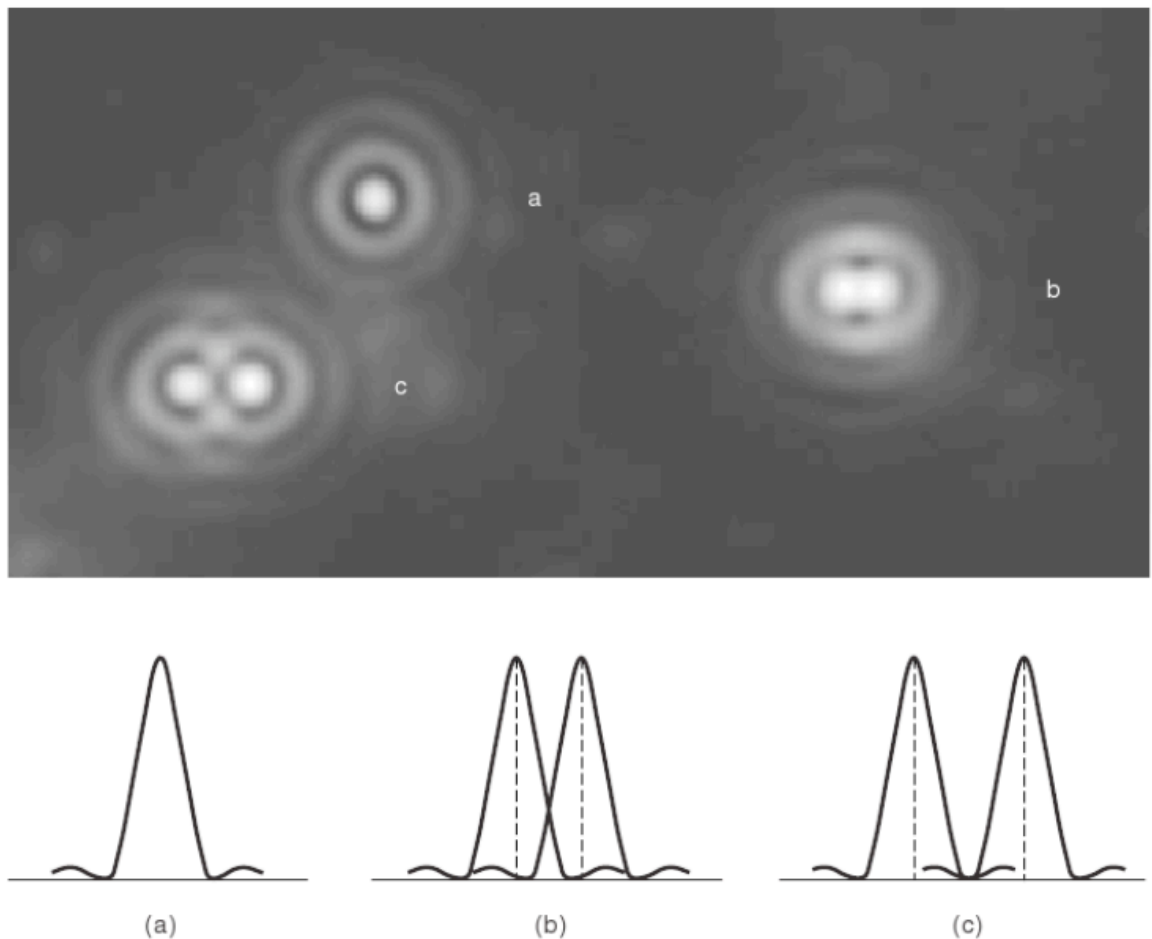


**Figure 1-21 Rayleigh criterion for spatial resolution. (a) Profile of a single diffraction pattern: The bright Airy disk and 1<sup>st</sup>- and 2<sup>nd</sup>-order diffraction rings are visible. (b) Profile of two disks separated at the Rayleigh limit such that the maximum of a disk overlaps the first minimum of the other disk: The points are now just barely resolved. (c) Profile of two disks at a separation distance such that the maximum of each disk overlaps the second minimum of the other disk: The points are clearly resolved. Taken from (Murphy, 2001).**

The resolving power of the microscope can be estimated according to Ernst Abbe (1840-1905) and defined as

$$d = 0.61 \frac{\lambda}{NA} \quad (1.10)$$

where  $d$  is the minimum resolved distance in  $\mu\text{m}$ ,  $\lambda$  is the wavelength of light, and  $NA$  is the numerical aperture of the objective lens. This equation describes the *Rayleigh criterion* for the resolution of two closely spaced PSF in the image plane. The *Rayleigh criterion* says: “two adjacent object points are defined as being resolved when the central diffraction spot (Airy disk) of one point

coincides with the first diffraction minimum of the other point in the image plane” (Figure 1-21) (Murphy, 2001).

Practically there are two microscopic techniques used for single molecule spectroscopy and detection. They are wide-field and confocal microscopy. The wide-field microscope is used to scan for area detection and imaging of many molecules at the same time. The confocal microscope is used, in contrast, to detect fluorescence spectra from a small diffraction-limited focal volume excited in the sample, i.e. one single molecule.

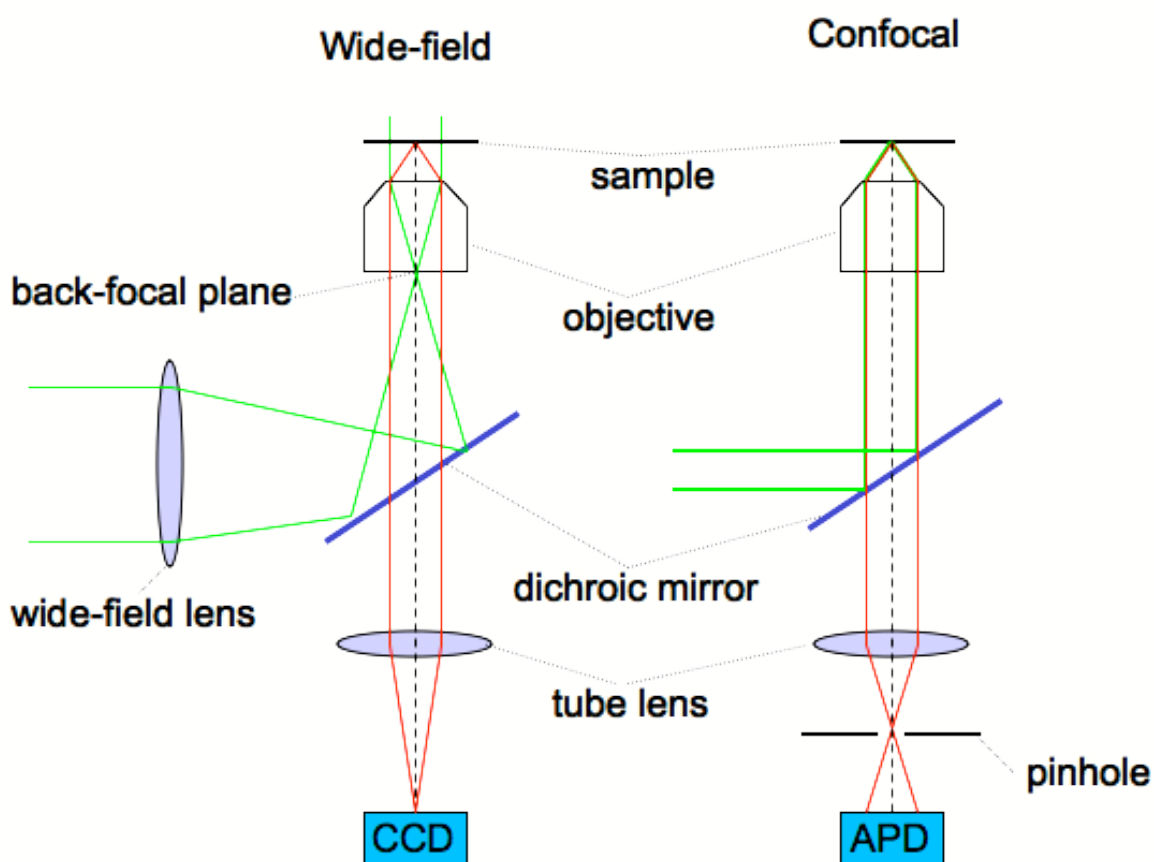


**Figure 1-22** Single molecule fluorescence microscopy methods. The laser beam is in green and the fluorescence from the sample is in red. In wide-field the molecules spread over an area are simultaneously excited by a widened laser beam. In confocal, the laser beam is focused into the diffraction limited focal volume. The pinhole assures that only light from the focal volume is detected.

Technically in wide-field the laser excitation beam is expanded and focused at the back-focal plane of the objective using a lens (Figure 1-22). The objective collimates the beam and uniformly illuminates the sample. The excited fluorescence is collected by the same objective and residual excitation light is

filtered away by appropriate filters. In the confocal microscope the sample is irradiated with focused light originating from a point source, or single-mode laser beam and the response from the sample is directed into a pinhole (**Figure 1-22**). Light not originating from the focal area cannot pass through the detection pinhole and hence is not detected. The advantages and limitations of confocal and wide-field microscopy are compared in **Table 1-2**.

**Table 1-2 Comparison of single molecule fluorescence methods**

	Wide-field	Confocal
<b>Advantages</b>	Imaging with high temporal and spatial resolution	Spot scan with high temporal resolution
	Array detection	Spectral information
	Low z-resolution	High z-resolution
<b>Limitations</b>	No spectral information	Slow acquisition times
	Out of focus contribution	Limited to one molecule at a time

## 1.10 Principles of protein crystallisation

A detailed understanding of the function of proteins requires knowledge of their three-dimensional structure. X-ray crystallography has been recognised to be an important tool in resolving detailed structural information of proteins. The pioneering studies on the X-ray crystal structures of myoglobin (1950) and hemoglobin (1955) were honoured with the Noble Prize in Chemistry in 1962 (Forster, 1966).

Generally proteins crystallise when they are gradually induced to precipitate. This is usually achieved by equilibration with precipitants, e.g. ammonium sulphate or polyethylene glycols, which influence the solubility of the proteins and yet do not denature them. Working with membrane proteins requires an appropriate detergent in order to maintain the membrane protein in solution. During the process of crystallisation of membrane proteins, very often the precipitant reacts with the detergent and causes the detergent to phase separate. When phase separation happens the membrane protein usually denatures in the oily detergent phase and crystals will never be formed. The problem was then overcome when Michel (Michel, 1982a, Michel *et al.*, 1980) and Garavito (Garavito *et al.*, 1980) independently discovered that addition of specific small molecules, e.g. heptane-1,2,3-triol (Michel, 1982b) could alter the phase boundaries. This small amphiphile shifts the phase separation point to be above the critical precipitation point, so that the crystallisation becomes possible.

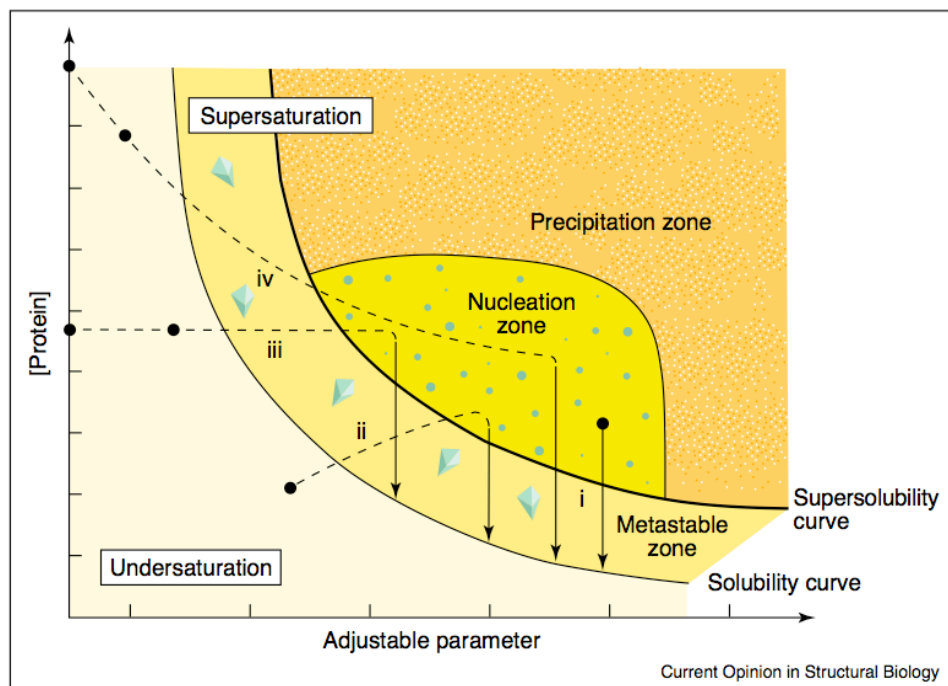


**Figure 1-23** Schematic illustration of a protein crystallisation phase diagram, a systematic approach in crystallography (Chayen, 2004). Methods used in crystallisation are (i) batch, (ii) vapour diffusion, (iii) Dialysis, and (iv) free interface diffusion. The black spot indicates the initial condition of the protein. The progress of the protein crystallisation is indicated in dashed lines. The arrows indicate the final state.

The detailed process of protein crystallisation is systematically illustrated by the crystallisation phase diagram in **Figure 1-23** (Chayen, 2004, Chayen, 2005, Pusey *et al.*, 1986). In this diagram, the crystallisation process can be differentiated into two steps: nucleation and crystal growth. The crystal nucleation and growth can happen within the supersaturation area (**Figure 1-23**). Unfortunately, one needs a higher degree of supersaturation. The protein has to be brought slowly to the nucleation zone and subsequently to the metastable zone, where the crystal is able to grow (**Figure 1-23**). Therefore the different processes of crystal nucleation and growth are often difficult to control individually. Inappropriate protein/precipitant mixtures lead to the formation of an amorphous protein precipitate. Rational design of crystallisation trials using knowledge of the phase diagram has been successfully applied for crystallising PSI and PSII (Fromme *et al.*, 2009). However, this approach has not been generally applied so far.

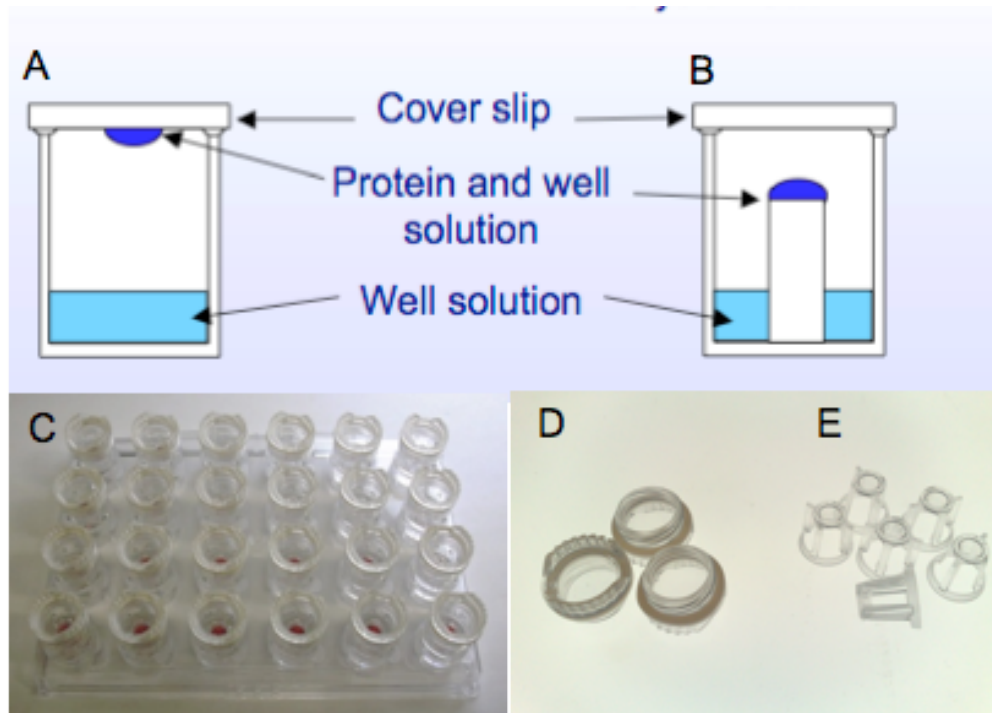


**Figure 1-24** Typical apparatus used for vapour diffusion crystallisation. For hanging drops (A), the protein droplet hangs from the lid (D), whereas for the case of sitting drops (B), the protein droplet sits in the bridge well (E). The vapour diffusion plate from EasyXtal (QIAGEN) (C) offers 24-well plates easier setup for hanging or sitting drop. Bridges (E) are needed for sitting drop.

There are four standard methods used in the crystallisation of proteins: batch, vapour diffusion, dialysis and free interface diffusion (**Figure 1-23**). Among them the vapour diffusion method is the most widely used and it is proven to be very successful in crystallizing proteins (see statistics presented by <http://www.mpdb.ul.ie/index.asp>). There are two common methods in vapour diffusion, hanging drops and sitting drops (**Figure 1-24**). Both entail a droplet containing purified protein, buffer, and precipitant being allowed to equilibrate with a larger reservoir containing similar buffers and precipitants in higher concentrations. Initially, the droplet of protein solution contains a lower concentration of precipitant than required to induce precipitation. As water vaporises from the drop to the reservoir, the precipitant concentration increases to a level optimal for crystallisation (**Figure 1-23**). Since the system is in equilibrium, these optimum conditions are maintained until the crystallisation is complete.

Screening protocols for the crystallisation of new membrane protein plays very important role nowadays. From 59277 structures that have been released in the Protein Data Bank (PDB, [www.rcsb.org/pdb](http://www.rcsb.org/pdb)) up to 28<sup>th</sup> July 2009, only 644 structures are classified as membrane proteins that have been defined by X-ray crystallography. Although crystallisation of membrane proteins still remains a challenge, sparse-matrix screens have been formulated based on information mined from that available the PDB database. Commercial screening kits, e.g. MemSys, MemStr, MemGold from Molecular Dimensions Ltd or MemFac and AdditiveScreen HT from Hampton Research, provide 48 or 96 crystallisation conditions (varying pH, precipitants, and additives) designed for membrane proteins. As detergents must also be tested when working with membrane proteins (Prive, 2007), detergent screening kits are available. Such kits contain five or twelve popular detergents, e.g. from Anatrace, and are particularly useful when searching for appropriate detergent for crystallisation.

In line with the growth of the number of screening protocols, robots have proved useful in automating routine crystal screening. The ThermoFisher robotic system, for example, is an integrated crystallisation system able to prepare plates, set up drops (nano drop), store plates, image them and then stores the data.

## 1.11 Project background

A microscopic understanding of the interplay between the organisation of the pigments in light harvesting complexes and their spectral properties requires high-resolution structural information. This is, unfortunately, available only for very few types of peripheral light-harvesting complexes, two B800-850 complexes (*Rps. acidophila* 10050 and *Rhsp. molischianum*) and one B800-820 complex (*Rps. acidophila* 7050). In each of these cases the LH2 complexes have a well-defined apoprotein composition.

When cells of *Rps. palustris* are grown at high-light (HL) intensity they synthesise a standard LH2 complex. At low light intensity *Rps. palustris* strain 216 replaces the standard B800-850 with a B800-low-850 LH2 complex (Figure 1-13). This ability to adapt and to synthesis LH2 complexes with different NIR absorption spectra is related to the presence of the multiple genes encoding LH2  $\alpha/\beta$ -polypeptides (Evans *et al.*, 1990, Larimer *et al.*, 2004). In *Rps. palustris* 261, the structural explanation of the spectral changes going from B800-850 to B800-low-850 LH2 is still a matter of debate (Evans *et al.*, 1990, Fowler *et al.*, 1996, Gall *et al.*, 1999, Nishimura *et al.*, 1993). The ability to shift the type of LH2 allows these bacteria to be able to grow at ten times lower light intensity than most species that cannot do this. It is not currently understood how changing the types of LH2 allows the bacteria to grow photosynthetically at these lower light intensities.

An unusual B800 LL LH2 complex from *Rps. palustris* that only contains LH2 PucBA<sub>d</sub> proteins has been crystallised. A model based on these low resolution crystals (7.5 Å) has been described (Hartigan *et al.*, 2002). This model suggests that this complex is an  $\alpha\beta$ -octamer and that each of its  $\alpha\beta$ -apoprotein pairs binds an extra Bchl *a* relative to LH2 from *Rps. acidophila*. An AFM study of LL membranes from *Rps. palustris* also suggested that the B800 LL LH2 is predominantly octameric (Scheuring *et al.*, 2006).

However in *Rps. palustris* the situation is potentially more complicated since the bacteria expresses multiple  $\alpha\beta$ -polypeptides, PucBA<sub>a</sub>, PucBA<sub>b</sub>, PucBA<sub>c</sub> and PucBA<sub>d</sub>, even under the HL condition (Evans *et al.*, 1990, Larimer *et al.*, 2004).

The possibility, therefore, exists that there may be more than just two types of LH2 in this organism. When this PhD work was started, it was unclear whether the LH2 complexes from *Rps. palustris* had rings with a mixture of apoprotein types or whether the preparations contain mixtures of rings where each individual ring in the mixture has a homogenous apoprotein composition, but where different rings have different compositions. The work in this thesis aimed to try and resolve this situation.

## 1.12 Thesis aims

The aims of this thesis are

1. To isolate and to purify stable LH2 complexes from *Rhodopseudomonas palustris* 2.1.6 grown at different light intensities.
2. To characterise the arrangement and the binding of the pigments in the LH2 complexes from *Rhodopseudomonas palustris* 2.1.6 grown at different light intensities in relation with their optical properties.
3. To probe and study the energetic heterogeneity of LH2 from *Rhodopseudomonas palustris* 2.1.6 grown at different light intensities by single molecule spectroscopy.
4. To study the energy transfer reaction within the LH2 complexes from *Rhodopseudomonas palustris* 2.1.6 grown at different light intensities.
5. To set crystallisation trials in order to obtain suitable crystals for structural analysis of the LH2 complexes.

---

## 2 Materials and Methods

---

### 2.1 Culture storage

The species used in this study is *Rps palustris* strain 2.1.6. (colloquially termed French palustris). The culture was maintained in agar stabs (1.5 g agar in 100 ml C-succinate media) on the laboratory shelf until required (**Figure 2-1A**). The cultures were checked regularly by the use of agar plates to ensure their purity.

### 2.2 Culture growth and harvest

*Rps. palustris* strain 2.1.6. was grown anaerobically photoheterotrophic in C-succinate media (see **Appendices**). The stab culture was overlaid with the liquid media and placed in the growth room at 30° C between rows of incandescent bulbs (**Figure 2-1B**). The intensity of light that illuminated at the bottle was measured to be ~220 lx. After the cells reached a sufficient density ( $OD_{850} = 0.3 \text{ cm}^{-1}$ ), they were transferred to 500 ml flat-sided bottles and incubated in the growth room. To minimize any self-shading caused by the cells themselves, the cultures were regularly transferred into a fresh media in 500 ml flat-sided bottles, thereby ensuring a constant low culture optical density. At the optimum density ( $OD_{850} = 0.5 \text{ cm}^{-1}$ ) the cells can be harvested or further transferred. In this study cultures were placed at different distances away from the bulb so that the intensity of light that reached the cell culture was able to be varied from 220 lx, 90 lx, 20 lx, 10 lx, 6.5 lx to 5.5 lx (**Figure 2-1C**). In the results section, these light intensities have been called high-light (HL), low-light intermediate 1 (LL1), low-light intermediate 2 (LL2), low-light (LL), far low-light (FLL1) and extreme low-light (FLL2), respectively. The cells were harvested after 120 h growth by centrifugation (1,248 g, 30 min) and resuspended in 20 mM MES buffer pH 6.8 (Sigma-Aldrich) containing 100 mM KCl. The cells were stored at -20 °C until required.



**Figure 2-1** A. Stab culture of purple bacteria in agar media on the laboratory shelf. B. Liquid cell culture in 500 ml flat-sided bottles placed in the high-light area. C. Growing cultures at different light intensities by varying the distance of the culture from the light bulb.

## 2.3 Isolation of light-harvesting complexes

The harvested cells were broken by 3 passages through a French Press (9500 psi) in the presence of a little of DNAase and  $MgCl_2$ . The broken membranes were then sedimented by centrifugation at 184,000 g for 2 h. The pellet was resuspended and homogenised in 20 mM Tris-HCl pH 8.0 (Fisher Scientific) and its concentration adjusted to give an absorption at 850 nm of  $70\text{ cm}^{-1}$ . The membranes were then solubilised by the addition of 1% v/v lauryldimethylamine N-oxide (LDAO) (Fluka). After stirring for 30 min in the dark, at room temperature any unsolubilized material was removed by centrifugation at 16,000 g for 10 min. The supernatant was then layered onto a sucrose step gradient. The gradient consisted of 0.8, 0.6, 0.4, 0.2 M sucrose prepared in 20 mM Tris-HCl pH 8.0 containing 0.1% v/v LDAO. The gradients were then centrifuged overnight at 149,000 g at 4 °C. The upper-pigmented band contained the LH2 complexes and the lower pigmented band the LH1-RC complexes. The band containing LH2 complexes was collected and purified on a DE-52 cellulose column (Whatman). After desalting step through PD-10 column, the LH2 complexes were further

purified by chromatography on a Resource-Q column. To ensure high purity, fractions of the LH2 complex with a ratio between the absorption maximum at ~800 nm and the maximum at the protein absorption ( $A_{280}$ ) above 3.0 were collected for spectroscopic analysis, crystallisations, etc.

## 2.4 Characterisation of LH2 complexes

### 2.4.1 Apoprotein identification by NuPAGE Gels

The purity and the size of the LH2 apoproteins were assessed by running 12% NuPAGE Novex Bis-Tris mini gels (Invitrogen) using SeeBlue Plus2 pre-stained standard (Invitrogen) molecular weight markers. Protein (10  $\mu$ l,  $OD_{850} = 40 \text{ cm}^{-1}$ ) sample was mixed with 5  $\mu$ l 300 mM dithiothreitol (DTT) and 5  $\mu$ l NuPAGE LDS sample Buffer. After heating the sample in the water bath at 70° C for 20 min, the mixture was loaded on the NuPAGE gel. NuPAGE SDS 1x running buffer (Invitrogen) in deionised water was used for the running buffer. The electrophoresis conditions were constant at 200 V for 40 min. The gels were stained with SimplyBlue SafeStain (Invitrogen) and destained with deionised water overnight.

### 2.4.2 Protein identification by mass spectroscopy

The purified HL and LL LH2 complexes were sent to the FingerPrint Proteomic Facility, University of Dundee, for polypeptide identification. The sample was first digested with trypsin in-gel prior to analysis by one dimensional nano-liquid chromatography coupled to ESI-MS-MS using a 4000 QTRAP (Applied Biosystems) tandem MS system. The molecular mass of the fragments of the LH2 peptides ( $m/z [M+H]^+$ ) were compared with hypothetical fragment masses predicted from their gene sequences published online by UniProtKB/Swiss-Prot, which is based on the complete genomic sequence of *Rps. palustris* reported by Larimer et. al. (Larimer *et al.*, 2004).

### 2.4.3 Bacteriochlorophyll assay

Assay of the concentration of bacteriochlorophyll was carried out in order to quantify the molar ratio between LH2 and the core (LH1-RC) complexes in the

photosynthetic membrane of *Rps. palustris* grown at different light intensities. The method used was that according to Clayton (Clayton, 1966). This assay was carried out in a dark room. The solubilized membrane or complexes were extracted using acetone/methanol (7:2 v/v). Any insoluble material was removed from the extract by centrifugation. The procedure was repeated two or three times until the supernatant was colourless. The “wet” extract was first dried with N<sub>2</sub> and then redissolved in acetone/methanol. Afterwards the Bchl concentration could be determined spectroscopically using the extinction coefficient at 772 nm ( $\epsilon_{772}$ ) of 76 mM<sup>-1</sup> cm<sup>-1</sup> (Clayton, 1966).

#### **2.4.4 Carotenoid assay**

The carotenoid assays were carried out in autumn 2008 during my stay with Prof. Yasushi Koyama at Kwansai Gakuin University, Sanda, Hyogo, Japan. The experimental method was adapted from Qian et al. (2001) (Qian *et al.*, 2001). Carotenoids were extracted from a 5 ml suspension of high- (HL) and low-light (LL) LH2 complexes (OD at their near IR absorption maximum = 10 cm<sup>-1</sup>) isolated from *Rps. palustris* strain 2.1.6 by 15 ml acetone:MeOH (7:2 v/v). Any insoluble material was removed from the extract by centrifugation. This procedure was repeated two or three times until the supernatant was colourless. The raw carotenoid extract was transferred to a separating funnel containing 5 ml petroleum-ether, to which some saturated NaCl solution was then added. After the aqueous and organic layers separated, the aqueous layer was discarded. The organic layer was washed three times with 10 ml of the saturated NaCl solution. The organic layer was collected, dried under N<sub>2</sub>, and the carotenoids were then dissolved in benzene.

The extracted carotenoids were then separated by HPLC, using a silica gel column (Lichrosorb Si-60, 4.6×300 mm) and eluted with 2.5% acetone in benzene. The flow rate was 0.6 ml min<sup>-1</sup> and the detection wavelength was at 480 nm. Absorption spectra of the Cars were recorded with a photodiode-array detector (Waters 996). Each separated Car was identified based on its retention time and its absorption spectrum. In order to determine the amount of each Car, the area under each peak in the HPLC elution profile was divided by the value of  $\epsilon$  in eluent (2.5 % acetone in benzene) of the corresponding reference carotenoid (Qian *et al.*, 2001). The following carotenoids (gift from Prof. Y. Koyama) were

used as reference: lycopene ( $N = 11$ ,  $\epsilon_{480} = 147900$ ), anhydrovibrin ( $N = 12$ ,  $\epsilon_{480} = 90560$ ), spirilloxanthin ( $N = 13$ ,  $\epsilon_{480} = 105800$ ) and rhodovibrin ( $N = 12$ ,  $\epsilon_{480} = 138800$ ). The carotenoids, which have major peaks in the HPLC profile, were collected for structural determination using  $^1\text{H}$ -NMR spectroscopy. In order to prepare sample for the structural determination of the carotenoid, about 1.5 mg of the above collected sample was re-purified by HPLC at the dark. Then  $^1\text{H}$ -NMR spectroscopy (Kyoto, Japan) was used to determine the structure of the carotenoid. The purified carotenoids were submitted to the NMR facility, where the NMR spectra were recorded and data interpreted. The data and the interpretation are shown in **Appendices**.

#### **2.4.5 Steady state absorption spectroscopy**

The room temperature absorption spectra were measured in a Shimadzu (UV-1700 Spectrophotometer) scanning from 250-950 nm. The 10 K absorption spectra of LH2 complexes were measured using a Varian Cary E5 double-beam scanning spectrophotometer (Varian, Les Ulis, France). The LH2 samples were prepared in 60 % (v/v) glycerol in Tris buffer (20 mM Tris-HCl pH 8.0) containing 0.1% LDAO. LDAO wasn't used for membrane samples. The temperature of the samples was maintained by a Helium bath cryostat (Maico Metriks, Tartu, Estonia). In order to ensure the equilibrium between the sample and the helium bath, the sample was stabilised at each measured temperature for at least 10 minutes. The low-temperature absorption measurements were performed at the Institut de Biologie et Technologies de Saclay, CEA Saclay, France, together with the help of Dr. Andrew Gall.

#### **2.4.6 Circular dichroism spectroscopy**

The CD measurements were carried out in Departments of Biology and Chemistry, Washington University in St. Louis by Aaron Collins. Concentrated LH2 samples were prepared in 66 % (v/v) glycerol in 20 mM Tris-HCl buffer pH 8.0, containing 0.1 % LDAO. The low temperature environment was created using a liquid nitrogen cryostat (OptistatDN, Oxford Instruments, Bucks, UK). The CD spectra were recorded with a Jasco J-815 spectropolarimeter (JASCO Inc., Easton, MD, USA) with a bandwidth to 4 nm. Samples were measured in 1 mm,

demountable quartz cuvette (Starna Scientific Limited, Hainault, Essex, England).

### **2.4.7 Raman spectroscopy**

The resonance Raman measurements were carried out during my stay with Dr. Andrew Gall, the Institut de Biologie et Technologies de Saclay, CEA Saclay, France in summer 2009. Raman spectra, in resonance with the Soret transition of Bchl a, were recorded with a Jobin-Yvon U1000 spectrometer equipped with a back-thinned CCD camera (Jobin Yvon Spectra ONE). The spectra were recorded with a 90° geometry with the samples maintained at 77 K in a SMC-TBT flow cryostat (Air Liquide, Sassenage, France) cooled with liquid nitrogen. The samples were excited at 363.8 nm with a Coherent Inova 100 Ar+ laser with an incident intensity of less than 10 mW at the sample surface.

## **2.5 Single molecule spectroscopy**

The single molecule experiments were carried out during my stay with Prof. Jürgen Köhler, Universität Bayreuth, Germany, in autumn 2007 and summer 2008. I would like to thank Ralf Kunz (Phd Student) for assistance with measurements and Paul Böhm (Diplom student) for his helping hand with the laser alignment.

### **2.5.1 Sample preparation**

For SMS the purified LL LH2 complexes were diluted to less than  $10^{-9}$  M in 20 mM Tris-HCl buffer pH 8.0 containing 0.1% (v/v) LDAO. In the last dilution step 2 % (w/w) polyvinyl alcohol (PVA, mw 30,000-70,000 g mol<sup>-1</sup>) was added to the LL LH2 and a drop of the solution was spin-coated onto a quartz substrate for 10 s at 500 rpm and 60 s at 2,500 rpm (model P6700, Speciality Coating System). This produces thin amorphous polymer films of less than 1 μm thickness in which the LH2 complexes were embedded. Then the sample was immediately mounted in a helium-bath cryostat and cooled down to 1.4 K.

## 2.5.2 Experimental setup

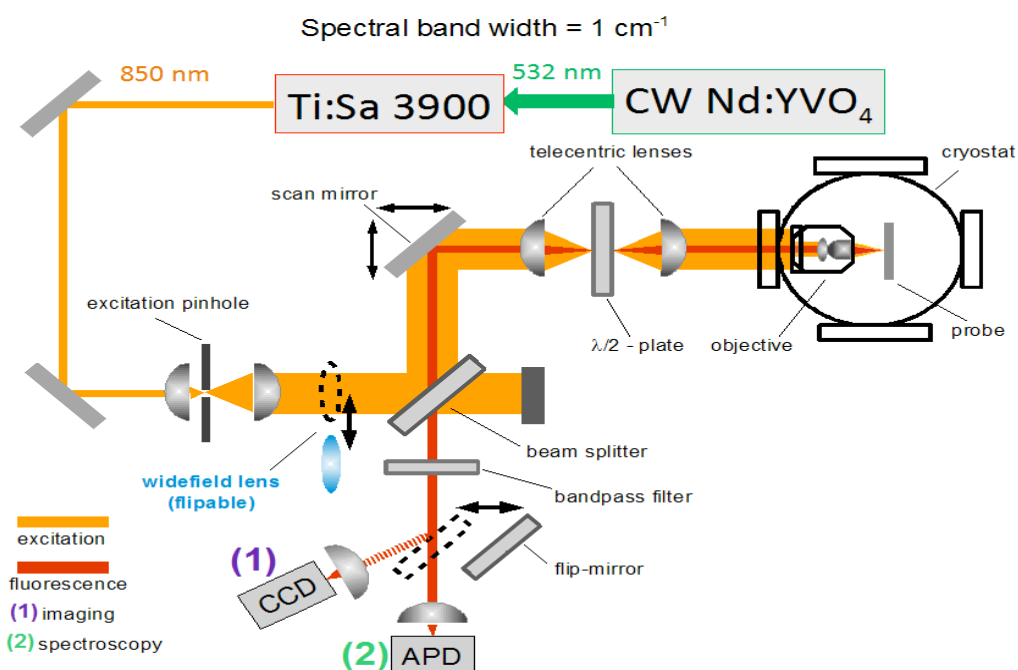


**Figure 2-2** Optical setup for 1.4K single molecule spectroscopy. The objective is a single aspheric lens (NA 0.55).

Fluorescence-excitation spectroscopy was performed using a home-built microscope that can be operated either in wide-field or confocal mode (**Figure 2-2**). The excitation source was a continuous-wave tunable Titanium-Sapphire laser (3900S, Spectra Physics, Mountain View, CA, USA) pumped by a frequency-doubled continuous-wave Neodymium:Yttrium-Vanadate (Nd:YVO<sub>4</sub>) laser (Millennia Vs, Spectra Physics). Well-defined changes of the wavelength of the Titanium:Sapphire laser were achieved by rotation of the intracavity birefringent filter with a motorized micrometer screw. For calibration purposes, a wavemeter was used and accuracy of the laser frequency as well as a reproducibility of  $1 \text{ cm}^{-1}$  was verified. First, a  $50 \times 50 \text{ }\mu\text{m}^2$  wide-field image of the sample was taken by exciting the sample at 800 nm and detecting the fluorescence with a back-illuminated CCD camera (512 SB, Roper Scientific Princeton Instruments, Trenton, NJ, USA) after passing suitable band pass filters (BP893/21, Dr. Hugo Anders, Nabburg, Germany), which blocked the residual laser light. Subsequently, a spatially well-isolated complex was selected from the wide-field image and a fluorescence-excitation spectrum of this complex

was obtained. The setup was switched to the confocal mode and the fluorescence detected by a single-photon counting avalanche photodiode (APD) (SPCM-AQR-16, EG&G Optoelectronics, Vaudreuil, Canada) while scanning the laser repetitively between 784 and 872 nm. The recorded traces were stored separately in computer memory. A scan speed of the laser of  $3 \text{ nm}\cdot\text{s}^{-1}$  ( $\approx 50 \text{ cm}^{-1} \text{ s}^{-1}$ ) and an acquisition time of 10 ms per data point yields a nominal resolution of  $0.5 \text{ cm}^{-1}$ , ensuring that the spectral resolution is limited by the spectral bandwidth of the laser ( $1 \text{ cm}^{-1}$ ). In order to examine the polarisation dependence of the spectra, a  $\lambda/2$ -plate was placed in the confocal excitation path and rotated in steps of  $3.2^\circ$  between two successive scans, changing the angle of the polarisation of the excitation light by twice this value. The excitation intensity was about  $50 \text{ W cm}^{-2}$ .

## 2.6 Transient absorption measurements

The transient absorption spectra of LH2 complexes from *Rps. palustris* grown at different light intensities were measured by Dr. Vladimira Moulisova and myself during our stay with Dr. Larry Luer, CNR/INFM ULTRAS, Department of Physics, Politecnico di Milano, Milan, Italy. I would like to thank Sajjad Husheinkhani and Dr. Larry Luer for the assistance with measurements, laser alignment and for valuable discussions. The transient absorption difference  $\Delta A/A$  spectra (see figures in Chapter 5) were recorded using a conventional pump-probe set-up (Polli *et al.*, 2007). The ultrafast spectroscopic configuration used in these experiments started with a regeneratively amplified mode-locked Ti:sapphire laser (Clark-MXR Inc., Dexter, Michigan, USA) delivering pulses at 1 kHz repetition rate with a 790 nm centre wavelength, 150 fs duration, and 500  $\mu\text{J}$  energy. The pump energy was reduced to 50 nJ ( $0.03 \text{ mJ cm}^{-2}$ ). A fraction of the pulse energy was focused onto a thin sapphire plate to generate the white light broadband probe pulse. The near infra-red (NIR) range from 790 to 950 nm was used. The pump beam was modulated at 500 Hz by a mechanical chopper. After the probe pulse has traversed the sample, a two dimensional  $\Delta A/A$  readout as a function of pump-probe delay time was measured using an optical multichannel analyser in a single shot configuration. The chirp of the white light supercontinuum has been corrected for in the displayed spectra as previously described (Polli *et al.*, 2007).

## 2.7 Crystallisation

The LH2 complex from *Rps. palustris* was crystallised by a vapour diffusion technique (sitting drop) using crystallisation plates (NBS Biologicals, Huntingdon, UK). The experimental method was adapted from the conditions used to obtain crystals from the B800-850 LH2 from *Rps. acidophila* 10050 (Howard, 2000, McDermott *et al.*, 1995). After the RESOURCE-Q column, the LH2 protein was washed three to four times with 20 mM Tris-HCl pH 8.0 containing 0.1% (v/v) LDAO, concentrated using a Vivaspin concentrator (50,000 MWCO, Sartoriusstedim biotech, Surrey, UK) and the concentration adjusted to give an  $OD_{850} = 100 \text{ cm}^{-1}$ . A mixture of the LH2 protein and 4.0 M  $K_2HPO_4$  (KPi) (3:1 v/v) was then centrifuged at 13,000 rpm in an Eppendorf mini-centrifuge for 5 min to pellet any solid materials. This prepared protein solution (20  $\mu$ l) was pipetted in to the well on a sitting drop bridge and then was equilibrated against a 1 ml reservoir of 2.1 M ammonium sulphate (AMS) pH 9.35. The 24-well crystallisation tray was then sealed and kept in the incubator (20° C)

The crystallisation method when using the commercial screens was as follows: after RESOURCE-Q column the LH2 protein was washed three to four times with 20 mM Tris-HCl pH 8.0 containing 0.1% (v/v) LDAO, concentrated using a Vivaspin concentrator (50,000 MWCO, Sartoriusstedim Biotech, Surrey, UK) and the concentration of LH2 protein was adjusted to give an  $OD_{850} = 80 \text{ cm}^{-1}$ . LH2 protein (10  $\mu$ l) in 20 mM Tris-HCl buffer pH 8.0 containing 0.1% (v/v) LDAO was pipetted onto a sitting drop bridge, while the reservoir chamber contained 1 ml of precipitant solution. Precipitant solution (10  $\mu$ l) of was mixed gently into the LH2 drop. The crystallisation tray was then sealed and kept in the temperature-controlled incubator (10° C or 20° C). Crystallisation trays from NBS Biologicals were replaced in the later trials by the 24-well EasyXtall tool trays (QIAGEN, Crawley, UK) that have screw-topped lids so allow better and reversible sealing. Crystallisation screens (MemSt and MemSys from Molecular Dimension) were used for preliminary trials. These screens are a targeted sparse matrix of 1 ml x 96 conditions allowing the pH range, precipitants and salts used in membrane protein crystallisation to be screened with a detergent-containing protein drop.

The crystals obtained from the initial screens were first tested for their X-ray diffraction with the University of Glasgow X-ray Diffractometer. More promising crystals were then either characterised at the European Synchrotron Radiation Facility (ESRF), Grenoble, France or at the Diamond Light Source, Oxfordshire, UK. Any condition that produced promising results in the preliminary screens, was then optimised by introducing additives or amphiphiles (Hampton Research) and/or varying the buffer pH, the concentration of the precipitant or salt.

---

## 3 Isolation, purification and characterisation of LH2 complexes

---

This chapter is divided into three parts. The first part is about isolation and purification protocols to obtain pure and stable LH2 complexes from cells of *Rhodospseudomonas (Rps.) palustris* strain 2.1.6 grown under different light intensities. The second part is their spectroscopic characterisation. The third part describes the carotenoid compositions of the HL and LL LH2 complexes.

### 3.1 Isolation and purification protocols

#### 3.1.1 Growing cells at different light intensities

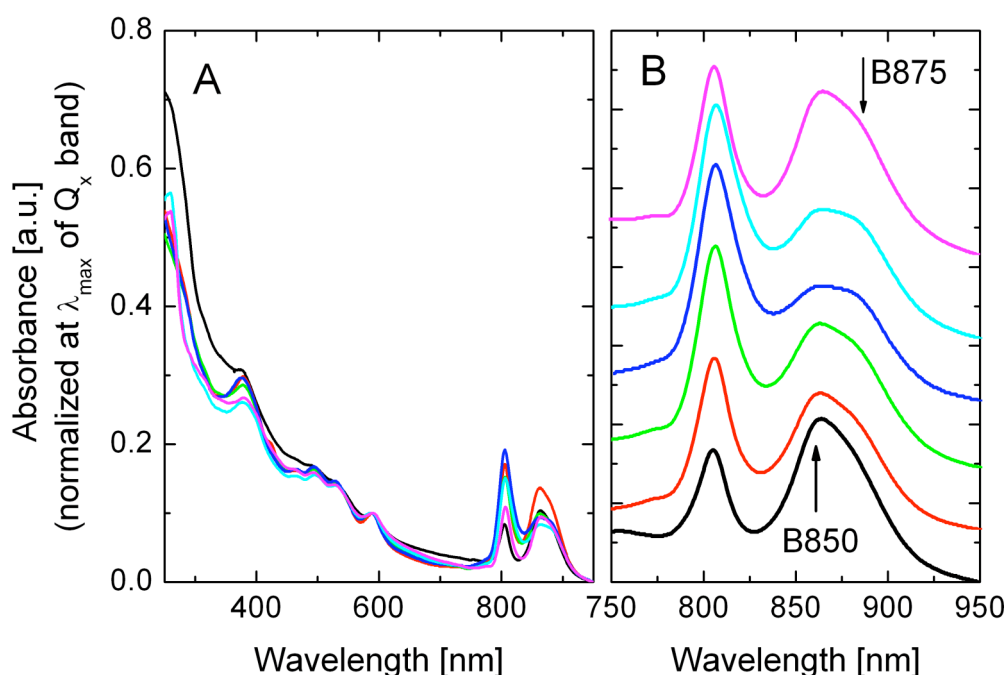
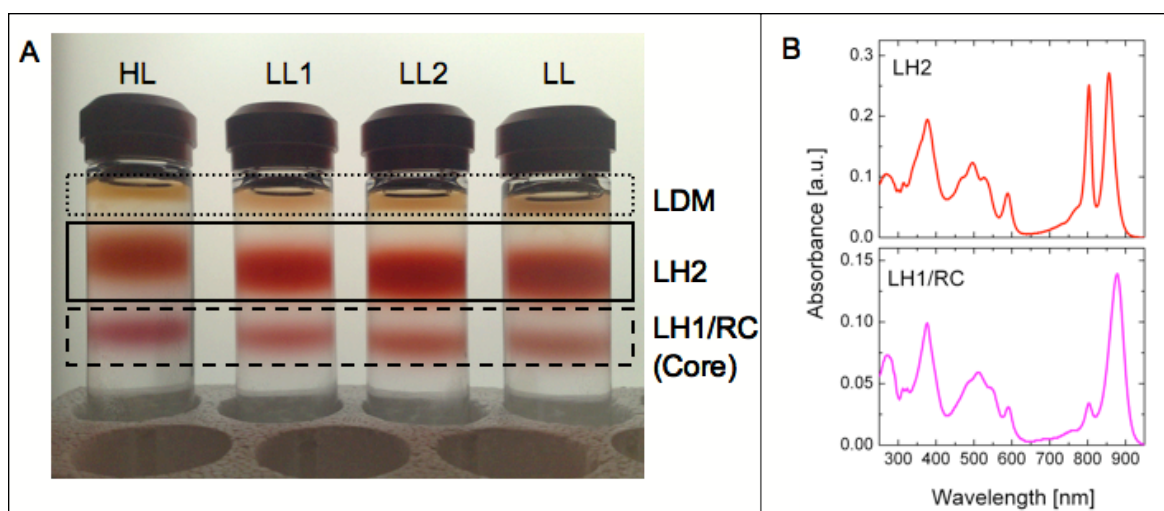


Figure 3-1 (A) Room temperature absorption spectra of whole cells from *Rps. palustris* grown at decreasing light intensities: high-light (HL, 220 lx, black line), intermediate 1 low-light (LL1, 90 lx, red line), intermediate 2 low-light (LL2, 20 lx, green line), low-light (LL, 10 lx, blue line), far 1 low-light (FLL1, 6.5 lx, cyan line) and far 2 low-light (FLL2, 5.5 lx, magenta line). A magnification of the NIR region is shown (B).

*Rhodospseudomonas (Rps.) palustris* strain 2.1.6. was grown in C-succinate medium (Böse, 1963) (Appendices 8.1) at successively decreasing light intensities. The light intensities at the surface of culture bottles were varied from 220 lx, 90 lx, 20 lx, 10 lx, 6.5 lx to 5.5 lx. The cultures were regularly transferred to ensure constant low optical density, thus any self-shading caused by the cells themselves could be minimised. Absorption spectra of whole cells grown at different light intensities were recorded and are presented in **Figure 3-1**.

The high-light grown cells (**Figure 3-1 black line**) show an absorption spectrum in NIR region that is rather similar to those from *Rps. acidophila* and *Rba. sphaeroides*, with two strong absorption maxima at 800 nm and 850 nm (Gardiner *et al.*, 1993). The 850 band is the most intense and has a shoulder at around 875 nm, indicating the presence of LH1-RC (core) complexes (**Figure 3-1**). As the light intensity is decreased, the NIR absorption spectra of the cells become markedly different. The 800 nm absorption band is more intense in the low-light grown cells, whereas the 850 nm band becomes correspondingly weaker. As result, the core 875 band is more apparent in the low-light (LL) grown cells (**Figure 3-1 blue line**). This situation reverses when the *Rps. palustris* cells are grown at the extreme lowest-light intensities, FLL1 and FLL2 (**Figure 3-1 cyan and magenta lines**), respectively. Under such extreme condition the intensity of 850 nm absorption band recovers toward the intensity of the high-light spectrum.

### 3.1.2 Isolation, purification and identification of LH2 proteins



**Figure 3-2 (A)** Typical results of sucrose gradient centrifugation runs of *Rps. palustris* 2.1.6 solubilised membranes. From the left to the right the *Rps. palustris* 2.1.6 were grown at HL, LL1, LL2 and LL, respectively. The solubilised membranes of HL, LL1, LL2 and LL were adjusted to have an equal concentration of the Bchl *a* and then gently layered onto the top of the gradients. After high-speed centrifugation (149,000 g at 4°C) for 14 h the two major LH complexes were separated. The two complexes have different colour, the LH2 is red and the LH1-RC (core) is pink. The low-density cellular materials and denatured complex are yellow. **(B)** Absorption spectra of LH2 and LH1/RC (core) complexes collected from the HL sucrose gradient tubes.

Sucrose-density gradient centrifugation of solubilised *Rps. palustris* membranes results in a good separation of the two complexes, LH2 and LH1-RC (core) (**Figure 3-2**). The solubilised membranes from cells of *Rps. palustris* grown at different light intensities were set to have an equal concentration of the Bchl *a* before being layered onto the top of sucrose-density gradient. The bottom pink band (**Figure 3-2**) contains core, whereas the middle red band contains the LH2 complexes. The two complexes have a different colours as they preferentially bind different carotenoids (Cogdell *et al.*, 2006). The upper yellowish band contains low-density cellular materials and denatured complexes. It is apparent from the intensity of the colored bands in **Figure 3-2** that the ratio between the isolated complexes, the LH2 and the core, varies depending on the light intensity at which the cells were grown.

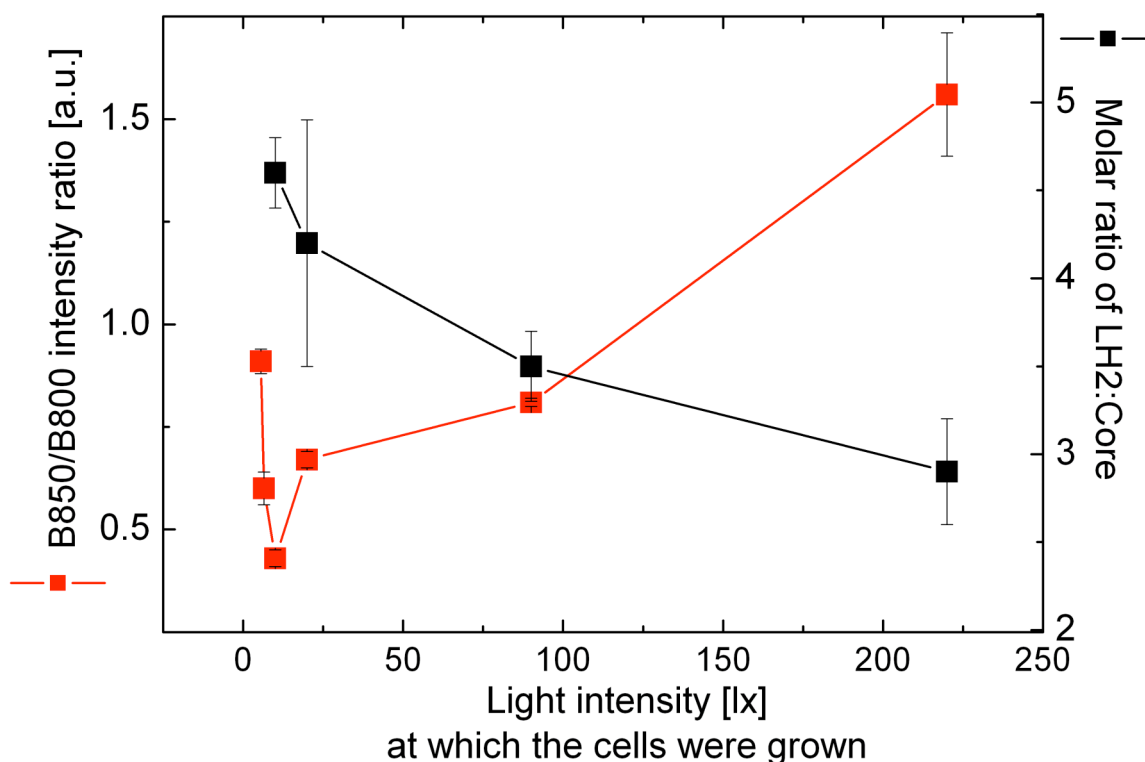


**Figure 3-3** The intensity ratio of bands B850:800 of the whole cell RT absorption spectra (red line) and molar ratio of LH2:Core (black) depending on the light intensity at which the cells were grown. The bars indicate standard deviations with  $n = 4$ .

The intensity ratio of the 850 nm band to the 800 nm band and the relative molar ratio of LH2:Core vary depending on the light intensity at what the cells were grown. These results are shown in **Figure 3-3**. This figure suggests that the *Rps. palustris* cells grown at LL intensity have photosynthetic membranes that contain relatively more LH2 complexes than the cells grown at HL intensity. This chromatic adaptation is consistent with previous reports (Cohen-Bazire, 1966, Hunter *et al.*, 1988, Kaplan, 1978, Sistrom, 1978, Sturgis *et al.*, 1996, Wassink, 1939) and from recent AFM studies on the *in situ* organization of the light harvesting complexes from *Rps. photometricum* (Scheuring *et al.*, 2005).

The LH2 complexes, collected from the sucrose-density gradient, were then further purified. The purification protocol uses anion-exchange chromatography and gel filtration (Superdex 200). In order to follow the purification progress, the core and LH2 complexes collected from sucrose gradients were loaded on the NuPAGE gel together with DE52 purified LH2 complexes (**Figure 3-4**). The lane 'core' records the composition of apoproteins of the core complex. It shows

bands at ~7 kDa and at ~17-36 kDa (Figure 3-4A). The LH2 collected directly from sucrose gradient has four bands at approximately 6 kDa with some bands at ~28-62 kDa (which suggest that there are some contaminants present). After purification of LH2 complex using DE52 anion exchange, the lane looks cleaner and just four bands at ~6kDa can be seen. The smeared bands at the bottom (1-2 kDa) correspond to the pigments and lipids. After the DE52 column LH2 was further purified by gel filtration. The composition of apoproteins of the LH2 was compared with the LH2 complex from *Rps. acidophila* 10050 on the NuPAGE gel (Figure 3-4B). The middle lane in Figure 3-4B shows the LH2 from *Rps. acidophila* 10050, having two bands, one at ~ 6 kDa and one at ~4 kDa. Both high- and low-light LH2 complexes of *Rps. palustris* are shown to have four bands, two at ~5kDa (H3/H4 and L3/L4) and two at ~6kDa (H1/H2 and L1/L2) (Figure 3-4B).

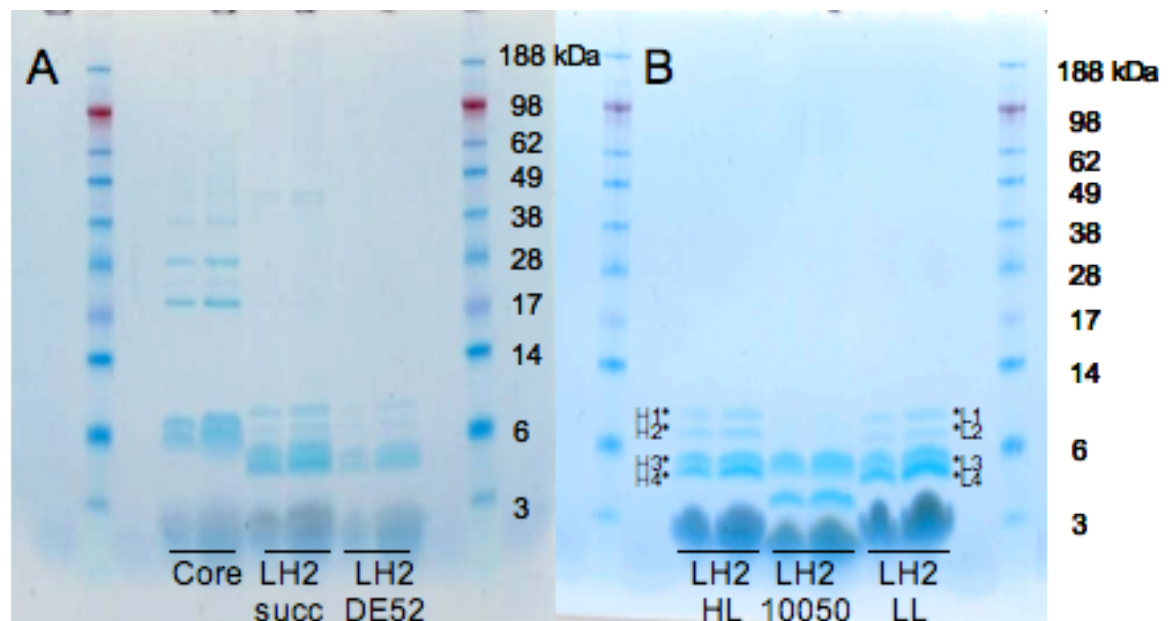


**Figure 3-4 Progress in purification of LH2 complexes examined by a NuPAGE 12% Bis-Tris-Gel. (A) Lane Core and LH2 succ correspond to the two complexes isolated from sucrose-density gradient. Lane LH2 DE52 indicates the LH2 after DE 52 purification. (B) The LH2 complexes were further purified by gel filtration.**

**Table 3-1 Peptide identification of the gel bands H1-H4 and L1-L4 (see Figure 3-4) by nLC-ESI-MS/MS**

LH2	Peptide residues	[M+H] <sup>+</sup> Expt	[M+H] <sup>+</sup> Calc	Assignment
<b>HL</b>				
Band H1				hypothetical protein RPA1495
Band H2				hypothetical protein RPA1495
Band H3				hypothetical protein RPA4760
Band H4	MNQAR	618.5	619.2	PucA <sub>a</sub>
	YWNGKAAAIIESSVNVG	1663.9	1664.8	PucA <sub>a</sub>
	MNQGR	604.9	605.2	PucA <sub>b</sub> , PucA <sub>c</sub> , PucA <sub>d</sub> , PucA <sub>e</sub>
	TLTGLTVEESEELHK	1684.7	1684.9	PucB <sub>a</sub>
	ADDPNKVWPTGLTIAESEELHK	2449.3	2449.2	PucB <sub>e</sub>
<b>LL</b>				
Band L1				hypothetical protein RPA1495
Band L2				hypothetical protein RPA1495 and RPA3011
				PucA <sub>a</sub> / PucA <sub>e</sub>
Band L3	YWNGK	667.3	667.3	PucA <sub>d</sub>
Band L4	FMNGK	596.2	596.2	PucA <sub>b</sub> , PucA <sub>c</sub> , PucA <sub>d</sub> , PucA <sub>e</sub>
	MNQGR	604.9	605.2	PucA <sub>b</sub> , PucA <sub>c</sub> , PucA <sub>d</sub> , PucA <sub>e</sub>
	TLTGLTVEESEELHK	1684.7	1684.9	PucB <sub>a</sub>
	MVDDPNK	817.5	818.3	PucB <sub>d</sub>
	VDDPNKVWPTGLTIAESEELHK	2477.5	2477.2	PucB <sub>d</sub>
	ADDPNKVWPTGLTIAESEELHK	2449.3	2449.2	PucB <sub>e</sub>

In order to identify the apoprotein composition of the antenna complexes, both purified HL and LL LH2 complexes were sent to the FingerPrint Proteomic Facility, University of Dundee, to be analysed by using nano-scale liquid chromatography tandem mass spectroscopy (nLC-ESI-MS/MS). The bands (H1-H4 and L1-L4) were excised from the gel prior to the trypsin digestion, and then followed by the nLC-ESI-MS/MS analysis. The molecular mass of the fragments of the LH2 peptides ( $m/z$  [M+H]<sup>+</sup>) were matched to predicted *Rps. palustris* antenna polypeptide masses that have published online by UniProtKB/Swiss-Prot. The results from the FingerPrint Proteomic Facility, Dundee, are shown in Table 3-1. Five peptides, PucA<sub>a</sub>, PucA<sub>e</sub>, PucA<sub>b</sub>, PucB<sub>a</sub> and PucB<sub>e</sub> have been identified in

band H4 from HL LH2 complexes (**Table 3-1**). The assignment of the peptide residue MNQGR ( $m/z$  604.9,  $[M+H]^+$ ) for the band H4 from HL LH2 was inconclusive, because the amino acid sequence (MNQGR) could be found in any of the PucA<sub>b</sub>, PucA<sub>c</sub>, PucA<sub>d</sub> and PucA<sub>e</sub> polypeptides at position 1-5 in their sequence. Similar ambiguous results are also found for the assignment of YWNGK ( $m/z$  = 667.3,  $[M+H]^+$ ) in the band L3 and MNQGR ( $m/z$  604.9,  $[M+H]^+$ ) in the band L4 from the LL LH2. The results in **Table 3-1** show that only the bands on the SDS gel at lower molecular weight (H4, L3 and L4) were identified as the  $\alpha$ - (PucA) and  $\beta$ - (PucB) polypeptides. While the bands H1, H2 and H3 from the HL LH2 as well as the bands L1 and L2 from the LL LH2 (**Table 3-1** and **Figure 3-4**) have been identified as putative uncharacterised proteins based on the complete genomic sequence of *Rps. palustris* published by Larimer et. al. (Larimer *et al.*, 2004).

In order to reduce contamination by irrelevant uncharacterised proteins, the purification protocol was improved by replacing the gel filtration with chromatography on a RESOURCE-Q strong anion-exchange column. The LH2 complex was first desalted through a PD-10 column, then loaded on the RESOURCE Q column. Elution of the bound complex was subsequently achieved with a salt gradient 0-100% (1M NaCl in 20 mM Tris-HCl pH 8.0 containing 0.1% LDAO) (**Figure 3-5**). To ensure high purity, only fractions, which are at the maximum of the elution profile peak, were used for further analysis. Those fractions are fractions #15 and #16 (**Figure 3-5A**) for the HL LH2 complex, and fractions #16 and #17 (**Figure 3-5B**) for the LL LH2 complex. These fractions were then also sent for sequencing to the FingerPrint Proteomic Facility, University of Dundee.

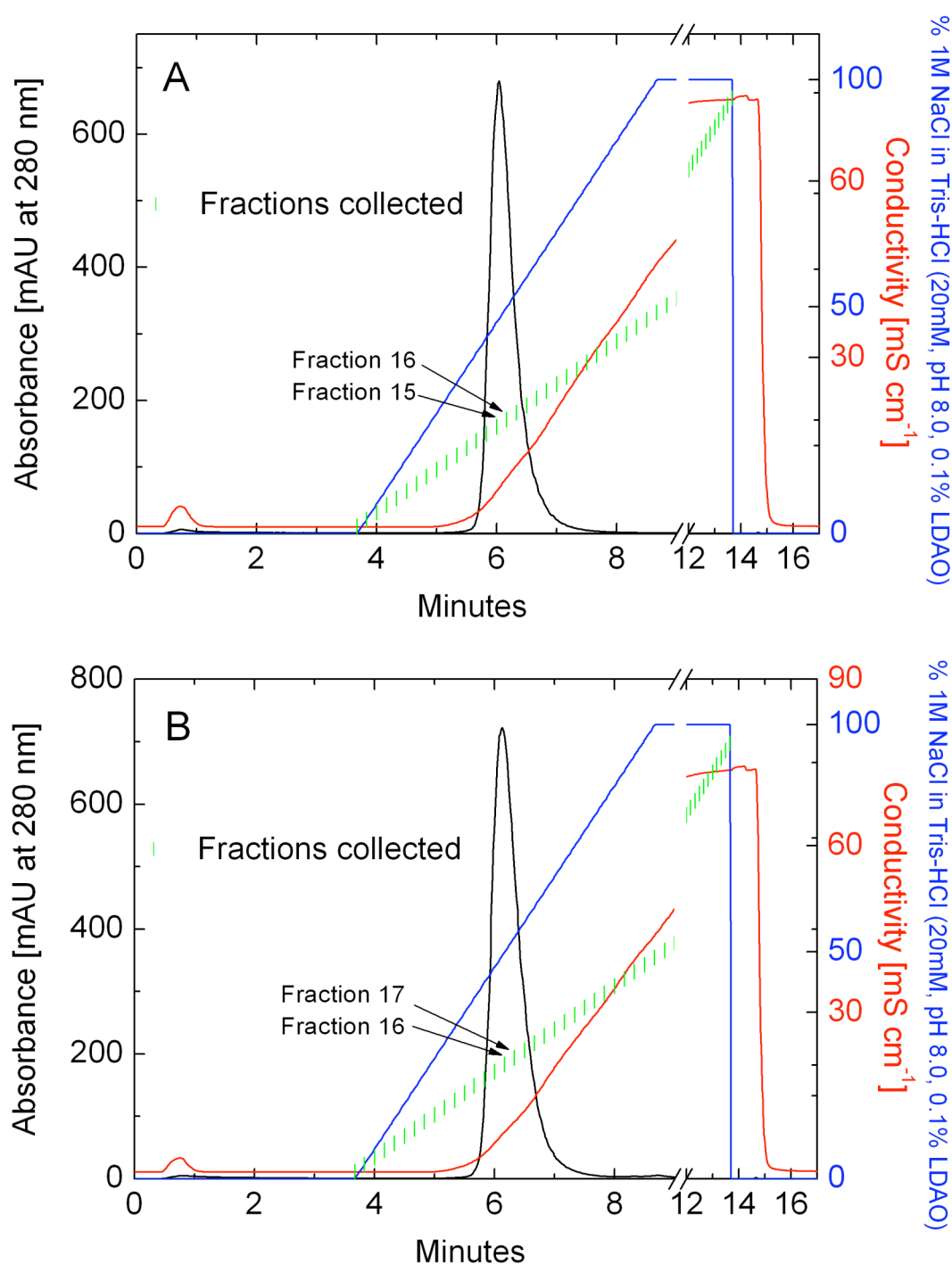


**Figure 3-5** Elution profile of HL (A) and LL (B) LH2 complexes from *Rps. palustris* when purified using RESOURCE 15Q 1 ml. The LH2s were desalted using PD10 column prior to application. RESOURCE 15Q was connected to AKTA system and equilibrated with Tris-HCl (20mM, pH 8.0) containing 0.1% LDAO. Elution of the bound complex was achieved with a salt gradient 0-100% (1 M NaCl in Tris-HCl [20mM, pH 8.0] containing 0.1% LDAO). Flow rate was  $4 \text{ ml min}^{-1}$ . The eluting protein was monitored at 280 nm and collected in 0.5 ml fractions. The purification experiments were carried out in the temperature-controlled room ( $4^\circ\text{C}$ ).

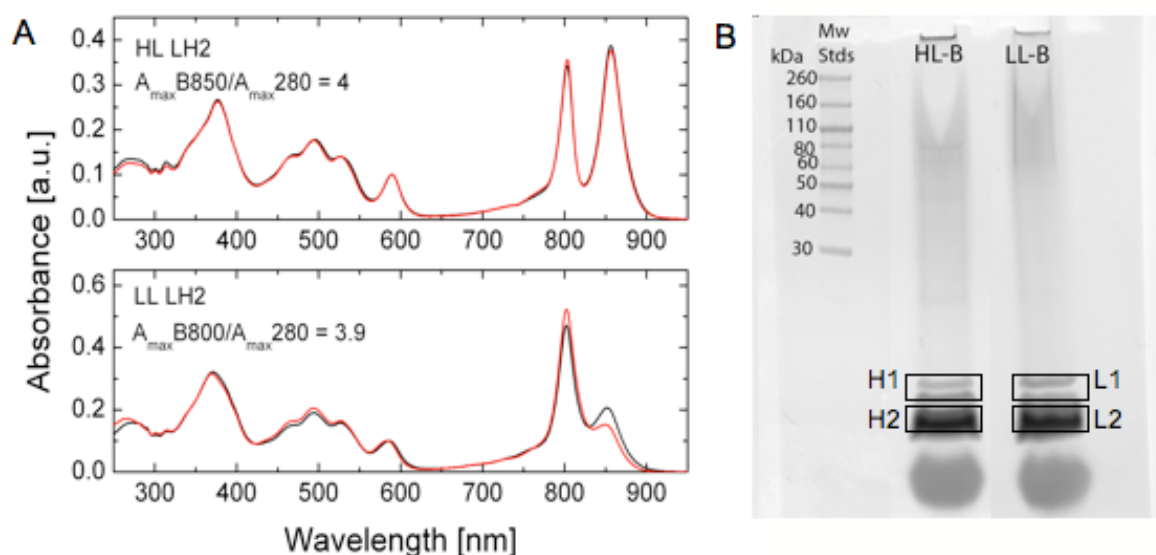


**Figure 3-6 (A)** The purity of the LH2 complexes was monitored using room temperature (RT) absorption spectrum. The absorption spectra of HL (top) and LL (bottom) LH2 complexes before (black line) and after (red line) purification using RESOURCE-Q are presented. The higher the ratio of A<sub>850</sub>/A<sub>280</sub> (for HL) or A<sub>800</sub>/A<sub>280</sub> (for LL), the greater is the purity of the LH complex is. **(B)** A NuPAGE 12% Bis-Tris gel profile of the apoproteins of the HL and LL LH2 complexes after their purification using the RESOURCE-Q column. The apoproteins are indicated in boxes. The large bands at the bottom correspond to pigments and lipids.

The integrity and the purity of the LH2 complex can be monitored by measuring the ratio of the absorption maximum at ~850 or ~800 nm band to that at ~280 nm band (Cogdell *et al.*, 1985). The Q<sub>y</sub> transition bands of Bchl *a* are at ~800-900 nm, when the Bchl *a*s are bound to their apoprotein. Therefore any reduction in the ratio of A<sub>850</sub>/A<sub>280</sub> (or A<sub>800</sub>/A<sub>280</sub>) indicates either a decreased bound Bchl *a*, from denatured complexes, or contamination of extraneous protein. The absorption spectra of the LH2 complexes before and after the purification by RESOURCE-Q column were recorded from 250 nm to 950 nm regions (**Figure 3-6A**). **Figure 3-6A** shows that after purification using RESOURCE-Q, the band at ~280 nm in the HL LH2 absorption spectrum is decreased with respect to the absorption intensity of the B850 band. In the case of LL LH2 complex fraction shown in **Figure 3-6A** (solid red line), the 850 nm band has lost some of its intensity and the 800 nm band is stronger. This suggests that some contamination from B800-850 HL LH2 in the B800-low-850 LL LH2 was reduced after chromatography on the RESOURCE-Q. The LH2 complexes with the ratio above 3.0 were used here for further analysis.

The NuPAGE Bis-Tris gel profile, **Figure 3-6B**, shows the apoprotein composition of the purified HL and LL LH2 complexes after the separation on the RESOURCE-Q column. Unlike the NuPAGE result shown in **Figure 3-4B** that shows 4 bands for both HL and LL LH2, here, the lane HL-B shows that the purified HL LH2 complexes have two weak bands (H1) and a strong band (H2) (**Figure 3-6B**). Similarly, lane LL-B for the purified LL LH2 complexes also indicates two weak bands (L1) and a strong band (L2).

**Table 3-2** Peptide identification of the gel bands H1, H2, L1 and L2 from the RESOURCE-Q purified LH2 complexes (**Figure 3-6B**) by nLC-ESI-MS/MS

LH2	Peptide residues	[M+H] <sup>+</sup> Expt	[M+H] <sup>+</sup> Calc	Assignment
<b>HL</b>				
Band H1	KAAAISSVNVG	1016.5	1016.5	PucA <sub>a</sub>
	KYWNGATVAAPAAAPAPAAPAAKK	2036.1	2036.1	PucA <sub>b</sub>
Band H2	KTLTGLTVEESEELHKH	1684.9	1684.9	PucB <sub>a</sub>
	KVWPTGLTIAESEELHKH	1808.9	1808.9	PucB <sub>e</sub>
<b>LL</b>				
Band L1	KAAAISSVNVG	1016.5	1016.5	PucA <sub>a</sub>
	KAAAISSIK	889.5	889.5	PucA <sub>d</sub>
Band L2	KTLTGLTVEESEELHKH	1684.9	1684.9	PucB <sub>a</sub>
	KVWPTGLTIAESEELHKH	1808.9	1808.9	PucB <sub>d</sub>
	KHVIDGTRIFGAIAIVAHFLAYVYSPWLH	3165.7	3165.7	PucB <sub>e</sub>

The results of the nLC-ESI-MS/MS protein sequencing identify that the bands H1, H2, L1 and L2 contain multiple type of  $\alpha$ - (PucA) and  $\beta$ - (PucB) polypeptides (**Table3-2**). In the case of HL LH2 complexes, two weak bands (H1) can be assigned as the PucA<sub>a</sub> and PucA<sub>b</sub> apoproteins, while the strong band (H2) can be assigned as the PucB<sub>a</sub> and PucB<sub>e</sub> apoproteins. In the case of LL LH2 complexes, the L1 bands are assigned as the PucA<sub>a</sub> and PucA<sub>d</sub> apoproteins, while the strong L2 band can be assigned as the PucB<sub>a</sub>, PucB<sub>d</sub> and PucB<sub>e</sub> apoproteins.

## 3.2 Spectroscopic characterisation

### 3.2.1 Photosynthetic membrane

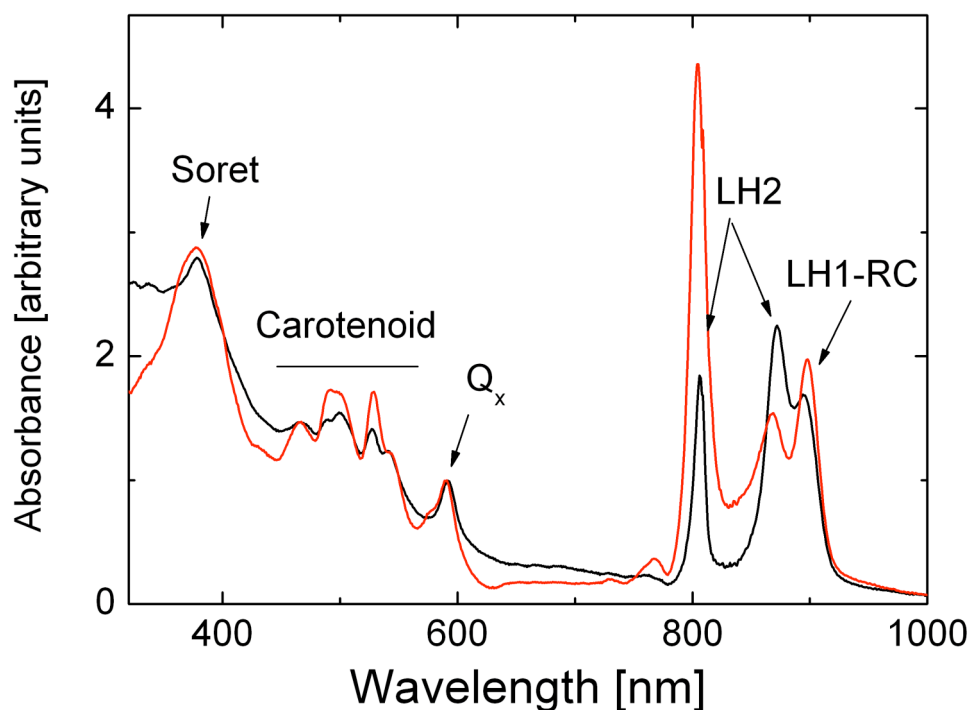


Figure 3-7 *In situ* identification of the LH2 and LH1-RC complexes in the intracytoplasmic membrane (ICM) can be directly demonstrated by absorption spectroscopy at cryogenic temperatures. Absorption spectra measured at 10 K of the photosynthetic membranes from *Rps. palustris* grown at high- (black line) and low-light (red line) intensities are shown. Membranes were prepared in 60% (v/v) glycerol in Tris-HCl (20 mM, pH 8.0). The spectra are normalized at Q<sub>x</sub>.

The absorption spectrum of the photosynthetic membrane at cryogenic temperature offers the possibility to distinguish optically the absorption bands of the LH2 and LH1-RC complexes *in situ* and gives information concerning the stoichiometry ratio of LH2 and LH1-RC complexes in the membrane. The membranes in a buffer solution are in solid state at 10K. The low-temperature (LT) absorption spectra (Figure 3-7) feature narrower absorption bands compared with room temperature (RT) measurement (Figure 3-1). This makes the Q<sub>y</sub>-bands of the LH2 (B800 and B850) and the LH1-RC (B875) clearly distinguishable. The absorption spectra of HL and LL membranes (Figure 3-8)

are very similar to LT spectra that were reported before (van Mourik *et al.*, 1992). The most striking feature in the absorption spectrum of the LL membrane is the intense B800 band located at ~804 nm. The maximum of the B850 band is blue shifted in the LL membrane (867 nm) compared to the HL membrane (870 nm). Interestingly, the maximum of the LH1 band is apparently red-shifted from 894 nm in the LL membrane to about 900 nm in the HL membrane.

The ratio between the absorption at ~872 nm (for HL) or ~804 nm (for LL), due to LH2, and at ~894 nm, due to LH1, quantifies that the relative ratio of LH2 to core complex depends on the available light intensity during growth. The HL membrane gives an absorption ratio  $A_{B850}/A_{B875}$  of 1.3 (**Figure 3-8**). While in the LL membrane, the absorption ratio  $A_{B800}/A_{B875}$  is 2.5 (**Figure 3-8**). Given the extinction coefficients ( $\epsilon_{B800} = 226 \text{ mM}^{-1}\text{cm}^{-1}$ ,  $\epsilon_{B850} = 170 \text{ mM}^{-1}\text{cm}^{-1}$ , and  $\epsilon_{B875} = 118 \text{ mM}^{-1}\text{cm}^{-1}$ ) from *Rba. sphaeroides* (Sturgis *et al.*, 1988) with stoichiometry of 18 Bchl *as* per LH2 ring and 32 Bchl *as* per LH1 ellipse in the core complex, the above absorption ratios correspond to a relative LH2 ring/Core ratio of 3.8 and 6.4, for HL and LL membranes respectively. These results are consistent with the results shown in **Figure 3-3**.

### 3.2.2 LT absorption spectra of LH2 complexes

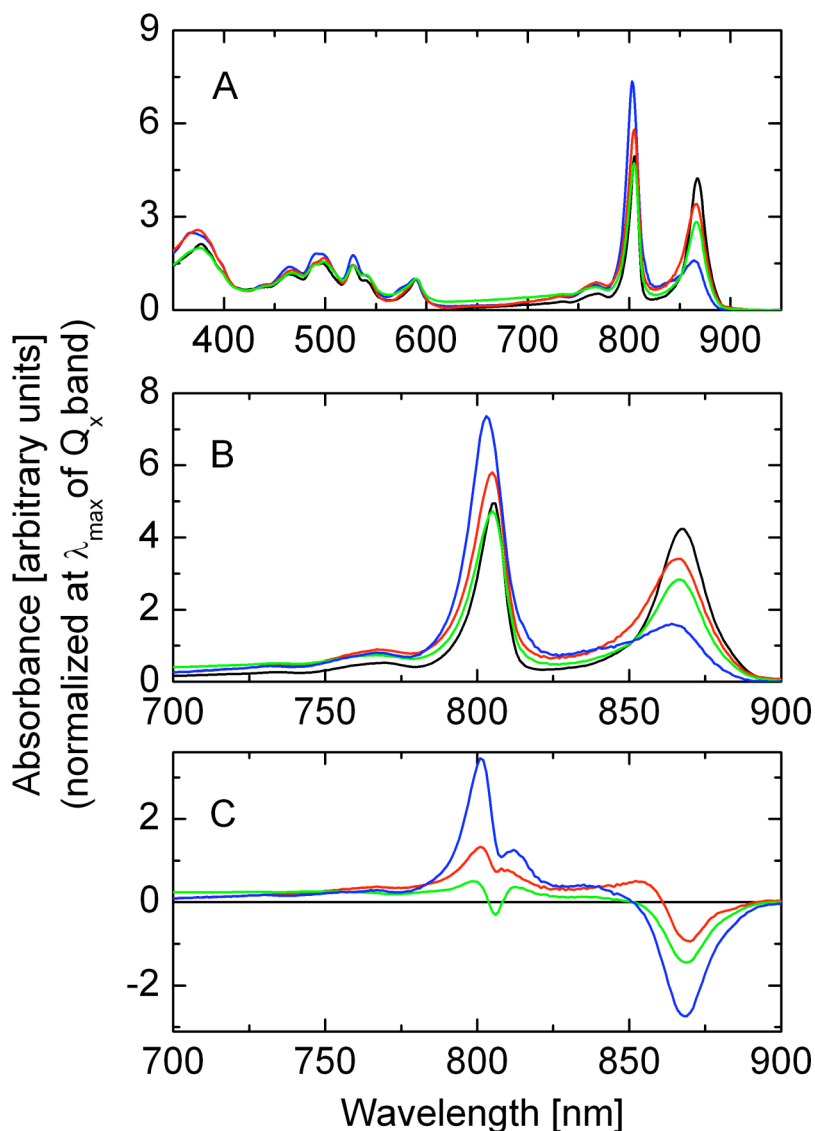


**Figure 3-8** Absorption spectra at 10 K of high-light (HL, black line), low-light intermediate 1 (LL1, red line), low-light intermediate 2 (LL2, green line) and low-light (LL, blue line) LH2 complexes. **A.** The absorption spectra at 350-950 nm regions. **B.** Magnification at NIR region. **C.** Difference spectra of LL1-HL (red line), LL2-HL (green line) and LL-HL (blue line) recorded at NIR region. The spectra are normalised at  $Q_x$  band. The LH2 complexes were diluted in 60 % glycerol in Tris-HCl (20 mM, pH 8.0) containing 0.1% LDAO.

The 10 K absorption spectra of HL and LL LH2 complexes are shown in **Figure 3-8**. In the HL LH2 complexes, the B800 and B850 bands have maxima at 805 and 867 nm, respectively (**Figure 3-8A and B**), which correspond to the absorption of

the weakly interacting B800 and strongly interacting B850 Bchl *a* molecules (see LH2 structure in Figure 1-9 of Chapter 1), respectively. Growth of the *Rps. palustris* under reduced light intensity leads to the changes in the intensity of the B800 and B850 bands: progressively, the absorption intensity of the B850 decreases, while the B800 increases. It is also quite clear that the B800 and B850 bands are slightly blue-shifted in the LL cases (Figure 3-8B). The absorption maximum ( $\lambda_{\max}$ ) of the B800 band of LL LH2 spectrum (803 nm) is blue-shifted compared to the HL LH2 (805 nm). The  $\lambda_{\max}$  B850 band of the LL LH2s is recorded at 864 nm and so is also slightly blue-shifted compared with the HL LH2 complexes  $\lambda_{\max}$  at 865 nm. However the main difference between these two complexes is that the B850 band of the LL LH2s is much broader compared to the HL LH2s. This broadening corresponds to a difference of the excitonic splitting in the strongly coupled B850 Bchl *a* (presented in Chapter 4 and 5). Modification of the Bchl-Bchl interactions and/or the interaction due to the H-bond between the Bchl *a* and the protein residues can alter the position of  $Q_y$ -transition of the B800 and B850 bands (Fowler *et al.*, 1992, Gall *et al.*, 1997, Silber *et al.*, 2008). These spectra are very similar to those that have been reported before (Gall *et al.*, 1999, van Mourik *et al.*, 1992). More about the characteristic changes in the ground state absorption spectra from HL to LL LH2 complexes will be discussed in Chapter 5.

Figure 3-8C shows the difference spectra of the LL1-HL, LL2-HL and LL-HL in the NIR region. It is clearly shown that the intensity of the remaining band at ~800 nm is progressively increased from LL1 to LL complexes. In addition a band at ~815 nm is visible in the difference spectrum of LL-HL (Figure 3-8C). The additional band at ~815 nm is attributed to the high-energy exciton band of the strongly interacting Bchl *as* (see Chapter 4 and 5). When comparing the absorption spectra of HL and LL LH2 complexes, the absorption spectra of LL1 and LL2 LH2 complexes look as though they could be just a mixture of the HL and LL LH2 complexes (Figure 3-8B). If indeed this is true then an isosbestic point should be observed. However there is no evidence of isosbestic point in the 10K absorption spectra (Figure 3-8). This indicates that the intermediate LL1 and LL2 LH2 complexes are not just mixtures between the HL and LL LH2 complexes. The difference spectra, therefore, of the LL1-HL, LL2-HL and LL-HL

(Figure 3-8C) support the conclusion that there are more than 2 types of LH2 complexes present.

### 3.2.3 LT circular dichroism (CD) spectra of LH2 complexes

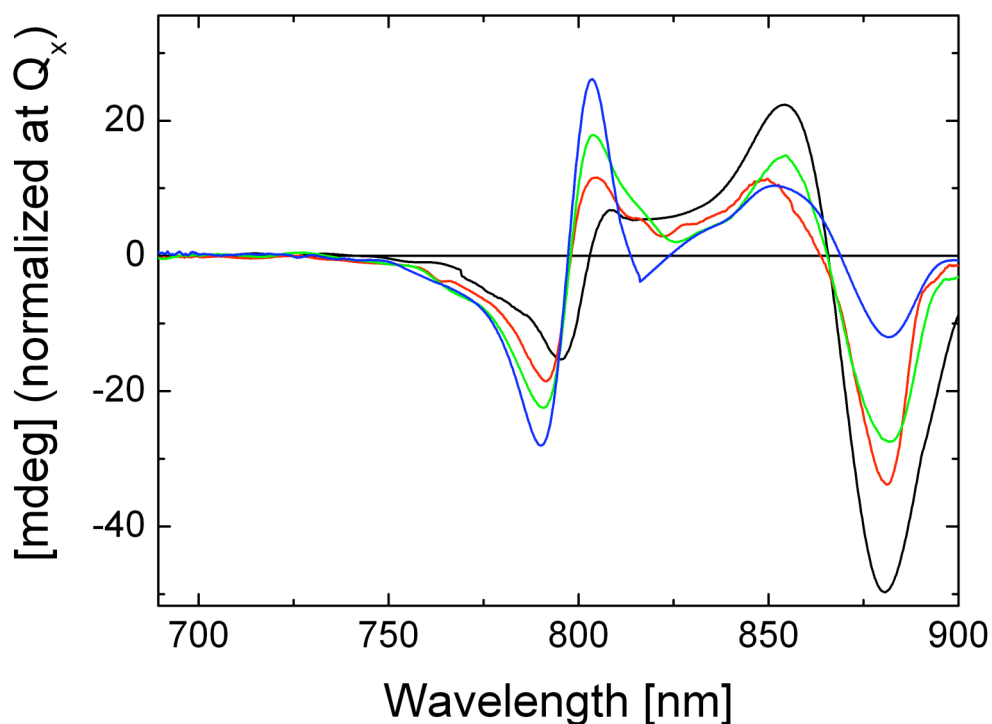


Figure 3-9 77K NIR Circular Dichroism (CD) spectra of HL (black line), LL1 (red line), LL2 (green line) and LL (blue line) LH2 complexes. The spectra are normalized at  $Q_x$  band.

The CD spectra of HL, LL1, LL2 and LL LH2 complexes (Figure 3-9) show some common features. There is a negative band at around 800 nm and an S-shaped band with the zero-crossing close to the absorption maximum of the 850 nm band. A detailed inspection of the CD spectrum of HL LH2 complexes shows the presence of a negative band (-) at 796 nm and a stronger S-shaped band (855 (+) and 880 (-) nm) with a zero-crossing at 869 nm. The circular dichroism spectra contain more information on the arrangement of the Bchl *a*s in the LH2 apoprotein matrix, than the corresponding absorption spectra. For example, the sign and the relative magnitude of the Bchl *a*  $Q_y$  CD bands depend on both the

orientation of the transition dipole moments of the Bchl *as* and their excitonic interactions (Georgakopoulou *et al.*, 2002, Sauer *et al.*, 1996a).

On moving from HL to LL LH2 complexes the CD spectra gradually change. The negative B800 band become more intense and shifts to the blue. This negative B800 band in the LL LH2 spectrum is located at 789 nm, whereas in the HL LH2 complexes this band was at 796 nm. The magnitude of the S-shaped band at B850 decreases dramatically on going from the LL1 to the LL LH2 complexes. The zero-crossing of this S-shaped band in the LL LH2 spectrum is red-shifted to 869 nm compared to that in the HL LH2. There is additional CD band (804 (+) and 816 (-) nm) in the CD spectrum of the LL LH2 complexes. Thus, the LL LH2 CD spectrum shows 789 (-) nm band and two S-shape bands (804(+)/ 816(-) nm and 851(+)/881(-) nm).

The CD spectra (**Figure 3-9**) of the HL and LL LH2 complexes are comparable with those previously reported (Gall *et al.*, 1999, Georgakopoulou *et al.*, 2002). The S-shape in the B850 band present in the LH2 CD spectra has been attributed to the collection of strongly coupled dimers of B850 Bchl *as* (Koolhaas *et al.*, 1997a, Koolhaas *et al.*, 1997b, Koolhaas *et al.*, 2000, Sauer *et al.*, 1996a), whereas the negative band (796 nm) in the CD spectrum has been assigned to the monomeric B800 Bchl *as*.

The CD spectrum of HL LH2 complex is analogous to the case of the B800-850 LH2 complex from *Rps. acidophila* 10050 and HL *Rps. acidophila* 7050 (Alden *et al.*, 1997, Cogdell *et al.*, 1985, Georgakopoulou *et al.*, 2002, van Mourik *et al.*, 1992). All CD spectra of the LH2 complexes from these species show two pronounced bands, one negative (-) band in the 800 nm region, and one S-shape (+/-) band around 860 nm. This indicates that the arrangement and the direction of the transition moment of Bchl *as* of HL LH2 complex from *Rps. palustris* are similar to those from *Rps. acidophila* 10050 and HL *Rps. acidophila* 7050. In the case of B800-820 LL LH2 from *Rps. acidophila* 7050, the CD spectrum shows a shift of the zero-crossing of the S-shape band at ~820 nm (Cogdell *et al.*, 1985, Georgakopoulou *et al.*, 2002, Koolhaas *et al.*, 1997b). This shift refers to the shift of the excited state energies of the strongly coupled Bchl *a* dimer and/or a change in the orientation of the transition moment of Bchl *as*, which are caused by the breaking of the H-bond between the protein residue and acetyl group of

B850 Bchl *a*s in the B800-820 LH2 complex (Koolhaas *et al.*, 1997a, Koolhaas *et al.*, 1997b).

The CD spectrum of LL LH2 complex from *Rps. palustris* is much more complicated, since it has one negative band at ~800 nm and two S-shaped (+/-) bands with zero-crossing at about ~810 and ~870 nm. It is clear from the single molecule spectra of the LL LH2 complexes (presented in Chapter 4) that these complexes contain mixtures of apoproteins. The consequence of this is that the strongly excitonically coupled ring of Bchl *a* molecules shows both B820 and B850 character. This mixing of different exciton bands is seen in the absorption spectra as a broadening of the B850 band on the high-energy end. The CD spectra shown in Figure 3-9 reinforce this picture. Both the B820 and B850 exciton bands can be seen in the CD spectrum of the LL LH2 complexes as the two S-shaped bands, rather than in the case of HL LH2 complexes, where the presence of only B850-like Bchl *a*s results in a single S-shaped band.

### 3.2.4 Resonance raman spectra of LH2 complexes

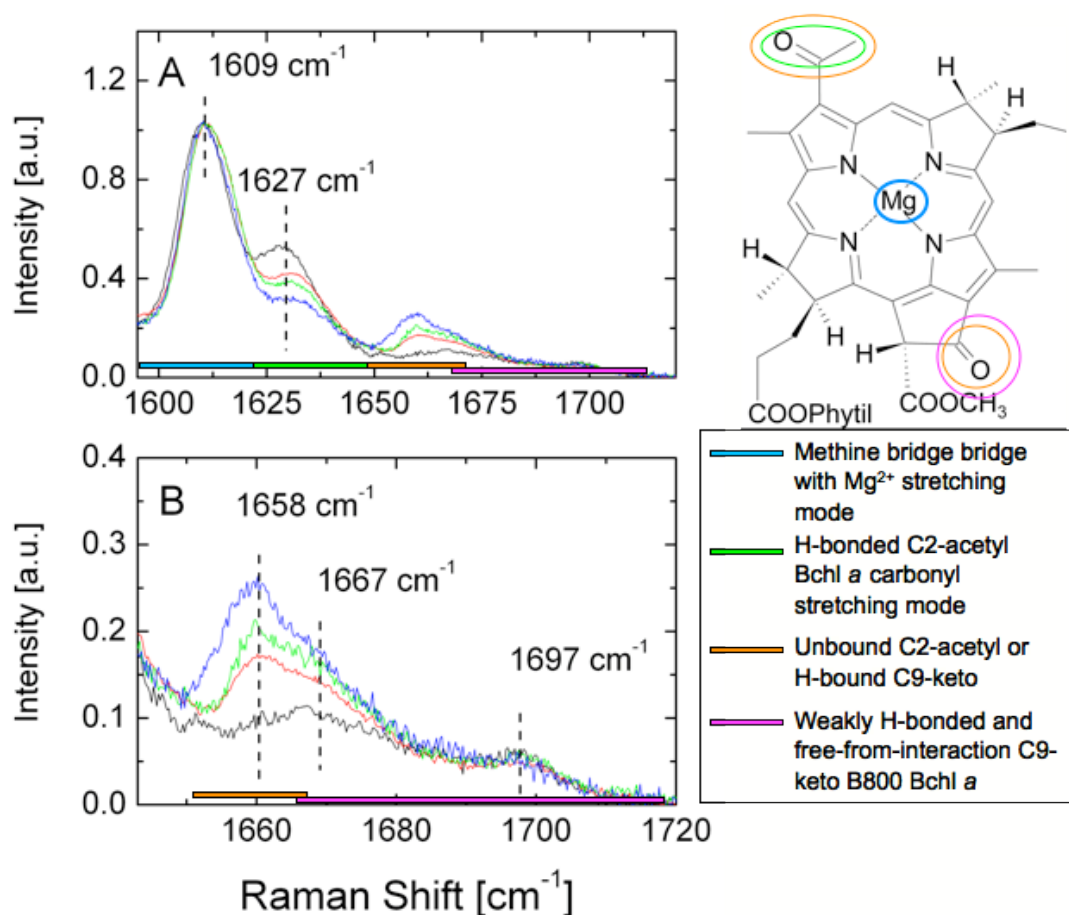


Figure 3-10 A. Low-temperature UV resonance Raman spectra of the HL (black line), LL1 (red line), LL2 (green line) and LL (blue line) LH2 complexes. B. The magnification at carbonyl region (1640-1710 cm<sup>-1</sup>). The spectra were normalised at the 1609 cm<sup>-1</sup> peak. Excitation wavelength of 363.8 nm, T = 77 K.

The LT (77K) resonance Raman (RR) spectra shown in **Figure 3-10** provide information about the binding interactions between Bchl *a* and the protein residues in the LH2 complexes. **Figure 3-10** records the resonance Raman spectra of HL, LL1, LL2 and LL LH2 complexes in the high-frequency region (1590-1725 cm<sup>-1</sup>). Common features can be seen in the RR spectra of HL, LL1, LL2 and LL LH2 complexes. They all have five discernable bands at approximately 1609, 1627, 1658, 1667 and 1697 cm<sup>-1</sup> (**Figure 3-10A and B**). The band at 1609 cm<sup>-1</sup> is quite stable in each spectrum. This band corresponds to the position of the methine bridge (macrocycle ring) stretching mode, indicating

that all the Bchl molecules ring are pentacoordinate (Cotton *et al.*, 1981, Fowler *et al.*, 1994). This band shifts to  $1595\text{ cm}^{-1}$  when the  $\text{Mg}^{+2}$  ion binds two axial ligands (6-coordination). Bands at  $1627$ ,  $1658$ ,  $1667\text{ cm}^{-1}$  are attributed to the  $\text{C}_2$ -acetyl and  $\text{C}_9$ -keto B850 Bchl *a* carbonyl stretching modes (Fowler *et al.*, 1994, Gall *et al.*, 1999, Sturgis *et al.*, 1995, Sturgis *et al.*, 1997) and the band at  $1697\text{ cm}^{-1}$  corresponds to the  $\text{C}_9$ -keto B800 Bchl *a* carbonyl group (Fowler *et al.*, 1994, Gall *et al.*, 1999, Sturgis *et al.*, 1997).

Variations in the intensity of the B850 Bchl *a* carbonyl stretching modes ( $1627$ ,  $1658$  and  $1667\text{ cm}^{-1}$ ) can be seen in **Figure 3-10A and B**. Looking from the LL1 spectrum and down to the LL LH2 spectrum there is a strong reduction in the intensity of the H-bonded  $\text{C}_2$ -acetyl Bchl *a* stretching mode ( $1627\text{ cm}^{-1}$ ) (**Figure 3-10A**), which is followed by a dramatic increase of the unbound  $\text{C}_2$ -acetyl Bchl *a* stretching mode ( $1658\text{ cm}^{-1}$ ) (**Figure 3-10B**). An increase of the  $1667\text{ cm}^{-1}$  peak intensity is also visible. While for the keto stretching mode of the B800 Bchl molecule ( $1697\text{ cm}^{-1}$ ), also minor change can be seen (**Figure 3-10C**).

Low-temperature RR spectra (**Figure 3-10**), especially the HL and LL LH2 complexes, are similar to those reported before (Gall *et al.*, 1999). The reduction of the intensity of the H-bonded  $\text{C}_2$ -acetyl Bchl *a* stretching mode ( $1627\text{ cm}^{-1}$ ) and the increased of the intensity of the unbound  $\text{C}_2$ -acetyl Bchl *a* stretching mode ( $1657\text{ cm}^{-1}$ ) in the LL LH2 from *Rps. palustris* is analogous to the case of B800-820 LH2 from *Rps. acidophila* 7050 or the LH2 mutants from *Rba. sphaeroides* and *Phs. molischianum*. In the B800-820 LH2 from *Rps. acidophila* the replacement of  $\alpha\text{Tyr44}$  and  $\alpha\text{Trp45}$  residues with Phe and Leu breaks the H-bonding interaction with the acetyl group of Bchl *a* molecule (Gall *et al.*, 1999, Sturgis *et al.*, 1995). In the two double mutants of *Rba. sphaeroides*, the replacement of  $\alpha\text{Tyr44}$  and  $\alpha\text{Tyr45}$  to Phe-Tyr and Phe-Leu, respectively, produced a B800-839 and B800-826 LH2s, respectively (Fowler *et al.*, 1992). The resonance Raman studies of these mutants identified the breakage of one or two H-bonds, respectively, between the protein residues and the respective  $\text{C}_2$ -acetyl carbonyl group of the B850 Bchl *a* molecules (Fowler *et al.*, 1994). The removal of a H-bond to the acetyl carbonyl group was signalled by a shift of the Raman peak expected for interaction-free acetyl carbonyl, i.e.  $1635\text{ cm}^{-1}$  in the wild-type LH2 to  $1659\text{ cm}^{-1}$ . Similarly it is also observed in the *Phs. molischianum*

mutant, when  $\alpha$ Tyr43 in the B800-850 LH2 is replaced a Phe in the B800-820 LH2 (Sauer *et al.*, 1996b). The B800-820 LH2 mutant from *Rs. molischianum* shows loss of H-bound C<sub>2</sub>-acetyl RR-stretching mode of B850 Bchl *a* molecule at 1642 cm<sup>-1</sup> and a dramatic increased of free-from-interaction acetyl carbonyls RR-stretching mode at 1663 cm<sup>-1</sup>.

The LL LH2 from *Rps. palustris* is however much more complicated, since the H-bonded C<sub>2</sub>-acetyl carbonyl stretching mode of Bchl *a* molecule at 1627 cm<sup>-1</sup> is only 50% reduced in its intensity. *Rps. palustris* has been found to express multiple  $\alpha\beta$ -polypeptides under high-light as well as low-light intensity conditions (Table 3-2). The  $\alpha$ -polypeptides LL LH2 from *Rps. palustris* have been identified as a mixture of PucA<sub>d</sub> and PucA<sub>a</sub> proteins (Table 3-2). At position 44 and 45 the PucA<sub>a</sub> protein has Tyr and Trp, respectively, while the PucA<sub>d</sub> has Phe and Met, respectively. Considering the presence of these multiple polypeptides as detected by nLC-ESI-MS/MS (Table 3-2), the hypothesis that has been proposed previously (Gall *et al.*, 1999) is that LH2 complexes from *Rps. palustris* may have a heterogeneous polypeptide composition and so could explain the present RR data. This hypothesis suggests that the LL LH2 from *Rps. palustris* is composed of a ring that consists of a heterogeneous mixture of different  $\alpha$ -polypeptides, where some have Tyr/Trp residues able to provide a H-bond with the acetyl group of B850 Bchl *as*, and the others have Phe/Met residues, providing no H-bond.

### 3.3 Carotenoid composition

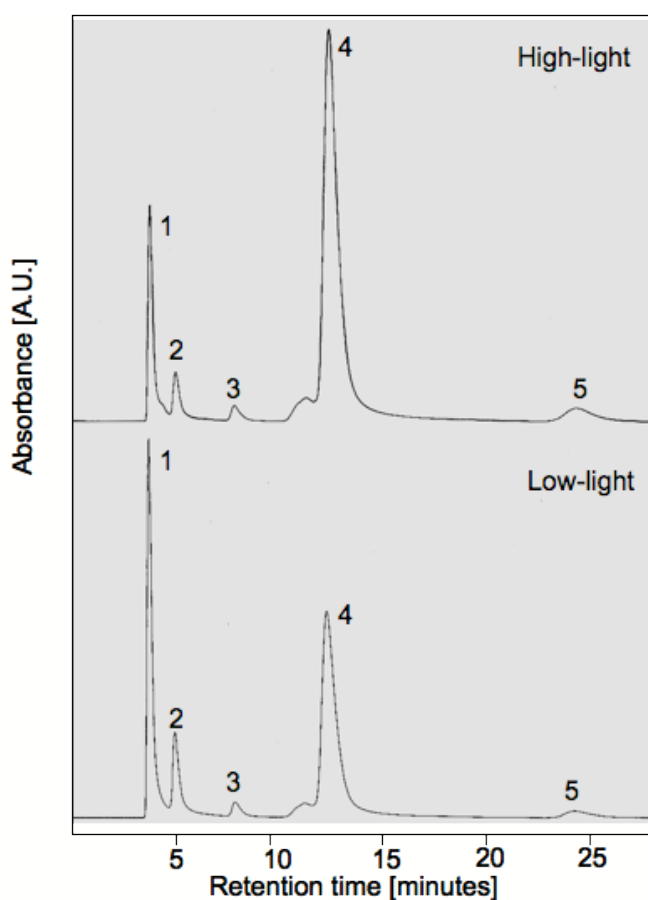


Figure 3-11 HPLC elution profile for the extracts from high- and low-light LH2 from *Rps. palustris* strain 2.1.6 The HPLC analysis was performed by the use of normal-phase chromatography using a silica gel column (Lichrosorb Si-60, 4.6×300 nm), the eluent was with 2.5% (v/v) acetone in benzene, the flow rate was 0.6 ml/min and the detection was at a wavelength of 480 nm.

Car extracts from HL and LL LH2 complexes were injected into a normal-phase HPLC column and the Car composition of the eluent was monitored by detection at 480 nm. The chromatograms (Figure 3-11) reveal that the HL and LL LH2 complexes from *Rps. palustris* produce in total five main Car. These are named according to the order of elution, i.e. Car #1-#5 (Figure 3-11). The retention time, which is recorded on the chromatogram (Figure 3-11), shows the order in which carotenoids elute off from the column. In the normal-phase chromatography used here, the most non-polar carotenoids elute first and the most polar carotenoids elute last (Britton, 1993). Table 3-3 lists the retention times and the absorption maxima  $1A_g^-(0) \rightarrow 1B_u^+(0)$  of all five carotenoids, which were successfully separated by the Lichrosorb Si-60 column. Carotenoid

standards were also injected into the system in order to identify the carotenoids #1-#5.

**Table 3-3 Retention times and  $\lambda_{\max}$  wavelengths obtained from all five carotenoids identified in HL and LL LH2 complexes from *Rps. palustris* and the carotenoid standards used as references. The solvent was 2.5% (v/v) acetone in benzene.**

Peak#	High-light		Low-light		Carotenoid Standard			
	In HPLC	RT (min)	RT (min)	RT (min)	Name	N	RT (min)	RT (min)
		$1B_u^+(0)$ /nm		$1B_u^+(0)$ /nm				$1B_u^+(0)$ / nm
1	3.6	519	3.7	519	Lycopene	11	3.5	519
2	4.8	532	4.9	532	Anhydrorhodovibrin	12	4.9	532
3	7.6	544	7.9	545	Rhodovibrin	12	23.7	533
4	12.1	521	12.3	523	Spirilloxanthin	13	7.6	544
5	23.7	533	24.2	533				

To identify the carotenoids present in the HL and LL LH2 *Rps palustris*, their absorption maximum of  $1A_g^-(0) \rightarrow 1B_u^+(0)$  and the retention times were compared with those of the carotenoid standards (Table 3-3). The Car #1 (RT = 3.6 min;  $1B_u^+(0)$  = 519 nm) is assigned to lycopene (RT = 3.5 min;  $1B_u^+(0)$  = 519 nm). Correspondingly, Car #2, #3 and #5 for the HL and LLLH2 complexes can be identified as anhydrorhodovibrin, spirilloxanthin and rhodovibrin, respectively (Table 3-4). The assignment of Car #4 was not possible because a carotenoid standard for it was not available. In order to identify Car #4,  $^1\text{H-NMR}$  spectroscopy was used. Most carotenoids have three absorption maxima, the positions of which are characteristic of the carotenoid chromophore, although the solvent does influence this too (Britton, 1993). The position of  $\lambda_{\max}$ , especially in  $1A_g^-(0) \rightarrow 1B_u^+(0)$ , undergoes a bathochromic shift as the degree of  $\pi$ -electron conjugation (n) increases (Table 3-3 for carotenoid standards) (Britton, 1993, Britton, 2004, Takaichi, 1992). It is clear from in the chromatogram that the car #1 and #4 appear to be the major carotenoids in both HL and LL LH2 (Figure 3-11). These were collected prior to the chemical structure determination using  $^1\text{H-NMR}$  spectroscopy. The  $^1\text{H-NMR}$  chemical shifts of Car #1 and #4 were compared with references (Appendices 8.2) (Britton,

2004). These results confirmed that car #1 and #4 are lycopene and rhodopin, respectively.

**Table 3-4 Comparison of the amount (%) of all five carotenoids collected from HL and LL LH2 complexes *Rps. palustris*.**

Peak # in HPLC	Assignment	# of conjugated C=C ( <u>N</u> )	HL %	LL %
1	Lycopene	11	15.5	37.7
2	Anhydrorhodovibrin	12	3.1	8.6
3	Spirilloxanthin	13	1.6	1.2
4	Rhodopin	11	72.9	48.9
5	Rhodovibrin	12	4.9	1.9

**Table 3-4** records the full assignment of all five carotenoids present in both HL and LL LH2 from *Rps. palustris*. Rhodopin (N = 11) is the most abundant in both HL LH2 complex (72.9%) and the LL LH2 complex (48.9%). These results are in agreement with the previous determination of the carotenoid composition in the LH2 complexes from *Rps. palustris* using reversed-phase HPLC (Evans, 1989, Gall *et al.*, 2005).

### 3.4 Conclusions

LH2 isolated from *Rps palustris* strain 2.1.6 grown at different light intensities have been successfully separated by sucrose-density gradient centrifugation. Highly purified stable LH2 complexes were produced by an additional purification using a RESOURCE-Q column after a DE-52 anion-exchange column. The results of the nLC-ESI-MS/MS protein sequencing identified that both HL and LL LH2 complexes contain multiple type of  $\alpha$ - (PucA) and  $\beta$ -(PucB) polypeptides. Furthermore, the PucA<sub>d</sub> and PucB<sub>d</sub> apoprotein pairs were only present in the LL LH2 complexes.

The absorption spectrum of the photosynthetic membrane at 10 K showed that the relative LH2 ring/Core ratio in the LL membranes is higher than that in the HL membrane. Spectroscopic characterisations of HL, LL1, LL2 and LL LH2 complexes reveals that there are more than two types of LH2s that have different spectroscopic properties. The LT (10 K) absorption spectrum of LL LH2 complexes shows 800 and broad low-850 nm absorbing bands in the NIR region. The broadening of the B850 band corresponds to the strongly excitonically coupled ring of Bchl *a* molecules that shows both B820 and B850 character. The two S-shape bands with zero-crossing at ~810 and 870 nm in the CD spectrum of LL LH2 complex reinforces this picture. LT (77K) resonance Raman (RR) spectra provide information about the binding interactions between Bchl *a* and the protein residues in the LH2 complexes. As the PucA<sub>d</sub> apoprotein is only expressed in the LL LH2 complexes, it is hypothesised that the LL LH2 from *Rps. palustris* is composed of a ring consisting of a heterogeneous mixture of different  $\alpha\beta$ -polypeptides. Some have Tyr/Trp residues to provide H-bonds with the acetyl group of the B850 Bchl *as* and others have Phe/Met residues, providing no H-bonding. The major carotenoid in both HL and LL LH2 complexes from *Rps. palustris* is rhodopin.

---

## 4 Single molecule spectroscopy of low-light LH2 from *Rps. palustris*

---

### 4.1 Introduction

It has now been well established that the spatial arrangement of the pigments in LH2 determines, to a large extent, the spectroscopic features of the complexes and that in these systems collective effects (especially in the case of the B850 Bchls) have to be considered in order to appropriately describe their electronically excited states (Damjanovic *et al.*, 2002, Hu *et al.*, 2002, Matsushita *et al.*, 2001, Zigmantas *et al.*, 2006). This leads to so-called Frenkel excitons, which arise from the interactions of the transition-dipole moments of the individual pigments, and which correspond to delocalised electronically excited states (Davydov, 1971, Knox, 1964). Since the interaction strength between the individual pigments can be calculated on the basis of the available structural data, information about the pigment arrangement within the LH complexes becomes accessible via optical spectroscopy. As high-resolution structure of *Rps. acidophila* has been resolved, the LH2 from *Rps. acidophila* served as a cornerstone for the development of a detailed understanding of structure-function relationships in such antenna systems (Cogdell *et al.*, 1997, Georgakopoulou *et al.*, 2002).

A question that still remains from the previous chapter is whether the LH2 complexes from *Rps. palustris* consist of rings where each ring has a mixture of apoprotein types, rather than the homogeneous case as in *Rps. acidophila* (Gall *et al.*, 1999, Nishimura *et al.*, 1993). It is, however, difficult experimentally to distinguish between a mixture of LH2 complexes where each ring is homogeneous but there are various types of rings present, and where each individual ring has an heterogeneous apoprotein composition. It is interesting to consider the possible effect that rings with a heterogeneous population of apoproteins might induce spectral changes, especially since some of the *Rps.*

*palustris* apoproteins have sequences that would change the site energies of the 'B850' Bchls, from the standard high-light ones to those more reminiscent of the B820 complex from *Rps. acidophila*. How would such an energetic heterogeneity affect the absorption properties of LH2? Indeed does such heterogeneity actually exist? One way to look for this is to use SMS.

The usefulness of SMS in providing a tool with which to unravel the spectroscopic complexities of LH proteins has been well demonstrated (Bopp *et al.*, 1997, Hofmann *et al.*, 2005, Ketelaars *et al.*, 2002, Rutkauskas *et al.*, 2005, Tietz *et al.*, 1999, van Oijen *et al.*, 1999b, van Oijen *et al.*, 2000, Wörmke *et al.*, 2007). Reviews illustrating single-molecule studies on bacterial LH complexes can be found (Berlin *et al.*, 2007, Cogdell *et al.*, 2006). In this chapter single molecule fluorescence-excitation spectroscopy has been used to investigate individual LL LH2 complexes from *Rps. palustris*. The idea was to investigate whether different classes of single complexes exist and to establish if there is any evidence for spectral properties that can only be explained by rings with a heterogeneous apoprotein composition.

## 4.2 Results

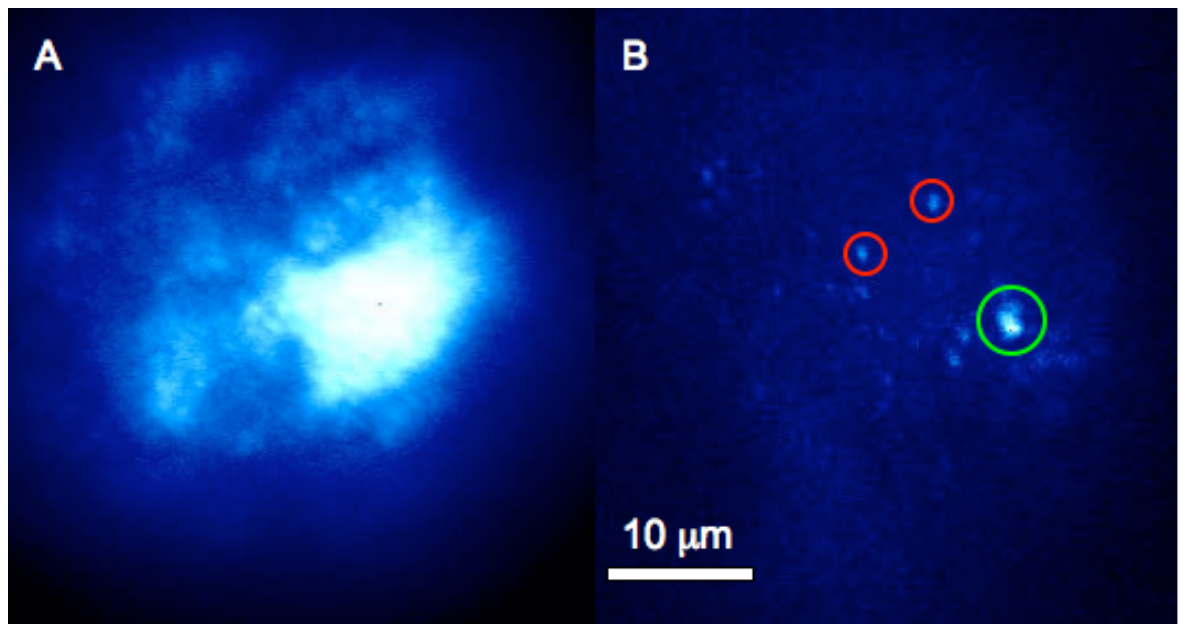
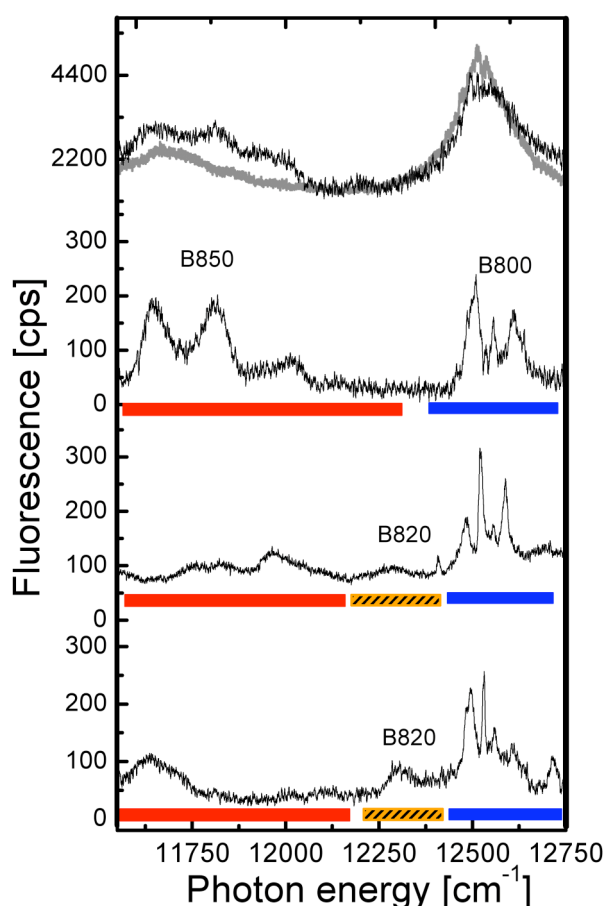


Figure 4-1 LT (1.5K) widefield fluorescence images of low-light LH2 complexes from *Rps. palustris* showing the ensemble (A) and single LH2 complexes (B) are obvious after the LH2 complexes were diluted less than  $10^{-9}$  M in Tris-HCl buffer (20 mM, pH 8.0) containing 0.1% LDAO. Red circles indicate candidates for single LH2 complex. Green circle shows an aggregate.

**Figure 4-1** shows the images of the LH2 complexes from *Rps. palustris* recorded with a widefield fluorescence microscope. It indicates that by adjusting the concentration of the probe, individual LH2 complexes can be monitored. In **Figure 4-1B** purified LH2 complexes had been diluted to less than  $10^{-9}$  M from the ensemble level (**Figure 4-1A**). Here, well-separated small bright spots can be seen (red circles) and have been assigned to be single LH2 molecules. A single big spot (green circle) corresponds to a cluster, a large colony of single complexes. In order to gain spectroscopic information from a particular single complex, the system was then switched to the confocal mode, allowing a single bright spot to be measured.



**Figure 4-2** LT (1.4 K) fluorescence-excitation spectra of LH2 complexes from LL *Rps. palustris* 2.1.6. The top traces show the spectrum from an ensemble (grey line) and the spectrum that corresponds to the sum of 31 spectra from individual LH2 complexes (black line). The lower three traces display typical fluorescence-excitation spectra from individual LH2 complexes. The spectra have been averaged over all polarisations of the incident laser field. The bars indicate the spectral positions of the 800, 820 and 850 nm bands, respectively. The excitation intensity was  $50 \text{ W cm}^{-2}$ . The vertical scale is given in counted photons per second (cps).

The fluorescence-excitation (absorption) spectra of several individual LL LH2 complexes from *Rps. palustris* are shown in **Figure 4-2**. The top trace shows, for comparison, the fluorescence-excitation spectrum taken from an ensemble of LL LH2 complexes (grey line, see **Figure 4-1A**) together with the spectrum that results from the summation of the spectra of 31 individual LL LH2 complexes (black line). The two spectra are in reasonable agreement indicating that the selected individual LL LH2 complexes are a fair statistical representation of the ensemble. The ensemble spectrum shows two broad bands centred at  $11,684\text{ cm}^{-1}$  (856 nm) and  $12,524\text{ cm}^{-1}$  (798 nm) with widths (FWHM) of  $353\text{ cm}^{-1}$  and  $174\text{ cm}^{-1}$ , respectively. The peak intensity of the B850 band is about three times lower than that of the B800 band, which agrees with previously published absorption spectra that have been taken at both RT and at 77 K (van Mourik *et al.*, 1992).

By measuring the fluorescence-excitation spectra of the individual complexes, as shown for three examples in the lower traces of **Figure 4-2**, remarkable features become visible, which are obscured in the ensemble average. Around  $12,500\text{ cm}^{-1}$  (800 nm) the spectra show a distribution of narrow absorption bands, with linewidths (FWHM) below  $10\text{ cm}^{-1}$ , whereas around  $11,750\text{ cm}^{-1}$  (850 nm) a few broad bands, with linewidths (FWHM) in the order of  $160\text{ cm}^{-1}$ , are present. This observation is reminiscent of the situation for LH2 from *Rps. acidophila* (Hofmann *et al.*, 2004, Ketelaars *et al.*, 2001). However, in striking contrast to the single molecule spectra from LH2 from *Rps. acidophila*, about 90% of the individual LL LH2 complexes from *Rps. palustris* show an additional broad band in the B820 spectral region. The peak position of this band varies between  $12,048\text{ cm}^{-1}$  (830 nm) and  $12,288\text{ cm}^{-1}$  (813 nm) (centre of mass at  $12,206\text{ cm}^{-1}$  (819 nm)) and its linewidth covers the range between  $31\text{ cm}^{-1}$  and  $158\text{ cm}^{-1}$  (average  $79\text{ cm}^{-1}$ ).

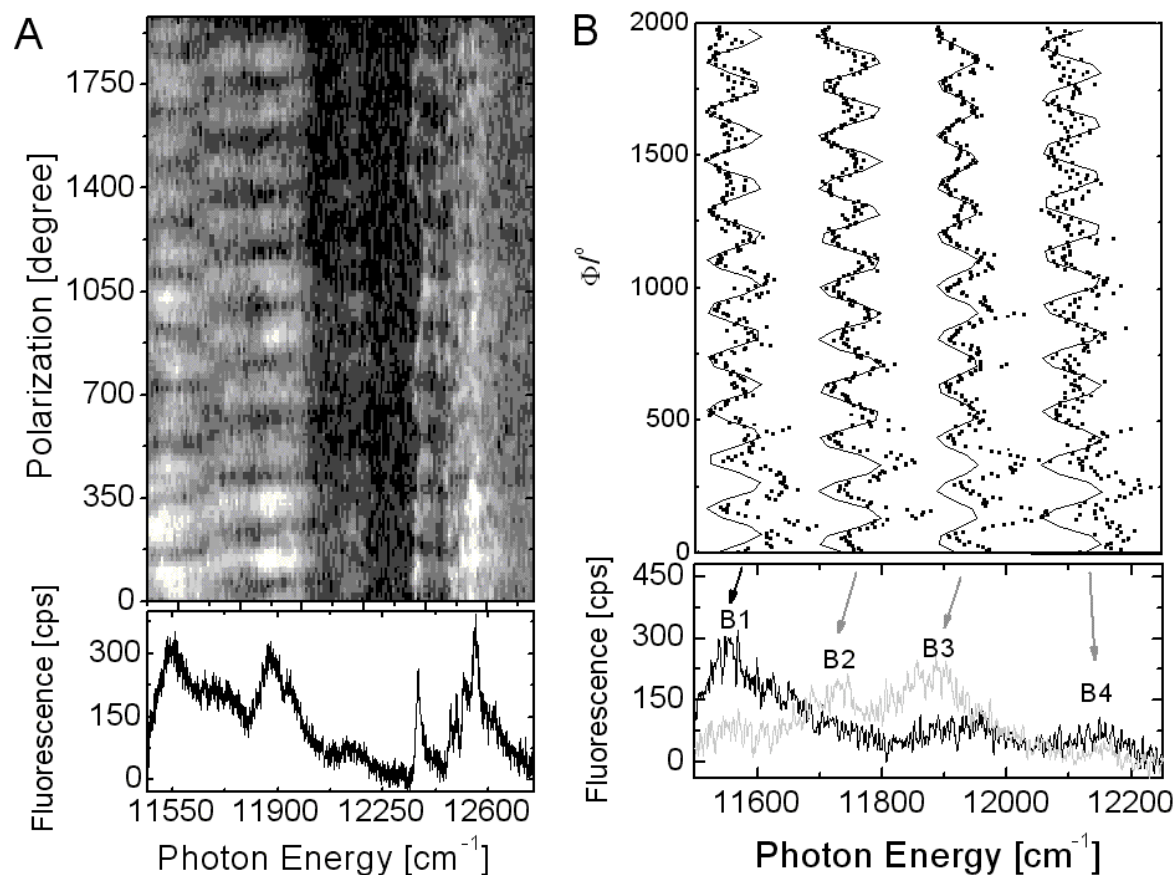


**Figure 4-3** Fluorescence-excitation spectra from an individual B800-820/850 LH2 complex from *Rps. palustris* as a function of the polarisation of the excitation light. (A) Top: Stack of 410 individual spectra recorded consecutively. Between two successive spectra the polarisation of the incident radiation has been rotated by 6.4°. The horizontal axis corresponds to the photon energy; the vertical axis to the scan number or equivalently to the polarisation angle and the intensity is given gray coded. The excitation intensity was 50 W cm<sup>-2</sup>. Bottom: Spectrum that corresponds to the average of the 410 consecutively recorded spectra. B) Top: Expanded view of the fluorescence intensity of the four bands B1 - B4 marked by the arrows in the lower part as a function of the polarisation of the incident radiation (dots) together with cos<sup>2</sup>-type functions (black) fitted to the data. Bottom: Two fluorescence-excitation spectra from the stack that correspond to mutually orthogonal polarisation of the excitation light. ([SEE AVAILABLE MOVIE](#))

In order to analyse the spectral bands from the individual LL LH2 complexes in more detail, the fluorescence-excitation spectra as a function of the polarisation of the incident laser excitation were recorded. The excitation spectra were recorded in rapid succession as the polarisation of the excitation light was rotated by 6.4° between two consecutive scans. An example of this protocol is shown in the top part of **Figure 4-3A** in a two-dimensional representation where 410 individual scans are stacked on top of each other. The horizontal axis corresponds to excitation energy, the vertical axis to the individual scans, or equivalently to the polarisation of the excitation, and the detected fluorescence intensity is coded by the grey scale. In spectroscopy, the spectral lines can be

understood in quantum theory as reflecting differences between energy levels (energy being proportional to wavenumber ( $\text{cm}^{-1}$ )). Here in **Figure 4-3** the photon energy is corresponds to a wavenumber. The sum spectrum of these scans is presented at the bottom of **Figure 4-3A**. The pattern shown at the top of **Figure 4-3A** clearly reveals the polarisation dependence of the absorptions in the B850 region. This becomes even more evident in **Figure 4-3B**. In **Figure 4-3B**,  $\Phi$  corresponds to the polarisation angle of the excitation laser beam. At the bottom of **Figure 4-3B** two individual spectra are shown on an expanded energy scale. The spectra have been obtained for mutually orthogonal polarisations of the excitation light. For simplicity we refer in the following to the absorptions in the B820/850 region as B1, B2, B3 and B4, in order of increasing photon energy, where B stands for band. The angle of the polarisation that yields the maximum intensity for the band B1 has been set arbitrarily to  $0^\circ$  and provides the reference point. For this particular complex we find the absorption bands B1, B2, B3 and B4 at the peak positions of  $11,562 \text{ cm}^{-1}$  (865 nm),  $11,727 \text{ cm}^{-1}$  (853 nm),  $11,874 \text{ cm}^{-1}$  (842 nm) and  $12,150 \text{ cm}^{-1}$  (823 nm) and linewidths are  $174 \text{ cm}^{-1}$ ,  $125 \text{ cm}^{-1}$ ,  $187 \text{ cm}^{-1}$  and  $52 \text{ cm}^{-1}$ , respectively. The top part of **Figure 4-3B** shows the fluorescence intensity of the four bands as a function of the polarisation of the excitation light (dots). This variation is consistent with a  $\cos^2$ -dependence (black line).

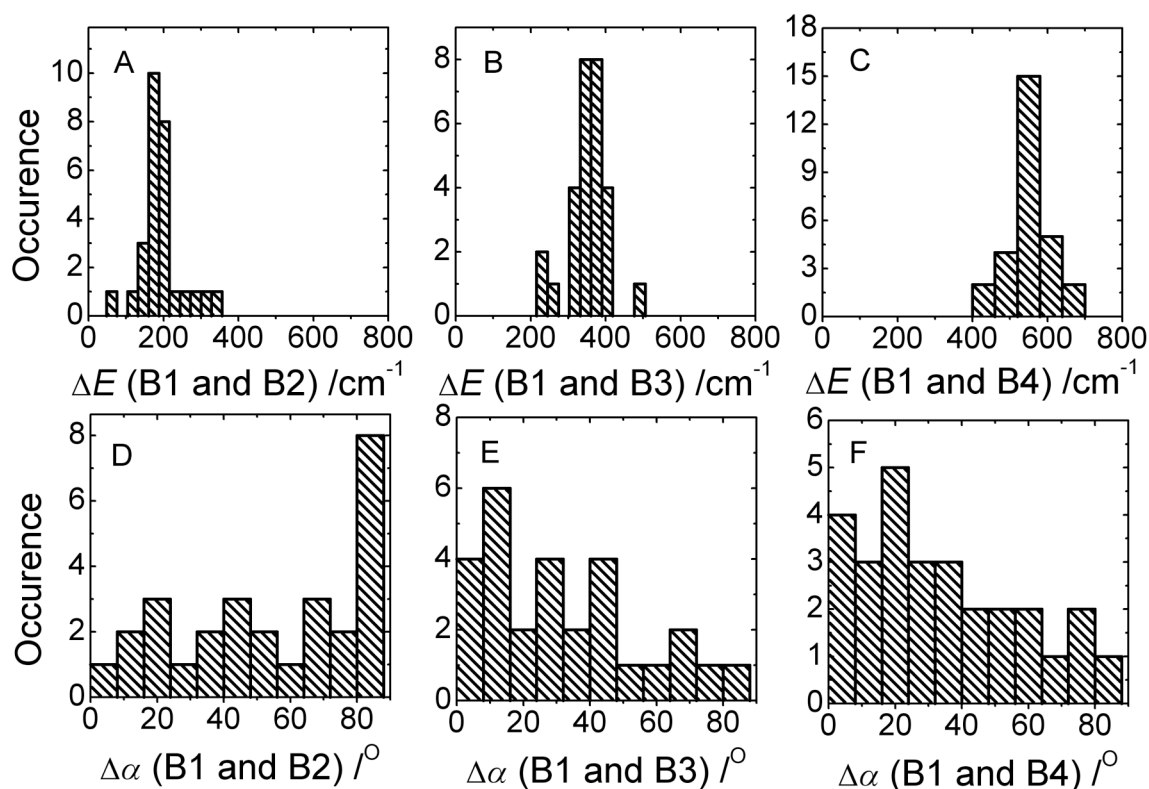


**Figure 4-4 Top:** Distributions of the energetic separations  $\Delta E$  observed between **A)** B1 and B2, **B)** B1 and B3, and **C)** B1 and B4. **Bottom:** Distributions of the mutual angles  $\Delta\alpha$  between the transition-dipole moments that are associated with **D)** B1 and B2, **E)** B1 and B3, and **F)** B1 and B4.

From such experiments the energetic separation ( $\Delta E$ ) can be determined between B1 and the other bands as well as the relative angle ( $\Delta\alpha$ ) between the transition-dipole moments that are associated with them. The distributions of these parameters for the full data set of 28 complexes are shown in the histograms, **Figure 4-4**. The energetic separation between the bands B1 and B2 varies between  $62 \text{ cm}^{-1}$  and  $342 \text{ cm}^{-1}$  and is centred at about  $174 \text{ cm}^{-1}$ , **Figure 4-4A**. The distribution of the mutual orientation of the transition-dipole moments that are associated with the B1 and B2 bands increases to a maximum at about  $90^\circ$ , **Figure 4-4D**. The energetic separation between B1 and B3 is distributed between  $230 \text{ cm}^{-1}$  and  $491 \text{ cm}^{-1}$  with a maximum at about  $361 \text{ cm}^{-1}$ , **Figure 4-4B**. The distribution of relative orientations of the transition-dipole moments that is associated with B1 and B3 decreases from a maximum value at about  $10^\circ$  when going to larger angles, **Figure 4-4E**. The distribution of the energetic separation

between B1 and B4 is between  $430\text{ cm}^{-1}$  and  $670\text{ cm}^{-1}$  and is centred at about  $550\text{ cm}^{-1}$ , while the distribution of the relative orientations of the transition-dipole moments associated with B1 and B4 shows a slow decrease from a maximum value at about  $20^\circ$ .

### 4.3 Discussion

When the single molecule spectra obtained with HL B800-850 complexes from both *Rps. palustris* and *Rps. acidophila* are compared with those recorded from LL LH2 complexes from *Rps. palustris* there are both common and strikingly different features. In the spectral region around  $12,500\text{ cm}^{-1}$  (800 nm) all three types of complexes show narrow bands. These narrow bands have been previously well explained and arise from essentially monomeric weakly interacting Bchl molecules (the B800 manifold) (Cheng *et al.*, 2006, Hofmann *et al.*, 2003, van Oijen *et al.*, 1999a, van Oijen *et al.*, 2000). The single molecule spectra in the region from approximately  $11,600\text{--}12,250\text{ cm}^{-1}$  (815-860 nm) are very different in the LL complexes compared with the HL complexes. The HL complexes show two and sometimes three broad bands in the 850 nm region. Previous studies have shown that these broad bands arise from the excitonic interactions among the strongly coupled B850 Bchls (Ketelaars *et al.*, 2001, Matsushita *et al.*, 2001, van Oijen *et al.*, 1999b).

All of the LL complexes studied here show not only broad bands in the  $11,750\text{ cm}^{-1}$  (850 nm) region but also broad bands in the  $12,200\text{ cm}^{-1}$  (820 nm) region. They appear to have a mixed composition that gives rise to exciton bands in both the 850 and 820 nm regions. In an effort to explain these differences a series of simulations was undertaken to try to understand the structural features that are required to accurately reproduce the experimental data.

The general approach to describe the electronically excited states of the B850 LH2 ring is based on a model Hamiltonian using the Heitler-London approximation (Hofmann *et al.*, 2004, Ketelaars *et al.*, 2001).

$$H = \sum_{n=1}^N (E_0 + \Delta E_n) |n\rangle\langle n| + \frac{1}{2} \sum_{n=1}^N \sum_{m \neq n}^N V_{nm} |n\rangle\langle m| \dots \dots \dots (4.1)$$

where  $N$  refers to the number of Bchl  $a$  molecules.  $|n\rangle$  and  $|m\rangle$  correspond to excitations localized on molecule “n” and “m”, respectively, and  $(E_0 + \Delta E_n)$  denotes the site energy of pigment “n”. Due to local variations in the protein environment of the Bchl  $a$  binding site there is a separation of the individual site energies into an average,  $E_0$ , and a deviation from this average,  $\Delta E_n$ , which is commonly termed diagonal disorder. This energetic disorder is usually modelled by a Gaussian distribution of site energies. The simplest approach to evaluate the dependence of the interaction on the distance and the mutual orientation of the pigments is to use a dipole-dipole type function (Sauer *et al.*, 1996a).

$$V_{nm} = V_0 \frac{\kappa_{nm}}{r_{nm}^3} \dots\dots\dots(4.2)$$

where  $\kappa_{nm}$  denotes the usual orientation factor, and  $r_{nm}$  is the distance between pigments “n” and “m”. The coupling strength  $V_0$  was set to  $135,072 \text{ cm}^{-1} \text{ \AA}^3$  (43). Two limiting cases for the dipolar interaction can be distinguished. That is weak,  $|V/\Delta E| \ll 1$ , and strong,  $|V/\Delta E| \gg 1$ , coupling. In the case of the B850 Bchls, there is strong coupling due to much larger interaction energy ( $V_{nm}$ ) than the difference in their site energies ( $\Delta E_{nm}$ ). As a result of this the eigenfunctions of the Hamiltonian (Eq. 1) are given by the combinations of the excited state wavefunctions of the individual pigments.

In the case of both the 9-mers (HL LH2s from *Rps. acidophila* 10050 and *Rps. palustris*) and the 8-mer (LH2 from *Phs. molischianum*), the energy scheme of the excited-state manifold of the B850 ring has been constructed by symmetric or antisymmetric linear combinations of the localised wave functions of the  $\alpha\beta$ -dimers, in such a way that they form the basis for the irreducible representations of the  $C_9$  and  $C_8$  pure-rotational point groups, respectively (Matsushita *et al.*, 2001). As previously described for the  $C_9$ -symmetry case the symmetric and the antisymmetric manifold consist of one non-degenerate ( $k=0$ ) and four doubly degenerate ( $k= \pm 1, \pm 2, \dots, \pm 4$ ) exciton states (Matsushita *et al.*, 2001). The corresponding  $C_8$ -symmetry case has the ( $k= 0, \pm 1, \pm 2, \pm 3, 4$ ) exciton states. In order to understand which exciton states are involved in giving rise to the measured bands B1, B2, B3 and B4 the absorption spectra were calculated by

Monte Carlo simulations treating the diagonal disorder as random variable. This simulation was carried out for both 9-mer and 8-mer possibilities.

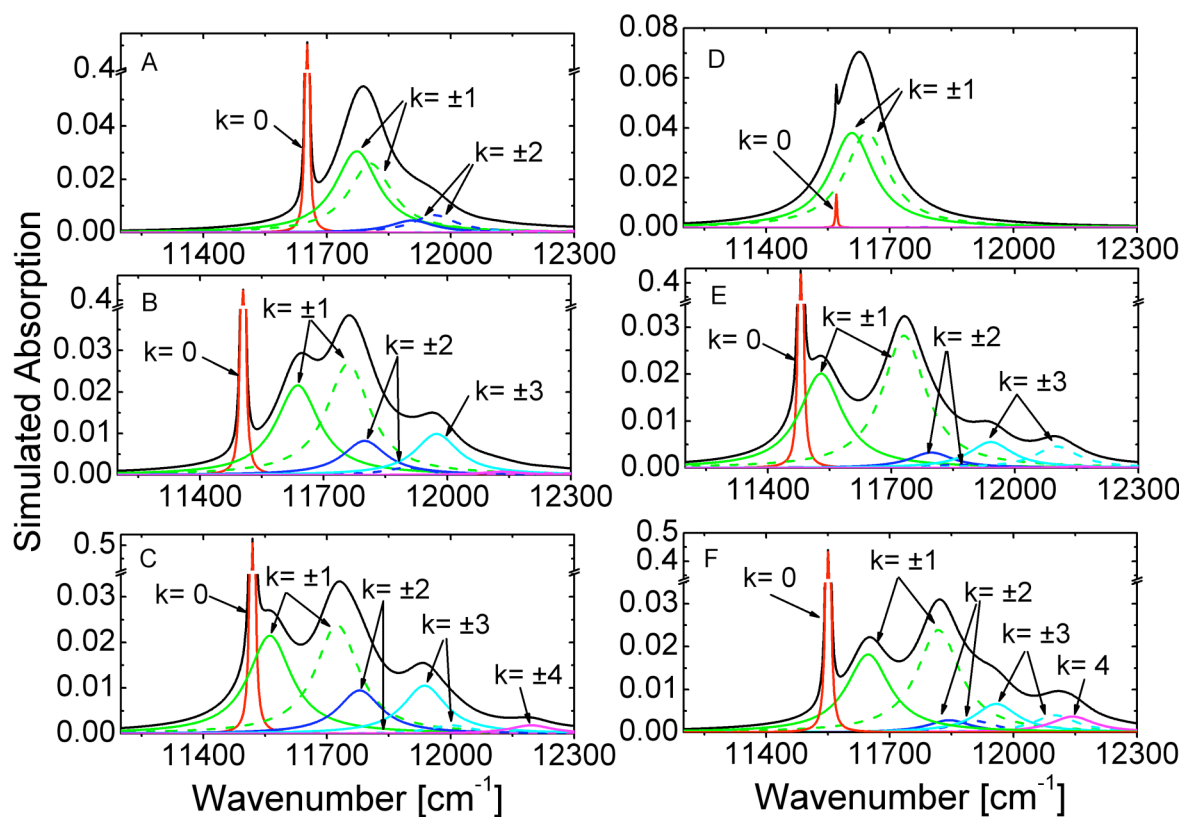


**Figure 4-5** Examples for simulated absorption spectra for an individual LH2 complex (solid line). The spectra correspond to a single realisation of the disorder. The calculated energies of the exciton states have been dressed by a Lorentzian with a width of  $5\text{ cm}^{-1}$  for the  $k=0$  state and a width of  $130\text{ cm}^{-1}$  for all other exciton states (dashed lines). The simulations A-C (left) are based on a nonameric structure; the simulations D-F (right) are based on an octameric structure. The simulations vary with respect to the type of diagonal disorder: A, D: random diagonal disorder taken from a Gaussian distribution of width  $160\text{ cm}^{-1}$  (FWHM). B, E: random diagonal disorder like for A, D and additionally correlated diagonal disorder. C, F: like B, E and additionally using B820-pair ( $E_0(\alpha\text{B820}) = 12,860\text{ cm}^{-1}$ ,  $dE = 260\text{ cm}^{-1}$ ) and B850-pair ( $E_0(\alpha\text{B850}) = 12,300\text{ cm}^{-1}$ ,  $dE = 240\text{ cm}^{-1}$ ) like randomly distributed site energies across the ring assembly. For more details see text.

Typical examples for simulated spectra of individual realisations of the disorder are shown in **Figure 4-5**. The first simulated spectrum of an LL LH2 complex was obtained by the introduction of diagonal disorder into the circular 9- and 8-mer models, **Figure 4-5A, D**. For simplicity the site energies of B850 Bchl *a* dimers were set according to the previously determined site energies of LH2 from *Rps. acidophila* ( $E_0(\alpha\text{B850}) = 12,300\text{ cm}^{-1}$  and  $E_0(\beta\text{B850}) = 12,060\text{ cm}^{-1}$ ) (Hofmann *et al.*, 2004). The random diagonal disorder is taken from a Gaussian distribution with a width of  $\Gamma_{\text{intra}} = 160\text{ cm}^{-1}$ , where  $\Gamma_{\text{intra}}$  stands for intracomplex

heterogeneity (Ketelaars *et al.*, 2001). Within each complex the 18 or 16 Bchl *a* molecules will show variations of their site-energies with respect to their spectral means. In the case of a 9-mer ring this simulation produces a sharp band from the  $k=0$  state, broad bands from the  $k=\pm 2$  states, and broad bands from the  $k=\pm 1$  states, which are split in energy and feature mutually orthogonal transition-dipole moments, **Figure 4-5A**. Whereas in the case of the 8-mer ring only a sharp  $k=0$  band and the two orthogonally polarised  $k=\pm 1$  bands are present, **Figure 4-5D**. In **Figure 4-5B, E** this simulation was extended by inserting the expression  $\Delta E_n = \Delta E_n^{(0)} + E_{\text{mod}} \cos[2\phi(n+1/2)]$  for the site energies. Here  $\Delta E_n^{(0)}$  refers to the random diagonal disorder chosen from the Gaussian distribution described above and  $E_{\text{mod}} \cos[2\phi(n+1/2)]$  introduces an additional correlated modulation of  $C_2$ -type symmetry into the site energies of the pigments, where  $\phi = 2\pi/N$  and  $N$  refers to the number of the pigments in the ring (Hofmann *et al.*, 2004). When this modulation is taken into account the 9-mer model shows a sharp  $k=0$  band, broad orthogonally polarised  $k=\pm 1$  bands and broad  $k=\pm 2$  bands. Furthermore the  $k=\pm 3$  states gain significant oscillator strength, but they have no observable splitting. Though the  $k=\pm 2$  bands do contribute, it is apparent that the overall spectrum of the 9-mer model is dominated by the contributions of the  $k=0$ ,  $k=\pm 1$  and  $k=\pm 3$  states. In case of the 8-mer model a sharp  $k=0$  band, broad orthogonally polarised  $k=\pm 1$  bands, broad  $k=\pm 2$  bands and  $k=\pm 3$  bands is also present. The splitting of the  $k=\pm 3$  bands are clear in the 8-mer model. The overall spectrum of the 8-mer model is dominated by the  $k=0$ ,  $k=\pm 1$  and  $k=\pm 3$  states.

There is strong evidence from mass spectroscopic analysis of LL LH2 polypeptides from *Rps. palustris* that this LL complex contains multiple types of  $\alpha\beta$ -polypeptides (see **Chapter 3**). The sequence of some of these polypeptides features changes in key amino acids shown to be involved in H-bonding to the Bchl *a* macrocycles of the strongly coupled ring of Bchls in LH2. This heterogeneity raises a possibility of some of these Bchl *a* molecules having quite different site energies from each other. In other words some may have site energies characteristic of B850 and some characteristic of B820. The simulation, therefore, was extended to introduce two different site energies,  $E_0$  ( $\alpha$ B850) = 12,300  $\text{cm}^{-1}$ ,  $E_0$  ( $\beta$ B850) = 12,060  $\text{cm}^{-1}$  (B850-pair) (Hofmann *et al.*, 2004) and  $E_0$

( $\alpha$ B820) = 12,860 cm<sup>-1</sup>,  $E_0$  ( $\beta$ B820) = 12,600 cm<sup>-1</sup>) (B820-pair) (de Rujter *et al.*, 2007), for the Bchl *a*-pairs where the B850- and the B820- pairs of Bchl *a* are randomly distributed in the ring, **Figure 4-5C, F**. In this case the 9-mer model shows the gain of the oscillator strength of all of the exciton states, **Figure 4-5C**. The bands at 11500 cm<sup>-1</sup> (870 nm) and 11700 cm<sup>-1</sup> (855 nm) are due to the  $k=+1$  and  $k=-1$  states, respectively. The  $k=\pm 2$  bands are obscured under the  $k=-1$  band. Although the splitting of the  $k=\pm 3$  and  $k=\pm 4$  states are seen, the  $k=+3$  and  $k=+4$  bands are the most intense. The overall features of the simulated spectrum (solid line) from the 9-mer model are dominated by the  $k=0, \pm 1, +3$  and  $+4$  states (dashed lines) and is blue shifted compared to the case shown in **Figure 4-5B**. In the case of 8-mer model, the simulated spectrum is identical to that of the 9-mer, **Figure 4-5F**.

When the absorption spectra for the simulations are compared with the experimental spectrum of the LL LH2 (**Figure 4-3**) it can be seen that the traces in **Figure 4-5A, B and D** are not consistent with the experimental data. The simulations presented in **Figure 4-5C, E and F**, however, all are in reasonable agreement with the experimental spectra. Simulations with a 9-mer model can only account for the experimental spectrum if two different site energies for Bchl *a*-pairs are considered, **Figure 4-5C**. If this model describes the situation properly then the experimentally measured bands B1, B2, B3 and B4 can be assigned to the  $k=+1, -1, +3$  and  $+4$  states, respectively. Simulations with an 8-mer model produce agreement with the experimental data both with and without taking into account different site energies for the pairs of Bchl *a* molecules. If the model, in **Figure 4-5E**, provides a proper description of the experimentally determined situation then the B1, B2, B3 and B4 bands in the experimental data can be assigned to the  $k=+1, -1, -3$  and  $+3$  states, respectively. If on the other hand the model that corresponds to the simulation that is shown in **Figure 4-5F** is appropriate then the B1, B2, B3 and B4 bands can be assigned to the  $k=+1, -1, +3$  and  $4$  states, respectively. Therefore, it is unclear at this stage which of the underlying models that led to the simulations presented in **Figure 4-5** represents a realistic approximation for the description of the real structure of the LL LH2.

In order to distinguish between the three different options presented in Fig. 4-5C, E and F one needs to consider the extra experimental spectroscopic information that is available and has been presented in Fig. 4-4, i.e. the energetic separation of the spectral bands and the mutual orientation of their transition-dipole moments. The experimental histograms, therefore, have been compared with these parameters calculated from the respective simulations for 2000 realisations of the energetic disorder (circles, triangles and black squares), Fig. 4-6.

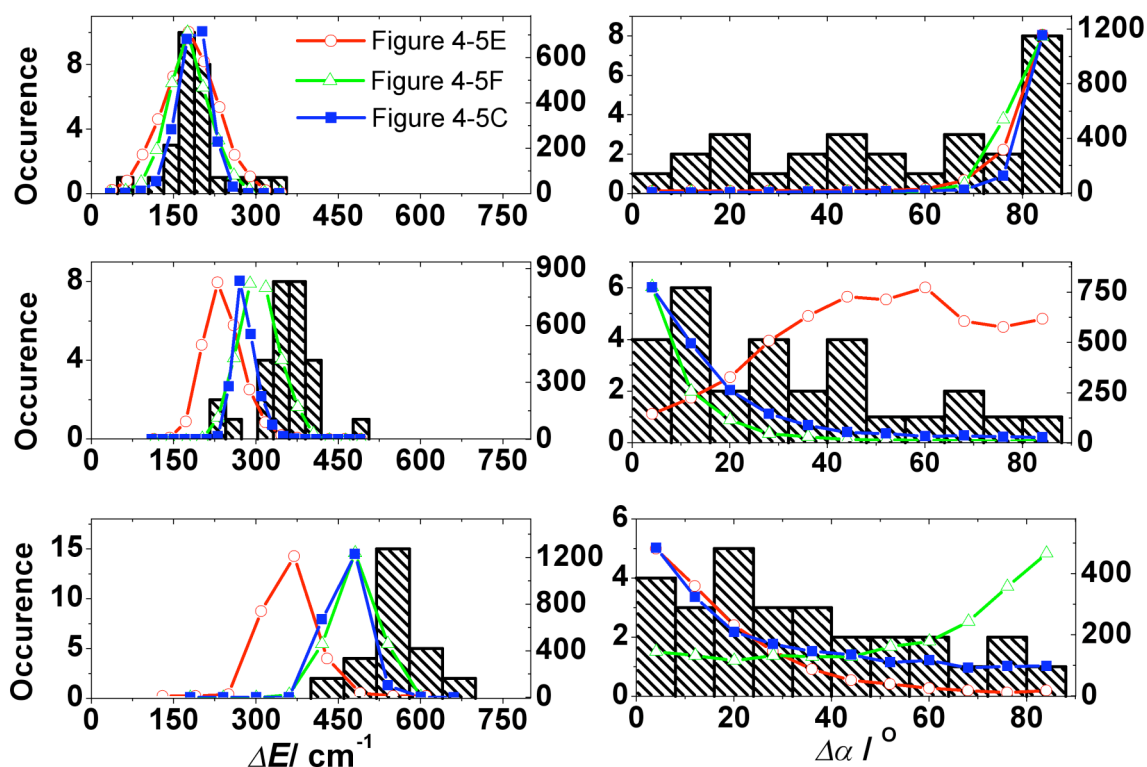
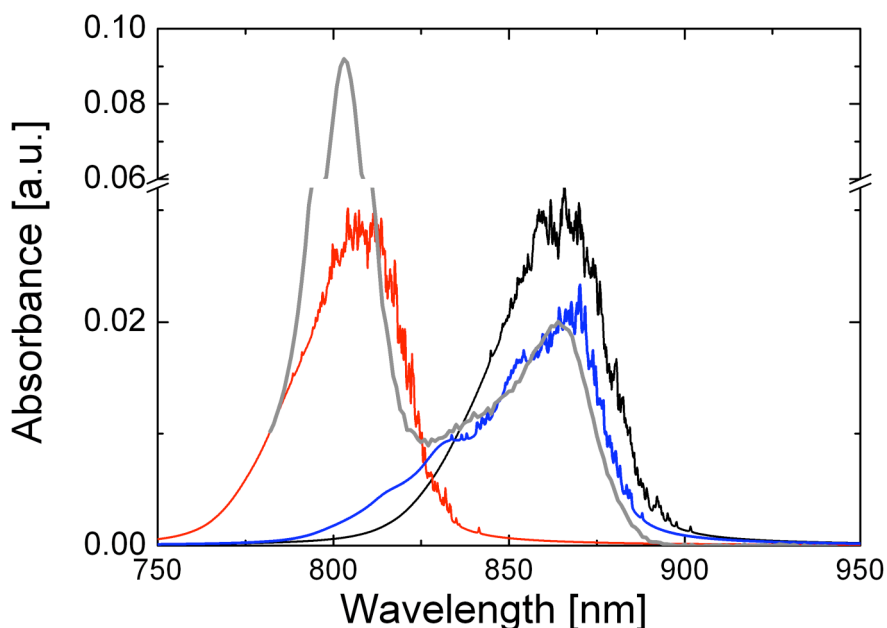


Figure 4-6 Comparison of the energetic separation of the bands B1-B4 with those of the respective exciton states (left) and the mutual orientation of the associated transition-dipole moments (right) as predicted from Monte Carlo simulations for 2000 realisations of the disorder (circles,  $-\circ-$ ) for the model shown in Figure 4-5E, (triangles,  $-\triangle-$ ) the model shown in Figure 4-5F and (squares,  $-\square-$ ) the model shown in Figure 4-5C.

Using the 8-mer model represented by Figure 4-5E it can be seen that the simulated distributions of  $\Delta E$  and the mutual angle between the transition-dipole moments of the  $k = \pm 1$  states can be reproduced, however, the simulated distributions of the energetic separations between  $k = +1$  and  $k = -3$  as well as between  $k = +1$  and  $k = +3$  with maxima around  $200 \text{ cm}^{-1}$  and around  $400 \text{ cm}^{-1}$  are

not, **Figure 4-6**. Moreover the simulated distribution for the mutual angle between the transition-dipole moments of the  $k= +1$  and  $k= -3$  states is even worse with a broad maximum covering the range from  $40^\circ$  to  $60^\circ$ . Simulations based on the 8-mer model represented by **Figure 4-5F** are able to satisfactorily account for the distribution of the simulated mutual angles between the transition-dipole moments of the  $k= \pm 1$  states, **Figure 4-6**. However these simulations also do not satisfactorily reproduce the distributions of the angles between the transition-dipole moments of the  $k= +1$  and  $k= 4$  states. Simulations based on the 9-mer model represented by **Figure 4-5C** show quite good agreement with the distribution of all three mutual angles, **Figure 4-6**. There is, however, a significant though smaller (than the two 8-mer models) mismatch between this simulation and the distribution of energetic separations,  $\Delta E$ , ( $k= +1$  and  $k= +3$ ) and  $\Delta E$  ( $k= +1$  and  $k= +4$ ).

At this stage it appears that the 9-mer model is able to more closely account for the experimental data. The low-light LH2 complexes from *Rps. palustris* have at least 4 types of  $\alpha$ -polypeptides. One, the  $\alpha_d$ -polypeptide, has phenylalanine and methionine residues at positions 44 and 45 (Evans *et al.*, 2005, Tadros *et al.*, 1989). The other polypeptides have tyrosine and tryptophan residues at these positions. The presence of H-bonding residues at positions 44 and 45, such as tyrosine and tryptophan, correlates with B850 type site energies, whereas if non-H-bonding residues, such as phenylalanine and methionine, are present this correlates with B820 site energies. Shifting in the site energy of one  $\alpha$ -bound Bchl *a* will also effect the nearest-neighbour  $\beta$ -bound Bchl *a* within a pair. These Bchls are associated with new B820-like site energies  $E_0$  ( $\alpha$ B820-like) =  $12,640 \text{ cm}^{-1}$  and  $E_0$  ( $\beta$ B820-like) =  $12,400 \text{ cm}^{-1}$ , calculated by modelling a 10K ensemble absorption spectrum of B850 band of low-light LH2 *Rps. palustris* (blue line in **Figure 4-7**). The parameters of the coordinate arrangement of the Bchls for this simulation were taken by mixing the parameters of the crystal structures of the B800-850 and B800-820 LH2 complexes (see **Table 4-1** and **Figure 4-8**). According to previous reports the difference of the excitation energies ( $E_\alpha - E_\beta$ ) has been estimated about the same as the nearest neighbour interaction ( $240 \text{ cm}^{-1}$ ) (Koolhaas *et al.*, 2000, Matsushita *et al.*, 2001, Scholes *et al.*, 2000).



**Figure 4-7** Simulations of ensemble spectra of B850 band (black, red and blue lines) were overlaid on 10K absorption spectrum (grey line) of low-light LH2 from *Rps. palustris*. The simulations using the site energies of LH2 (B850, black line) [ $E_0$  ( $\alpha$ B850) = 12,300  $\text{cm}^{-1}$ ,  $E_0$  ( $\beta$ B850) = 12,060  $\text{cm}^{-1}$  (B850-pair) (Hofmann *et al.*, 2004)] and LH3 (B820, red line) [ $E_0$  ( $\alpha$ B820) = 12,860  $\text{cm}^{-1}$ ,  $E_0$  ( $\beta$ B820) = 12,600  $\text{cm}^{-1}$  (B820-pair) (de Ruijter *et al.*, 2007)]. The blue line shows a simulation using the site-energies of  $E_0$  ( $\alpha$ B820-like) = 12,640  $\text{cm}^{-1}$  with  $dE$  = 240  $\text{cm}^{-1}$  and the B850-pair site energy of  $E_0$  ( $\alpha$ B850) = 12,300  $\text{cm}^{-1}$  with  $dE$  = 240  $\text{cm}^{-1}$ ; the position of the pairs are randomly distributed. 3000 realisations were carried out in order to build the simulated ensemble spectra.

In **Figure 4-7**, for comparison, the simulated ensemble absorption spectra of B850 LH2 (black line) and B820 LH2 (red line) from *Rps. acidophila* and low-B850 LH2 from *Rps. palustris* (blue line) were overlaid on the 10K absorption spectrum of B800-low-B850 LH2 from *Rps. palustris*. In order to reproduce the low-B850 LH2 spectrum, the site energies of B820-like Bchl *a* pairs were adjusted as  $E_0$  ( $\alpha$ B820-like) = 12,640  $\text{cm}^{-1}$  ( $\Delta E$  = 240  $\text{cm}^{-1}$ ) and the site energies of the B850 Bchl *a* pairs were set as  $E_0$  ( $\alpha$ B850) = 12,300  $\text{cm}^{-1}$  with  $dE$  = 240  $\text{cm}^{-1}$ . Intercomplex heterogeneity ( $\Gamma_{\text{inter}}$  = 160  $\text{cm}^{-1}$ ) and 3000 realisations were needed to build an ensemble spectrum. This resulted in the simulated low-B850 LH2 spectrum, shown in **Figure 4-7** blue lines, which has a broad band (at ~860 nm) with shoulders at 830 nm, being closest to the experimental spectrum (grey line).

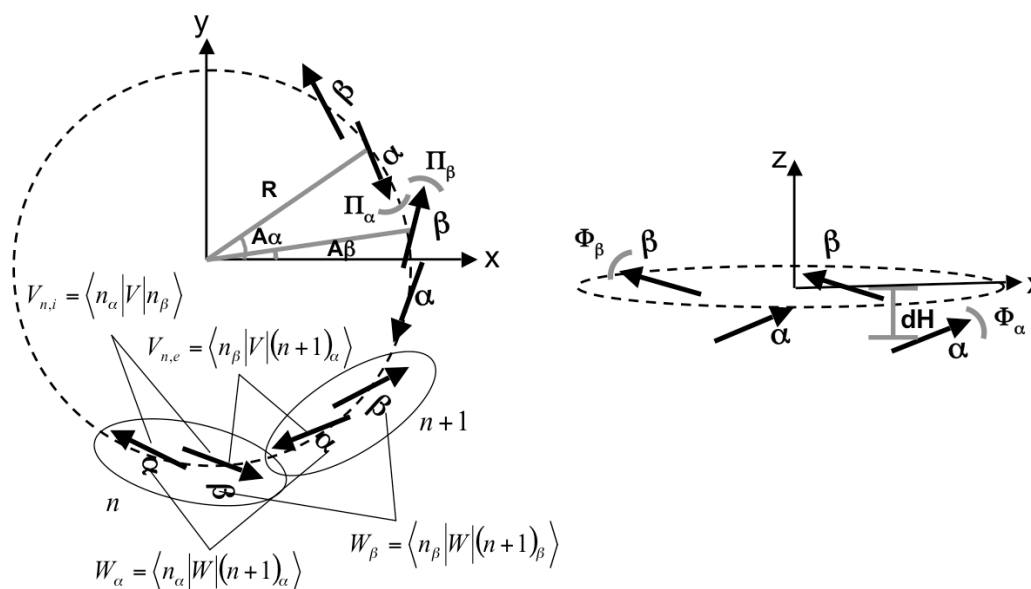


Figure 4-8 A schematic representation of the transition-dipole moments and the coordinate arrangement of the  $\alpha$ - and  $\beta$ -bound Bchl *a* molecules in the  $xy$ -plane (left) and  $zy$ -plane (right). The  $|n_\alpha\rangle$  etc. correspond to the wavefunctions of the electronically excited state localised on the  $\alpha$ -bound Bchl *a* molecule in dimer  $n$ , respectively. The strongest contributions to the interaction result from the matrix elements for the intradimer nearest-neighbour interaction  $V_{n,i}$ , the interdimer nearest neighbour interaction  $V_{n,e}$ , the  $\alpha$ -next-nearest-neighbour interaction  $W_\alpha$ , and the  $\beta$ -next-nearest-neighbour interaction  $W_\beta$ , respectively. The geometrical arrangement of the  $\alpha$ - and  $\beta$ -bound Bchl *a* molecules are defined by the radius of  $\alpha$ - and  $\beta$ -unit circle in  $xy$ -plane  $R_u$  ( $u = \alpha, \beta$ ), the geometrical angle of the pigment of  $\alpha$ - and  $\beta$ -unit in  $xy$ -plane  $A_u$ , the in-plane tilt of the transition-dipole moment of the  $\alpha$ - and  $\beta$ -Bchl *a* from the circular tangent in  $xy$ -plane  $\Pi_u$ , the height differences between the centres of the  $\alpha$ - and  $\beta$ -Bchl *a* in the  $z$ -plane  $dH_u$ , and the out-of-plane tilt of the transition-dipole moment of the  $\alpha$ - and  $\beta$ -Bchl *a* in the  $z$ -plane  $\Phi$ . The actual values of these parameters are summarised in Table 4-1 together with the respective data for LH2 and LH3 from *Rhodospseudomonas acidophila*. The circles with the dashed line help to orient our eyes.

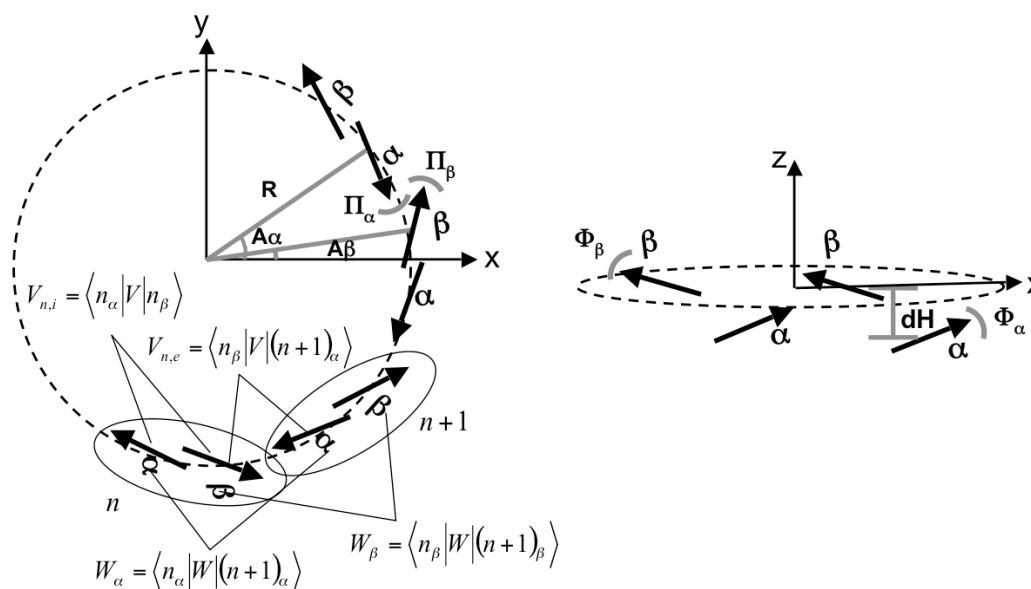


Figure 4-8 A schematic representation of the transition-dipole moments and the coordinate arrangement of the  $\alpha$ - and  $\beta$ -bound Bchl *a* molecules in the  $xy$ -plane (left) and  $zy$ -plane (right). The  $|n_\alpha\rangle$  etc. correspond to the wavefunctions of the electronically excited state localised on the  $\alpha$ -bound Bchl *a* molecule in dimer  $n$ , respectively. The strongest contributions to the interaction result from the matrix elements for the intradimer nearest-neighbour interaction  $V_{n,i}$ , the interdimer nearest neighbour interaction  $V_{n,e}$ , the  $\alpha$ -next-nearest-neighbour interaction  $W_\alpha$ , and the  $\beta$ -next-nearest-neighbour interaction  $W_\beta$ , respectively. The geometrical arrangement of the  $\alpha$ - and  $\beta$ -bound Bchl *a* molecules are defined by the radius of  $\alpha$ - and  $\beta$ -unit circle in  $xy$ -plane  $R_u$  ( $u = \alpha, \beta$ ), the geometrical angle of the pigment of  $\alpha$ - and  $\beta$ -unit in  $xy$ -plane  $A_u$ , the in-plane tilt of the transition-dipole moment of the  $\alpha$ - and  $\beta$ -Bchl *a* from the circular tangent in  $xy$ -plane  $\Pi_u$ , the height differences between the centres of the  $\alpha$ - and  $\beta$ -Bchl *a* in the  $z$ -plane  $dH_u$ , and the out-of-plane tilt of the transition-dipole moment of the  $\alpha$ - and  $\beta$ -Bchl *a* in the  $z$ -plane  $\Phi$ . The actual values of these parameters are summarised in Table 4-1 together with the respective data for LH2 and LH3 from *Rhodospseudomonas acidophila*. The circles with the dashed line help to orient our eyes.

**Table 4-1** The coordinates of the arrangement of Bchl *a* molecules in an LH2 complex according to the x-ray structural data.

	B850*	B820§	Mixed†
$R_\alpha$ (Å)	26.09	26.02	26.02
$R_\beta$ (Å)	26.92	26.95	26.92
$A_\alpha$ (rad)	-0.2043	-0.2015	-0.2015
$A_\beta$ (rad)	0.1566	0.1592	0.1566
$\Pi_\alpha$ (rad)	-3.4957	-3.4598	-3.4598
$\Pi_\beta$ (rad)	-0.5058	-0.5620	-0.5058
$\Phi_\alpha$ (rad)	-0.1361	-0.0801	-0.0801
$\Phi_\beta$ (rad)	-0.1284	-0.1288	-0.1284
dH (Å)	0.00725	-0.0785	0.00725
$V_{n,i}; V_{n,e}$ (cm <sup>-1</sup> )	254 <sup>a</sup> ;226 <sup>a</sup>	256 <sup>b</sup> ;210 <sup>b</sup>	270 <sup>c</sup> ;230 <sup>c</sup>
$W_\alpha; W_\beta$ (cm <sup>-1</sup> )	-35 <sup>a</sup> ;-26 <sup>a</sup>	-38 <sup>b</sup> ;22 <sup>b</sup>	-38 <sup>c</sup> ;-25 <sup>c</sup>

**Note:**  $R_\alpha$  and  $R_\beta$ , radius of  $\alpha$ - and  $\beta$ -bound Bchl *a* circle in xy-plane;  $A_\alpha$  and  $A_\beta$ , geometrical angle of the pigment of  $\alpha$ - and  $\beta$ - bound Bchl *a* in xy-plane;  $\Pi_\alpha$  and  $\Pi_\beta$ , in-plane dipole tilt from circular tangent of the  $\alpha$ - and  $\beta$ - bound Bchl *a* in xy-plane;  $\Phi_\alpha$  and  $\Phi_\beta$ , out-of-plane dipole tilt of the  $\alpha$ - and  $\beta$ - bound Bchl *a* in z-plane; dH, height differences between centres  $\alpha$ - and  $\beta$ -unit in z-plane.  $V_{n,i}$  and  $V_{n,e}$ , the nearest-neighbour intra- and inter-dimer interaction;  $W_\alpha; W_\beta$ , the  $\alpha$ -next-nearest-neighbour interaction and the  $\beta$ -next-nearest-neighbour interaction

\* McDermott, S.M., et al., 1995, *Nature* 375, 517-521 and Papiz, M.Z., et al., 2003, *J Mol Biol* 326, 1523-1538. § McLuskey, K., et al., 2001, *Biochemistry* 40(30), 8783-8789.

<sup>a</sup>Hofmann, C., et al., 2004, *Chem Phys Lett* 395, 373-378. <sup>b</sup>de Ruijter, W.P.F., et al., 2007, *Chem Phys* 341, 320-325.

†<sup>c</sup> This work

Now, having the site energies of the  $\alpha$ -bound-B820-like Bchl *a* molecules ( $E_0$  ( $\alpha$ B820) = 12,640 cm<sup>-1</sup>) and the  $\beta$ -bound-B820-like Bchl *a* molecule ( $E_0$  ( $\beta$ B820) = 12,400 cm<sup>-1</sup>), extended single molecule simulations were carried out. The position of the B820-like pairs was randomly distributed, **Figure 4-9**. The simulation based on this model, though not perfect, shows closer agreement to the experimental distribution of energetic separations  $\Delta E$  ( $k= +1$  and  $k= +3$ ) than the simulations based on taking the same site energy for all the B850 Bchl *as*.

Again the match to the distributions of the mutual angles of the respective transition-dipole moments between ( $k= +1$  and  $k= +3$ ) and ( $k= +1$  and  $k= +4$ ) is good.

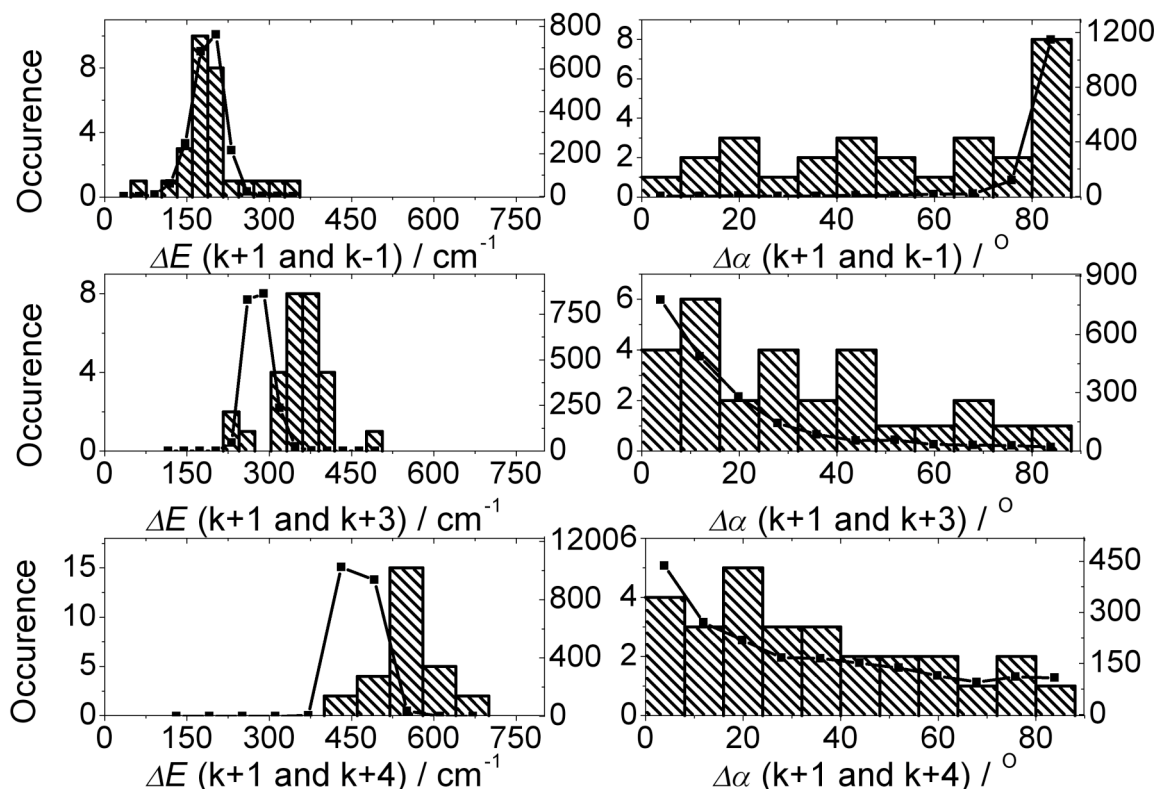


**Figure 4-9** Extended simulations based on the model shown in Fig. 4C, i.e. a nonameric structure with random- and correlated diagonal disorder and multipolypeptide composition. The B820-like-pair site-energies of  $E_0(\alpha\text{B820}) = 12,640 \text{ cm}^{-1}$  with  $dE = 240 \text{ cm}^{-1}$  and the B850-pair site energy of  $E_0(\alpha\text{B850}) = 12,300 \text{ cm}^{-1}$  with  $dE = 240 \text{ cm}^{-1}$ . The position of the B820-like-pairs are randomly distributed.

This simulation was extended further by systematically setting fewer B820-like site energies pairs. In none of these simulations was an improved reproduction of the experimental data obtained (Figure 4-10 and Figure 4-11).

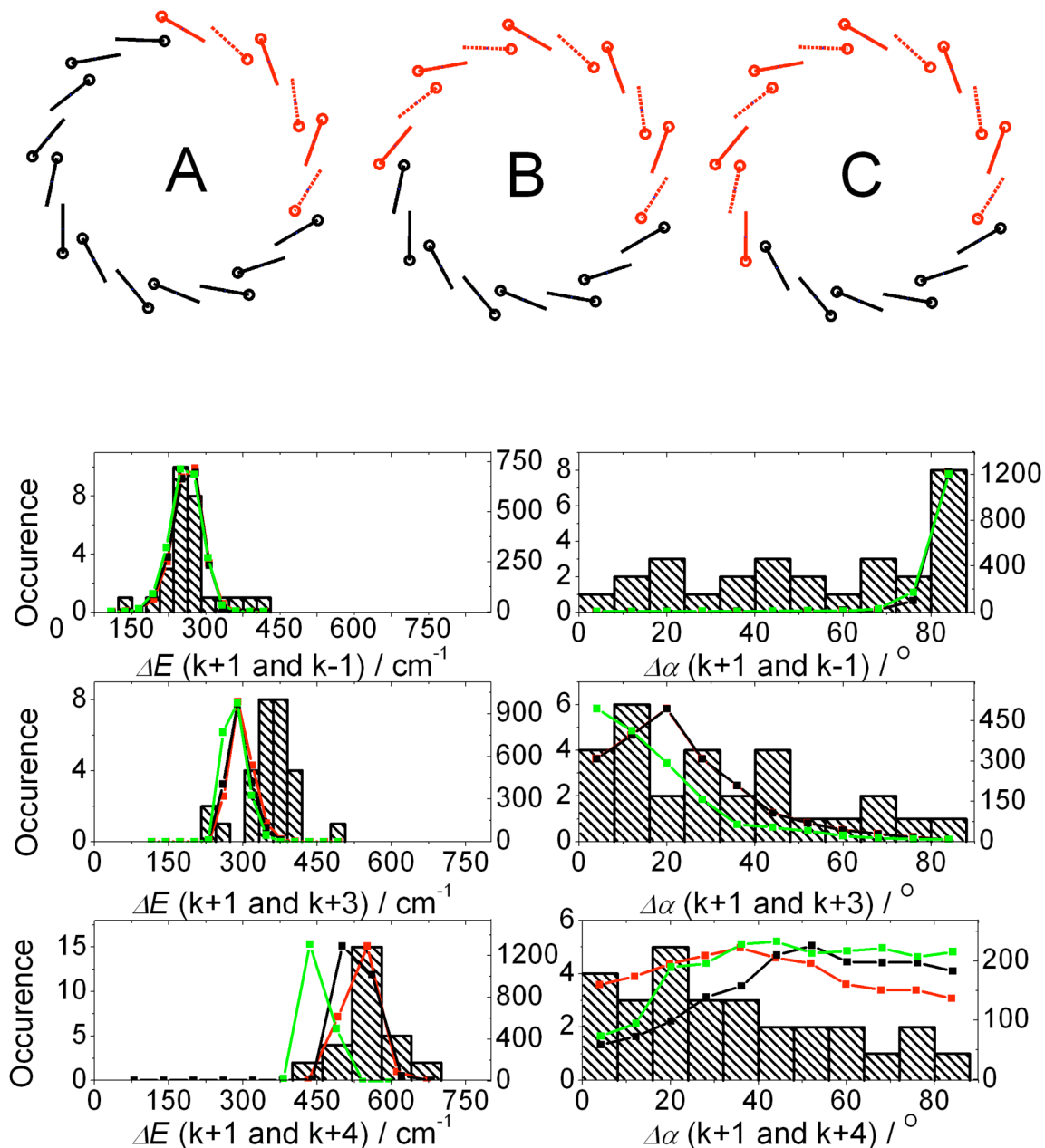


**Figure 4-10** Extended simulations based on the nonameric structure model with random and correlated diagonal disorder and multipolypeptide composition. Top: The model structures show variations in positioning the B820-like-pairs (red lines, the dashed red lines indicate the  $\alpha$ -bound-Bchl a). Bottom: Comparison of the experimental data with the Monte Carlo simulation (2000 realisations) of model A (squared black lines), model B (squared red lines) and model C (squared green lines). B820-like-pair site-energies of  $E_0(\alpha\text{B820}) = 12,640 \text{ cm}^{-1}$  with  $dE = 240 \text{ cm}^{-1}$  and the B850-pair site energy of  $E_0(\alpha\text{B850}) = 12,300 \text{ cm}^{-1}$  with  $dE = 240 \text{ cm}^{-1}$ .

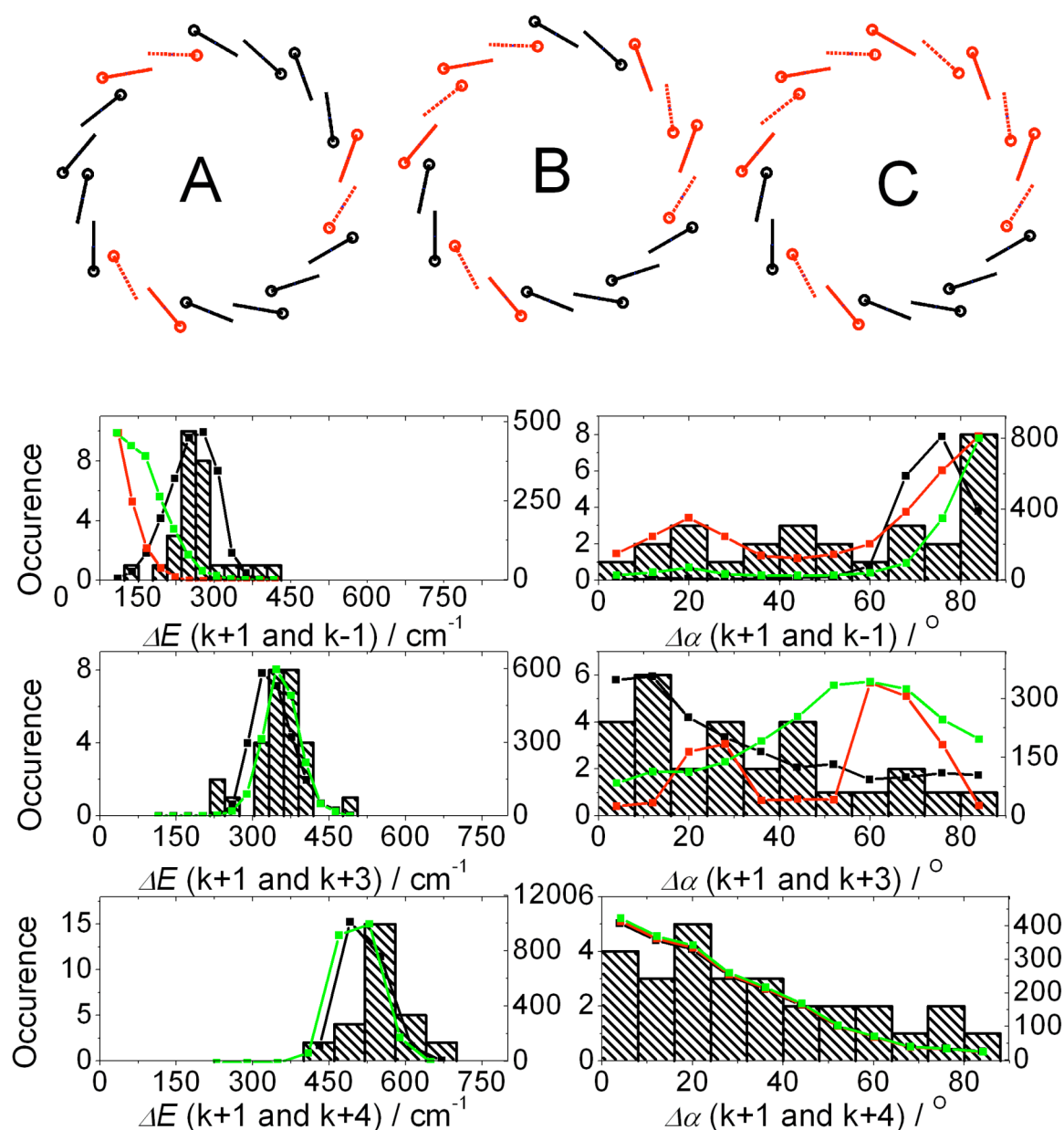


**Figure 4-11** Extended simulations from Figure 4-10 showing the model structures with more variations in positioning the B820-like-pairs pairs (red lines, the dashed red lines indicate the  $\alpha$ -bound-Bchl *a*). Bottom: Comparison of the experimental data with the Monte Carlo simulation (2000 realisations) of model A (squared black lines), model B (squared red lines) and model C (squared green lines). B820-like-pair site-energies of  $E_0(\alpha\text{B820}) = 12,640 \text{ cm}^{-1}$  with  $dE = 240 \text{ cm}^{-1}$  and the B850-pair site energy of  $E_0(\alpha\text{B850}) = 12,300 \text{ cm}^{-1}$  with  $dE = 240 \text{ cm}^{-1}$ .

Next the effect of a symmetrical arrangement of these B820-like site energies in the ring was tested. Six B820-like site energies were distributed symmetrically with respect to the 3-fold axis in the ring. The other 12 Bchl *a* molecules were given B850-site energies. This simulation now yields the best agreement between the simulations and the experimental data that have been found,

Figure 4-12, but only when a rather high intracomplex heterogeneity,  $\Gamma_{\text{intra}}$ , at  $320 \text{ cm}^{-1}$  was introduced. This value is significant higher than those that have been reported for the B800-850 LH2 of *Rps. acidophila* ( $\Gamma_{\text{intra}}$  is  $250 \text{ cm}^{-1}$ ) (Hofmann *et al.*, 2004, Ketelaars *et al.*, 2001). This might be a consequence of having individual rings with a heterogeneous polypeptide composition.

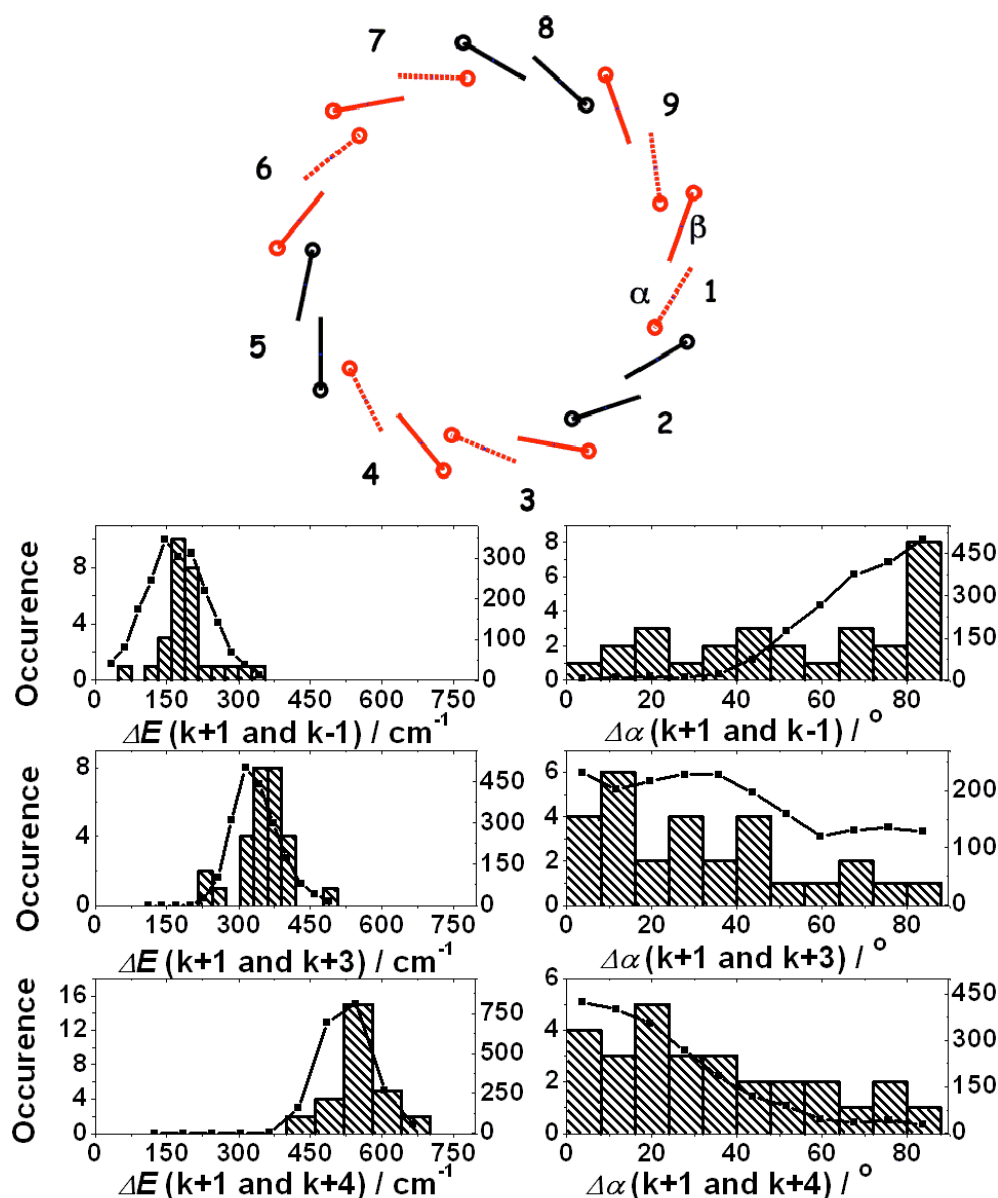
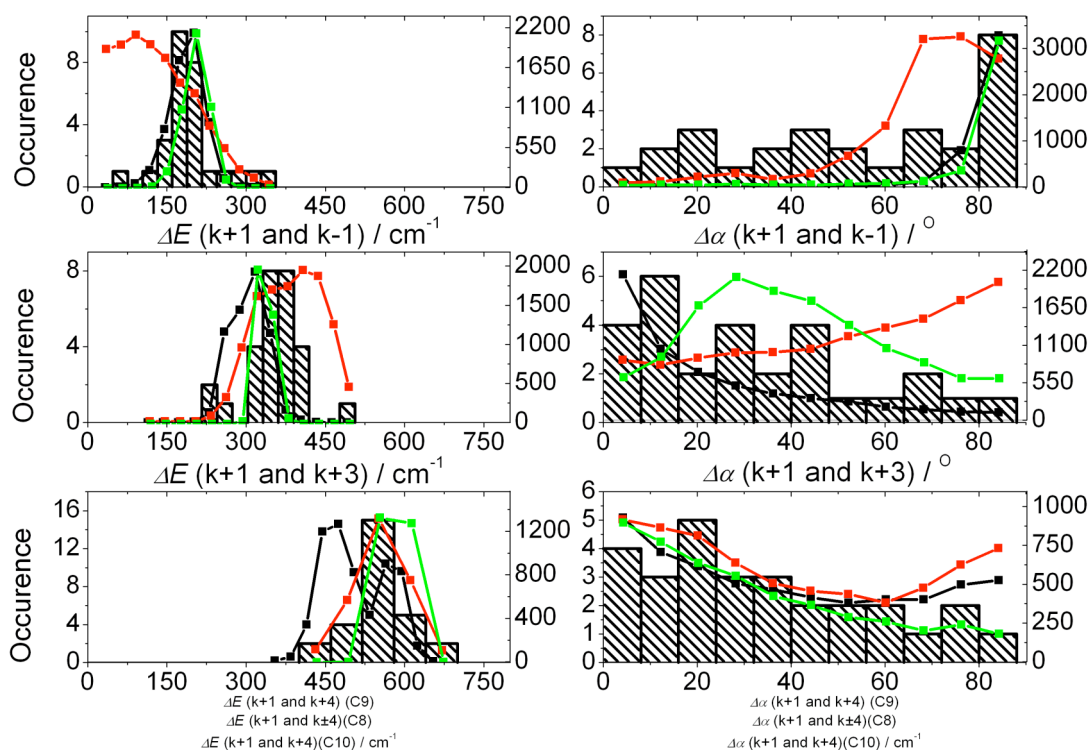


Figure 4-12 Top: Model structure that features 6 B820-like-pair Bchl a molecules pairs (red lines, the dashed red lines indicate the  $\alpha$ -bound-Bchl a) distributed in  $C_3$  symmetry around the ring. Bottom: Comparison of the experimental data with the results from Monte Carlo simulations (2000 realisations) for the nonameric structure as shown in the top part taking random- and correlated diagonal disorder into account (black squares). The site energies of the pigments have been chosen as detailed in Fig. 6. The intracomplex heterogeneity ( $\Gamma_{\text{intra}}$ ) is  $320 \text{ cm}^{-1}$ . The full and the dashed lines in the top part of the figure indicate the B820 like (dashed) and B850 like (full) site energies.



**Figure 4-13** Comparison between the experimental data and the summation of Monte Carlo simulations (each 2000 realisations) for best 8-mer, 9-mer and 10-mer models (black line), the summation for best 8-mer and 9-mer model (red line) and the simulation for best 10-mer model only (green line).

It has been suggested that some species of purple bacteria may contain LH2 complexes where rings of multiple sizes co-exist (Kereiche *et al.*, 2008, Scheuring *et al.*, 2005). In order to test whether various mixtures of rings of different sizes could satisfactorily account for our experimental data we added together simulations for the best 8-mer, 9-mer, and 10-mer models in a number of different combinations (Figure 4-13 black line). This shows that most of the distribution of the relative angles of the transition dipole moments of the simulated data could satisfy the experimental data. However the distribution of the energetic separation  $\Delta E$  ( $k = +1$  and  $k = +3$ ) and  $\Delta E$  ( $k = +1$  and  $k = +4$ ) (Figure 4-13 black line) does not agree with the experimental histograms. Simulations using mixtures of the 8-mer and 9-mer models (Figure 4-13 red line) also show mismatch in the  $\Delta E$  ( $k = \pm 1$ ) and  $\Delta E$  ( $k = +1$  and  $k = +3$ ) as well as the  $\Delta\alpha$  ( $k = \pm 1$ ) and  $\Delta\alpha$  ( $k = +1$  and  $k = +3$ ). Simulations with the best 10-mer model shown in (Figure 4-13 green line) indicate that a 10-mer model cannot

satisfactorily reproduce the experimental data, especially for  $\Delta\alpha$  ( $k = +1$  and  $k = +3$ ) (Figure 4-13 green line).

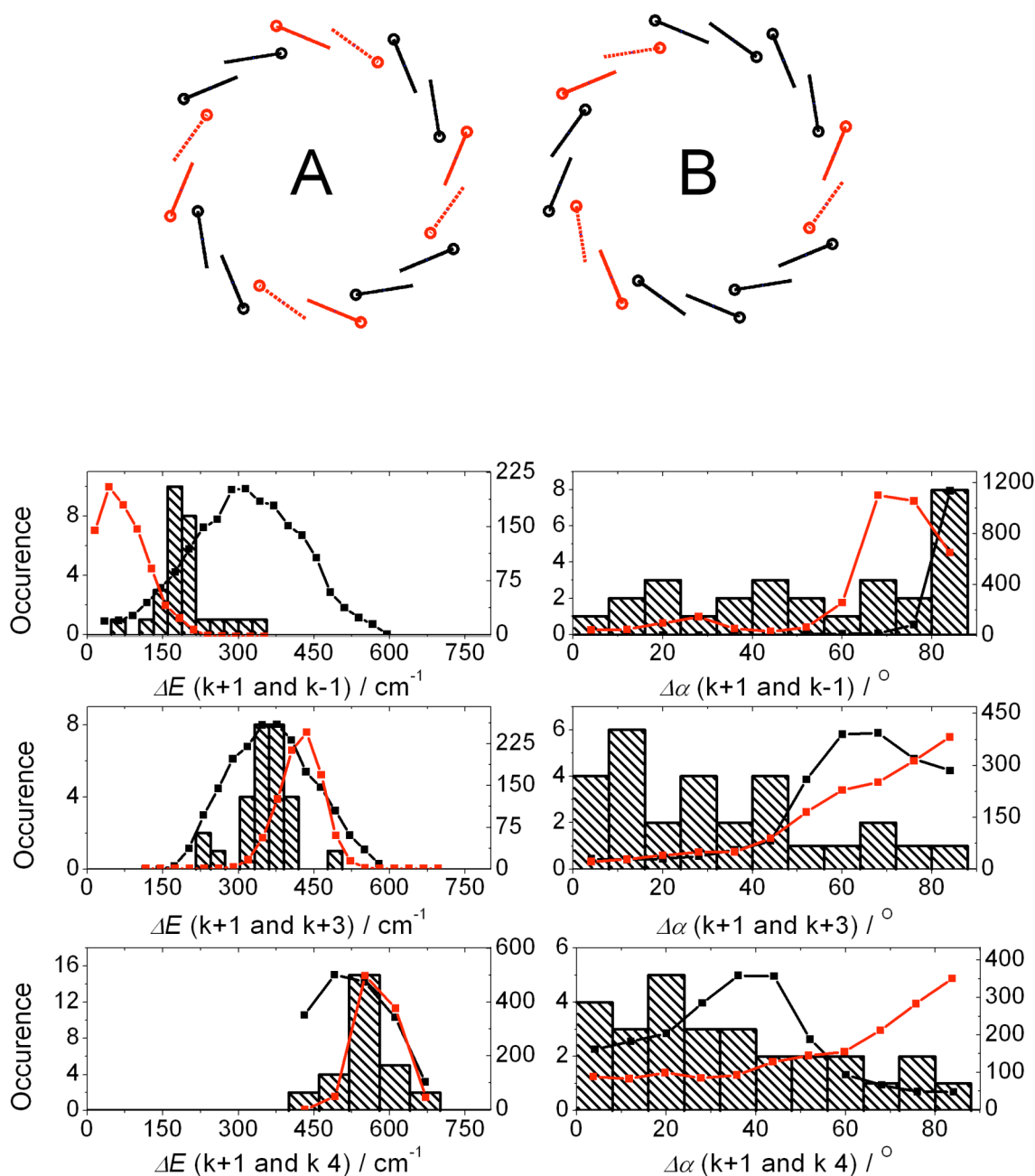


**Figure 4-14** Comparison of the experimental data with simulations based on octameric model structures with symmetrical (A) and unsymmetrical (B) distributions for the  $\alpha$ -B820-like Bchl molecules. The squared black lines and the squared red lines (bottom) correspond to the results based on the model A (top left) and on the model B (top right).

In order to be sure of the ring size issue additional simulations with symmetrical and unsymmetrical options for the octameric model were re-evaluated and are shown in Figure 4-14. In no cases do the results of these simulations agree as well with experimental data as shown for nonameric model in Figure 4-12.

Though it is not possible to claim that these simulations can provide a definitive proof of the structure of the LL LH2 complex from *Rps. palustris* they do strongly favour both a nonameric model and one where the assembly has multiple apoprotein types within a single LH ring. It is also worth pointing out that the absorption spectrum of the native LL LH2 complex from *Rps. palustris* studied in this thesis is not the same as that of the B800-only LH2 complex used in the structural studies mentioned above (de Ruijter *et al.*, 2004). It is clear that additional work will be required before a complete understanding is obtained as to why it was not possible to isolate a LL LH2 complex from *Rps. palustris* that has the spectrum described by Hartigan *et al.* (Hartigan *et al.*, 2002). Photosynthetic bacteria such as *Rps. palustris* have a very complicated set of control mechanisms that can modify which of the multi-gene family of LH2  $\alpha\beta$ -gene pairs are expressed (Evans *et al.*, 2005, Tadros *et al.*, 1993, Tadros *et al.*, 1989). These differences, therefore, may reflect variations in the growth conditions that the bacteria were cultured in, in the various laboratories, where they have been studied.

## 4.4 Conclusions

The single-molecule spectra reported here can only be satisfactorily explained by assuming that the individual LL LH2 complexes from *Rps. palustris* contain a heterogeneous polypeptide composition, where multiple types of  $\alpha\beta$  apoproteins co-exist in the same individual complex, producing individual rings with Bchl molecules having both B820-like and B850-site energies. The simulations described above strongly reinforce this conclusion. The experimental data can be modelled best by taking an arrangement of the Bchl *a* molecules in the mixed B820/850 ring of 9  $\alpha\beta$  Bchls dimers, where in 6  $\alpha\beta$ -pairs the Bchl *a* molecules have B820-like site energies and are distributed around the ring a way that the symmetry of the nonameric assembly is reduced to  $C_3$ . High intracomplex disorder reflects the heterogeneity in the polypeptide composition.

---

## 5 Low light adaptation: Energy transfer processes in different types of light harvesting complexes from *Rps. palustris*

---

### 5.1 Introduction

This chapter describes the energy transfer reactions that take place within the LH2 complexes from *Rps. palustris* grown at different light intensities, especially the HL and LL LH2 complexes. At the time of writing, few time-resolved studies have looked at the energy transfer reactions that take place within the LL LH2 complexes from *Rps. palustris*. Hess and co-workers described the energy transfer in bacterial membranes isolated from *Rps. palustris* grown at low light conditions measured by picosecond pump probe spectroscopy (Hess *et al.*, 1993). A more detailed transient spectroscopic study on extensively purified LL LH2 complexes was conducted by Nishimura and colleagues who found a B824 component and suggested several possible kinetic models for the energy transfer pathways present (Nishimura *et al.*, 1993). This present study is focused on a detailed analysis of femtosecond pump-probe spectra obtained from LH2 samples isolated from *Rps. palustris* grown at four different light intensities, as well as on the analysis of their ground state absorption spectra. In **Chapter 4**, direct evidence has been found for the presence of Bchl *a* molecules with both 'B850' and 'B820' site energies in individual LL LH2 complexes from *Rps. palustris* by use of single molecule spectroscopy. This information has been used to help interpret the data from the present study and explain the ongoing specific spectral changes in LH2 complexes during low light adaptation.

### 5.2 Global analysis

A global fitting procedure was carried out by minimising the square of the error between the measured matrix,  $\Delta A_{\text{exp}}(E, t)$  of the spectroscopic data and the

calculated one,  $\Delta A_{calc}(E,t) = d \cdot \sum_i \sigma(i,E) \cdot c(i,t)$ , by optimising the absorption cross-sections  $\sigma(i,E)$  and the populations  $c(i,t)$  for all photoexcitations  $P_i$ , as defined in a standard kinetic equation scheme of the form  $GS \xrightarrow{pump} P_1 \xrightarrow{k_1(t)} P_2 \xrightarrow{k_2(t)} [P_3 \xrightarrow{k_3(t)} GS]$ , where “GS” refers to the molecules in the ground state. The optimisation is done iteratively by varying  $k_i(t); i \in \{1,2,3\}$ , while at each iteration step,  $\sigma(i,E)$  is found by a Gaussian elimination. The sheet thickness is given by  $d$ . This approach is a generalisation of the method described by van Stokkum and colleagues where time-dependent rate constants have been included (van Stokkum, 1994).

## 5.3 Results and discussion

### 5.3.1 Analysis of ground state absorption spectra

The ground state NIR absorption spectra of the LH2 complexes, were measured at 77 K and 293 K (Figure 5-1, left and right column, respectively, also see Chapter 3), and these give information about the  $Q_y$ -transition energies of B800 and B850 Bchl *a*s from the ground state to the excited states. Common features are observed in all spectra. At 1.55 eV (800 nm), there is a relatively sharp absorption band with a vibronic replica at 1.62 eV (765 nm). Both of these can be assigned to the  $Q_y$  band of the Bchl *a* molecules in the B800 ring (Sauer *et al.*, 1996a). At lower energy, there is a broader transition the position of which is clearly temperature dependent: 1.43 eV (867 nm) at 77 K, and 1.45 eV (855 nm) at 293 K. This transition is labelled  $\Gamma_{1L}$  and can be assigned to the transition from the ground state to the low energy one-exciton band of the B850 ring (Sauer *et al.*, 1996a). The thermally induced blue-shift of  $\Gamma_{1L}$  can be explained by a temperature-induced weakening of the excitonic interaction, and hence a reduction of exciton splitting. Recently, a similar temperature dependence of B850 blue-shift was observed in LH2 complexes from other bacteria and has been explained within the framework of the modified Redfield theory (Zerlauskiene *et al.*, 2008).

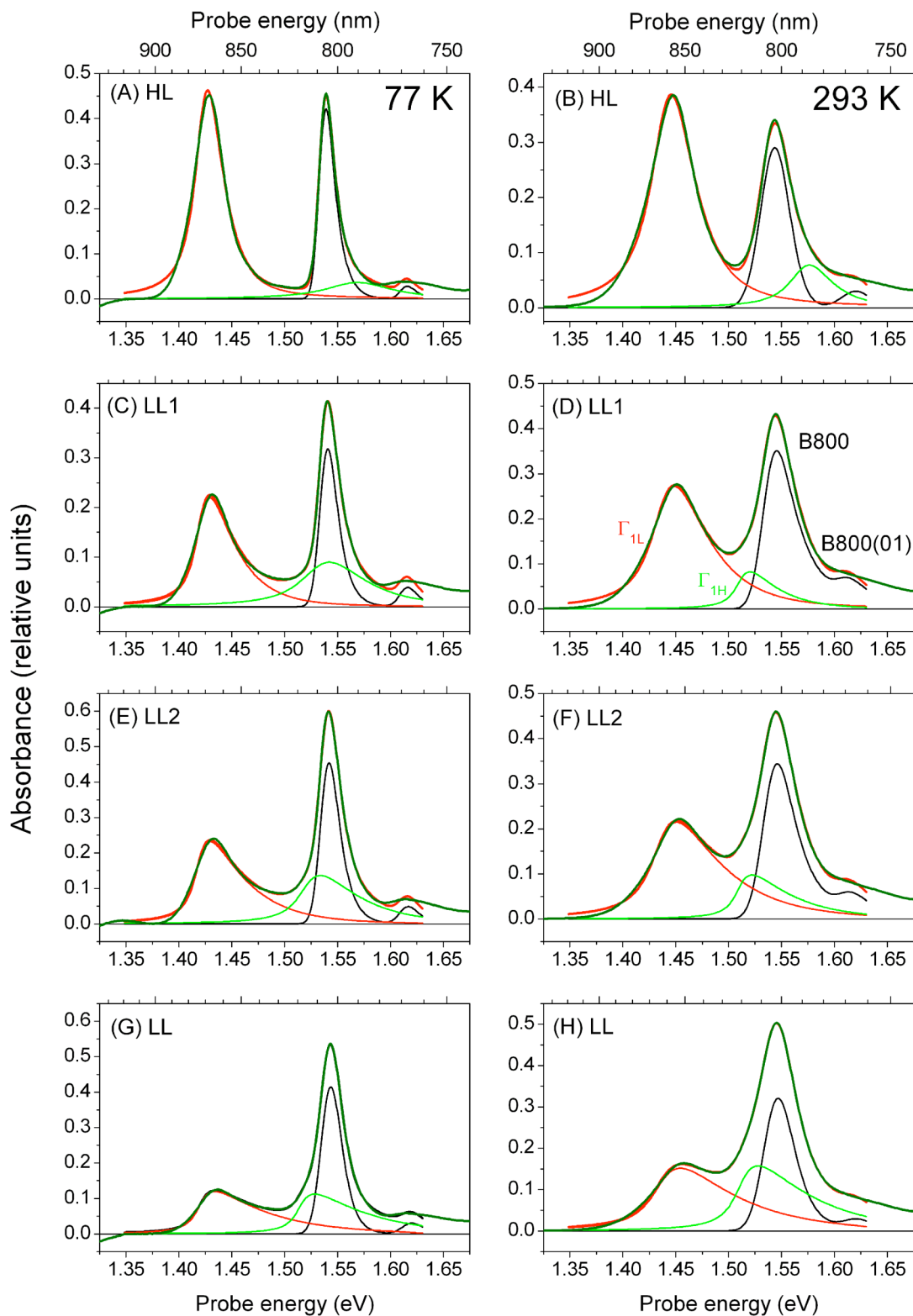


**Figure 5-1** Ground state absorption spectra (thick red lines, normalized to Bchl a  $Q_x$  band) as a function of growth conditions (rows) measured at two different temperatures (left column, 77 K; right column, 293 K). Thick green lines: calculated spectra according to the model explained in the text; thin red lines: calculated  $\Gamma_{1L}$ , thin blue lines: calculated  $\Gamma_{1H}$ , thin black lines: molecular transition of  $Q_y$  band in B800 molecule including vibronic progression. Panel D shows the labelling of the transitions that is used in the text.

Growth of the *Rps. palustris* under reduced illumination leads to characteristic changes in the ground state absorption spectra (**Chapter 3**):  $\Gamma_{1L}$  loses oscillator strength, while the B800 band apparently becomes stronger and larger. This progression holds for both low and high temperature measurements (compare panels *A-C-E-G* and *B-D-F-H* in **Figure 5-1** for low and high temperature, respectively). Furthermore,  $\Gamma_{1L}$  becomes more asymmetric in the samples from cells grown at lower light intensities. As discussed below, it is a reasonable assumption that the apparent increase of both intensity and width of the B800 transition is in reality caused by a superposition of the (unchanged) B800 absorption with changes in the spectral properties in the ‘B850’ ring.

The absorption spectra of LH2 under all conditions were simulated using the following model: the B800 transition is regarded as a molecular transition together with its vibronic progression of one prominent normal mode; the B850 molecules form two excitonic bands,  $\Gamma_{1L}$  close to 1.43 eV (867 nm) and  $\Gamma_{1H}$  at 1.53 eV (810 nm). Both bands were assumed to be Lorentzians and inhomogeneous broadening was introduced by an exponential distribution with characteristic distribution energies of  $t_{800}$  for the B800 band and  $t_{850}$  for the one-exciton bands. Hereby, the distribution of states was assumed to decay exponentially towards higher energies.

**Table 5-1 Fitting parameters for the reproduction of ground state absorption spectra (Figure 5-1) at 293 K (values for 77 K are in brackets). All data are in meV except the ratio  $r(\Gamma_{1H}/\Gamma_{1L})$ , which has no unit.**

	HL	LL1	LL2	LL
E(B800)	1539 (1535)	1536 (1536)	1536 (1537)	1539 (1539)
E( $\Gamma_{1L}$ )	1439 (1422)	1437 (1421)	1435 (1419)	1436 (1421)
E( $\Gamma_{1H}$ )	1569 (1562)	1511 (1530)	1511 (1521)	1512 (1515)
$r(\Gamma_{1H}/\Gamma_{1L})$	0.20 (0.20)	0.21 (0.73)	0.34 (0.74)	0.90 (0.95)
$t_{800}$	6 (9)	24 (10)	21 (10)	14 (9)
$t_{850}$	11 (9)	25 (21)	38 (32)	50 (50)

The simulated spectra shown in **Figure 5-1** (green lines) closely reproduce the measured spectra (red). The individual contributions to the calculated spectra are shown as thin lines. The best fitting parameters as a function of growth conditions are given in **Table 5-1**. Going from HL to LL, the ratio  $r(\Gamma_{1H}/\Gamma_{1L})$  increases from 1:5 to nearly 1:1. This is a clear sign of a change in the ‘B850’ molecules, leading to a different excitonic splitting. The exponential broadening parameter  $t_{850}$  for the B850 excitonic features increases strongly under low light conditions, while it is only weakly temperature dependent. In contrast, the broadening  $t_{800}$  is not significantly dependent on the growth conditions but rather on the temperature. This clearly distinct behaviour of the broadening parameters can be related to different broadening mechanisms affecting the monomeric and excitonic bands, respectively. According to the available literature, the B800 ring seems to be not influenced by growth conditions, so a dependence of the broadening parameter  $t_{800}$  on growth conditions is not expected (Evans *et al.*, 1990, Gardiner *et al.*, 1993, McLuskey *et al.*, 2001). The temperature dependence of  $t_{800}$  can be assigned to dynamic disorder, caused by temperature-induced occupation of low-energetic intramolecular vibrational modes. The thermal occupation is governed by Boltzmann's law, hence the exponential broadening (Gierschner *et al.*, 2002).

### **5.3.2 Transition absorption spectra measurements**

Transient absorption spectra of HL, LL, and two intermediate (LL1, LL2) samples of LH2 complexes from *Rps. palustris* were measured in the NIR region to trace energy transfer and relaxation processes. Excited states in B800 were created by pumping at 795 nm (1.6 eV). An overall view of the pump probe spectra of LH2 samples (HL, LL1, LL2, and LL) is shown in the contour plots in **Figure 5-2A, B, C and D**, respectively. Photoinduced absorption (positive values, red colour) progressively disappears when going from HL to LL samples; at the same time, the transient bleach (green and blue) of  $\Gamma_{1L}$  broadens. The changes in the higher energy region of pump-probe spectra point to the presence of a higher excitonic band in the LL LH2 exciton manifold.

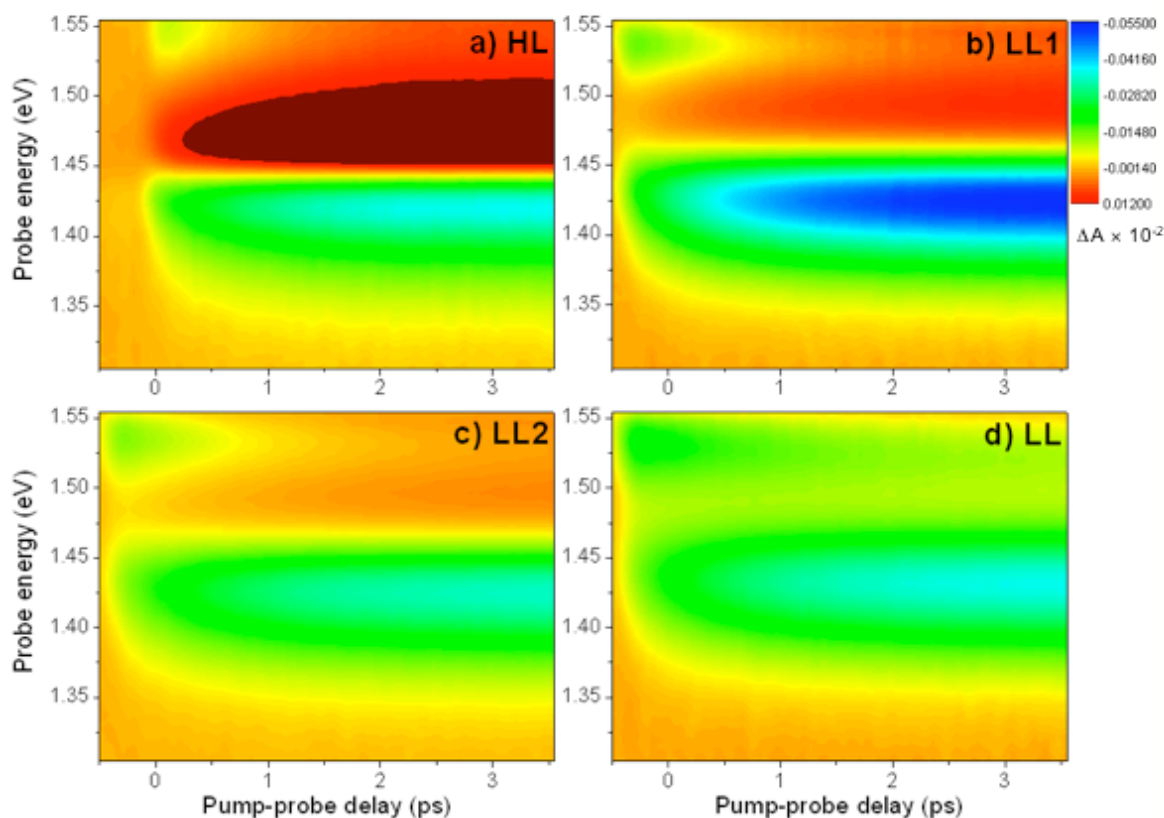


**Figure 5-2** Contour plots of measured transient absorption spectra of LH2 complexes from *Rps. palustris* grown at four different illumination; changes in differential absorption (colour scale is identical in all four panels) is dependent on pump probe delay and probe energy are shown in high light (HL), two intermediate (LL1, LL2), and low light (LL) sample (A, B, C, and D, resp.); red colour, photoinduced absorption; green and blue, transient bleach.

**Figure 5-3** and **5-4** show vertical and horizontal cuts of the contour plots from **Figure 5-2**. **Figure 5-3** shows pump-probe spectra at different pump-probe delay times, coded by colour. In the case of the HL LH2 complexes (**Figure 5-3A**), at  $t = 0$  (during the pump pulse), the spectrum shows the presence of a transient bleaching of both B800 and the  $\Gamma_{1L}$  ground state absorption bands, together with the excitonic state transition  $\Gamma_{L2}$ , i.e., from the lowest one-exciton level to the two-exciton level (Novoderezhkin *et al.*, 1999). The presence of excitonic B850-related features prior to energy transfer from B800 to B850 can be explained by a resonant generation of B850 excited states by the 1.6 eV pump pulse (black line in **Figure 5-3A**). Within 3 ps, the photobleaching signal from excited B800 completely disappears, while the photoinduced absorption ( $\Gamma_{L2}$ ) and ground state bleaching ( $\Gamma_{1L}$ ) of B850 increase strongly. This is a well-known process and is due to energy transfer from B800→B850. It is important to note that during this energy transfer (ET) process, the increase of  $\Gamma_{1L}$  is much stronger than the

concomitant bleaching recovery of B800. This clearly shows the excitonic nature of the B850. After 3 ps, no further spectral changes are observed in the HL sample until much longer times (magenta, yellow and green curves in **Figure 5-3A** are almost identical). All the curves in **Figure 5-3A** show a very clear isosbestic point at 1.44 eV (862 nm). This reflects the simple  $A \rightarrow B$  reaction for ET from B800 to B850 in the absence of further spectral changes.

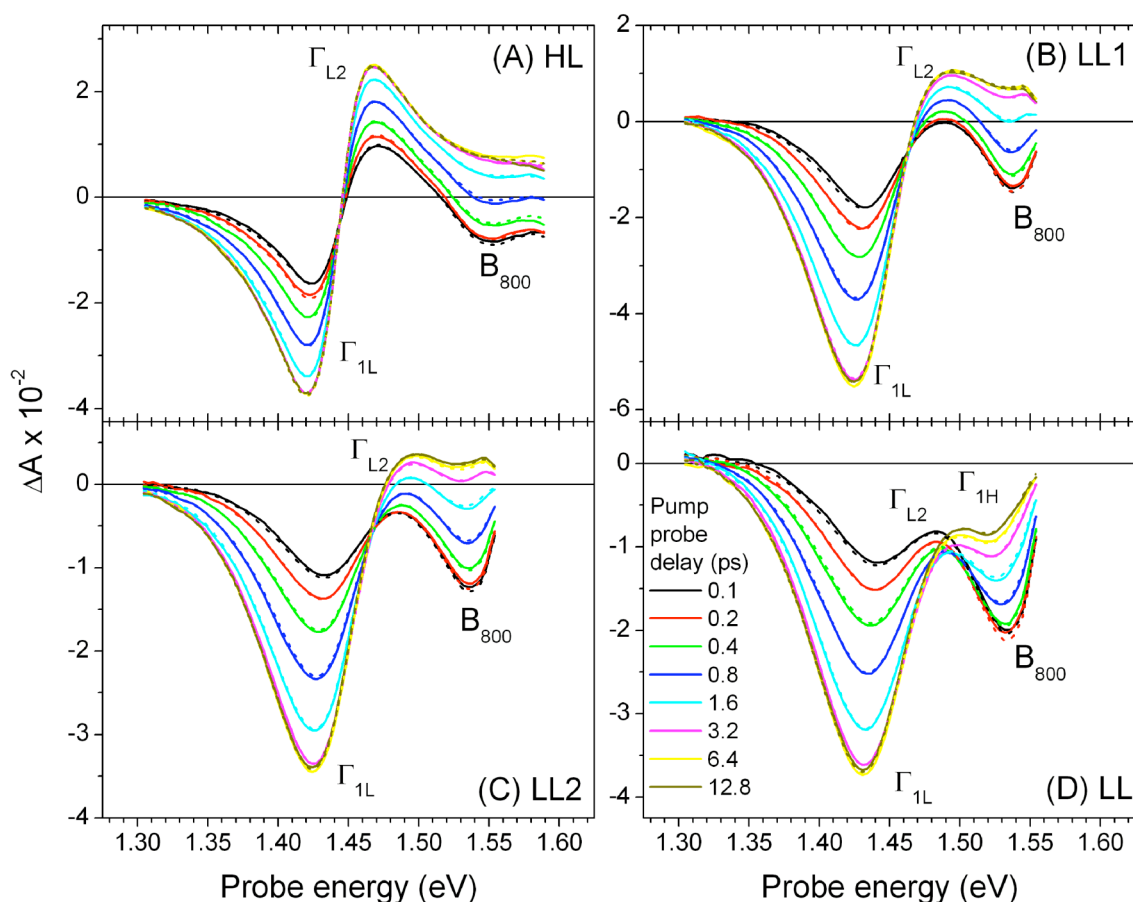


**Figure 5-3** Difference absorption spectra of LH2 complexes at individual pump-probe delays; HL complex (A) shows  $\Gamma_{1L}$  transition, there is no change after 3.2 ps (pink curve), LL complex (D) presents an additional transition  $\Gamma_{1H}$  changing till  $\sim 10$  ps (yellow and olive curves); panels of intermediate samples LL1 and LL2 (B, and C, respectively) represent increasing contribution of  $\Gamma_{1H}$  band to the spectra. In all panels: solid lines, measured values; dashed lines, global fit. The difference spectra ( $\Delta A$ ) is the absorption spectrum of the excited molecule minus the absorption spectrum of the molecule in the ground state.

Pump-probe spectra of the LL samples at  $t = 0$  are similar to those of the HL sample; compare **Figure 5-3B**, C and D to **Figure 5-3A**, respectively. The spectral evolution after the pump pulse is, however, dramatically different for the LL samples. The positive  $\Delta A$  band at  $t = 3$  ps decreases on going from LL1 to LL2, and no positive signal can be observed at all in the fully LL sample

(magenta curves in Figure 5-3). This loss of the positive band can be explained by superposition of positive and negative bands in close proximity. There is a positive  $\Gamma_{L2}$  band at 1.48 eV (840 nm) and a negative signal from the  $\Gamma_{1H}$  band, resulting in a local minimum at 1.53 eV (813 nm). This provides evidence of a second, higher excitonic band of B850 in LL LH2 complexes in the region of 810 nm (Figure 5-3D). These findings are in agreement with the spectral assignment of the room temperature ground state absorption spectra; see Figure 5-1 and Chapter 3. Finally, the positive ( $\Delta A$ ) band for the transition from the high-energy one-exciton band to the two-exciton band  $\Gamma_{H2}$  can be observed at 1.56 eV (794 nm). In the lower light samples the presence of delayed kinetics is observed on the high energy side of the  $\Gamma_{1H}$  bleach (1.53 and 1.48 eV) (magenta and olive curves in Figure 5-3B, C and D). The shapes of the spectra on the low energy side are very similar for individual pump-probe delays (Figure 5-3).

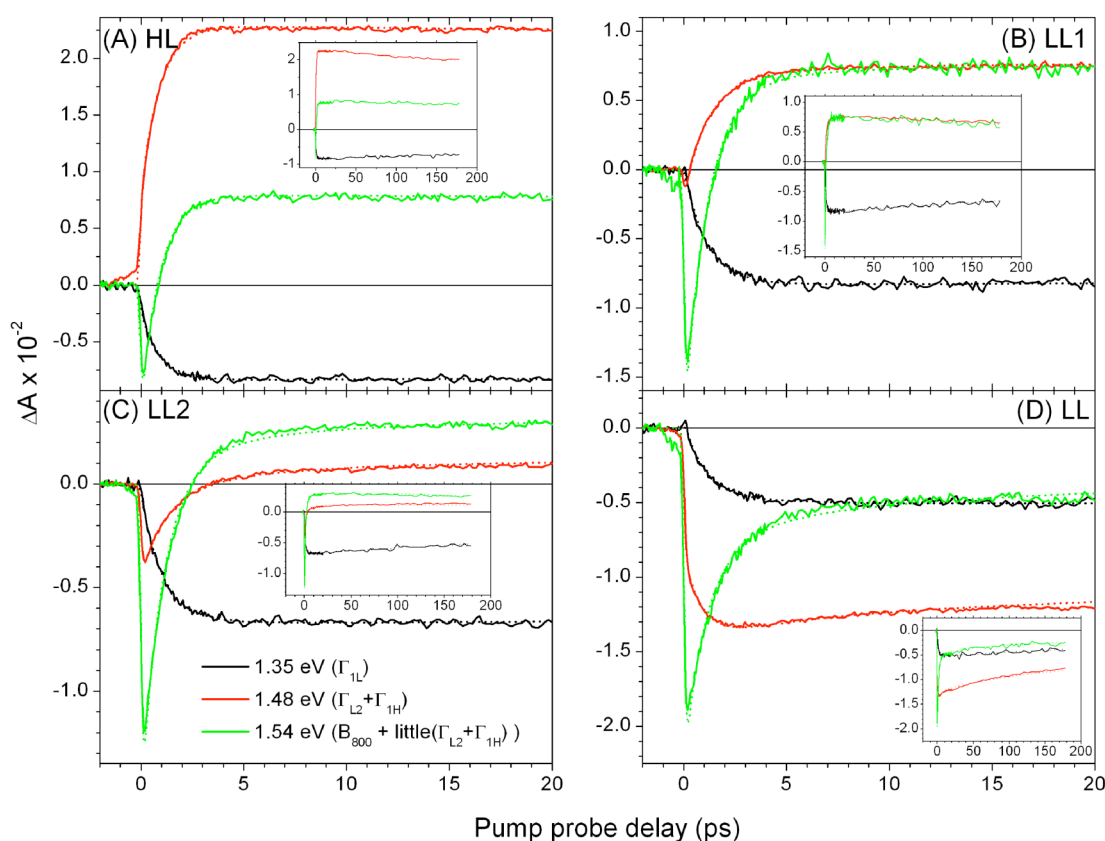


**Figure 5-4** Time traces of differential absorption spectra of LH2 complexes from HL (A), LL1 (B), LL2 (C) and LL (D) samples at three representative probe energies: 1.54 eV (805 nm), 1.48 eV (838 nm), and 1.35 eV (918 nm) (green, red, and black lines, resp.). Panels show processes from  $t = 0$  until 20 ps, inserts processes until 200 ps. In all panels: solid lines, measured values; dashed lines, global fit.

To illustrate more clearly the kinetics of the spectral evolutions in the LL samples, **Figure 5-4** presents time traces obtained as horizontal cuts through **Figure 5-2** at following probe energies: 1.35, 1.48, and 1.54 eV. In the HL sample, all time traces show mono-exponential behaviour. In contrast, the LL samples show a clearly delayed contribution in the range from 1.48 to 1.54 eV, where several photoinduced features are superposed, namely B800,  $\Gamma_{L2}$  and  $\Gamma_{1H}$ . In principle, the observed slow kinetics could be due to delayed ET from B800 to B850, causing a slow decrease of B800 and a concomitant slow build-up of the  $\Gamma_{L2}$  and  $\Gamma_{1H}$  transitions. However, no corresponding slow kinetic phase in the build-up of the  $\Gamma_{1L}$  bleach can be observed in time traces at 1.35 eV, where the signal is caused nearly exclusively by the  $\Gamma_{1L}$  transition (**Figure 5-4**, black lines). Instead there is mono-exponential behaviour for all samples. The picosecond spectral evolutions of B850 in the LL samples should therefore be associated with B850 exciton relaxation dynamics after B800→B850 energy transfer. This picture is confirmed by a global fitting procedure (see below).

In the insets of **Figure 5-4**, the same time traces are shown but on a longer time scale. It is evident that the decay of the B850 excitons to the ground state occurs significantly faster in the LL samples than in the HL sample. This difference is not due to exciton annihilation since in both cases the kinetics have been shown to be independent of the pump energy at pump intensities used here (data not shown). In LL samples, the forbidden transition from the B850 exciton back to the ground state is more allowed probably because of a disorder introduced into the LL LH2 structure due to the presence of different apoproteins (see **Chapter 3 and 4**) (Tharia *et al.*, 1999).

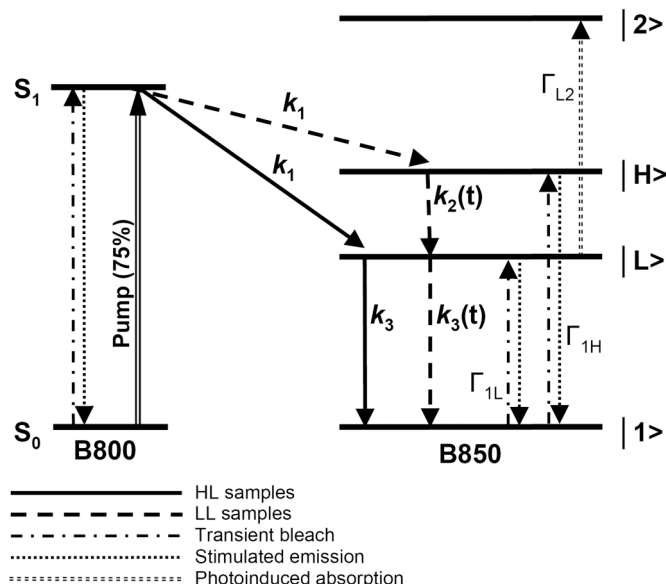


**Figure 5-5** Photophysical model of energy transfer paths and associated rate constants between Bchl *a* molecules in the B800 and the B850 ring. Processes for HL and LL samples are given as solid and dashed arrows, and the population probes that can be detected in transient absorption are given as dot-dashed and dotted lines.

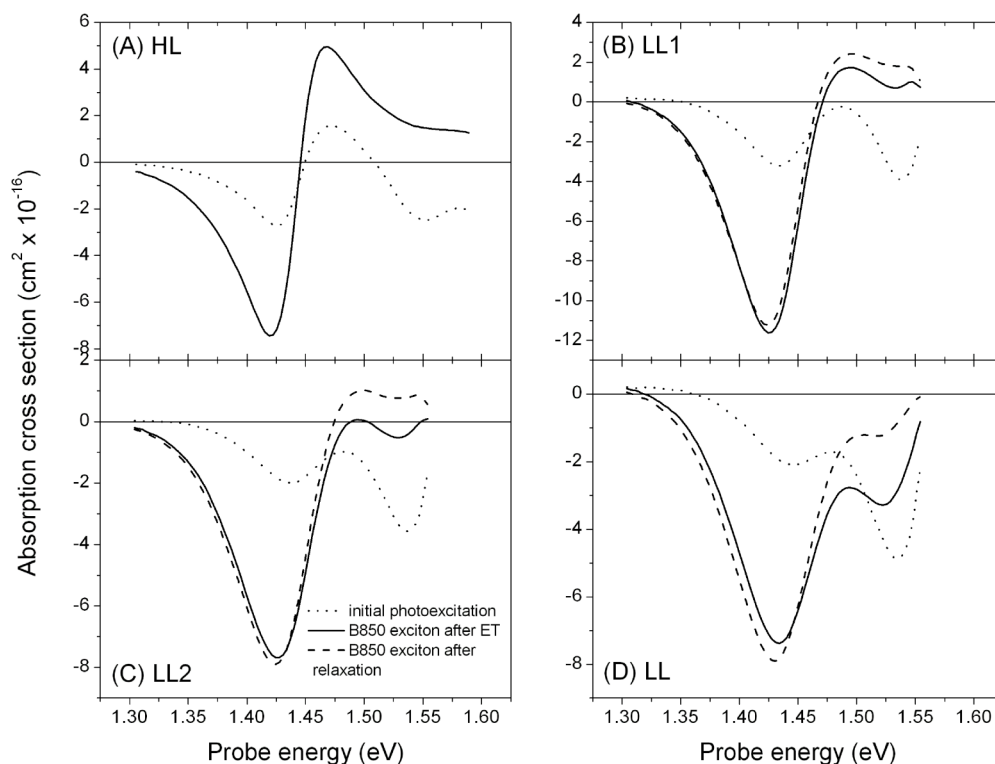


**Figure 5-6** Photoexcitation spectra of LH2 complexes calculated by global fitting of pump probe spectra. Absolute absorption cross-section spectra are given for the initial, intermediate and final photoexcitation (dotted, solid, and dashed lines, resp.) of HL, LL1, LL2, and LL complexes (A, B, C, and D, respectively).

### 5.3.3 ET rate constants for HL from global fitting

A global fitting procedure has been performed to properly characterise the time-resolved measurements (see section 5.2). Perfect fits have been obtained for all measurements; see dashed lines in Figure 5-3 and 5-4. The fits are rationalised by a photophysical model that is shown in Figure 5-5. For the HL sample, two basis spectra and two simple exponential rate constants are required. The first basis spectrum (dotted curve in Figure 5-6A) is assigned to the B800 excited state, created by resonant excitation by the pump pulse. The negative absorption feature at 1.55 eV is caused by transient bleaching of the respective ground state transition. The fitted absorption cross-section of this band is about  $3 \cdot 10^{-16} \text{ cm}^2$ , which is close to the literature value of  $2.3 \cdot 10^{-16} \text{ cm}^2$  for this ground state transition (Connolly, 1982). The first spectrum converts into the second spectrum in the process assigned to B800→B850 energy transfer with decay constant  $k_1$ . The second basis spectrum (solid curve in Figure 5-6A) represents the excited state spectrum of the B850 exciton that decays with the rate constant  $k_3$  to the ground state. It is characterised by a negative absorption band, centred at 1.42 eV, and a positive absorption band at 1.47 eV. The observed transfer times  $\hat{\sigma}_i = 1/k_i$  are in line with literature data where B800→B850 transfer times of around 0.9 ps have been widely published for a variety of purple bacterial LH2 complexes (Herek *et al.*, 2000, Hess *et al.*, 1995a, Ihalainen *et al.*, 2001, Kennis *et al.*, 1997b, Ma *et al.*, 1997, Ma *et al.*, 1998). The shape of this second basis spectrum can be represented by a superposition of two Lorentzian bands of equal integral area, where the negative Lorentzian is centred at 1.45 eV, and the positive one at 1.46 eV (fit not shown). They are assigned to the  $\Gamma_{1L}$  and  $\Gamma_{L2}$  transitions, respectively. The slight blue-shift of the two-exciton transition vs. the one-exciton transition is typical for strongly delocalised molecular excitons. From the lowest one-exciton state, the transition strength into higher exciton states is negligible because both transitions have equal oscillator strengths. This behaviour is predicted for the  $k = 0$  exciton (Novoderezhkin *et al.*, 2002). Since the resonance energy transfer from the B800 state should result in the creation of a “hot”,  $k \neq 0$ , exciton, it can be concluded that exciton relaxation is much faster than the B800→B850 transfer rate, and cannot be observed in the present time-resolved spectra. The

values of the rate constants are summarised in **Table 5-2**. Interestingly, in **Figure 5-5**, the dotted spectrum contains the same features as the solid one in the B850 region, compressed by roughly a factor of 3. It is possible to conclude that under current experimental conditions approximately 25% of the total B850 population is not created by energy transfer but by direct excitation.

**Table 5-2** Rate constants from global fitting of transient absorption spectra;  $k_1$  for energy transfer B800→B850 is not dispersive,  $k_2$  for the process of exciton relaxation has the dispersive parameter  $\gamma_2$ ;  $k_3$  for exciton decay to the ground state with dispersive parameter  $\gamma_3$ .

Sample	$1/k_1$ (ps)	$1/k_2$ (ps)	$\gamma_2$	$1/k_3$ (ps)	$\gamma_3$
HL	0.91	-	-	1 250	0*
LL1	1.10	2.00	-1.00	280	-0.16
LL2	1.00	1.60	-0.93	300	-0.16
LL	1.00	2.10	-0.94	220	-0.16

(-) Process not considered. Perfect fit obtained without this process, so inclusion was not justified. (\*) Value fixed

#### 5.3.4 Relaxation and dispersive decay of B850 excited states in LL samples

The absence of isosbestic points in **Figure 5-3**, which are apparent in the high resolution spectra (or see **Figure 5-6**) and the presence of slow transients in **Figure 5-4** suggest that more than two states are necessary for the global fit of the low light samples LL1, LL2, and LL. Indeed, for a good fit one needs three basis spectra, coupled with three processes out of which the second and third ones are dispersive with time-dependent rate coefficients of the form  $k_i(t) = k_i^0 \cdot (t/t_0)^{\alpha(i)}$ ;  $i \in \{2,3\}$ ,  $t_0 = 1ps$ . The fitted values are in **Table 5-2**. The basis spectra for the first photoexcitation ( $k_1$ , ET from B800-B850) are similar for LL and HL samples, containing contributions of both B800 bleach and B850 excitonic features (dotted curves in **Figure 5-6**). In analogy to the HL sample, the first process is assigned with the rate constant  $k_1$  to B800→B850 ET, and therefore, the second basis spectrum represents the B850 exciton. Interestingly, the ET rate constant  $k_1$  is only reduced by about 10 % in LL samples with respect to the

HL sample, see **Table 5-2**. Since spectral overlap changes dramatically, this is strong evidence for a non Förster type mechanism governing energy transfer (Beljonne *et al.*, 2009).

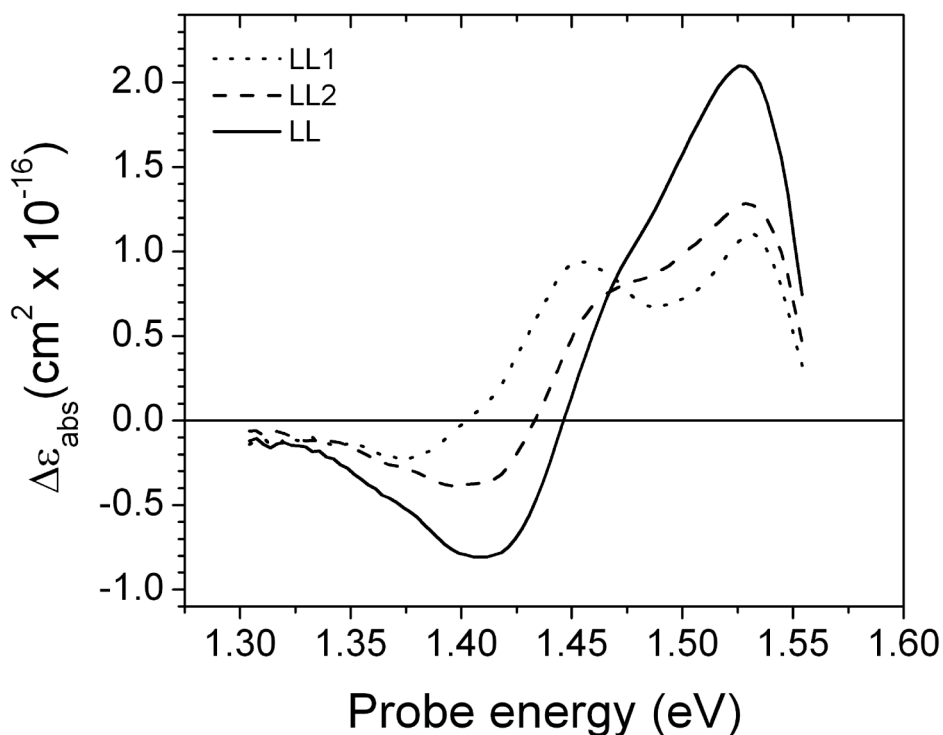


**Figure 5-7** Differential spectra for LL, LL2, and LL1 samples (solid, dashed, and dotted line, respectively), calculated from second and third photoexcitation spectra. A clear signature of  $\Gamma_{1H}$  band in each LL sample and no change in B800 bleach contribution (no sign of delayed B800→B850 ET) suggesting B850 exciton relaxation.

By comparing the second and the third basis spectra, it is possible to characterise the slow spectral changes typical for low light samples. In contrast to the HL sample, the low light samples show a negative band at 1.53 eV. In agreement with **Figure 5-1**, this band can be assigned to the  $\Gamma_{1H}$  transition, increasing in the order LL1→LL2→LL in both **Figure 5-1** and **5-6**. The transition from the second to the third basis spectrum (dashed curves in **Figure 5-6**) is characterised by a strong decrease of this  $\Gamma_{1H}$  transition, accompanied by a slight red-shift of the  $\Gamma_{1L}$  transition. The respective difference spectra are shown in **Figure 5-7** to show the differences between the second and third photoexcitation more clearly. In all cases, it is clear that the  $\Gamma_{1H}$  transition is weakened, and that there is no contribution of the B800 bleach to the observed

spectral changes. This excludes the assignment of this process to a delayed ET from B800→B850. According to the photophysical model suggested here and used for this analysis (**Figure 5-5**), this process can be assigned to slow exciton relaxation from the initially populated higher exciton band (which is in resonance with B800 emission) to the lower one. If this is correct then it should be possible to observe the population transfer by a decrease of stimulated emission (SE) from the higher exciton, correlated with an increase of SE from the lower exciton. This is exactly what is observed in **Figure 5-6D**. The SE features occur slightly red-shifted against the bleaching due to a small Stokes shift.

The observation of a time-dependent (dispersive) rate coefficient  $k_2(t)$  in the low light samples supports its assignment to an exciton relaxation. The  $k=0$  exciton is reached via a cascade of intermediate steps, additionally superposed by vibronic relaxation (Novoderezhkin *et al.*, 2002). This sequence of elementary transfer steps with progressively increasing transfer times is the reason for the observed time-dependent relaxation coefficient. A possible reason for a much slower exciton relaxation in LL than in HL samples could be weaker electronic coupling between Bchl *a* molecules in the LL B850 ring, where some of these molecules have "B850-like" and some others "B820-like" spectral properties due to a more complex apoprotein composition. In the LH2 complexes in general, the pigment binding apoproteins provide a quasi-continuum ("bath") of states and the coupling of the Bchl *a* to this bath causes fluctuations in the exciton energy. It has been pointed out that the coupling parameter (the amplitude of the bath-induced fluctuations of the Bchl *a* molecules) determines the time of exciton relaxation in different light harvesting systems. For LH1 complexes in *Blastochloris viridis*, a value of  $490\text{ cm}^{-1}$  for this parameter has been obtained, resulting in a relaxation time below 100 fs (Novoderezhkin *et al.*, 2002). The loss of excitonic coherence in HL LH2 samples of *Rps. acidophila* strain 10050 has been measured to be 160 fs (Mercer *et al.*, 2009). Justifying relaxation times in the picosecond time regime, as obtained here, requires a coupling term of less than  $50\text{ cm}^{-1}$ . The "bath" in the case of the LH2 complexes consists of the many degrees of freedom of the binding apoproteins; the resulting dynamic fluctuations of atomic positions lead to a change in exciton splitting and/or site energies for the single Bchl *a* molecules.

### 5.3.5 LH2 apoproteins vs. spectral properties of B850 Bchl *a* in LL

Previous studies have identified two key amino acid residues in LH2  $\alpha$ -apoprotein that are associated with the blue spectral shift of the B850 absorption band depending on light intensity during bacterial growth (Cogdell *et al.*, 2002, McLuskey *et al.*, 2001). In HL *Rps. acidophila*, Tyr-44 and Trp-45 form two hydrogen bonds that hold two carbonyl oxygen atoms in planar orientation with respect to the two B850 bacteriochlorin rings. In LH2 complexes isolated from *Rps. acidophila* strain 7050 grown at LL conditions, Tyr-44 and Trp-45 are replaced by Phe and Leu, respectively. Phe and Leu do not form hydrogen bonds with the carbonyl oxygens, leaving them out of the plane of the bacteriochlorin rings. This reorientation of the carbonyl groups results in a lower degree of conjugation in the bacteriochlorin rings followed by the blue-shift of B850 band from 850 nm to 820 nm. When *Rps. palustris* is grown at LL one of the LH2  $\alpha$ -apoproteins that is expressed also has these 'key' amino acid residues replaced by Phe and Met (Tharia *et al.*, 1999). Under LL conditions, HL-type  $\alpha$ -apoproteins are also expressed. This suggests that LL LH2 complexes could have Bchl *a* molecules with mixed site-energies (both 'B820-like' and 'B850-like') in the same individual LL LH2 complex. Indeed, in our experiments with LL LH2, both a higher exciton state  $\Gamma_{1H}$  and a lower exciton state  $\Gamma_{1L}$  have been observed. This result fits well with previous spectroscopic data that have been published suggesting the presence of mixtures of Bchl *a* molecules with 'B820-like' and 'B850-like' site energies in one LH2 ring (see also Chapter 4) (Gall *et al.*, 1999, Georgakopoulou *et al.*, 2002, Tadros *et al.*, 1989, van Mourik *et al.*, 1992). Formally, this spectroscopic data does not distinguish between mixed rings and mixtures of different but homogenous B850 rings. However, single molecule spectroscopic study on individual LL LH2 isolated from *Rps. palustris*, described in Chapter 4, provides data that are consistent with the existence that there are single LL LH2 complexes from *Rps. palustris* that do contain mixed rings. In the chapter of single molecule spectroscopy, it was shown that in HL LH2 complexes, all exciton states where  $k > 2$  are optically forbidden. In the case of LL LH2 complexes, the  $k = 3$  exciton was significantly allowed, which explains the redistribution of oscillator strength towards higher energies seen in the absorption spectra of the LL complexes (Chapter 4). In the present analysis, the measurements represent an ensemble of energy bands, the single ( $k = 1, 2,$

and 3) exciton bands cannot be observed individually. Therefore, the decrease of oscillator strength towards higher energies is smooth and can be approximated by an exponential function that has been used in the kinetic model described above. It is not yet clear whether all the LL LH2 complexes have the same internal organisation of the different antenna apoproteins that are present in the ensemble population. To help to answer this question more detailed quantitative analyses of the apoprotein composition are required.

## 5.4 Conclusions

This study of LH2 complexes isolated from *Rps. palustris* grown at different light conditions has revealed novel characteristics of the ring of strongly coupled Bchl *a* molecules in LL samples. In the case of HL LH2 complexes the spectroscopic properties of the B850 ring can be satisfactorily accounted for by assuming the presence of one major exciton band  $\Gamma_{1L}$ . In contrast, a second, higher energy exciton band  $\Gamma_{1H}$  is required to account for the properties of the LL LH2 complexes. The presence of the  $\Gamma_{1H}$  feature in the LL case is also supported by the decomposition analysis of the ground state absorption spectra of the LL samples.

The mono-exponential rate constant  $k_1$  for ET from B800 to 'B850' is only slightly reduced (by about 10%) in LL samples in comparison to HL ones. The rate constant  $k_2$  for the exciton relaxation from  $\Gamma_{1H}$  to  $\Gamma_{1L}$  is only seen in LL samples and is strongly dispersive. The decay of the 'B850' exciton back to ground state is faster in the LL samples by about a factor of 5, however, the decay is still very slow. The rate constant  $k_3$  for this process is mono-exponential in the case of the HL complexes but is weakly dispersive in the LL ones. A simple photophysical model has been used to fully reproduce the transient absorption spectra of LH2 complexes.

---

## 6 B800-850 HL and B800-low-850 LL LH2 complexes from *Rps. palustris*: crystallisation trials and low-resolution model structures

---

This chapter describes attempts to produce 3D crystals from HL and LL LH2 complexes from *Rps. palustris* that are suitable for an X-ray structure determination. Crystallisation protocols used for producing crystals of the B800-850 LH complexes from *Rhodospseudomonas acidophila* strain 10050 and the commercial crystals screen protocols, e.g. from Molecular Dimension and Hampton Research, were used. The optimised conditions for the HL and LL LH2 complexes successfully produced bigger crystals, though still disappointingly with only low-resolution diffraction (4.5 Å).

### 6.1 Crystallisation trials

**Table 6-1** Initial crystallisation conditions tested with the LH2 complexes from *Rps. palustris*.

Parameter	Unit	Values	In steps of
Detergent: Lauryl-DimethylAmine N-Oxide (LDAO)	%	0.1	n/a
Protein absorption at 850 nm (HL) or 800 nm (LL)	cm <sup>-1</sup>	30-110	20
Precipitant: K <sub>2</sub> HPO <sub>4</sub> (KP <sub>i</sub> ) pH 9.7	M	0.5-1.2	0.1
Reservoir solution: (NH <sub>4</sub> ) <sub>2</sub> SO <sub>4</sub> pH 9.35 (AMS)	M	1.5-2.0	0.1
LH2 drop size	μl	20	n/a
pH in the drop	-	8.15	n/a
Volume reservoir	ml	1	n/a
Incubation temperature	°C	20	n/a

In the initial screening, crystallisation of HL LH2 from *Rps. palustris* was attempted using the protocols described for the crystallisation of B800-850 LH2s from *Rps. acidophila* 10050 as they were reported by Howard et. al. (Howard,

2000), but without an additive (i.e. Benzamidine). These conditions use  $KP_i$  as a precipitant and AMS as the salt in the reservoir solution. The details of the initial parameters used are listed in Table 6-1. Many of these initial trials resulted in phase separation, amorphous precipitation, and the LH2 protein was often denatured (Figure 6-1G and H). However, in some of these initially tested conditions there were crystals formed. The HL LH2 complex produces large tetragonal crystals ( $\sim 0.25 \times 0.4$  mm) (Figure 6-1A) and cubic crystal ( $\sim 0.7$  mm long) (Figure 6-1B), but only after extended periods such as 6 months. These crystals were obtained from the following conditions: protein at an  $OD_{850}$  of  $50 \text{ cm}^{-1}$  0.1% (v/v) LDAO and 1.0 M  $KP_i$  pH 9.7 in the droplet and 1.9 M AMS pH 9.35 in the reservoir (Figure 6-1A) and with the concentration of phosphate reduced to 0.7 M pH 9.7 in the droplet and 1.8 M AMS pH 9.35 in the reservoir (Figure 6-1B). These crystals only diffracted poorly (9-10 Å) at the synchrotron beam (ESRF, Grenoble, France).

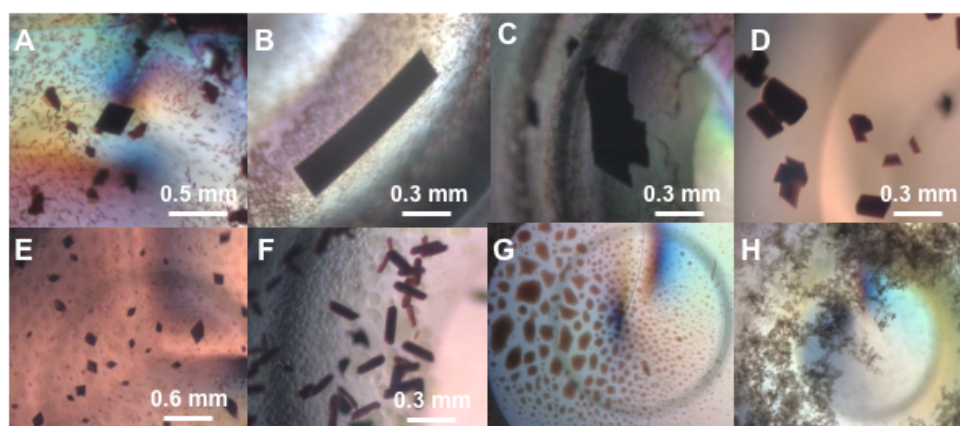


**Figure 6-1** Typical results of initial crystallisation screens from HL and LL LH2 *Rps. palustris* grown at 20°C :

- A.** HL LH2 crystals grown with 1.0 M  $KP_i$  pH 9.7 in the droplet and 1.9 M AMS pH 9.35 in the reservoir;
- B.** HL LH2 crystal grown with 0.6 M  $KP_i$  pH 9.7 in the droplet and 1.8 M AMS pH 9.35 in the reservoir;
- C.** HL LH2 crystals grown with 0.8 M  $KP_i$  pH 9.7, CsCl [0.1M] and 2% Benzamidine-HCl in the droplet and 1.8 M AMS pH 9.35 in the reservoir;
- D.** HL LH2 crystals grown with 0.1M Tris-HCl pH9.5, 0.1 M NaCl, 0.1 M  $MgCl_2$  and 30% PEG 400 in the reservoir;
- E.** LL LH2 crystals grown with 1.2 M  $KP_i$  pH 9.7 in the droplet and 1.6 M AMS pH 9.35 in the reservoir;
- F.** LL LH2 crystals grown with 0.1 M Tris-HCl pH9.5, 0.1 M NaCl, 0.1 M  $MgCl_2$  and 30 % PEG 400 in the reservoir;
- G.** Example of phase separation;
- H.** Example of precipitate.

**Table 6-2 Optimisation of the initial crystallisation conditions of LH2 complexes from *Rps. palustris*.**

Parameter	Unit	Values	In steps of
Detergent: Lauryl-DimethylAmine N-Oxide (LDAO)	% (v/v)	0.1	n/a
Protein absorption at 850 nm (HL) or 800 nm (LL)	cm <sup>-1</sup>	30-110	20
Precipitant: K <sub>2</sub> HPO <sub>4</sub> (KPi) pH 9.7	M	0.5-1.2	0.1
Reservoir solution (1 ml): (NH <sub>4</sub> ) <sub>2</sub> SO <sub>4</sub> pH 9.35 (AMS)	M	1.5-2.0	0.1
LH2 drop size	μl	20	n/a
pH in the drop	-	8.15	n/a
Incubation temperature	°C	20	n/a
Additional salt: NaCl or (KCl, CsCl, CaCl <sub>2</sub> or MgCl <sub>2</sub> )	mM	0-100	10
Amphiphile: Benzamidine-HCl or (1,2,3-Heptanetriol or Spermidine)	% (w/v) or v/v)	0-20	2

Optimisations around the initial conditions were carried out by varying the type of salt at different concentrations and with an addition of small amphiphiles, e.g. 1,2,3-Heptanetriol, Benzamidine or Spermidine (Table 6-2) and by using a commercial additive screen (see Appendix 6). Many of the optimisation trials, unfortunately, also produced amorphous precipitation or phase separation and denatured proteins. The only crystals observed in these trials were from the HL LH2 protein, which crystallised with 0.8 M KPi pH 9.7 with 100 mM CsCl and 2% (w/v) Benzamidine-HCl as the additives in the droplet and 1.8 M AMS pH 9.35 in the reservoir solution (Figure 6-1C). This crystal was however not a single crystal and give very poor diffraction (22 Å) at our home X-ray source.

LL LH2 crystals were obtained with the same initial conditions used for the HL complexes but with a higher concentration of protein, OD<sub>800</sub> = 110 cm<sup>-1</sup>. These were small crystals that had tetragonal shapes (~0.2-0.3 mm, Figure 6-1E) and gave diffraction up to 10 Å resolution at the ESRF. Trials to optimise the initial conditions (Table 6-2) unfortunately only gave amorphous precipitation and phase separation.

In the case of phase separation, the concentration of the precipitant at which these phase separations occur was below that required to precipitate the protein. Under these conditions the LH2 complexes denature in the oily

detergent phase (**Figure 6-1G**). In the case of amorphous precipitation, the concentration of the precipitant is too high and the protein precipitates too quickly (**Figure 6-1H**). The most challenging problem of using the ‘standard’ *Rps. acidophila* conditions for the LH2 from *Rps. palustris* was the irreproducibility of the shape and size of the crystals shown in **Figure 6-1**. Very often, even, successful initial crystallisation conditions did not give crystals in subsequent attempts.

Therefore commercial screens, i.e. MemSys and MemStr from Molecular Dimensions (**Appendix 3 and 4**), were tried. These screens consist of a targeted sparse matrix set of 1 ml x 96 conditions allowing the pH range, precipitants and salts used in membrane protein crystallisation to be screened with the detergent-containing protein drop. These screens produced promising hits with crystallisation conditions containing polyethylene glycol (PEG) 400 (**Figure 6-1D and F**). The crystals from these conditions diffracted in our home X-ray system up to 15 Å and 9 Å for HL and LL LH2, respectively.

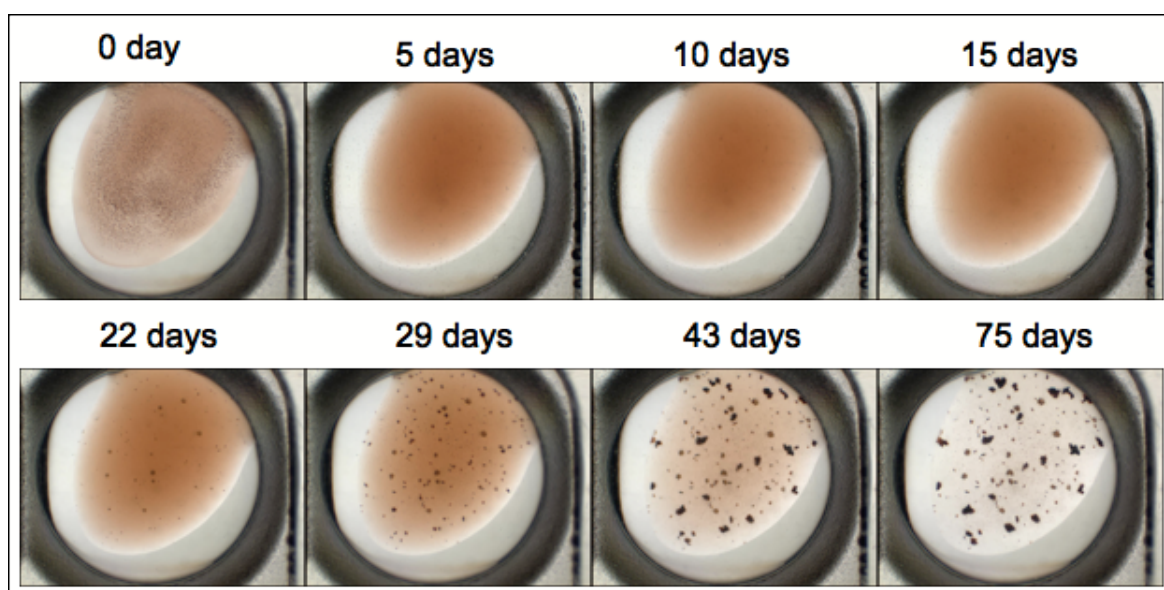


**Figure 6-2** Monitoring the crystallisation process using a visualisation robot. In this example, the HL LH2 complex from *Rps. palustris* was crystallised using a condition from the MemGold screen containing 0.1 M Tris-HCl pH9.5, 0.1 M NaCl, 0.1 M MgCl<sub>2</sub> and 30% PEG 400. The reservoir volume was 50 µl, while the sample drop size was 1 µl (0.5 µl LH2 protein:0.5 µl precipitant). Temperature for the crystal growth was 20°C. ([SEE AVAILABLE MOVIE](#))

In order to search more comprehensively, different commercial screens, i.e. MemGold, PEG/ION screen and JCSG screen (Appendix 5, 7 and 8), were tried. All these screens are optimised sparse-matrix polyethylene glycol (PEG)-based screens. Each screen contains crystallisation conditions with different PEGs, pH, salts and additives. In trying these screens, the crystallisation robots (Hamilton liquid dispensing robot and Cartesian Honeybee 8+1 nanodrop robot) were used to speed up the tedious process of screening many conditions for crystallisation. These robots are able to accurately dispense small volume, e.g. 0.5  $\mu\text{l}$ , and so allow many more conditions to be tested with the same amount of protein. In these screens, micro-crystals were observed from the crystallisation condition containing 0.1 M Tris-HCl pH9.5, 0.1 M NaCl, 0.1 M  $\text{MgCl}_2$ , 30% PEG 400 in the reservoir (this solution was diluted 1:1 with the protein to form the droplet) (Figure 6-2). The time course of the nucleation process and the crystal growth of HL LH2 complexes in this crystallisation condition were followed by crystal plate (Thermo Electron) visualisation robot (Figure 6-2). The nucleation starts on the 22<sup>nd</sup> day and the crystallisation growth is completed within 75 days.

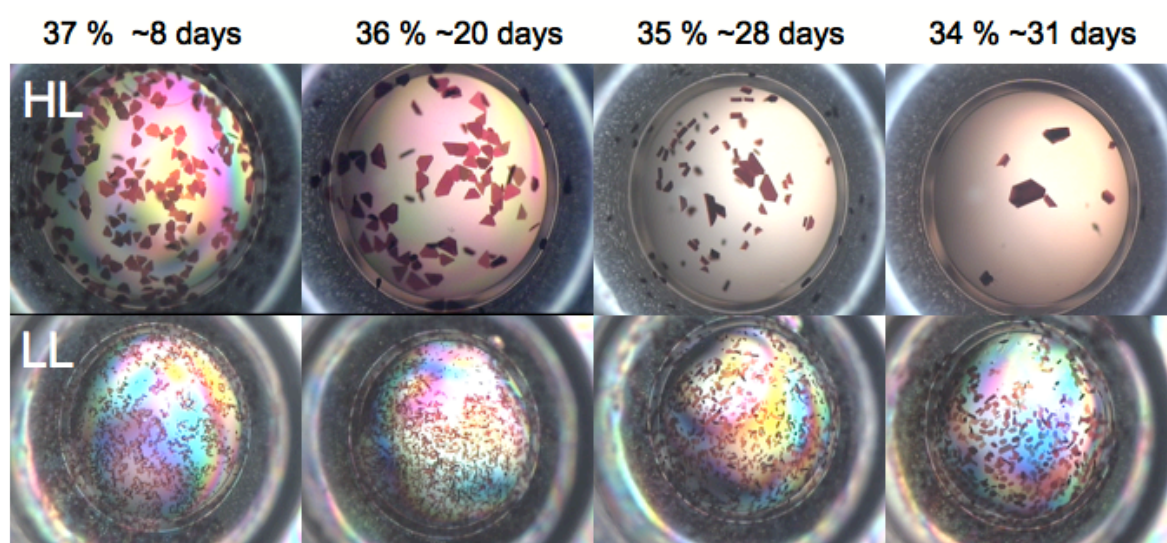
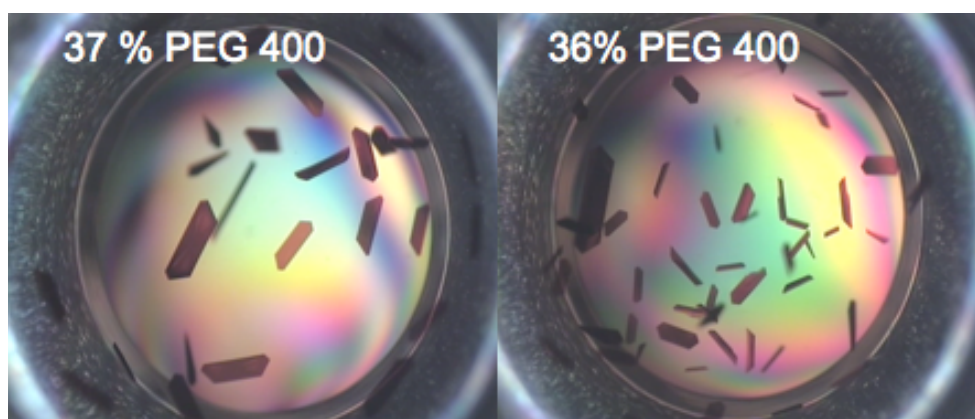


Figure 6-3 HL and LL LH2 crystals of *Rps. palustris* grown in 0.1 M Tris-HCl pH9.5, 0.1 M NaCl, 0.1 M  $\text{MgCl}_2$  containing different PEG 400 concentration. 0.1 % LDAO was as the detergent. Temperature in the incubator was kept constant at 10°C.

Attempts to improve the size and quality of these crystals were then made by varying the concentration of PEG 400 (Figure 6-3). Furthermore, the crystallisation plates were incubated at lower temperature (10°C) in order to

speed up the nucleation process. **Figure 6-3** shows that the HL LH2 crystals can be grown systematically and reproducibly under these conditions. The crystals grew larger and thicker as the concentration of PEG 400 decreased, but longer nucleation times were needed. The size of the HL LH2 crystals could be enhanced to about 0.2×0.4 mm large with 35 % PEG 400 in the reservoir and even more (about 0.4×0.6 mm) with 34% PEG 400 in the reservoir. The HL LH2 crystals grown with 35% PEG 400 at 10°C gave the best diffraction to 5.5 Å at the synchrotron beam (ESRF). In the case of LL LH2 complexes, the crystals were also obtained in the same systematic manner as described above for the HL LH2. However, the LL LH2 crystals grown at 10°C were very small and thin (**Figure 6-4**). Larger LL LH2 crystals were successfully grown by increasing the incubation temperature to 19° C (**Figure 6-4**). However, longer times (~45 days for 37% PEG 400 in the reservoir) were needed in order to complete the growth of the crystals at this temperature. The crystals that grew with 37% PEG 400 in the reservoir gave the best diffraction, up to 6 Å resolution at Glasgow University X-ray Diffractometer and to 4.5 Å at the synchrotron (Diamond Light Source, Oxford, UK). There are also crystals observed from the MemGold crystallisation condition containing 20 mM glycine pH 10, 33% PEG 1000 and 50 mM NaCl in the reservoir. Further attempts to optimise the diffraction quality of these crystals under this particular condition were carried out using the 48 additives screen (Hampton Research Ltd.) as well as using different detergents, e.g.  $\beta$ -octyl-glucopyranoside ( $\beta$ -OG) or dodecyl- $\beta$ -D-maltoside (DDM). So far unfortunately no improved resolution has been obtained.



**Figure 6-4** LL LH2 crystals of *Rps. palustris* grown in 0.1 M Tris-HCl pH9.5, 0.1 M NaCl, 0.1 M MgCl<sub>2</sub> containing different PEG 400 concentration. 0.1 % LDAO was used as detergent. Temperature in the incubator was kept constant at 19°C.

In order to be sure that the LH2 complexes in the crystals were still fully native, the room temperature absorption spectra of re-dissolved HL and LL LH2 crystals (**Figure 6-5**) were recorded. A single large crystal from the condition that produced the best diffracting LH2 crystals was dissolved in 20 mM Tris-HCL pH 8.0 containing 0.1% LDAO and its absorption spectrum was recorded. **Figure 6-5** shows that the absorption spectrum of B800-850 HL LH2 complexes from a re-dissolved crystal is identical to the absorption spectrum of the purified B800-850 HL LH2 complexes shown in **Figure 3-6A** (see **Chapter 3**). The absorption spectrum of a dissolved LL LH2 crystal (**Figure 6-5**) was also identical to its absorption spectrum prior to crystallisation (**Figure 3-6A**).

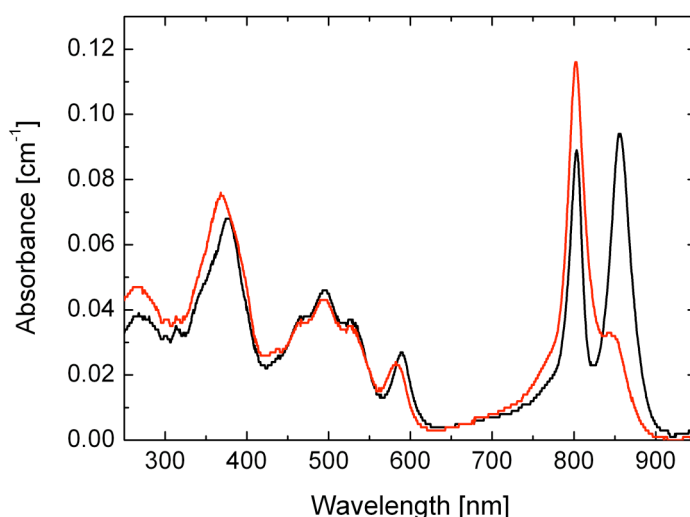


**Figure 6-5** RT absorption spectra of a dissolved single crystal of HL (35% PEG 400, black line) and LL (37% PEG 400, red line) LH2.

## 6.2 Low resolution model structure

### 6.2.1 HL LH2 complex

Promising 0.2×0.4 mm large HL LH2 crystals were obtained using 0.1 M Tris-HCL pH 9.5, 35% PEG 400, 0.1 M NaCl and 0.1 M MgCl<sub>2</sub> in the reservoir. Loop-mounted crystals were flash-cooled to 100K. Since 35% PEG 400 is a cryoprotectant, the crystals could be directly taken from the crystallisation well. Upon exposure at beamline ID14-4 at the European Synchrotron Radiation

Facility (ESRF), Grenoble, France, this crystal diffracted X-rays to beyond resolution of 5.5 Å. A full 360° data set was collected using the oscillation method and Q315r ADSC CCD X-ray detector. Intensity data were processed by the data processing program d\*TREK (Pflugrath, 1999). In the first stage called the indexing, the program identifies the cell dimensions and the symmetry of the crystal lattice. In the next stage, the program performs an integration of the intensities detected in individual pixels of the CCD image. In the final stage, scaling of data between images and merging of intensities - by averaging intensities of multiply measured reflections and their symmetry related equivalents - is performed.

Summary of data indexing and processing statistics calculated by d\*TREK program is presented in **Table 6-3**.

**Table 6-3 Summary of data-processing statistics for a HL LH2 crystal**

Space group	P 2 <sub>1</sub>
Unit cell dimension	
a/ b/ c (Å)	94.62/ 124.28/ 95.07
$\alpha/ \beta/ \gamma$ (°)	90.00 / 111.20/ 90.00
Resolution range (Å)	39.13-6.30 (6.52-6.30)
Total number of reflections	24299
Number of unique reflections	4457
Average redundancy	5.45 (5.76)
% Completeness	99.2 (100.0)
R <sub>merge</sub>	0.057 (0.400)
Output signal to noise ratio $\langle I/\sigma I \rangle$	14.4 (1.7)

**Note: Values in parenthesis are for the last resolution shell.**

**Table 6-3** summary data processing statistics for these HL LH2 crystals. The completeness of the data set was good and the R<sub>merge</sub> was satisfactory. Unfortunately, the diffraction was anisotropic, i.e. the diffraction limits were different in different spatial directions. As a result of this a satisfactory merging

of diffraction data was only obtained to resolution 6.3 Å in the case of the crystal with the  $P2_1$  space-group. Diffraction data provide both the intensities of the spots and their positions. However, in order to use this information to calculate an electron density map the phases must be determined. Phases can be deduced by various methods. In this case the molecular replacement (MR) method has been used. In the MR method, a protein model, called a search model, that has high homology in sequence and folding to the unknown structure is needed. This model is oriented and positioned within the asymmetric unit of the crystal cell to achieve highest correlation between the Patterson function calculated for the model and the Patterson function of the experimental data. The Patterson function is a Fourier synthesis that uses the indices and the square of the structure factor amplitude, i.e. intensities of each diffracted beam. Subsequently the packing of this protein model within the crystal lattice was examined. If this packing is satisfactory then the phases produced by the model (in the correct orientation and position) can be used with the amplitudes from the diffraction pattern of the unknown structure to generate an initial electron density map. The program PHASER (McCoy *et al.*, 2007, McCoy *et al.*, 2005) was used for phasing of the HL LH2 diffraction data. Search models consisting of the structure of the whole ring of the B800-850 LH2s from both *Rps. acidophila* 10050 (McDermott *et al.*, 1995) and *Phs. molischianum* (Koepke *et al.*, 1996) were tested. In these tests, the models were stripped of the surface solvent molecules before being used to obtain a MR solution. The whole LH2 ring was assumed to be present in the asymmetric unit based on the assumption of similar content of solvent as it was found for the *Rps. acidophila* crystals. The PHASER solutions were tested by rigid-body refinement with the use of the program REFMAC (Murshudov *et al.*, 1997). The MR solution figures of merit and the refinement R factors (REFMAC) for the crystal data indicate much more satisfactory agreement for the *acidophila* model compared to that with the *molischianum* model (see Appendix for details). For example the electron density maps generated using the *molischianum* model do not reproduce as satisfactory density for the Bchl *a* pigments as with the *acidophila* model. The limited resolution of the diffraction data, however, does not allow for detailed modelling of the unknown structure.

**Figure 6-6** shows an overlay of the electron density map generated from the HL LH2 data using the *acidophila* model. The electron density is shown in red. Looking down the long axis of the molecule (**Figure 6-6A**) it is clear that the electron density covers  $\alpha$ - and  $\beta$ -helices rather well. This is confirmed in the side view where it can be again seen that the electron density corresponding these helices is quite good (**Figure 6-6B**). There is also electron density, seen as a belt between the  $\alpha$ - and  $\beta$ -helices, that can accommodate the bacteriochlorin rings of the strong coupled Bchl *a*s (**Figure 6-6B**). This MR solution also produces clear electron density for the bacteriochlorin rings of the monomeric Bchl *a* molecules (**Figure 6-6A**). This suggests that the HL LH2 complexes from *Rps. palustris* are structurally very similar to the LH2 complexes from *Rps. acidophila* 10050. It must be borne in mind that at this low resolution these conclusions are still tentative.

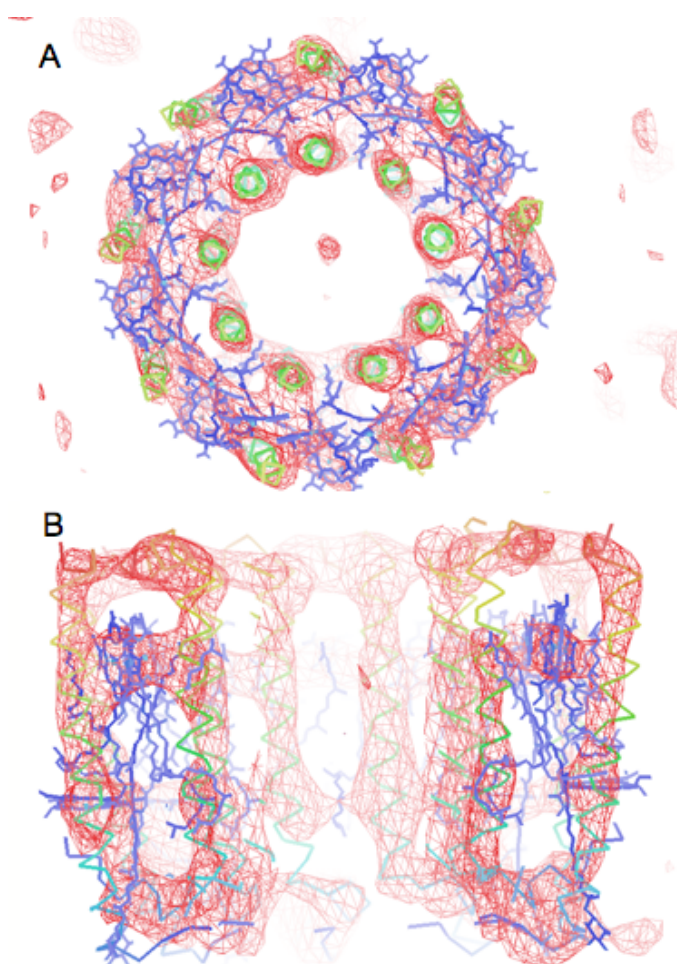


**Figure 6-6** Axial view (A) and side view (B) of the low resolution (6.5 Å) electron density map (at 1.5 sigma) of HL LH2 complex *Rps. palustris* generated by molecular replacement solution using B800-850 LH2 complex from *Rps. acidophila* 10050 as a model for the HL LH2 P2<sub>1</sub> crystal. Viewed by Coot Program (Emsley *et al.*, 2004).

### 6.2.2 LL LH2 complex

A LL LH2 crystal, obtained from the crystallisation solution containing precipitant 37% PEG 400, salts 0.1M NaCl and 0.1M MgCl<sub>2</sub>, and buffer 0.1M Tris-HCl pH 9.5 in the reservoir, produced diffraction spots up to 5 Å resolution at the synchrotron beamline I04 of the Diamond Light Source, Oxford, UK. Recently, another LL LH2 crystal, obtained from different crystallisation conditions (a solution containing precipitant 33% PEG 1000, salt 50 mM NaCl and buffer 50 mM glycine pH 10 in the reservoir) was found to diffract to resolution beyond 4.65 Å at the beamline ID23-1 of the European Synchrotron Radiation Facility, Grenoble, France. Full data sets were collected for each crystal. The first crystal belonged to space-group C2, while the second one belonged to space-group P2<sub>1</sub>. In each case the completeness of the data and the value of R<sub>merge</sub> was satisfactory. A summary of data processing from LL LH2 crystals is listed in Table 6-4.

**Table 6-4 Summary of data-processing statistics for the LL LH2 crystals**

Space group (symmetry)	C 2	P 2 <sub>1</sub>
Unit cell dimension		
a/ b/ c (Å)	157.78/ 114.00/ 146.79	98.37/ 129.67/ 98.37
$\alpha$ / $\beta$ / $\gamma$ (°)	90.00 /114.58/ 90.00	90/ 110.12/ 90.00
Resolution range (Å)	44.71-6.50 (6.73-6.50)	42.53-6.20 (6.42-6.20)
Total number of reflections	23297	31357
Number of unique reflections	4690	5257
Average redundancy	4.97 (5.33)	5.96 (6.22)
% Completeness	98.6 (100.0)	98.5 (99.8)
R <sub>merge</sub>	0.046 (0.479)	0.057 (0.558)
Output signal to noise ratio $\langle I/\sigma I \rangle$	15.1 (1.9)	11.1 (2.0)

**Note:** Values in () are for the last resolution shell.

Unfortunately as in the case of the HL LH2 crystals, the diffraction from LL LH2 crystals was also anisotropic. The crystal with C2 symmetry gave diffraction in the range of 5 to 6.5 Å, while diffraction of the crystal with symmetry P2<sub>1</sub> was in the range of 5.7 to 6.0 Å. Special anisotropic scaling and ellipsoidal truncation with the use of the Diffraction Anisotropic Server (Strong *et al.*, 2006) was applied to both data sets in an attempt to correct for these anisotropic effects.

Again MR was used to try to obtain a structure solution. The structures of the LH2 from *Rps. acidophila* 10050 and from *Phs. molischianum* were again used as search models. Both search models gave possible solutions. At this low resolution it is problematic to determine which of these two solutions is the correct one. The MR solution figures of merit and the refinement R factors (REFMAC) of the structural solutions for LL LH2 crystal data show much better agreement with the *acidophila* model compared to with the *molischianum* model (see Appendix for details). Both models are able to give some electron density that corresponds to the  $\alpha\beta$ -helices (Figure 6-7).

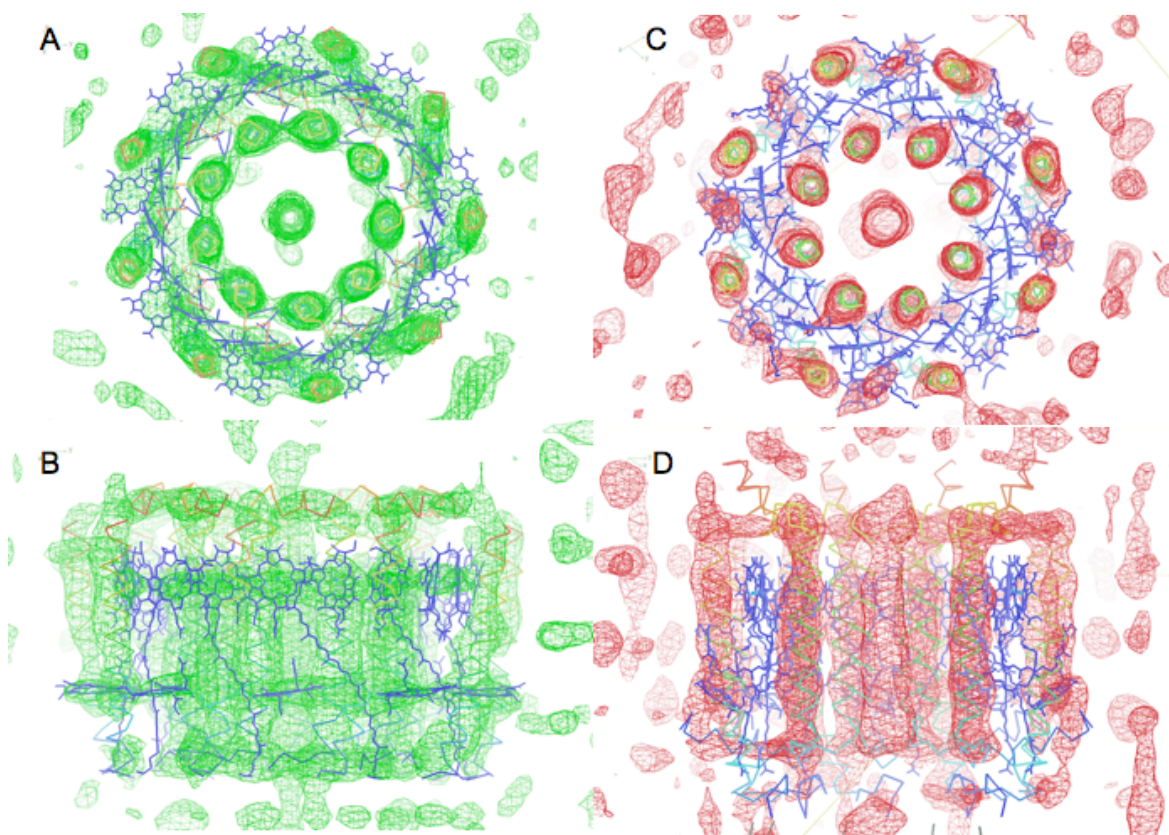


**Figure 6-7** Low resolution (6.7 Å) electron density map (at 1.5 sigma) of LL LH2 complex *Rps. palustris* generated by molecular replacement solution using model from B800-850 LH2 complex from *Rps. acidophila* 10050 (A and B) and from *Phs. molischianum* (C and D). Image generated using the Coot Program (Emsley *et al.*, 2004).

The electron density for the  $\beta$ -helices calculated using the *acidophila* model is more complete than that calculated using the *molischanum* model. The structural solution using the *molischanum* model does not reveal any electron density that would correspond to the bacteriochlorin rings of the tightly coupled Bchl *a* molecules. In the corresponding region of the structure calculated from the *acidophila* model there is a ring of electron density for these bacteriochlorin rings (Figure 6-7B). Moreover, the solution using the *acidophila* model also produces electron density for the bacteriochlorin rings of the monomeric Bchl *as* (Figure 6-7B). The electron density for these bacteriochlorins is shown more clearly in the detailed view shown in Figure 6-8. At this point these MR solutions suggest that the most probable structure for the LL LH2 complex from *Rps. palustris* is a nonamer. Higher resolution is now required in order to test this hypothesis and to allow the full details of the structure to be determined.

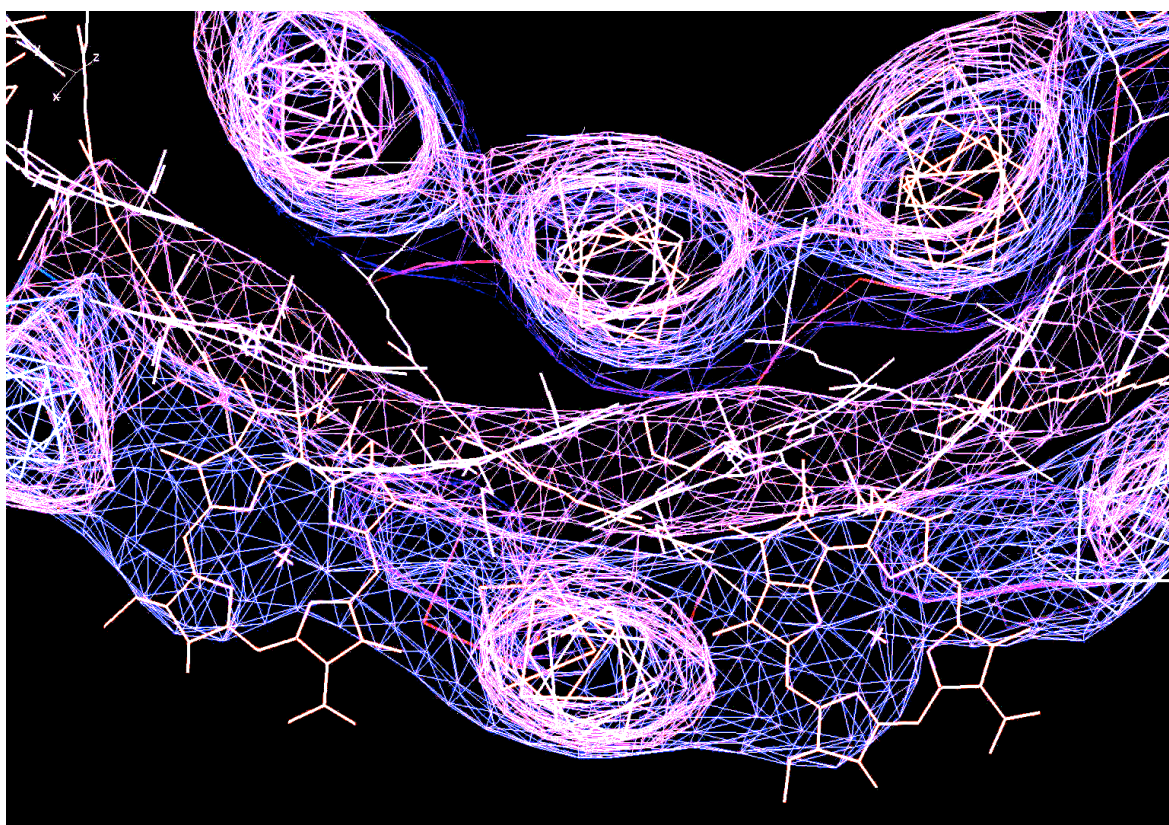


Figure 6-8 Detailed view of the low resolution (6.7 Å) electron density map (at 1.5 sigma) of LL LH2 complex *Rps. palustris*, generated by molecular replacement solution using model from B800-850 LH2 complex from *Rps. acidophila* 10050, shows the occupancy of the electron density in  $\alpha\beta$ -polypeptides as well as the B800 and B850 Bchl *a* molecules.

## 6.3 Conclusions

The B800-850 HL and B800-low-850 LL LH2 complexes from *Rps. palustris* have been crystallised by the sitting-drop vapor-diffusion method. A promising monoclinic (P21) HL LH2 crystal, obtained from 0.1 M Tris-HCl pH 9.5, 35% PEG 400, 0.1 M NaCl and 0.1 M MgCl<sub>2</sub> in the reservoir, diffracted to beyond 5.5 Å resolution. The LL LH2 complexes were also crystallised using the same method. A promising crystal was obtained from the condition containing 0.1 M Tris-HCl pH 9.5, 37% PEG 400, 0.1 M NaCl and 0.1 M MgCl<sub>2</sub> in the reservoir. This monoclinic (C21) crystal diffracted to beyond 4.7 Å resolution. Promising LL crystals were also obtained from the condition containing 50 mM glycine pH 10, 33% PEG 1000 and 50 mM NaCl in the reservoir. However, because these crystals were strongly anisotropic the diffraction data was only useful at significantly lower resolution. In both cases MR solutions suggest that these LH2 complexes are nonamers. At this point these results conflict with the AFM pictures seen in (Scheuring *et al.*, 2006).

MR solutions on data sets at such low resolution must always be treated with caution. Further work is now required to produce crystals that are both better ordered and more isotropic in their diffraction properties. It will very interesting when it is possible to see real high resolution structures of both HL and LL LH2 complexes from *Rps. palustris* and be able to understand structural bases the different spectroscopic properties.

---

## 7 Summary and outlook

---

Photosynthesis provides an example of a natural process that has been optimised over billions of years of evolution to harness the energy of sunlight efficiently and safely and finally to use it to produce a carbon-based fuel. The light harvesting antenna systems are very important not only for capturing the energy of sunlight but also for funnelling that energy downhill to the RC. A molecular understanding of these energy transfer processes will be very helpful for providing a “natural blueprint” for use in the construction of an artificial leaf design to use solar energy to produce fuels.

Some purple bacteria species, such as *Rps. palustris* strain 2.1.6, produce LH antennas with unusual absorption spectra when they are grown under low light intensities. Under these conditions, *Rps. palustris* strain 2.1.6 replaces the B800-850 LH2 complexes with the B800-low-850 LH2 complex. This ability to adapt is often related to the presence of the multiple LH2  $\alpha\beta$ -polypeptides, which are encoded by multiple gene pairs.

In this PhD work, pure stable LH2 complexes from *Rps palustris* strain 2.1.6 grown at different light intensities have been successfully isolated. The polypeptide composition of the HL and LL LH2 complexes has been characterised by mass spectroscopy. Both the high- (HL) and low-light (LL) LH2 complexes contain multiple types of  $\alpha$ -(PucA) and  $\beta$ -(PucB) polypeptides, i.e. the HL LH2 complex contains the PucA<sub>a</sub>, PucA<sub>b</sub>, PucB<sub>a</sub> and PucB<sub>e</sub> polypeptides, while the LL LH2 complex contains the PucA<sub>a</sub>, PucA<sub>d</sub>, PucB<sub>a</sub>, PucB<sub>d</sub> and PucB<sub>e</sub> polypeptides. When this thesis work was started, it was not clear whether the LH2 complexes consisted of rings where each ring has a mixture of apoprotein types or whether the preparation contains a mixture where each individual ring in the mixture has a homogeneous apoprotein composition, but where different rings have different compositions.

Various spectroscopic methods, i.e. absorption, circular dichroism, resonance Raman and single-molecule spectroscopy, have been used to characterise the

spectroscopic properties of both types of LH2 complexes. The question of whether rings with a heterogeneous apoprotein composition do exist were tested with the use of the SMS. In the case of individual LL LH2 complexes the single-molecule spectra could only be satisfactorily explained by assuming the presence of both B820-like energies and B850-like site energies within single rings.

The ET from the B800 to the B850 ring and exciton relaxation in the B850 ring for both HL and LL LH2 complexes were studied by femtosecond transient absorption spectroscopy. All the ET data could be explained with a simple kinetic model. One important feature of this model for the LL LH2 complexes was the presence of a high-energy exciton state in the region of 820 nm. This finding nicely confirms the conclusion of the single-molecule studies.

Attempts to crystallise the HL and LL LH2 complexes from *Rps. palustris* resulted in promising crystals, but with rather low-resolution diffraction. In both cases the best molecular replacement (MR) solutions suggest that these complexes are nonameric. However, definite conclusions must await better quality crystals. Hopefully high resolution structures will provide an explanation of why the data shown in this thesis do not agree with the AFM results of Scheuring et al. (Scheuring *et al.*, 2006).

As well as the need in the future to produce better crystals it will be interesting to try to characterise more systematically the types of LH2 complexes that are present when cells of *Rps. palustris* are grown at intermediate light intensities. Spectroscopic data presented in this thesis clearly show that there must be more than two types of LH2 present in these intermediate cases.

---

## 8 Appendices

---

### 8.1 Composition growth media

#### 8.1.1 *C-succinate media (Bose, 1969) per litre*

Concentrated Base	20 ml
1M K <sub>2</sub> HPO <sub>4</sub>	10 ml
1M KH <sub>2</sub> PO <sub>4</sub>	10 ml
10% (NH <sub>4</sub> ) <sub>2</sub> SO <sub>4</sub>	5 ml
1M Na or K succinate (pH 6.8)	10 ml
Growth Factors	1ml
Casamino Acids	1 g

#### 8.1.2 *Concentrated base per 5 litre*

Nitritotriacetic Acid (C <sub>6</sub> H <sub>9</sub> NO <sub>6</sub> )	50 g
MgSO <sub>4</sub> ·7H <sub>2</sub> O	25 g
CaCl <sub>2</sub> ·2H <sub>2</sub> O	17 g
(NH <sub>4</sub> ) <sub>6</sub> Mo <sub>7</sub> O <sub>24</sub> ·4H <sub>2</sub> O	0.0462 g
FeSO <sub>4</sub> ·7H <sub>2</sub> O	0.495 g
Thiamine hydrochloride	0.125 g
Biotin	0.0025 g
Nicotinic acid	0.25 g
Metos 44	250 ml
Adjust the final pH to 6.8 with 5N KOH	

#### 8.1.3 *Metos 44 per litre*

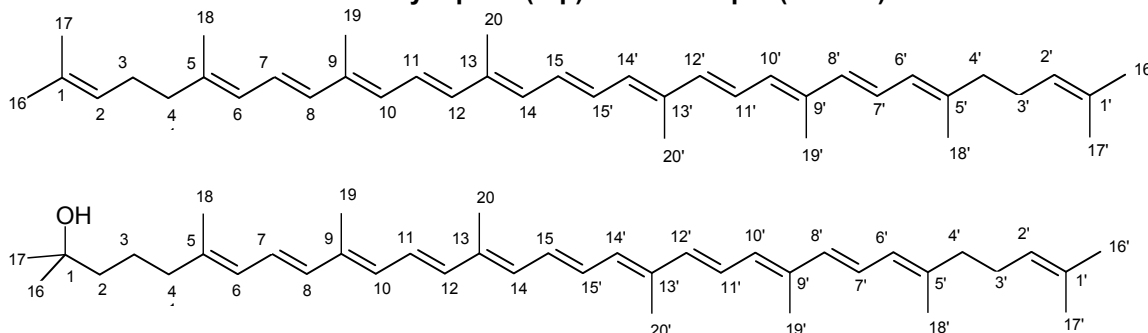
EDTA	2.5 g
Zn(II)SO <sub>4</sub>	10.95 g
Mn(II)SO <sub>4</sub> ·4H <sub>2</sub> O	1.54 g
Cu(II)SO <sub>4</sub> ·5H <sub>2</sub> O	0.392 g
CoNO <sub>3</sub> ·6H <sub>2</sub> O	0.248 g
FeSO <sub>4</sub> ·7H <sub>2</sub> O	5.5 g
Na <sub>2</sub> B <sub>4</sub> O <sub>7</sub> ·10H <sub>2</sub> O	0.177 g
add 20 drops of conc. H <sub>2</sub> SO <sub>4</sub>	

**8.1.4 Growth factor per 100 ml**

Biotin	0.002 g
NaHCO <sub>3</sub>	0.05 g
Then add water to dissolved	
Nicotinic Acid	0.1 g
Aneurine HCl	0.05 g
NH <sub>2</sub> .C <sub>6</sub> H <sub>4</sub> COOH (4-aminobenzoic acid)	0.1 g

## 8.2 Identification of major carotenoid isolated from HL and LL LH2 *Rps. palustris* by $^1\text{H-NMR}$

The Chemical Structure of the Lycopene (top) and Rhodopin (bottom).



$^1\text{H}$  chemical shifts ( $\delta$  in ppm) in chloroform solution for carotenoid (peak #1 and #5) isolated from *Rps. palustris*.

Peak #1 Lycopene				Peak #5 Rhodopin			
Measurement		Reference		Measurement		Reference	
Proton Atom	$\delta$ (ppm)	Proton Atom	$\delta$ (ppm)	Proton Atom	$\delta$ (ppm)	Proton Atom	$\delta$ (ppm)
2-H	5.11 <sup>f</sup>	2-H	5.11	2-H	1.435	2-H	1.4-1.5
3-H	2.118 <sup>a</sup>	3-H	2.11	3-H	2.118 <sup>a</sup>	3-H	-
4-H	2.118 <sup>a</sup>	4-H	2.11	4-H	2.118 <sup>a</sup>	4-H	2.11
6-H	5.96(d)	6-H	5.95	6-H	5.96(d)	6-H	5.96
7-H	6.50(dd)	7-H	6.49	7-H	6.48(dd)	7-H	6.49
8-H	5.25(d)	8-H	6.25	8-H	6.25(d)	8-H	6.25
10-H	6.19(d)	10-H	6.19	10-H	6.19(d)	10-H	-
11-H	6.63(dd)	11-H	6.64	11-H	6.63(dd)	11-H	-
12-H	6.36(d)	12-H	6.35	12-H	6.36(d)	12-H	-
14-H	6.24(m)	14-H	6.23	14-H	6.24(m)	14-H	5.88
15-H	6.63(m)	15-H	6.63	15-H	6.65(m)	15-H	6.32
16-CH <sub>3</sub>	1.691 <sup>b</sup>	16-CH <sub>3</sub>	1.62	16-CH <sub>3</sub>	1.219	16-CH <sub>3</sub>	1.22
17-CH <sub>3</sub>	1.617 <sup>c</sup>	17-CH <sub>3</sub>	1.69	17-CH <sub>3</sub>	1.120	17-CH <sub>3</sub>	1.22
18-CH <sub>3</sub>	1.822 <sup>d</sup>	18-CH <sub>3</sub>	1.82	18-CH <sub>3</sub>	1.821 <sup>b</sup>	18-CH <sub>3</sub>	1.81
19-CH <sub>3</sub>	1.972 <sup>e</sup>	19-CH <sub>3</sub>	1.97	19-CH <sub>3</sub>	1.972 <sup>c</sup>	19-CH <sub>3</sub>	1.97
20-CH <sub>3</sub>	1.972 <sup>e</sup>	20-CH <sub>3</sub>	1.97	20-CH <sub>3</sub>	1.972 <sup>c</sup>	20-CH <sub>3</sub>	-

2 <sup>1</sup> -H	5.11 <sup>f</sup>	2 <sup>1</sup> -H	-	2 <sup>1</sup> -H	5.11	2 <sup>1</sup> -H	1.4- 1.5
3 <sup>1</sup> -H	2.118 <sup>a</sup>	3 <sup>1</sup> -H	2.11	3 <sup>1</sup> -H	2.118 <sup>a</sup>	3 <sup>1</sup> -H	-
4 <sup>1</sup> -H	2.118 <sup>a</sup>	4 <sup>1</sup> -H	2.11	4 <sup>1</sup> -H	2.118 <sup>a</sup>	4 <sup>1</sup> -H	2.11
6 <sup>1</sup> -H	5.96(d)	6 <sup>1</sup> -H	5.95	6 <sup>1</sup> -H	5.96(d)	6 <sup>1</sup> -H	5.96
7 <sup>1</sup> -H	6.50(dd)	7 <sup>1</sup> -H	6.49	7 <sup>1</sup> -H	6.48(dd)	7 <sup>1</sup> -H	6.49
8 <sup>1</sup> -H	5.25(d)	8 <sup>1</sup> -H	6.25	8 <sup>1</sup> -H	6.25(d)	8 <sup>1</sup> -H	6.25
10 <sup>1</sup> -H	6.19(d)	10 <sup>1</sup> -H	6.19	10 <sup>1</sup> -H	6.19(d)	10 <sup>1</sup> -H	-
11 <sup>1</sup> -H	6.63(dd)	11 <sup>1</sup> -H	6.64	11 <sup>1</sup> -H	6.63(dd)	11 <sup>1</sup> -H	-
12 <sup>1</sup> -H	6.36(d)	12 <sup>1</sup> -H	6.35	12 <sup>1</sup> -H	6.36(d)	12 <sup>1</sup> -H	-
14 <sup>1</sup> -H	6.24(m)	14 <sup>1</sup> -H	6.23	14 <sup>1</sup> -H	6.24(m)	14 <sup>1</sup> -H	5.88
15 <sup>1</sup> -H	6.63(m)	15 <sup>1</sup> -H	6.63	15 <sup>1</sup> -H	6.65(m)	15 <sup>1</sup> -H	6.32
16 <sup>1</sup> -CH <sub>3</sub>	1.691 <sup>b</sup>	16 <sup>1</sup> -CH <sub>3</sub>	1.62	16 <sup>1</sup> -CH <sub>3</sub>	1.616	16 <sup>1</sup> -CH <sub>3</sub>	1.22
17 <sup>1</sup> -CH <sub>3</sub>	1.617 <sup>c</sup>	17 <sup>1</sup> -CH <sub>3</sub>	1.69	17 <sup>1</sup> -CH <sub>3</sub>	1.691	17 <sup>1</sup> -CH <sub>3</sub>	1.22
18 <sup>1</sup> -CH <sub>3</sub>	1.822 <sup>d</sup>	18 <sup>1</sup> -CH <sub>3</sub>	1.82	18 <sup>1</sup> -CH <sub>3</sub>	1.821 <sup>b</sup>	18 <sup>1</sup> -CH <sub>3</sub>	1.81
19 <sup>1</sup> -CH <sub>3</sub>	1.972 <sup>e</sup>	19 <sup>1</sup> -CH <sub>3</sub>	1.97	19 <sup>1</sup> -CH <sub>3</sub>	1.972 <sup>c</sup>	19 <sup>1</sup> -CH <sub>3</sub>	1.97
20 <sup>1</sup> -CH <sub>3</sub>	1.972 <sup>e</sup>	20 <sup>1</sup> -CH <sub>3</sub>	1.97	20 <sup>1</sup> -CH <sub>3</sub>	1.972 <sup>c</sup>	20 <sup>1</sup> -CH <sub>3</sub>	-

<sup>a,b,c,d,e,f</sup> Overlapping each other; d, doublet; dd, doublet doublet; m, multiplet

Reference: A. Young and G. Britton, 1993, Carotenoids in Photosynthesis, Chapman & Hall, London

### 8.3 MemStart screen (Molecular Dimension, UK)

Tube #	Salt	Buffer	pH	Precipitant
1	None	0.1 M sodium acetate	4.6	2 M ammonium sulfate
2	None	0.1 M ADA	6.5	1 M ammonium sulfate
3	None	None	-	2 M ammonium sulfate
4	None	0.1 M Tris	8.5	2 M ammonium sulfate
5	None	0.1 M Na HEPES	7.5	1.5 M lithium sulfate
6	None	0.1 M sodium acetate	4.6	1 M magnesium sulfate
7	None	0.1 M tri-sodium citrate	5.6	1 M magnesium sulfate
8	0.1 M lithium sulfate	0.1 M ADA	6.5	1 M magnesium sulfate
9	None	0.1 M ammonium dihydrogen phosphate	6.5	None
10	0.1 M ammonium sulfate	0.5 M di-potassium hydrogen phosphate/ 0.5 M di-sodium hydrogen phosphate	7.5	None
11	0.1 M lithium sulfate	0.1 M sodium acetate	4.6	1 M ammonium dihydrogen phosphate
12	None	0.1 M tri-sodium citrate	5.6	1 M ammonium dihydrogen phosphate
13	None	0.1 M Tris	8.5	2 M ammonium dihydrogen phosphate
14	None	None	4.6	2 M sodium formate
15	None	None	-	4 M sodium formate
16	None	0.1 M MES	6.5	1.4 M sodium acetate
17	None	0.1 M Na HEPES	7.5	1.4 M tri-sodium citrate
18	None	0.1 M Na HEPES	7.5	1 M potassium sodium tartrate
19	None	0.1 M Na HEPES	7.5	2 % v/v PEG 200/ 2 M ammonium sulfate
20	0.1 M magnesium chloride	0.1 M sodium acetate	4.6	30 % v/v PEG 400
21	0.1 M sodium chloride	0.1 M tri-sodium citrate	5.6	30 % v/v PEG 400
22	0.1 M lithium sulfate	0.1 M tri-sodium citrate	5.6	30 % v/v PEG 400
23	0.3 M lithium sulfate	0.1 M ADA	6.5	30 % v/v PEG 400
24	0.1 M magnesium chloride	0.1 M Na HEPES	7.5	30 % v/v PEG 400
25	0.1 M ammonium sulfate	0.1 M Na HEPES	7.5	30 % v/v PEG 400
26	0.2 M tri-sodium citrate	0.1 M Tris	8.5	30 % v/v PEG 400
27	0.1 M zinc acetate	0.1 M sodium acetate	4.6	12 % v/v PEG 4K
28	0.2 M ammonium sulfate	0.1 M sodium acetate	4.6	12 % v/v PEG 4K
29	None	0.1 M sodium acetate	4.6	12 % v/v PEG 4K
30	0.1 M lithium sulfate	0.1 M tri-sodium citrate	5.6	12 % v/v PEG 4K
31	0.1 M sodium chloride	0.1 M tri-sodium citrate	5.6	12 % v/v PEG 4K
32	0.1 M lithium sulfate	0.1 M ADA	6.5	12 % v/v PEG 4K
33	0.1 M sodium chloride	0.1 M Na HEPES	7.5	12 % v/v PEG 4K
34	0.1 M ammonium sulfate	0.1 M Na HEPES	7.5	12 % v/v PEG 4K
35	0.2 M magnesium chloride	0.1 M Tris	8.5	12 % v/v PEG 4K
36	0.2 M lithium sulfate hydrate	0.1 M Tris	8.5	12 % v/v PEG 4K
37	0.2 M ammonium sulfate	None	-	12 % v/v PEG 4K
38	0.1 M sodium chloride	0.1 M sodium acetate	4.6	12 % v/v PEG 6K
39	0.1 M magnesium chloride	0.1 M sodium acetate	4.6	12 % v/v PEG 6K
40	0.1 M magnesium chloride	0.1 M ADA	6.5	12 % v/v PEG 6K
41	0.1 M di-ammonium hydrogen phosphate	0.1 M Tris	8.5	12 % v/v PEG 6K
42	1 M lithium sulfate	None	-	2 % w/v PEG 8K
43	0.2 M sodium acetate	0.1 M MES	6.5	10 % w/v PEG 8K
44	0.2 M zinc acetate	0.1 M MES	6.5	10 % w/v PEG 8K
45	0.2 M calcium acetate	0.1 M MES	6.5	10 % w/v PEG 8K
46	None	0.1 M Tris	8.5	10 % w/v PEG 8K
47	0.2 M ammonium sulfate	None	-	10 % w/v PEG 8K
48	0.5 M lithium sulfate	None	-	10 % w/v PEG 8K

**Abbreviations:**

ADA; N-(2-Acetamido)iminodiacetic Acid, HEPES; N-(2-hydroxyethyl)-piperazine-N'-2-ethanesulfonic acid, MES; 2-(N-morpholino)ethanesulfonic acid, MME; Monomethylether, PEG; Polyethylene glycol (4K, 6K and 8K correspond to the molecular weight, in thousands of Daltons, of PEG), Tris; 2-Amino-2-(hydroxymethyl)propane-1,3-diol.

## 8.4 MemSys screen (Molecular Dimension, UK)

Tube #	Salt 1	Salt 2	Buffer	pH	Precipitant
1	None	None	0.1 M Na citrate	5.5	2.5 M ammonium sulfate
2	0.1 M sodium chloride	0.1 M lithium sulfate	0.1 M Na citrate	3.5	30 % v/v PEG 400
3	0.1 M sodium chloride	0.1 M magnesium chloride	0.1 M Na acetate	4.5	30 % v/v PEG 400
4	0.1 M sodium chloride	None	0.1 M Na citrate	5.5	30 % v/v PEG 400
5	0.1 M sodium chloride	0.1 M lithium sulfate	0.1 M Na citrate	6.5	30 % v/v PEG 400
6	0.1 M sodium chloride	0.1 M magnesium chloride	0.1 M Na citrate	5.5	30 % v/v PEG 400
7	None	None	0.1 M MES	6.5	2.5 M ammonium sulfate
8	None	None	0.1 M MES	6.5	30 % v/v PEG 400
9	0.1 M sodium chloride	None	0.1 M MES	6.5	30 % v/v PEG 400
10	0.1 M sodium chloride	0.1 M lithium sulfate	0.1 M MES	6.5	30 % v/v PEG 400
11	0.1 M sodium chloride	0.1 M magnesium chloride	0.1 M MES	6.5	30 % v/v PEG 400
12	None	None	0.1 M MOPS	7.0	2.5 M ammonium sulfate
13	None	None	0.1 M Na HEPES	7.5	30 % v/v PEG 400
14	0.1 M sodium chloride	None	0.1 M MOPS	7.0	30 % v/v PEG 400
15	None	None	0.1 M Na HEPES	7.5	30 % v/v PEG 400
16	0.1 M sodium chloride	None	0.1 M Na HEPES	7.5	30 % v/v PEG 400
17	0.1 M sodium chloride	0.1 M lithium sulfate	0.1 M Na HEPES	7.5	30 % v/v PEG 400
18	0.1 M sodium chloride	0.1 M magnesium chloride	0.1 M Na HEPES	7.5	30 % v/v PEG 400
19	None	None	0.1 M Tris	8.5	1.5 M lithium sulfate
20	0.1 M sodium chloride	None	0.1 M Tris	8.5	30 % v/v PEG 400
21	0.1 M sodium chloride	0.1 M lithium sulfate	0.1 M Tris	8.5	30 % v/v PEG 400
22	0.1 M sodium chloride	0.1 M magnesium chloride	0.1 M Tris	8.5	30 % v/v PEG 400
23	0.1 M sodium chloride	0.1 M lithium sulfate	0.1 M CAPSO	9.5	30 % v/v PEG 400
24	0.1 M sodium chloride	0.1 M magnesium chloride	0.1 M CAPSO	9.5	30 % v/v PEG 400
25	None	None	0.1 M Na citrate	5.5	1.5 M sodium phosphate
26	0.1 M sodium chloride	0.1 M magnesium chloride	0.1 M Na citrate	3.5	12 % w/v PEG 4K
27	0.1 M sodium chloride	0.1 M lithium sulfate	0.1 M Na acetate	4.5	12 % w/v PEG 4K
28	0.1 M sodium chloride	None	0.1 M Na citrate	5.5	12 % w/v PEG 4K
29	0.1 M sodium chloride	0.1 M lithium sulfate	0.1 M Na citrate	5.5	12 % w/v PEG 4K
30	0.1 M sodium chloride	0.1 M magnesium chloride	0.1 M Na citrate	5.5	12 % w/v PEG 4K
31	None	None	0.1 M MES	6.5	1.5 M sodium phosphate
32	None	None	0.1 M MES	6.5	12 % w/v PEG 4K
33	0.1 M sodium chloride	None	0.1 M MES	6.5	12 % w/v PEG 4K
34	0.1 M sodium chloride	0.1 M lithium sulfate	0.1 M MES	6.5	12 % w/v PEG 4K
35	0.1 M sodium chloride	0.1 M magnesium chloride	0.1 M MES	6.5	12 % w/v PEG 4K
36	None	None	0.1 M MOPS	7.0	12 % w/v PEG 4K
37	None	None	0.1 M Na HEPES	7.5	1.5 M potassium phosphate
38	0.1 M sodium chloride	None	0.1 M MOPS	7.0	12 % w/v PEG 4K
39	None	None	0.1 M Na HEPES	7.5	12 % w/v PEG 4K
40	0.1 M sodium chloride	None	0.1 M Na HEPES	7.5	12 % w/v PEG 4K
41	0.1 M sodium chloride	0.1 M lithium sulfate	0.1 M Na HEPES	7.5	12 % w/v PEG 4K
42	0.1 M sodium chloride	0.1 M magnesium chloride	0.1 M Na HEPES	7.5	12 % w/v PEG 4K
43	None	None	0.1 M Tris	8.5	1.5 M potassium phosphate
44	0.1 M sodium chloride	None	0.1 M Tris	8.5	12 % w/v PEG 4K
45	0.1 M sodium chloride	0.1 M lithium sulfate	0.1 M Tris	8.5	12 % w/v PEG 4K
46	0.1 M sodium chloride	0.1 M magnesium chloride	0.1 M Tris	8.5	12 % w/v PEG 4K
47	0.1 M sodium chloride	0.1 M lithium sulfate	0.1 M CAPSO	8.5	12 % w/v PEG 4K
48	0.1 M sodium chloride	0.1 M magnesium chloride	0.1 M CAPSO	8.5	12 % w/v PEG 4K

### Abbreviations:

**CAPSO**; 3-(Cyclohexylamino)-2-hydroxy-1-propanesulfonic Acid Sodium Salt, **Na HEPES**; N-(2-hydroxyethyl)-piperazine- N'-2-ethanesulfonic acid sodium salt, **MES**; 2-(N-morpholino)ethanesulfonic acid, **MOPS**; 3-(N-Morpholino)- propanesulfonic acid, **PEG**; Polyethylene glycol (4K corresponds to the molecular weight, in thousands of Daltons, of PEG), **Tris**; 2-Amino-2-(hydroxymethyl)propane-1,3-diol

## 8.5 MemGold screen (Molecular Dimension, UK)

Tube #	Salt	Buffer	pH	Precipitant
1	None	0.8 M sodium citrate	5.2	2.2 M ammonium sulfate
2	None	0.1 M tris	8.0	1.2 M tri-sodium citrate
3	None	0.015 M tricine	8.5	24 % w/v PEG 4000
4	0.36 M sodium chloride/ 0.1 % w/v sodium azide	0.015 M sodium phosphate	7.0	9.9 % w/v PEG 4000
5	0.3 M sodium chloride	0.01 M tris	8.0	27.5 % w/v PEG 4000
6	None	0.225 M MES/bis-tris	6.6	6.6 % w/v PEG 4000
7	0.1 M ammonium sulfate	0.1 M HEPES	7.5	12.0 % w/v PEG 4000/ 22 % v/v glycerol
8	0.02 M calcium chloride/ 0.01 M magnesium sulfate/ 0.02 M sodium chloride	0.02 M MES	6.5	7.7 % w/v PEG 1500
9	None	0.05 M HEPES	7.5	2.5 M ammonium sulfate
10	None	0.0665 M HEPES	7.5	1.1 M tri-sodium citrate
11	None	0.15 M potassium phosphate	6.5	3.3 M ammonium sulfate
12	0.1 M magnesium acetate	0.1 M sodium citrate	5.8	14 % w/v PEG 5000 MME
13	0.1 M sodium chloride	0.02 M sodium citrate	5.6	11 % w/v PEG 3350
14	0.1 M sodium chloride	0.02 M sodium citrate	5.6	5.5 % w/v PEG 3350
15	0.05 M calcium chloride/ 0.05 M barium chloride	0.1 M tris	8.2	32 % v/v PEG 400
16	0.05 M sodium chloride	0.1 M sodium phosphate	6.2	16 % w/v PEG 4000
17	0.1 M magnesium chloride	0.03 M tris-hydrochloride	8.2	19 % w/v PEG 4000
18	0.2 M sodium chloride	0.025 M HEPES	7.5	13 % w/v PEG 4000
19	None	0.1 M HEPES	7.5	11 % w/v PEG 3350
20	0.1 M sodium chloride	0.02 M KMES	6.7	6.6 % w/v PEG 4000
21	0.1 M potassium chloride	0.02 M tris	7.0	20 % w/v PEG 4000
22	0.05 M magnesium chloride/ 0.1 % w/v sodium azide	0.1 M sodium cacodylate	6.7	6.6 % w/v PEG 3350
23	0.2 M potassium chloride	0.1 M sodium citrate	5.5	37 % v/v pentaerythritol propoxylate (5/4 PO/OH)
24	None	0.1 M tris	8.0	5.5 % w/v PEG 4000
25	0.1 M sodium chloride	0.02 M tris	7.0	7.7 % w/v PEG 4000
26	0.1 M magnesium chloride	0.1 M tris	7.5	22 % v/v PEG 400
27	0.04 M sodium chloride	0.04 M tris	8.0	27 % v/v PEG 350 MME
28	0.05 M sodium chloride/ 0.02 M magnesium chloride	0.1 M sodium citrate	6.0	22 % v/v PEG 400
29	None	0.1 M sodium acetate	5.5	8.8 % w/v PEG 2000 MME
30	None	0.4 M ammonium acetate	8.0	13 % w/v PEG 2000 MME
31	None	0.02 M bis tris	7.0	15 % w/v PEG 2000
32	0.1 M sodium chloride/ 0.1 M magnesium chloride	0.02 M tris	7.5	11 % w/v PEG 1500
33	0.1 M sodium chloride/ 0.1 M magnesium chloride	0.1 M HEPES	8.0	11 % w/v PEG 1500
34	0.2 M sodium acetate/ 0.2 M potassium chloride	0.1 M HEPES	7.0	22 % w/v PEG 3000
35	0.02 M nickel sulfate	0.01 M HEPES	7.0	33% v/v jeffamine-M600
36	0.15 M sodium chloride	0.1 M tris	8.0	13 % w/v PEG 6000
37	0.2 M calcium chloride	0.1 M HEPES	7.5	53 % v/v PEG 400
38	0.05 M magnesium acetate	0.05 M sodium acetate	5.0	28 % v/v PEG 400
39	None	0.05 M HEPES	7.5	22 % v/v PEG 4000
40	0.2 M calcium chloride	0.1 M tris hydrochloride	8.0	44 % v/v PEG 400
41	0.05 M magnesium acetate	0.05 M sodium acetate	5.4	24 % v/v PEG 400
42	0.2 M calcium chloride	0.1 M MES	6.5	26 % v/v PEG 350 MME
43	0.1 M potassium chloride	0.1 M tris	8.5	39 % v/v PEG 400
44	0.05 M magnesium chloride	0.1 M glycine	9.0	22 % v/v PEG 400
45	0.1 M ammonium sulfate	0.1 M glycine	3.8	28 % w/v tri-ethylene glycol
46	0.15 M sodium formate	0.1 M HEPES	7.2	18 % w/v PEG 3500
47	None	0.2 M sodium acetate	6.8	8.8 % w/v PEG 6000
48	0.2 M potassium chloride	0.1 M MES	6.5	18 % w/v PEG 6000
49	0.22 M sodium citrate	0.1 M tris	8.0	35 % v/v PEG 400
50	None	0.1 M sodium acetate	4.5	17 % v/v PEG 400
51	None	0.02 M tris	8.5	1.0 M lithium sulfate/ 1.8 % w/v PEG 8000
52	None	0.02 M tris	7.5	22 % v/v PEG 550 MME
53	0.05 M sodium chloride	0.02 M glycine	10	33 % w/w PEG 1000
54	0.2 M magnesium chloride	0.1 M tris	8.5	25 % w/v PEG 4000
55	0.2 M magnesium chloride	0.1 M sodium cacodylate	6.5	31 % w/v PEG 2000

56	None	0.64 M sodium acetate	4.6	18 % v/v PEG 3350
57	0.1 M sodium chloride/ 0.1 M cadmium sulfate	0.1 M tris hydrochloride	8.0	33 % v/v PEG 400
58	None	0.1 M bicine	8.9	31 % PEG 2000
59	0.05 M sodium sulfate/ 0.05 M lithium sulfate	0.05 M tris	8.5	35 % v/v PEG 400
60	0.1 M sodium chloride	0.05 M glycine	9.5	33 % v/v PEG 300
61	0.3 M magnesium nitrate	0.1 M tris	8.0	23 % w/v PEG 2000
62	0.12 M lithium sulfate	0.02 M tris/ 0.1 M sodium citrate	7.5/ 5.0	20 % v/v PEG 300
63	0.1 M sodium chloride	0.12 M tris	9.4	20 % v/v PEG 400
64	0.2 M sodium chloride	0.1 M HEPES	7.0	22 % v/v PEG 550 MME
65	0.1 M sodium chloride/ 0.325 M sodium acetate	0.1 M tris	8.0	21 % v/v PEG 400
66	0.02 M sodium citrate	0.08 M sodium phosphate	6.2	18 % w/v PEG 2000
67	0.02 M potassium nitrate	0.03 M potassium citrate	6.5	7.7 % w/v PEG 4000
68	0.1 M sodium chloride/ 0.005 M magnesium chloride	0.1 M tris	8.5	30 % w/v PEG 2000 MME
69	0.2 M calcium chloride	0.1 M HEPES	7.0	33 % v/v PEG 400
70	0.1 M calcium chloride	0.1 M tris	6.5	13 % w/v PEG 2000 MME
71	0.2 M ammonium sulfate/ 0.02 M sodium chloride	0.02 M sodium acetate	4.0	33 % v/v PEG 200
72	0.07 M sodium chloride	0.05 M sodium citrate	4.5	22 % v/v PEG 400
73	0.2 M ammonium sulfate	0.1 M sodium acetate	4.6	28 % PEG 550 MME
74	None	0.05 M glycine	9.0	55 % v/v PEG 400
75	0.1 M magnesium chloride/ 0.1 M sodium chloride	0.1 M tris	8.5	33 % v/v PEG 400
76	0.1 M lithium sulfate/ 0.05 M disodium hydrogen phosphate	0.05 M citric acid	None	19 % w/v PEG 1000
77	0.2 M magnesium chloride/ 0.1 M potassium chloride	0.025 M sodium citrate	4.0	33 % v/v PEG 400
78	0.05 M zinc acetate	0.05 M MES	6.1	11 % w/v PEG 8000
79	0.3 M magnesium nitrate	0.1 M tris	8.0	22 % w/v PEG 8000
80	0.1 M sodium chloride/ 4 % v/v ethylene glycol	0.1 MES	6.5	33 % v/v PEG 400
81	0.05 M sodium chloride	0.1 M sodium citrate	5.5	26 % v/v PEG 400
82	0.1 M lithium sulfate	0.1 M glycine	9.3	30 % v/v PEG 400
83	0.15 M potassium citrate/ 0.05 M lithium citrate	0.1 M sodium phosphate	-	22 % w/v PEG 6000
84	0.001 M zinc sulphate	0.05 M HEPES	7.8	28 % v/v PEG 600
85	0.1 M sodium chloride	0.1 M sodium phosphate	7.0	33 % v/v PEG 300
86	0.1 M sodium chloride	0.05 M Bicine	9.0	33 % v/v PEG 300
87	0.05 M zinc acetate/ 6 % v/v ethylene glycol	0.1 M sodium cacodylate	6.0	6.6 % w/v PEG 8000
88	0.2 M lithium sulfate	0.1 M sodium citrate	3.5	28 % v/v PEG 400
89	0.1 M sodium chloride	0.1 M tris	7.5	11 % w/v PEG 4000
90	0.05 M lithium sulfate	0.1 M tricine	7.4	7 % w/v PEG 3000
91	0.2 M calcium chloride	0.1 M MES	6.5	33 % v/v PEG 400
92	1 M sodium chloride	0.1 M sodium citrate	6.0	28 % w/v PEG 4000
93	None	0.1 M HEPES	7.5	11 % w/v PEG 4000
94	0.002 M zinc sulfate	0.08 M HEPES	7.0	25 % v/v/ Jeffamine ED2001
95	0.001 M cadmium chloride/ 0.03 M magnesium chloride	0.1 M MES	6.5	30 % v/v PEG 400
96	None	0.1 M bis-tris-propane	7.0	3.0 M sodium chloride

**Abbreviations:**

ADA; N-(2-Acetamido)iminodiacetic Acid, Bicine; N,N-Bis(2-hydroxyethyl)glycine, CHES; 2-(N-Cyclohexylamino)ethane sulfonic Acid, HEPES; N-(2-hydroxyethyl)-piperazine-N'-2-ethanesulfonic acid, KMES; 2-(N-morpholino)ethanesulfonic acid potassium salt, MES; 2-(N-morpholino)ethanesulfonic acid, MME; Monomethylether, PEG; Polyethylene glycol, Tricine; N-[Tris(hydroxymethyl)methyl]glycine, Tris; 2-Amino-2-(hydroxymethyl)propane-1,3-diol, Tris HCl; 2-Amino-2-(hydroxymethyl)propane-1,3-diol, hydrochloride.]

## 8.6 Additive Screen (Hampton Research)

Tube #	Additive
1	0.1 M barium chloride
2	0.1 M cadmium
3	0.1 M calcium chloride
4	0.1 M cobaltous chloride
5	0.1 M cupric chloride
6	0.1 M magnesium chloride
7	0.1 M manganese (II) chloride
8	0.1 M strontium chloride
9	0.1 M Yttrium chloride
10	0.1 M Zinc chloride
11	30 % v/v ethylene glycol
12	30 % v/v glycerol
13	30 % w/v 1,6 hexanediol
14	30 % v/v 2-methyl-2,4-pentanediol
15	40 % v/v polypropylene glycol P400
16	0.1 M trimethylamine HCl
17	0.1 M guanidine HCl
18	0.1 M urea
19	15 % w/v 1,2,3-heptanetriol
20	20 % w/v benzamidine HCl
21	30 % v/v dioxane
22	30 % v/v ethanol
23	30 % v/v iso-propanol
24	30 % v/v methanol
25	1.0 M sodium iodide
26	1.0 M l-cysteine
27	0.1 M EDTA sodium salt
28	0.1 M nicotinamide adenine dinucleotide
29	0.1 M adenosine-5-triphosphate disodium salt
30	30 % w/v D(+)-glucose
31	30 % w/v D(+)-sucrose
32	0.1 M spermidine
33	0.1 M spermine tetra-HCl
34	30 % w/v 6-aminocaproic di-HCl
35	30 % w/v 1,5-diaminopentane di-HCl
36	30 % w/v 1,6-diaminohexane
37	30 % w/v 1,8-diaminooctane
38	1.0 M glycine
39	0.3 M glycyl-glycyl-glycine
40	0.1 M hexamine cobalt (III) chloride
41	0.1 M taurine
42	0.1 M betaine monohydrate
43	5 % w/v polyvinylpyrrolidone K15
44	3.0 M NDSB-195
45	2.0 M NDSB-201
46	30 % dimethyl sulfoxide

47	0.1 M phenol
48	1.0 M ammonium sulfate
49	1.0 M cesium chloride
50	1.0 M potassium chloride
51	1.0 M lithium chloride
52	1.0 M sodium chloride
53	0.5 M sodium fluoride
54	2.0 M sodium thiocyanate
55	30 % dextran sulfato-sodium salt
56	50 % jefframine M-600 pH 7.0
57	40 % 2,5-hexanediol
58	40 % $\pm$ 1,3-butanediol
59	40 % polypropylene glycol
60	40 % 1,4-butanediol
61	40 % tert-butanol
62	40 % 1,3-propanediol
63	40 % Acetonitrile
64	5 % ethyl acetate
65	40 % acetone
66	0.25 % dichloromethane
67	7 % n-butanol
68	40 % 2,2,2-trifluoroethanol
69	0.1 M 1,4-dithio-DL-threitol

## 8.7 PEG /ION Screen (Hampton Research)

Reagent #	[Salt]	[Salt] units	Salt	pH	[Buffer]	[Buffer] units	Buffer	pH	[Ppt]	[Ppt] units	Precipitant
1	0.2	M	Sodium fluoride						20	% w/v	Polyethylene glycol 3,350
2	0.2	M	Potassium fluoride						20	% w/v	Polyethylene glycol 3,350
3	0.2	M	Ammonium fluoride						20	% w/v	Polyethylene glycol 3,350
4	0.2	M	Lithium chloride						20	% w/v	Polyethylene glycol 3,350
5	0.2	M	Magnesium chloride hexahydrate						20	% w/v	Polyethylene glycol 3,350
6	0.2	M	Sodium chloride						20	% w/v	Polyethylene glycol 3,350
7	0.2	M	Calcium chloride dihydrate						20	% w/v	Polyethylene glycol 3,350
8	0.2	M	Potassium chloride						20	% w/v	Polyethylene glycol 3,350
9	0.2	M	Ammonium chloride						20	% w/v	Polyethylene glycol 3,350
10	0.2	M	Sodium iodide						20	% w/v	Polyethylene glycol 3,350
11	0.2	M	Potassium iodide						20	% w/v	Polyethylene glycol 3,350
12	0.2	M	Ammonium iodide						20	% w/v	Polyethylene glycol 3,350
13	0.2	M	Sodium thiocyanate						20	% w/v	Polyethylene glycol 3,350
14	0.2	M	Potassium thiocyanate						20	% w/v	Polyethylene glycol 3,350
15	0.2	M	Lithium nitrate						20	% w/v	Polyethylene glycol 3,350
16	0.2	M	Magnesium nitrate hexahydrate						20	% w/v	Polyethylene glycol 3,350
17	0.2	M	Sodium nitrate						20	% w/v	Polyethylene glycol 3,350
18	0.2	M	Potassium nitrate						20	% w/v	Polyethylene glycol 3,350
19	0.2	M	Ammonium nitrate						20	% w/v	Polyethylene glycol 3,350
20	0.2	M	Magnesium formate dihydrate						20	% w/v	Polyethylene glycol 3,350
21	0.2	M	Sodium formate						20	% w/v	Polyethylene glycol 3,350
22	0.2	M	Potassium formate						20	% w/v	Polyethylene glycol 3,350
23	0.2	M	Ammonium formate						20	% w/v	Polyethylene glycol 3,350
24	0.2	M	Lithium acetate dihydrate						20	% w/v	Polyethylene glycol 3,350
25	0.2	M	Magnesium acetate tetrahydrate						20	% w/v	Polyethylene glycol 3,350
26	0.2	M	Zinc acetate dihydrate						20	% w/v	Polyethylene glycol 3,350
27	0.2	M	Sodium acetate trihydrate						20	% w/v	Polyethylene glycol 3,350
28	0.2	M	Calcium acetate hydrate						20	% w/v	Polyethylene glycol 3,350

29	0.2	M	Potassium acetate					20	% w/v	Polyethylene glycol 3,350
30	0.2	M	Ammonium acetate					20	% w/v	Polyethylene glycol 3,350
31	0.2	M	Lithium sulfate monohydrate					20	% w/v	Polyethylene glycol 3,350
32	0.2	M	Magnesium sulfate heptahydrate					20	% w/v	Polyethylene glycol 3,350
33	0.2	M	Sodium sulfate decahydrate					20	% w/v	Polyethylene glycol 3,350
34	0.2	M	Potassium sulfate					20	% w/v	Polyethylene glycol 3,350
35	0.2	M	Ammonium sulfate					20	% w/v	Polyethylene glycol 3,350
36	0.2	M	Sodium tartrate dibasic dihydrate					20	% w/v	Polyethylene glycol 3,350
37	0.2	M	Potassium sodium tartrate tetrahydrate					20	% w/v	Polyethylene glycol 3,350
38	0.2	M	Ammonium tartrate dibasic					20	% w/v	Polyethylene glycol 3,350
39	0.2	M	Sodium phosphate monobasic monohydrate					20	% w/v	Polyethylene glycol 3,350
40	0.2	M	Sodium phosphate dibasic dihydrate					20	% w/v	Polyethylene glycol 3,350
41	0.2	M	Potassium phosphate monobasic					20	% w/v	Polyethylene glycol 3,350
42	0.2	M	Potassium phosphate dibasic					20	% w/v	Polyethylene glycol 3,350
43	0.2	M	Ammonium phosphate monobasic					20	% w/v	Polyethylene glycol 3,350
44	0.2	M	Ammonium phosphate dibasic					20	% w/v	Polyethylene glycol 3,350
45	0.2	M	Lithium citrate tribasic tetrahydrate					20	% w/v	Polyethylene glycol 3,350
46	0.2	M	Sodium citrate tribasic dihydrate					20	% w/v	Polyethylene glycol 3,350
47	0.2	M	Potassium citrate tribasic monohydrate					20	% w/v	Polyethylene glycol 3,350
48	0.2	M	Ammonium citrate dibasic					20	% w/v	Polyethylene glycol 3,350
49	0.1	M	Sodium malonate	4.0				12	% w/v	Polyethylene glycol 3,350
50	0.2	M	Sodium malonate	4.0				20	% w/v	Polyethylene glycol 3,350
51	0.1	M	Sodium malonate	5.0				12	% w/v	Polyethylene glycol 3,350
52	0.2	M	Sodium malonate	5.0				20	% w/v	Polyethylene glycol 3,350
53	0.1	M	Sodium malonate	6.0				12	% w/v	Polyethylene glycol 3,350
54	0.2	M	Sodium malonate	6.0				20	% w/v	Polyethylene glycol 3,350
55	0.1	M	Sodium malonate	7.0				12	% w/v	Polyethylene glycol 3,350
56	0.2	M	Sodium malonate	7.0				20	% w/v	Polyethylene glycol 3,350
57	4	% v/v	Tacsimate	4.0				12	% w/v	Polyethylene glycol 3,350
58	8	% v/v	Tacsimate	4.0				20	% w/v	Polyethylene glycol 3,350
59	4	% v/v	Tacsimate	5.0				12	% w/v	Polyethylene glycol 3,350
60	8	% v/v	Tacsimate	5.0				20	% w/v	Polyethylene glycol 3,350
61	4	% v/v	Tacsimate	6.0				12	% w/v	Polyethylene glycol 3,350

62	8	% v/v	Tacsimate	6.0					20	% w/v	Polyethylene glycol 3,350
63	4	% v/v	Tacsimate	7.0					12	% w/v	Polyethylene glycol 3,350
64	8	% v/v	Tacsimate	7.0					20	% w/v	Polyethylene glycol 3,350
65	4	% v/v	Tacsimate	8.0					12	% w/v	Polyethylene glycol 3,350
66	8	% v/v	Tacsimate	8.0					20	% w/v	Polyethylene glycol 3,350
67	0.1	M	Succinic acid	7.0					12	% w/v	Polyethylene glycol 3,350
68	0.2	M	Succinic acid	7.0					20	% w/v	Polyethylene glycol 3,350
69	0.1	M	Ammonium citrate tribasic	7.0					12	% w/v	Polyethylene glycol 3,350
70	0.2	M	Ammonium citrate tribasic	7.0					20	% w/v	Polyethylene glycol 3,350
71	0.1	M	DL-Malic acid	7.0					12	% w/v	Polyethylene glycol 3,350
72	0.2	M	DL-Malic acid	7.0					20	% w/v	Polyethylene glycol 3,350
73	0.1	M	Sodium acetate trihydrate	7.0					12	% w/v	Polyethylene glycol 3,350
74	0.2	M	Sodium acetate trihydrate	7.0					20	% w/v	Polyethylene glycol 3,350
75	0.1	M	Sodium formate	7.0					12	% w/v	Polyethylene glycol 3,350
76	0.2	M	Sodium formate	7.0					20	% w/v	Polyethylene glycol 3,350
77	0.1	M	Ammonium tartrate dibasic	7.0					12	% w/v	Polyethylene glycol 3,350
78	0.2	M	Ammonium tartrate dibasic	7.0					20	% w/v	Polyethylene glycol 3,350
79	2	% v/v	Tacsimate	4.0	0.1	M	Sodium acetate trihydrate	4.6	16	% w/v	Polyethylene glycol 3,350
80	2	% v/v	Tacsimate	5.0	0.1	M	Sodium citrate tribasic dihydrate	5.6	16	% w/v	Polyethylene glycol 3,350
81	2	% v/v	Tacsimate	6.0	0.1	M	BIS-TRIS	6.5	20	% w/v	Polyethylene glycol 3,350
82	2	% v/v	Tacsimate	7.0	0.1	M	HEPES	7.5	20	% w/v	Polyethylene glycol 3,350
83	2	% v/v	Tacsimate	8.0	0.1	M	Tris	8.5	16	% w/v	Polyethylene glycol 3,350
84					0.07	M	Citric acid,	3.4	16	% w/v	Polyethylene glycol 3,350
					0.03	M	BIS-TRIS propane				
85					0.06	M	Citric acid,	4.1	16	% w/v	Polyethylene glycol 3,350
					0.04	M	BIS-TRIS propane				
86					0.05	M	Citric acid,	5.0	16	% w/v	Polyethylene glycol 3,350
					0.05	M	BIS-TRIS propane				
87					0.04	M	Citric acid,	6.4	20	% w/v	Polyethylene glycol 3,350
					0.06	M	BIS-TRIS propane				
88					0.03	M	Citric acid,	7.6	20	% w/v	Polyethylene glycol 3,350
					0.07	M	BIS-TRIS propane				
89					0.02	M	Citric acid,	8.8	16	% w/v	Polyethylene glycol 3,350
					0.08	M	BIS-TRIS propane				
90	0.02	M	Calcium chloride dihydrate						20	% w/v	Polyethylene glycol 3,350

	0.02	M	Cadmium chloride hydrate								
	0.02	M	Cobalt(II) chloride hexahydrate								
91	0.01	M	Magnesium chloride hexahydrate		0.1	M	HEPES sodium	7.0	15	% w/v	Polyethylene glycol 3,350
	0.005	M	Nickel(II) chloride hexahydrate								
92	0.02	M	Zinc chloride						20	% w/v	Polyethylene glycol 3,350
93	0.15	M	Cesium chloride						15	% w/v	Polyethylene glycol 3,350
94	0.2	M	Sodium bromide						20	% w/v	Polyethylene glycol 3,350
95	1	% w/v	Tryptone		0.05	M	HEPES sodium	7.0	12	% w/v	Polyethylene glycol 3,350
96	1	% w/v	Tryptone		0.05	M	HEPES sodium	7.0	20	% w/v	Polyethylene glycol 3,350

## 8.8 JCSG-Plus Screen (Molecular Dimension)

Reagent	pH	Conc [M]	Salt	Con [M]	Salt	Con [M]	Salt	Con [M]	Salt	Con [M]	Buffer	Con [M]	Buffer	Con [M]	Units	Precipitant	Con [M]	Units	Precipitant
A1	4.5	0.2	lithium sulfate							0.1	sodium acetate			50	% v/v	PEG 400			
A2	5.5									0.1	citrate			20	% w/v	PEG 3K			
A3		0.2	di-ammonium hydrogen citrate											20	% w/v	PEG 3350			
A4	4.6	0.02	calcium chloride							0.1	sodium acetate			30	% v/v	MPD			
A5		0.2	magnesium formate											20	% w/v	PEG 3350			
A6	4.2	0.2	lithium sulfate							0.1	phosphate	0.1	citrate	20	% w/v	PEG 1K			
A7	9.5									0.1	CHES			20	% w/v	PEG 8K			
A8		0.2	ammonium formate											20	% w/v	PEG 3350			
A9		0.2	ammonium chloride											20	% w/v	PEG 3350			
A10		0.2	potassium formate											20	% w/v	PEG 3350			
A11	8.5	0.2	ammonium dihydrogen phosphate							0.1	tris			50	% v/v	MPD			
A12		0.2	potassium nitrate											20	% w/v	PEG 3350			
B1	4									0.1	sodium citrate			0.8	M	ammonium sulfate			
B2		0.2	sodium thiocyanate											20	% w/v	PEG 3350			
B3	9									0.1	bicine			20	% w/v	PEG 6K			
B4	7.5									0.1	HEPES			10	% w/v	PEG 8K	8	% v/v	Ethylene glycol
B5	6.5									0.1	sodium cacodylate			40	% v/v	MPD	5	% w/v	PEG 8K
B6	4.2									0.1	phosphate	0.1	citrate	40	% v/v	Ethanol	5	% w/v	PEG 1K
B7	4.6									0.1	sodium acetate			8	% w/v	PEG 4K			
B8	7	0.2	magnesium chloride							0.1	tris			10	% w/v	PEG 8K			
B9	5									0.1	sodium citrate			20	% w/v	PEG 6K			



D11	4.6	0.14	calcium chloride						0.1	sodium acetate				25.5	% w/v	PEG 4K	15	% v/v	Glycerol
D12		0.04	potassium dihydrogen phosphate											40	% v/v	PEG 300			
E1	6.5								0.1	sodium cacodylate				14	% v/v	2-propanol	30	% v/v	Glycerol
E2	6.5	0.2	sodium chloride						0.1	sodium cacodylate				16	% w/v	PEG 8K	20	% v/v	Glycerol
E3	7.5	0.2	sodium chloride						0.1	HEPES				1	M	tri-sodium citrate			
E4	8.5	0.2	lithium sulfate						0.1	tris				2	M	ammonium sulfate			
E5	10.5								0.1	CAPS				10	% v/v	2-propanol			
E6	8	0.2	zinc acetate						0.1	imidazole				1.26	M	ammonium sulfate			
E7	6.5	0.2	zinc acetate						0.1	sodium cacodylate				40	% v/v	MPD			
E8	4.5								0.1	sodium acetate				20	% w/v	PEG 3K			
E9	6.5								0.1	MES				10	% v/v	2-propanol			
E10	9								0.1	bicine				1	M	di-ammonium hydrogen phosphate			
E11	6.5	0.16	calcium acetate						0.08	sodium cacodylate				1.6	M	magnesium sulfate			
E12	8								0.1	imidazole				10	% w/v	PEG 6K			
F1	6.5		caesium chloride						0.1	MES				14.4	% w/v	PEG 8K	20	% v/v	glycerol
F2	5								0.1	sodium citrate				10	% w/v	PEG 8K			
F3	8								0.1	tris				30	% v/v	Jeffamine M-600			
F4	7.5								0.1	HEPES				3.2	M	ammonium sulfate			
F5	8.5	0.2	magnesium chloride						0.1	tris				20	% v/v	MPD			
F6	9								0.1	bicine				20	% v/v	Jeffamine M-600			
F7	7													50	% v/v	ethylene glycol			
F8	7													10	% v/v	MPD			
F9	7													0.8	M	succinic acid			
F10	7	1.1	sodium malonate						0.1	HEPES				2.1	M	DL-malic acid			
F11	7	1	succinic acid						0.1	HEPES				2.4	M	sodium malonate			
F12	7								0.1	HEPES				0.5	% v/v	Jeffamine ED-2001			

G1	7									0.1	HEPES			1	% w/v	PEG 2K MME			
G2	7.5	0.02	magnesium chloride							0.1	HEPES			30	% v/v	Jeffamine M-600			
G3	8.5	0.01	cobalt chloride							0.1	tris			30	% v/v	Jeffamine ED-2001			
G4	8.5	0.2	tri-methylamine N-oxide							0.1	tris			22	% w/v	polyacrylic acid 5100 sodium salt			
G5	7.5	0.005	cobalt chloride	0.005	cadmium chloride	0.005	Magnesium chloride	0.005	nickel chloride	0.1	HEPES			20	% w/v	polyvinylpyrrolidone K15			
G6	7	0.2	sodium malonate											20	% w/v	PEG 2K MME			
G7	7	0.1	succinic acid											12	% w/v	PEG 3350			
G8	7	0.15	DL- malic acid											20	% w/v	PEG 3350			
G9		0.1	potassium thiocyanate											15	% w/v	PEG 3350			
G10		0.15	potassium bromide											20	% w/v	PEG 3350			
G11	5.5									0.1	Bis Tris			30	% w/v	PEG 2K MME			
G12	5.5									0.1	Bis Tris			30	% w/v	PEG 2K MME			
H1	5.5									0.1	Bis Tris			2	M	ammonium sulfate			
H2	5.5	1	ammonium sulfate							0.1	Bis Tris			3	M	sodium chloride			
H3	5.5									0.1	Bis Tris			0.3	M	magnesium formate			
H4	5.5	0.2	calcium chloride							0.1	Bis Tris			1	% w/v	PEG 3350			
H5	5.5	0.2	ammonium acetate							0.1	Bis Tris			25	% w/v	PEG 3350			
H6	5.5	0.1	ammonium acetate							0.1	Bis Tris			45	% v/v	MPD			
H7	5.5	0.2	ammonium sulfate							0.1	Bis Tris			45	% v/v	MPD			
H8	5.5	0.2	sodium chloride							0.1	Bis Tris			17	% w/v	PEG 10K			
H9	5.5	0.2	lithium sulfate							0.1	Bis Tris			25	% w/v	PEG 3350			
H10	5.5	0.2	ammonium acetate							0.1	Bis Tris			25	% w/v	PEG 3350			
H11	5.5	0.2	magnesium chloride							0.1	Bis Tris			25	% w/v	PEG 3350			
H12	7.5	0.2	ammonium acetate							0.1	HEPES			25	% w/v	PEG 3350			

## 8.9 Figure of merit from the molecular replacement solutions and the refinement REFMAC

### 8.9.1 HL LH2 crystal $P2_1$

Search Model	RFZ	TFZ	LLG	R-factor
LH2 <i>acidophila</i> pruned	5.4	6.6	201	0.496
LH2 <i>molischianum</i> pruned	3.8	3.5	83	0.581
Octamer builded from LH2 <i>acidophila</i>	4.1	2.5	56	0.606

### 8.9.2 LL LH2 crystal C2

#### Standard processing (6.5 Å)

Search Model	RFZ	TFZ	LLG	R-factor
LH2 <i>acidophila</i> pruned	6.1	7.6	326	0.581
LH2 <i>molischianum</i> pruned	5.9	5.5	221	0.603
Octamer builded from LH2 <i>acidophila</i>	5.0	5.4	130	0.631

#### Anisotropic processing (5.0 Å)

Search Model	RFZ	TFZ	LLG	R-factor
LH2 <i>acidophila</i> pruned	6.6	7.5	404	0.584
LH2 <i>molischianum</i> pruned	6.3	5.5	235	0.598
Octamer builded from LH2 <i>acidophila</i>	5.1	4.6	155	0.605

### 8.9.3 LL LH2 crystal $P2_1$

#### Standard processing (6.2 Å)

Search Model	RFZ	TFZ	LLG	R-factor
LH2 <i>acidophila</i> pruned	4.9	7.7	262	0.479
LH2 <i>molischianum</i> pruned	3.4	4.0	93	0.537
Octamer builded from LH2 <i>acidophila</i>	3.2	3.4	66	0.545

#### Anisotropic processing (5.6 Å)

Search Model	RFZ	TFZ	LLG	R-factor
LH2 <i>acidophila</i> pruned	5.5	6.6	293	0.499
LH2 <i>molischianum</i> pruned	3.3	2.8	46	0.569
Octamer builded from LH2 <i>acidophila</i>	3.2	4.7	63	0.550

#### Note:

RFZ and TFZ give the scores from the PHASER rotational and translational functions. LLG stands for log likelihood gain and compares the Patterson maps for the solution model and for the experimental data. R-factor is the reliability factor expressing the agreement between the refined model and the experimental data. The lower R-factor value the better is the agreement with experimental data.

The polypeptides of the LH2 models from *Rps. acidophila* 10050 and *Phs. molischianum* were pruned at the C and N termini, which were assumed to be possibly flexible. The molecular surface solvents were also removed.

---

## 9 List of references

---

Agarwal, R., Rizvi, A. H., Prall, B. S., Olsen, J. D., Hunter, C. N., and Fleming, G. R. **2002**. Nature of disorder and inter-complex energy transfer in LH2 at room temperature: A three pulse photon echo peak shift study. *J Phys Chem A* **106**:7573-7578.

Alden, R. G., Johnson, E., Nagarajan, V., Parson, W. W., Law, C. J., and Cogdell, R. G. **1997**. Calculations of spectroscopic properties of the LH2 bacteriochlorophyll - Protein antenna complex from *Rhodopseudomonas acidophila*. *J Phys Chem B* **101**:4667-4680.

Barz, W. P., Francia, F., Venturoli, G., Melandri, B. A., Vermeglio, A., and Oesterhelt, D. **1995a**. Role of PufX protein in photosynthetic growth of *Rhodobacter sphaeroides*. 1. PufX is required for efficient light-driven electron transfer and photophosphorylation under anaerobic conditions. *Biochemistry* **34**:15235-15247.

Barz, W. P., Vermeglio, A., Francia, F., Venturoli, G., Melandri, B. A., and Oesterhelt, D. **1995b**. Role of the PufX protein in photosynthetic growth of *Rhodobacter sphaeroides*. 2. PufX is required for efficient ubiquinone/ubiquinol exchange between the reaction center QB site and the cytochrome bc1 complex. *Biochemistry* **34**:15248-15258.

Bauer, C. E., and Bird, T. H. **1996**. Regulatory circuits controlling photosynthesis gene expression. *Cell* **85**:5-8.

Beljonne, D., Curutchet, C., Scholes, G. D., and Silbey, R. J. **2009**. Beyond forster resonance energy transfer in biological and nanoscale systems. *J Phys Chem B* **113**:6583-6599.

Berlin, Y., Burin, A., Friedrich, J., and Kohler, J. **2007**. Low temperature spectroscopy of proteins. Part II: Experiments with single protein complexes. *Physics of Life Reviews* **4**:64-89.

Bissig, I., Brunisholz, R. A., Suter, F., Cogdell, R. J., and Zuber, H. **1988**. The complete amino acid sequences of the B800-850 antenna polypeptides from *Rhodopseudomonas acidophila* strain 7750. *Z Naturforsch [C]* **43**:77-83.

Blankenship, R. E. **2002**. Molecular mechanisms of photosynthesis. Blackwell Science, Oxford.

Bopp, M. A., Jia, Y. W., Li, L. Q., Cogdell, R. J., and Hochstrasser, R. M. **1997**. Fluorescence and photobleaching dynamics of single light-harvesting complexes. *Proc Natl Acad Sci U S A* **94**:10630-10635.

Böse, S. K. **1963**. Bacterial photosynthesis. Antioch Press, Yellow Springs, Ohio.

- Britton, G., and Young, A.J. **1993**. Methods for the isolation and analysis of carotenoids. In *Carotenoids in Photosynthesis*. (Young, A., and Britton, G., ed). Chapman & Hall, London. 409-457.
- Britton, G., Liaaen-Jensen, S. and Pfander, H., editor. 2004. *Carotenoids handbook*. Birkhauser Verlag, Basel.
- Bullough, P. A., Qian, P., and Hunter, C. N. **2009**. Reaction center-light-harvesting core complex of purple bacteria. In *The Purple Phototrophic Bacteria*. (Hunter, C.N., Daldal, F., Thurnauer, C., and Thomas Beatty, J., ed). Springer, Dordrecht. 155-179.
- Burgess, J. G., Ashby, M. K., and Hunter, C. N. **1989**. Characterization and complementation of a mutant of *Rhodobacter sphaeroides* with a chromosomal deletion in the light-harvesting (LH2) genes. *J Gen Microbiol* **135**:1809-1816.
- Caldwell, D. E., and Tiedje, J. M. **1975a**. Morphological study of anaerobic bacteria from hypolimnia of 2 Michigan lakes. *Canadian Journal of Microbiology* **21**:362-376.
- Caldwell, D. E., and Tiedje, J. M. **1975b**. Structure of anaerobic bacterial communities in hypolimnia of several Michigan lakes. *Canadian Journal of Microbiology* **21**:377-385.
- Chayen, N. E. **2004**. Turning protein crystallisation from an art into a science. *Current Opinion in Structural Biology* **14**:577-583.
- Chayen, N. E. **2005**. Methods for separating nucleation and growth in protein crystallisation. *Prog Biophys Mol Biol* **88**:329-337.
- Cheng, Y. C., and Silbey, R. J. **2006**. Coherence in the B800 ring of purple bacteria LH2. *Phys Rev Lett* **96**:028103.
- Clark, W. G., Davidson, E., and Marrs, B. L. **1984**. Variation of levels of mRNA coding for antenna and reaction center polypeptides in *Rhodospseudomonas capsulata* in response to changes in oxygen concentration. *J Bacteriol* **157**:945-948.
- Clayton, R. K. **1966**. Spectroscopic analysis of bacteriochlorophylls in vitro and in vivo. *Photochem Photobiol* **5**:660-677.
- Cogdell, R. J., and Frank, H. A. **1987**. How carotenoids function in photosynthetic bacteria. *Biochim Biophys Acta* **895**:63-79.
- Cogdell, R. J., Gall, A., and Köhler, J. **2006**. The architecture and function of the light-harvesting apparatus of purple bacteria: from single molecules to in vivo membranes. *Q Rev Biophys* **39**:227-324.
- Cogdell, R. J., Gardiner, A. T., Hashimoto, H., and Brotosudarmo, T. H. P. **2008**. A comparative look at the first few milliseconds of the light reactions of photosynthesis. *Photochem Photobiol Sci* **7**:1150-1158.
- Cogdell, R. J., Howard, T. D., Isaacs, N. W., McLuskey, K., and Gardiner, A. T. **2002**. Structural factors which control the position of the Q(y) absorption band

of bacteriochlorophyll a in purple bacterial antenna complexes. *Photosynth Res* **74**:135-141.

Cogdell, R. J., Isaacs, N. W., Freer, A. A., Arrelano, J., Howard, T. D., Papiz, M. Z., Hawthornthwaite-Lawless, A. M., and Prince, S. **1997**. The structure and function of the LH2 (B800-850) complex from the purple photosynthetic bacterium *Rhodospseudomonas acidophila* strain 10050. *Prog Biophys Mol Biol* **68**:1-27.

Cogdell, R. J., and Scheer, H. **1985**. Circular-dichroism of light-harvesting complexes from purple photosynthetic bacteria. *Photochem Photobiol* **42**:669-678.

Cohen-Bazire, G. a. S., W.R. **1966**. The prokaryotic photosynthetic apparatus. In *The Chlorophylls*. (Vernon, L.P. And Seely, G.R., ed). Academic Press, New York. 313-341.

Connolly, J. S., Samuel, E. B., and Janzen, A. F. **1982**. Effects of solvent on the fluorescence properties of bacteriochlorophyll *a*. *Photochem Photobiol* **36**:565-574.

Cotton, T. M., and Vanduyne, R. P. **1981**. Characterization of bacteriochlorophyll interactions invitro by resonance Raman-spectroscopy. *J Am Chem Soc* **103**:6020-6026.

Damjanovic, A., Kosztin, I., Kleinekathofer, U., and Schulten, K. **2002**. Excitons in a photosynthetic light-harvesting system: A combined molecular dynamics, quantum chemistry, and polaron model study. *Phys Rev E* **65**:031919.

Davydov, A. S. **1964**. The theory of molecular excitons. *Sov Phys Usp* **82**:145-178.

Davydov, A. S. **1971**. Theory of molecular excitons. Plenum Press, New York.

de Ruijter, W. P., Oellerich, S., Segura, J. M., Lawless, A. M., Papiz, M., and Aartsma, T. J. **2004**. Observation of the energy-level structure of the low-light adapted B800 LH4 complex by single-molecule spectroscopy. *Biophys J* **87**:3413-3420.

de Ruijter, W. P. F., Segura, J. M., Cogdell, R. J., Gardiner, A. T., Oellerich, S., and Aartsma, T. J. **2007**. Fluorescence-emission spectroscopy of individual LH2 and LH3 complexes. *Chem. Phys.* **341**:320-325.

Emsley, P., and Cowtan, K. **2004**. Coot: model-building tools for molecular graphics. *Acta Crystallogr D* **60**:2126-2132.

Evans, K., Fordham-Skelton, A. P., Mistry, H., Reynolds, C. D., Lawless, A. M., and Papiz, M. Z. **2005**. A bacteriophytochrome regulates the synthesis of LH4 complexes in *Rhodospseudomonas palustris*. *Photosynth Res* **85**:169-180.

Evans, M. B. **1989**. The structure and function of the light-harvesting antenna complexes from purple photosynthetic bacteria. In Department of Botany. University of Glasgow, Glasgow.

Evans, M. B., Hawthornthwaite, A. M., and Cogdell, R. J. **1990**. Isolation and characterization of the different B800-850 light-harvesting complexes from low-light and high-light grown cells of *Rhodospseudomonas palustris*, strain 2.1.6. *Biochim Biophys Acta* **1016**:71-76.

Foote, C. S., Chang, Y. C., and Denny, R. W. **1970**. Chemistry of singlet oxygen .10. carotenoid quenching parallels biological protection. *J Am Chem Soc* **92**:5216-5218.

Forster, T. **1966**. Nobel lectures chemistry 1942-1962. *Zeitschrift Fur Physikalische Chemie-Frankfurt* **49**:339.

Fowler, G. J., Sockalingum, G. D., Robert, B., and Hunter, C. N. **1994**. Blue shifts in bacteriochlorophyll absorbance correlate with changed hydrogen bonding patterns in light-harvesting 2 mutants of *Rhodobacter sphaeroides* with alterations at alpha-Tyr-44 and alpha-Tyr-45. *Biochem J* **299** (3):695-700.

Fowler, G. J. S., and Hunter, C. N. **1996**. The synthesis and assembly of functional high and low light LH2 antenna complexes from *Rhodospseudomonas palustris* in *Rhodobacter sphaeroides*. *Journal of Biological Chemistry* **271**:13356-13361.

Fowler, G. J. S., Visschers, R. W., Grief, G. G., Vangrondelle, R., and Hunter, C. N. **1992**. Genetically modified photosynthetic antenna complexes with blueshifted absorbency bands. *Nature* **355**:848-850.

Francia, F., Wang, J., Venturoli, G., Melandri, B. A., Barz, W. P., and Oesterhelt, D. **1999**. The reaction center-LH1 antenna complex of *Rhodobacter sphaeroides* contains one PufX molecule which is involved in dimerization of this complex. *Biochemistry* **38**:6834-6845.

Frank, H. A., and Cogdell, R. J. **1993**. The photochemistry and function of carotenoids in photosynthesis. In *Carotenoids in Photosynthesis*. (Young, A., and Britton, G., ed). Chapman & Hall, London. 252-326.

Fromme, P., and Grotjohann, I. **2009**. Crystallization of photosynthetic membrane proteins. *Membrane Protein Crystallization* **63**:191-227.

Gall, A., Fowler, G. J., Hunter, C. N., and Robert, B. **1997**. Influence of the protein binding site on the absorption properties of the monomeric bacteriochlorophyll in *Rhodobacter sphaeroides* LH2 complex. *Biochemistry* **36**:16282-16287.

Gall, A., Henry, S., Takaichi, S., Robert, B., and Cogdell, R. J. **2005**. Preferential incorporation of coloured-carotenoids occurs in the LH2 complexes from non-sulphur purple bacteria under carotenoid-limiting conditions. *Photosynth Res* **86**:25-35.

Gall, A., and Robert, B. **1999**. Characterization of the different peripheral light-harvesting complexes from high- and low-light grown cells from *Rhodospseudomonas palustris*. *Biochemistry* **38**:5185-5190.

Garavito, R. M., and Rosenbusch, J. P. **1980**. Three-dimensional crystals of an integral membrane protein: an initial x-ray analysis. *J Cell Biol* **86**:327-329.

Gardiner, A. T., Takaichi, S., and Cogdell, R. J. **1993**. The effect of changes in light intensity and temperature on the peripheral antenna of *Rhodopseudomonas acidophila*. *Biochem Soc Trans* **21**:6S.

Georgakopoulou, S., Frese, R. N., Johnson, E., Koolhaas, C., Cogdell, R. J., van Grondelle, R., and van der Zwan, G. **2002**. Absorption and CD spectroscopy and modeling of various LH2 complexes from purple bacteria. *Biophys J* **82**:2184-2197.

Gierschner, J., Mack, H. G., Luer, L., and Oelkrug, D. **2002**. Fluorescence and absorption spectra of oligophenylenevinyls: Vibronic coupling, band shapes, and solvatochromism. *J Chem Phys* **116**:8596-8609.

Gouterman, M. **1978**. Optical spectra and electronic structure of porphyrins and related rings. In *The Porphyrins*. (Dolphyn, D., ed). Academic Press, New York. 1-156.

Gregor, J., and Klug, G. **1999**. Regulation of bacterial photosynthesis genes by oxygen and light. *FEMS Microbiol Lett* **179**:1-9.

Griffiths, M., Sistrom, W. R., Cohenbazire, G., and Stanier, R. Y. **1955**. Function of carotenoids in photosynthesis *Nature* **176**:1211-1214.

Hanson, L. K. **1991**. Visible absorption spectroscopy of chlorophylls. In *Chlorophylls*. (Scheer, H., ed). CRC Press, Boca Raton. 993-1014.

Hartigan, N., Tharia, H. A., Sweeney, F., Lawless, A. M., and Papiz, M. Z. **2002**. The 7.5-Å electron density and spectroscopic properties of a novel low-light B800 LH2 from *Rhodopseudomonas palustris*. *Biophys J* **82**:963-977.

Herek, J. L., Fraser, N. J., Pullerits, T., Martinsson, P., Polívka, T., Scheer, H., Cogdell, R. J., and Sundström, V. **2000**. B800-->B850 energy transfer mechanism in bacterial LH2 complexes investigated by B800 pigment exchange. *Biophys J* **78**:2590-2596.

Hess, S., Akesson, E., Cogdell, R. J., Pullerits, T., and Sundström, V. **1995a**. Energy transfer in spectrally inhomogeneous light-harvesting pigment-protein complexes of purple bacteria. *Biophys J* **69**:2211-2225.

Hess, S., Chachisvilis, M., Timpmann, K., Jones, M. R., Fowler, G. J. S., Hunter, C. N., and Sundstrom, V. **1995b**. Temporally and spectrally resolved subpicosecond energy transfer within the peripheral antenna complex (LH2) and from LH2 to the core antenna complex in photosynthetic purple bacteria. *Proc Natl Acad Sci U S A* **92**:12333-12337.

Hess, S., Feldchtein, F., Babin, A., Nurgaleev, I., Pullerits, T., Sergeev, A., and Sundström, V. **1993**. Femtosecond energy-transfer within the LH2 peripheral antenna of the photosynthetic purple bacteria *Rhodobacter sphaeroides* and *Rhodopseudomonas palustris* LL. *Chem Phys Lett* **216**:247-257.

Hofmann, C., Aartsma, T. J., and Köhler, J. **2004**. Energetic disorder and the B850-exciton states of individual light-harvesting 2 complexes from *Rhodopseudomonas acidophila*. *Chem Phys Lett* **395**:373-378.

Hofmann, C., Ketelaars, M., Matsushita, M., Michel, H., Aartsma, T. J., and Köhler, J. **2003**. Single-molecule study of the electronic couplings in a circular array of molecules: light-harvesting-2 complex from *Rhodospirillum rubrum*. *Phys Rev Lett* **90**:013004.

Hofmann, C., Michel, H., van Heel, M., and Köhler, J. **2005**. Multivariate analysis of single-molecule spectra: surpassing spectral diffusion. *Phys Rev Lett* **94**:195501.

Howard, T. D., McAuley-Hecht, K.E. and Cogdell, R.J. . **2000**. Crystallization of membrane proteins. In *Membrane Transport*. (Baldwin, S.A., ed). Oxford University Press, Oxford.

Hu, X., Ritz, T., Damjanovic, A., Autenrieth, F., and Schulten, K. **2002**. Photosynthetic apparatus of purple bacteria. *Q Rev Biophys* **35**:1-62.

Hunter, C. N., Ashby, M. K., and Coomber, S. A. **1987**. Effect of oxygen on levels of mRNA coding for reaction-centre and light-harvesting polypeptides of *Rhodobacter sphaeroides*. *Biochem J* **247**:489-492.

Hunter, C. N., Hundle, B. S., Hearst, J. E., Lang, H. P., Gardiner, A. T., Takaichi, S., and Cogdell, R. J. **1994**. Introduction of new carotenoids into the bacterial photosynthetic apparatus by combining the carotenoid biosynthetic pathways of *Erwinia herbicola* and *Rhodobacter sphaeroides*. *J Bacteriol* **176**:3692-3697.

Hunter, C. N., Pennoyer, J. D., Sturgis, J. N., Farrelly, D., and Niederman, R. A. **1988**. Oligomerization states and associations of light-harvesting pigment protein complexes of *Rhodobacter sphaeroides* as analyzed by lithium dodecyl-sulfate polyacrylamide-gel electrophoresis. *Biochemistry* **27**:3459-3467.

Ihalainen, J. A., Linnanto, J., Myllyperkio, P., van Stokkum, I. H. M., Ucker, B., Scheer, H., and Korppi-Tommola, J. E. I. **2001**. Energy transfer in LH2 of *Rhodospirillum rubrum*, studied by subpicosecond spectroscopy and configuration interaction exciton calculations. *J Phys Chem B* **105**:9849-9856.

Kaplan, S. **1978**. Control and kinetic of photosynthetic membrane development. In *The Photosynthetic bacteria*. (Clayton, R.K., and Sistrom, W.R., ed). Plenum Press, New York. 809-839.

Karrasch, S., Bullough, P. A., and Ghosh, R. **1995**. The 8.5-angstrom projection map of the light-harvesting complex-I from *Rhodospirillum rubrum* reveals a ring composed of 16 subunits. *Embo Journal* **14**:631-638.

Kennis, J. T. M., Streltsov, A. M., Permentier, H., Aartsma, T. J., and Amesz, J. **1997a**. Exciton coherence and energy transfer in the LH2 antenna complex of *Rhodospseudomonas acidophila* at low temperature. *J Phys Chem B* **101**:8369-8374.

Kennis, J. T. M., Streltsov, A. M., Vulto, S. I. E., Aartsma, T. J., Nozawa, T., and Amesz, J. **1997b**. Femtosecond dynamics in isolated LH2 complexes of various species of purple bacteria. *J Phys Chem B* **101**:7827-7834.

Kereiche, S., Bourinet, L., Keegstra, W., Arteni, A. A., Verbavatz, J. M., Boekema, E. J., Robert, B., and Gall, A. **2008**. The peripheral light-harvesting complexes from purple sulfur bacteria have different 'ring' sizes. *FEBS Lett* **582**:3650-3656.

Ketelaars, M., Hofmann, C., Köhler, J., Howard, T. D., Cogdell, R. J., Schmidt, J., and Aartsma, T. J. **2002**. Spectroscopy on individual light-harvesting 1 complexes of *Rhodopseudomonas acidophila*. *Biophys J* **83**:1701-1715.

Ketelaars, M., van Oijen, A. M., Matsushita, M., Köhler, J., Schmidt, J., and Aartsma, T. J. **2001**. Spectroscopy on the B850 band of individual light-harvesting 2 complexes of *Rhodopseudomonas acidophila*. I. Experiments and Monte Carlo simulations. *Biophys J* **80**:1591-1603.

Klug, G. **1993**. Regulation of expression of photosynthesis genes in anoxygenic photosynthetic bacteria. *Arch Microbiol* **159**:397-404.

Knox, R. S. **1964**. Theory of excitons. Academic Press, New York ; London.

Koepke, J., Hu, X., Muenke, C., Schulten, K., and Michel, H. **1996**. The crystal structure of the light-harvesting complex II (B800-850) from *Rhodospirillum molischianum*. *Structure* **4**:581-597.

Koolhaas, M. H., van der Zwan, G., van Mourik, F., and van Grondelle, R. **1997a**. Spectroscopy and structure of bacteriochlorophyll dimers. I. Structural consequences of nonconservative circular dichroism spectra. *Biophys J* **72**:1828-1841.

Koolhaas, M. H. C., van der Zwan, G., Frese, R. N., and van Grondelle, R. **1997b**. Red shift of the zero crossing in the CD spectra of the LH2 antenna complex of *Rhodopseudomonas acidophila*: A structure-based study. *J Phys Chem B* **101**:7262-7270.

Koolhaas, M. H. C., van der Zwan, G., and van Grondelle, R. **2000**. Local and nonlocal contributions to the linear spectroscopy of light-harvesting antenna systems. *J Phys Chem B* **104**:4489-4502.

Krueger, B. P., Scholes, G. D., Yu, J. Y., and Fleming, G. R. **1999**. The light harvesting process in purple bacteria. *Acta Physica Polonica A* **95**:63-83.

Kuki, M., Nagae, H., Cogdell, R. J., Shimada, K., and Koyama, Y. **1994**. Solvent effect on spheroidene in nonpolar and polar solutions and the environment of spheroidene in the light-harvesting complexes of *Rhodobacter sphaeroides* 2.4.1 as revealed by the energy of the  $^1A_g^- \rightarrow ^1B_u^+$  absorption and the frequencies of the vibronically coupled C=C stretching Raman lines in the  $^1A_g^-$  and  $^1B_u^-$  states. *Photochem Photobiol* **59**:116-124.

Lang, H. P., and Hunter, C. N. **1994**. The relationship between carotenoid biosynthesis and the assembly of the light-harvesting LH2 complex in *Rhodobacter sphaeroides* *Biochem J* **298**:197-205.

Larimer, F. W., Chain, P., Hauser, L., Lamerdin, J., Malfatti, S., Do, L., Land, M. L., Pelletier, D. A., Beatty, J. T., Lang, A. S., Tabita, F. R., Gibson, J. L., Hanson, T. E., Bobst, C., Torres, J. L., Peres, C., Harrison, F. H., Gibson, J., and

- Harwood, C. S. **2004**. Complete genome sequence of the metabolically versatile photosynthetic bacterium *Rhodopseudomonas palustris*. *Nat Biotechnol* **22**:55-61.
- Law, C. J., and Cogdell, R. **2008**. The light-harvesting system of purple anoxygenic photosynthetic bacteria. In *Primary Processes of Photosynthesis, Part 1 Principle and Apparatus*. (Renger, Gernot, ed). RSC Publishing, Cambridge. 205-259.
- Lee, J. K., Kiley, P. J., and Kaplan, S. **1989**. Posttranscriptional control of puc operon expression of B800-850 light-harvesting complex formation in *Rhodobacter sphaeroides*. *J Bacteriol* **171**:3391-3405.
- Limantara, L., Fujii, R., Zhang, J. P., Kakuno, T., Hara, H., Kawamori, A., Yagura, T., Cogdell, R. J., and Koyama, Y. **1998**. Generation of triplet and cation-radical bacteriochlorophyll a in carotenoidless LH1 and LH2 antenna complexes from *Rhodobacter sphaeroides*. *Biochemistry* **37**:17469-17486.
- Ma, Y. Z., Cogdell, R. J., and Gillbro, T. **1997**. Energy transfer and exciton annihilation in the B800-850 antenna complex of the photosynthetic purple bacterium *Rhodopseudomonas acidophila* (Strain 10050). A femtosecond transient absorption study. *J Phys Chem B* **101**:1087-1095.
- Ma, Y. Z., Cogdell, R. J., and Gillbro, T. **1998**. Femtosecond energy-transfer dynamics between bacteriochlorophylls in the B800-820 antenna complex of the photosynthetic purple bacterium *Rhodopseudomonas acidophila* (Strain 7750). *J Phys Chem B* **102**:881-887.
- Madigan, M. T., and Jung, D. O. **2009**. An overview of purple bacteria: systematic, physiology and habitats. In *The Purple Phototrophic Bacteria*. (Hunter, N. C., Daldal F., Thurnauer M. C., and Beatty J. T., ed). Springer, Dordrecht. 1-15.
- Makarow, M., Mareschal, M., Ceulemans, R., and Floud, R. **2008**. Harnessing solar energy for the production of clean fuel. *European Science Foundation (ESF) Science Policy Briefing* **34**:1-12.
- Matsushita, M., Ketelaars, M., van Oijen, A. M., Köhler, J., Aartsma, T. J., and Schmidt, J. **2001**. Spectroscopy on the B850 band of individual light-harvesting 2 complexes of *Rhodopseudomonas acidophila*. II. Exciton states of an elliptically deformed ring aggregate. *Biophys J* **80**:1604-1614.
- McCoy, A. J., Grosse-Kunstleve, R. W., Adams, P. D., Winn, M. D., Storoni, L. C., and Read, R. J. **2007**. Phaser crystallographic software. *Journal of Applied Crystallography* **40**:658-674.
- McCoy, A. J., Grosse-Kunstleve, R. W., Storoni, L. C., and Read, R. J. **2005**. Likelihood-enhanced fast translation functions. *Acta Crystallogr D Biol Crystallogr* **61**:458-464.
- McDermott, G., Prince, S. M., Freer, A. A., Hawthornthwaitelawless, A. M., Papiz, M. Z., Cogdell, R. J., and Isaacs, N. W. **1995**. Crystal structure of an integral membrane light-harvesting complex from photosynthetic bacteria. *Nature* **374**:517-521.

McLuskey, K., Prince, S. M., Cogdell, R. J., and Isaacs, N. W. **2001**. The crystallographic structure of the B800-820 LH3 light-harvesting complex from the purple bacteria *Rhodospseudomonas acidophila* strain 7050. *Biochemistry* **40**:8783-8789.

Mercer, I. P., El-Taha, Y. C., Kajumba, N., Marangos, J. P., Tisch, J. W., Gabrielsen, M., Cogdell, R. J., Springate, E., and Turcu, E. **2009**. Instantaneous mapping of coherently coupled electronic transitions and energy transfers in a photosynthetic complex using angle-resolved coherent optical wave-mixing. *Phys Rev Lett* **102**:057402.

Messinger, J., and Renger, G. **2008**. Photosynthetic water splitting. In Primary Processes of Photosynthesis - Part 2 Principle and Apparatus. (Renger, Gernot, ed). RSC Publishing, Cambridge. 291-349.

Michel, H. **1982a**. Characterization and crystal packing of three-dimensional bacteriorhodopsin crystals. *EMBO J* **1**:1267-1271.

Michel, H. **1982b**. Three-dimensional crystals of a membrane protein complex. The photosynthetic reaction centre from *Rhodospseudomonas viridis*. *J Mol Biol* **158**:567-572.

Michel, H., and Oesterhelt, D. **1980**. Three-dimensional crystals of membrane proteins: bacteriorhodopsin. *Proc Natl Acad Sci U S A* **77**:1283-1285.

Moerner, W. E., and Fromm, D. P. **2003**. Methods of single-molecule fluorescence spectroscopy and microscopy. *Review of Scientific Instruments* **74**:3597-3619.

Murphy, D. B. **2001**. Fundamentals of light microscopy and electronic imaging. A John Willey & Sons, Inc., New York.

Murshudov, G. N., Vagin, A. A., and Dodson, E. J. **1997**. Refinement of macromolecular structures by the maximum-likelihood method. *Acta Crystallogr D Biol Crystallogr* **53**:240-255.

Nagae, H., Kuki, M., Cogdell, R. J., and Koyama, Y. **1994**. Shift of the  $^1A_g^- \rightarrow ^1B_u^+$  electronic absorption of carotenoids in nonpolar and polar solvents *J Chem Phys* **101**:6750-6765.

Naylor, G. W., Addlesee, H. A., Gibson, L. C. D., and Hunter, C. N. **1999**. The photosynthesis gene cluster of *Rhodobacter sphaeroides*. *Photosynth Res* **62**:121-139.

Nishimura, Y., Shimada, K., Yamazaki, I., and Mimuro, M. **1993**. Energy transfer processes in *Rhodospseudomonas palustris* grown under low-light conditions. Heterogeneous composition of LH 2 complexes and parallel energy flow pathways. *FEBS Lett* **329**:319-323.

Novoderezhkin, V., Monshouwer, R., and van Grondelle, R. **1999**. Disordered exciton model for the core light-harvesting antenna of *Rhodospseudomonas viridis*. *Biophys J* **77**:666-681.

Novoderezhkin, V., and van Grondelle, R. **2002**. Exciton-vibrational relaxation and transient absorption dynamics in LH1 of *Rhodospseudomonas viridis*: A Redfield theory approach. *J Phys Chem B* **106**:6025-6037.

Novoderezhkin, V., Wendling, M., and van Grondelle, R. **2003**. Intra- and interband transfers in the B800-B850 antenna of *Rhodospirillum molischianum*: Redfield theory modeling of polarized pump-probe kinetics. *J Phys Chem B* **107**:11534-11548.

Olsen, J. D., Sturgis, J. N., Westerhuis, W. H., Fowler, G. J., Hunter, C. N., and Robert, B. **1997**. Site-directed modification of the ligands to the bacteriochlorophylls of the light-harvesting LH1 and LH2 complexes of *Rhodobacter sphaeroides*. *Biochemistry* **36**:12625-12632.

Papiz, M. Z., Prince, S. M., Howard, T., Cogdell, R. J., and Isaacs, N. W. **2003**. The structure and thermal motion of the B800-850 LH2 complex from *Rps. acidophila* at 2.0Å resolution and 100K: new structural features and functionally relevant motions. *J Mol Biol* **326**:1523-1538.

Pflugrath, J. **1999**. The finer things in X-ray diffraction data collection. *Acta Crystallogr Acta D* **55**:1718-1725.

Polli, D., Cerullo, G., Lanzani, G., De Silvestri, S., Hashimoto, H., and Cogdell, R. J. **2006**. Carotenoid-bacteriochlorophyll energy transfer in LH2 complexes studied with 10-fs time resolution. *Biophys J* **90**:2486-2497.

Polli, D., Luer, L., and Cerullo, G. **2007**. High-time-resolution pump-probe system with broadband detection for the study of time-domain vibrational dynamics. *Review of Scientific Instruments* **78**:-.

Prive, G. G. **2007**. Detergents for the stabilization and crystallization of membrane proteins. *Methods* **41**:388-397.

Pusey, M., and Naumann, R. **1986**. Growth kinetics of tetragonal lysozyme crystals. *Journal of Crystal Growth* **76**:593-599.

Qian, P., Hunter, C. N., and Bullough, P. A. **2005**. The 8.5Å projection structure of the core RC-LH1-PufX dimer of *Rhodobacter sphaeroides*. *J Mol Biol* **349**:948-960.

Qian, P., Saiki, K., Mizoguchi, T., Hara, K., Sashima, T., Fujii, R., and Koyama, Y. **2001**. Time-dependent changes in the carotenoid composition and preferential binding of spirilloxanthin to the reaction center and anhydrorhodovibrin to the LH1 antenna complex in *Rhodobium marinum*. *Photochem Photobiol* **74**:444-452.

Rabinowitch, E., and Govindjee. **1969**. Photosynthesis. John Willey & Sons, Inc., New York.

Renger, G. **2008**. Functional pattern of photosystem II. In Primary Processes of Photosynthesis - Part 2 Principle and Apparatus. (Renger, Gernot, ed). RSC Publishing, Cambridge. 237-290.

Richter, M. F., Baier, J., Prem, T., Oellerich, S., Francia, F., Venturoli, G., Oesterhelt, D., Southall, J., Cogdell, R. J., and Köhler, J. **2007a**. Symmetry matters for the electronic structure of core complexes from *Rhodopseudomonas palustris* and *Rhodobacter sphaeroides* PufX. *Proc Natl Acad Sci U S A* **104**:6661-6665.

Richter, M. F., Baier, J., Southall, J., Cogdell, R. J., Oellerich, S., and Köhler, J. **2007b**. Refinement of the x-ray structure of the RC LH1 core complex from *Rhodopseudomonas palustris* by single-molecule spectroscopy. *Proc Natl Acad Sci U S A* **104**:20280-20284.

Robert, B., Cogdell, R.J. and van Grondelle, R. **2003**. The light-harvesting system of purple bacteria. In *Light-Harvesting Antennas in Photosynthesis*. (Green, B. R., and Parson, W. W., ed). Kluwer, Dordrecht. 167-194.

Roszak, A. W., Howard, T. D., Southall, J., Gardiner, A. T., Law, C. J., Isaacs, N. W., and Cogdell, R. J. **2003**. Crystal structure of the RC-LH1 core complex from *Rhodopseudomonas palustris*. *Science* **302**:1969-1972.

Rutkauskas, D., Novoderezhkin, V., Cogdell, R. J., and van Grondelle, R. **2005**. Fluorescence spectroscopy of conformational changes of single LH2 complexes. *Biophys J* **88**:422-435.

Sauer, K., Cogdell, R. J., Prince, S. M., Freer, A., Isaacs, N. W., and Scheer, H. **1996a**. Structure-based calculations of the optical spectra of the LH2 bacteriochlorophyll-protein complex from *Rhodopseudomonas acidophila*. *Photochem Photobiol* **64**:564-576.

Sauer, P. R. R., Lottspeich, F., Unger, E., Mentele, R., and Michel, H. **1996b**. Deletion of a B800-850 light-harvesting complex in *Rhodospirillum molischianum* DSM119 leads to "revertants" expressing a B800-820 complex: Insights into pigment binding. *Biochemistry* **35**:6500-6507.

Scheer, H. **1991**. Chlorophylls. CRC Press, Boca Raton.

Scheer, H. **2003**. The pigments. In *Light-Harvesting Antennas in Photosynthesis*. (Green, B. R., and Parson, W. W., ed). Kluwer Academic Publishers, Dordrecht. 29-81.

Scheuring, S., Goncalves, R. P., Prima, V., and Sturgis, J. N. **2006**. The photosynthetic apparatus of *Rhodopseudomonas palustris*: Structures and organization. *J. Mol. Biol.* **358**:83-96.

Scheuring, S., and Sturgis, J. N. **2005**. Chromatic adaptation of photosynthetic membranes. *Science* **309**:484-487.

Scholes, G. D. **2003**. Long-range resonance energy transfer in molecular systems. *Annual Review of Physical Chemistry* **54**:57-87.

Scholes, G. D., and Fleming, G. R. **2000**. On the mechanism of light harvesting in photosynthetic purple bacteria: B800 to B850 energy transfer. *J Phys Chem B* **104**:1854-1868.

- Schulten, K., and Karplus, M. **1972**. Origin of a low-lying forbidden transition in polyenes and related molecules. *Chem Phys Lett* **14**:305-309.
- Sener, M., Hsin, J., Trabuco, L. G., Villa, E., Qian, P., Hunter, C. N., and Schulten, K. **2009**. Structural model and excitonic properties of the dimeric RC-LH1-PufX complex from *Rhodobacter sphaeroides*. *Chem Phys* **357**:188-197.
- Shinichi, T. **2004**. <http://lipidbank.jp/image/VCA0010SP1107.gif>.
- Siebert, C. A., Qian, P., Fotiadis, D., Engel, A., Hunter, C. N., and Bullough, P. A. **2004**. Molecular architecture of photosynthetic membranes in *Rhodobacter sphaeroides*: the role of PufX. *EMBO J* **23**:690-700.
- Siefert, E., Irgens, R. L., and Pfennig, N. **1978**. Phototropic purple and green bacteria in a sewage-treatment plant. *Applied and Environmental Microbiology* **35**:38-44.
- Silber, M. V., Gabriel, G., Strohmam, B., Garcia-Martin, A., Robert, B., and Braun, P. **2008**. Fine tuning of the spectral properties of LH2 by single amino acid residues. *Photosynth Res* **96**:145-151.
- Sistrom, W. R. **1978**. Control of antenna pigment components. In *The photosynthetic bacteria*. (Clayton, R.K. And Sistrom, W.R., ed). Plenum Press, New York. 841-848.
- Stark, W., Kuhlbrandt, W., Wildhaber, I., Wehrli, E., and Muhlethaler, K. **1984**. The structure of the photoreceptor unit of *Rhodospseudomonas viridis*. *EMBO J* **3**:777-783.
- Strong, M., Sawaya, M. R., Wang, S., Phillips, M., Cascio, D., and Eisenberg, D. **2006**. Toward the structural genomics of complexes: crystal structure of a PE/PPE protein complex from *Mycobacterium tuberculosis*. *Proc Natl Acad Sci U S A* **103**:8060-8065.
- Sturgis, J. N., Hunter, C. N., and Niederman, R. A. **1988**. Spectra and extinction coefficients of near-Infrared absorption bands in membranes of *Rhodobacter sphaeroides* mutants lacking light-harvesting and reaction center complexes. *Photochem Photobiol* **48**:243-247.
- Sturgis, J. N., Jirsakova, V., Reiss-Husson, F., Cogdell, R. J., and Robert, B. **1995**. Structure and properties of the bacteriochlorophyll binding site in peripheral light-harvesting complexes of purple bacteria. *Biochemistry* **34**:517-523.
- Sturgis, J. N., and Niedermann, R. A. **1996**. The effect of different levels of the B800-850 light-harvesting complex on intracytoplasmic membrane development in *Rhodobacter sphaeroides*. *Arch Microbiol* **165**:235-242.
- Sturgis, J. N., and Robert, B. **1997**. Pigment binding-site and electronic properties in light-harvesting proteins of purple bacteria. *J Phys Chem B* **101**:7227-7231.
- Sundström, V., and van Grondelle, R. **1995**. Kinetics of excitation transfer and trapping in purple bacteria. In *Anoxygenic Photosynthesis Bacteria*, vol 2.

- Advances in Photosynthesis. (Blankenship, R.E., Madigan, M.T., and Bauer, C.E., ed). Kluwer Academic Publisher, Dordrecht. 350-372.
- Sundström, V., Pullerits, T., and van Grondelle, R. **1999**. Photosynthetic light-harvesting: Reconciling dynamics and structure of purple bacterial LH2 reveals function of photosynthetic unit. *J Phys Chem B* **103**:2327-2346.
- Tadros, M. H., Katsiou, E., Hoon, M. A., Yurkova, N., and Ramji, D. P. **1993**. Cloning of a new antenna gene cluster and expression analysis of the antenna gene family of *Rhodospseudomonas palustris*. *Eur J Biochem* **217**:867-875.
- Tadros, M. H., and Waterkamp, K. **1989**. Multiple copies of the coding regions for the light-harvesting B800-850 alpha- and beta-polypeptides are present in the *Rhodospseudomonas palustris* genome. *EMBO J* **8**:1303-1308.
- Takaichi, S., and Shimada, K. **1992**. Characterization of carotenoids in photosynthetic bacteria. In *Methods in Enzymology: Carotenoids, Part A Chemistry, Separation, Quantitation and Antioxidation*. (Packer, L., ed). Academic Press Inc., San Diego. 374-385.
- Tavan, P., and Schulten, K. **1986**. The Low-Lying Electronic Excitations in Long Polyenes - a Ppp-Mrd-Cl Study. *J Chem Phys* **85**:6602-6609.
- Tharia, H. A., Nightingale, T. D., Papiz, M. Z., and Lawless, A. M. **1999**. Characterisation of hydrophobic peptides by RP-HPLC from different spectral forms of LH2 isolated from *Rps. palustris*. *Photosynth. Res.* **61**:157-167.
- Tichy, H. V., Albien, K. U., Gadon, N., and Drews, G. **1991**. Analysis of the *Rhodobacter capsulatus* puc operon: the pucC gene plays a central role in the regulation of LHII (B800-850 complex) expression. *EMBO J* **10**:2949-2955.
- Tichy, H. V., Oberle, B., Stiehle, H., Schiltz, E., and Drews, G. **1989**. Genes downstream from pucB and pucA are essential for formation of the B800-850 complex of *Rhodobacter capsulatus*. *J Bacteriol* **171**:4914-4922.
- Tietz, C., Chekhlov, O., Drabenstedt, A., Schuster, J., and Wrachtrup, J. **1999**. Spectroscopy on single light-harvesting complexes at low temperature. *J Phys Chem B* **103**:6328-6333.
- Tunnicliffe, R. B., Ratcliffe, E. C., Hunter, C. N., and Williamson, M. P. **2006**. The solution structure of the PufX polypeptide from *Rhodobacter sphaeroides*. *FEBS Lett* **580**:6967-6971.
- Turro, N. J. **1991**. *Modern molecular photochemistry*. University Science Books, Sausalito.
- Valeur, B. **2001**. *Molecular fluorescence: principle and applications*. Wiley-VCH Verlag Weinheim.
- van Mourik, F., Hawthornthwaite, A. M., Vonk, C., Evans, M. B., Cogdell, R. J., Sundström, V., and Vangrondelle, R. **1992**. Spectroscopic characterization of the low-light B800-850 light-harvesting complex of *Rhodospseudomonas palustris* strain 216. *Biochim Biophys Acta* **1140**:85-93.

- van Oijen, A. M., Ketelaars, M., Köhler, J., Aartsma, T. J., and Schmidt, J. **1999a**. Spectroscopy of individual LH2 complexes of *Rhodospseudomonas acidophila*: localized excitations in the B800 band. *Chem Phys* **247**:53-60.
- van Oijen, A. M., Ketelaars, M., Köhler, J., Aartsma, T. J., and Schmidt, J. **1999b**. Unraveling the electronic structure of individual photosynthetic pigment-protein complexes. *Science* **285**:400-402.
- van Oijen, A. M., Ketelaars, M., Köhler, J., Aartsma, T. J., and Schmidt, J. **2000**. Spectroscopy of individual light-harvesting 2 complexes of *Rhodospseudomonas acidophila*: Diagonal disorder, intercomplex heterogeneity, spectral diffusion, and energy transfer in the B800 band. *Biophys J* **78**:1570-1577.
- van Stokkum, I. H. M., Scherer, T., Brouwer, A. M., and Verhoeven, J. W. **1994**. Conformational dynamics of flexibly and semirigidly bridged electron donor-acceptor systems as revealed by spectrotemporal parameterization of fluorescence. *J Phys Chem* **98**:852-866.
- Visscher, K. J., Bergstrom, H., Sundström, V., Hunter, C. N., and Vangronnelle, R. **1989**. Temperature-dependence of energy transfer from the long wavelength antenna Bchl-896 to the reaction center in *Rhodospirillum rubrum*, *Rhodobacter sphaeroides* (WT and M21 mutant) from 77 to 177 K, studied by picosecond absorption spectroscopy *Photosynth Res* **22**:211-217.
- Wang, Z. Y., Suzuki, H., Kobayashi, M., and Nozawa, T. **2007**. Solution structure of the *Rhodobacter sphaeroides* PufX membrane protein: implications for the quinone exchange and protein-protein interactions. *Biochemistry* **46**:3635-3642.
- Wassink, E. C., Katz, E., and Dorrenstein, R. **1939**. Infrared absorption spectra of various strains of purple bacteria. *Enzymologia* **7**:113.
- Webb, R. H. **1996**. Confocal optical microscopy. *Reports on Progress in Physics* **59**:427-471.
- Weiss, C. **1978**. Electronic absorption spectra of chlorophylls. In *The Porphyrins*. (Dolphyn, D., ed). Academic Press, New York. 211-223.
- Weiss, S. **1999**. Fluorescence spectroscopy of single biomolecules. *Science* **283**:1676-1683.
- Wörmke, S., Mackowski, S., Brotosudarmo, T. H. P., Jung, C., Zumbusch, A., Ehrl, M., Scheer, H., Hofmann, E., Hiller, R. G., and Brauchle, C. **2007**. Monitoring fluorescence of individual chromophores in peridinin-chlorophyll-protein complex using single molecule spectroscopy. *Biochim Biophys Acta* **1767**:956-964.
- Xie, X. S. **1996**. Single-molecule spectroscopy and dynamics at room temperature. *Accounts of Chemical Research* **29**:598-606.
- Youvan, D. C., and Ismail, S. **1985**. Light-harvesting II (B800-B850 complex) structural genes from *Rhodospseudomonas capsulata*. *Proc Natl Acad Sci U S A* **82**:58-62.

Zerlauskiene, O., Trinkunas, G., Gall, A., Robert, B., Urboniene, V., and Valkunas, L. **2008**. Static and dynamic protein impact on electronic properties of light-harvesting complex LH2. *J Phys Chem B* **112**:15883-15892.

Zhu, Y. S., Cook, D. N., Leach, F., Armstrong, G. A., Alberti, M., and Hearst, J. E. **1986**. Oxygen-regulated mRNAs for light-harvesting and reaction center complexes and for bacteriochlorophyll and carotenoid biosynthesis in *Rhodobacter capsulatus* during the shift from anaerobic to aerobic growth. *J Bacteriol* **168**:1180-1188.

Zigmantas, D., Read, E. L., Mancal, T., Brixner, T., Gardiner, A. T., Cogdell, R. J., and Fleming, G. R. **2006**. Two-dimensional electronic spectroscopy of the B800-B820 light-harvesting complex. *Proc Natl Acad Sci U S A* **103**:12672-12677.

---

## 10 Biography

---

### Personal data

Date-place of birth      23<sup>rd</sup> April 1981-Pati, Indonesia  
Nationality:                Indonesian  
Languages:                 Indonesian, Javanese, English, and German

### Educations

2007                    Begin PhD study under Marie Curie Research Training Network Scheme, University of Glasgow, Glasgow, UK  
2003-2006          Diplom (Equivalent to MSc) in Chemistry, Ludwig Maximilians Universität, Munich, Germany  
1998-2001        BSc in Chemistry, Satya Wacana Christian University, Salatiga, Indonesia

### Papers in international peer reviewed journals

V. Moulisová, L. Luer, S. Hoseinkhani, T.H.P. Brotosudarmo, A.M. Collins, G. Lanzani, R.E. Blankenship, R.J. Cogdell (2009) Low light adaptation: Energy transfer processes in different types of light harvesting complexes from *Rhodopseudomonas palustris*, *Biophys. J.* 97: 3019-3028

T.H.P. Brotosudarmo, R. Kunz, P. Böhm, A.T. Gardiner, V. Moulisová, R.J. Cogdell and J. Köhler (2009) Single-molecule spectroscopy reveals that individual low-light LH2 complexes from *Rhodopseudomonas palustris* 2.1.6. have a heterogenous polypeptide composition, *Biophys. J.* 97: 1491-1500

R.J. Cogdell, A.T. Gardiner, T.H.P. Brotosudarmo and H. Hashimoto (2008) A Comparative Look at the First Few Milliseconds of the Light Reactions of Photosynthesis, *Photochem. Photobiol. Sci.*, 7: 1150-1158

S. Wörmke, S. Mackowski, A. Schalter, T.H.P. Brotsudarmo, S. Johanning, H. Scheer and C. Bräuchle (2008) Single Molecule Fluorescence of Native and Refolded Peridinin-Chlorophyll-Protein Complexes, *J. Fluoresc.* 18: 611-617

S. Mackowski, S. Wörmke, A.J. Maier, T.H.P. Brotsudarmo, H. Harutyunyan, A. Hartschuh, A.O. Govorov, H. Scheer and C. Bräuchle (2008) Metal-Enhanced Fluorescence of Chlorophylls in Single Light-Harvesting Complexes, *Nano Lett.* 8(2):558-646.

T.H.P. Brotsudarmo, S. Mackowski, E. Hofmann, R.G. Hiller, C. Bräuchle and H. Scheer (2008) Relative binding affinities of chlorophylls in peridinin-chlorophyll-protein reconstituted with heterochlorophyllous mixtures, *Photosynth. Res.* 95(2-3): 247-52

S. Mackowski, S. Wörmke, T.H.P. Brotsudarmo, H. Scheer and C. Bräuchle (2008) Fluorescence spectroscopy of reconstituted peridinin-chlorophyll-protein complexes, *Photosynth. Res.* 95(2-3): 253-60

S. Mackowski, S. Wörmke, T.H.P. Brotsudarmo, C. Jung, R.G. Hiller, H. Scheer and C. Bräuchle (2007) Energy transfer in reconstituted peridinin-chlorophyll-protein complexes: ensemble and single-molecule spectroscopy studies, *Biophys. J.* 93(9): 3249-58

S. Wörmke, S. Mackowski, T.H.P. Brotsudarmo, C. Jung, A. Zumbusch, M. Ehrl, H. Scheer, E. Hofmann, R.G. Hiller and C. Bräuchle (2007) Monitoring fluorescence of individual chromophores in peridinin-chlorophyll-protein complex using single molecule spectroscopy, *Biochimica et Biophysica Acta (BBA) - Bioenergetics* 1767: 956-964

S. Wörmke, S. Makowski, T.H.P. Brotsudarmo, C.H. Bäuchle, A. Gracia, P. Braun, H. Scheer, E. Hofmann (2007) Detection of Single Biomolecule Fluorescence Excited through Energy Transfer: Application to Light-Harvesting Complexes, *Appl. Phys. Lett.* 90: 193901-3

T.H.P. Brotsudarmo, E. Hofmann, R.G. Hiller, S. Wörmke, S. Mackowski, A. Zumbusch, C. Bräuchle, H. Scheer (2006) Peridinin-Chlorophyll-Protein

Reconstituted with Chlorophyll Mixtures: Preparation, Bulk and Single Molecule Spectroscopy, *FEBS Letters* 580: 5257-5262

### **Papers in international peer reviewed conferences**

H. Scheer, T. Brotsudarmo, S. Mackowski, S. Wörmke, E. Hofmann, R.G. Hiller, C. Bräuchle (2007) Binding Affinities of Chlorophylls in Hetero-Chlorophyllous Complexes of Peridinin-Chlorophyll-Protein as revealed by Ensemble and Single Molecule Spectroscopy, In Abstracts: 14th International Congress of Photosynthesis, 22nd - 27th July 2007, Glasgow, PS3.52., *Photosynth. Res.* 91: 133-324